Titel der Arbeit:

Parametrisation of Gas Flares Using FireBIRD Infrared Satellite Imagery

Dissertation

zur Erlangung des akademischen Grades

doctor rerum naturalium

(Dr. rer. nat.)

im Fach Informatik

eingereicht an der

Mathematisch-Naturwissenschaftlichen Fakultät der Humboldt-Universität zu Berlin

von

Magister Agnieszka Kazimiera Soszyńska

Präsidentin der Humboldt-Universität zu Berlin

Prof. Dr.-Ing. Dr. Sabine Kunst

Dekan der Mathematisch Naturwissenschaftlichen Fakultät

Prof. Dr. Elmar Kulke

Gutachtern:

1. Prof. Dr. Ralf Reulke
2. Prof. Dr. Patrick Hostert
3. Prof. Dr. Michael Birk

Tag der mündlichen Prüfung: 30.06.2021

Parametrisation of Gas Flares Using FireBIRD Infrared Satellite Imagery

Agnieszka Soszyńska

September 2, 2021

Berlin, 25.02.2021

Ich erkläre, dass ich die Dissertation selbständig und nur unter Verwendung der von mir gemäß § 7 Abs. 3 der Promotionsordnung der Mathematisch-Naturwissenschaftlichen Fakultät, veröffentlicht im Amtlichen Mitteilungsblatt der Humboldt-Universität zu Berlin Nr. 42/2018 am 11.07.2018 angegebenen Hilfsmittel angefertigt habe.

Agnieszka Soszyńska

Berlin, 25.08.2021

Ich erkläre, dass die von mir in der Universitätsbibliothek abgegebene schriftliche und elektronische Version der Dissertationsschrift mit der angenommenen Dissertation übereinstimmt.

Agnieszka Soszyńska

Acknowledgements

In this complex and long process of my doctorate research, I was lucky to receive much help from many different people.

I would like to thank Prof. Ralf Reulke for all the care and advice he had for me in the process.

I am very grateful to Thomas Säuberlich for his help and ideas, which allowed this work to thrive.

Also, I would like to thank Christian Fischer for his suggestions and critical remarks, which polished the work.

Apart from at the working environment, privately, I was also surrounded by help and support. Especially my partner, Jan, deserves appreciation and gratefulness, for his suggestions, and corrections, as well as for emotional support.

I would like to specially thank Hartmut Hieronymus, because without his engagement in my research, the work and the experiments would not be the same.

Lastly, I would like to mention my parents, whose work and dedication allowed me to come this far.

Berlin, 02.09.2021
Agnieszka Soszyńska

Contents

List of Figures

List of Tables

Abbreviations

BAM	Federal Institute for Material Research and Testing (Bundesanstalt für Materialforschung und -prüfung)
BCM	billion cubic meters
CCD	charged couple device
CST	Central Standard Time
DLR	German Aerospace Center (Deutsches Zentrum für Luft- und Raumfahrt)
DMSP	Defence Meteorological Satellite Program
DN	digital number
ESA	European Space Agency
FOV	field-of-view
FRP	fire radiative power
LHV	gross calorific value
GGFR	Global Gas Flaring Reduction
GMES	Global Monitoring for Environment and Security
GSD	ground sampling distance
HTE	high temperature event
IFOV	instantaneous field-of-view
IR	infrared
LPG	liquid petroleum gas
LWIR	long-wave infrared
MAE	mean average error
MCM	million cubic meters
MTF	modulation transfer function
MWIR	mid-wave infrared
NASA	National Aeronautics and Space Administration
NEDT	noise equivalent temperature difference
NIR	near infrared
NOAA	National Oceanic and Atmospheric Administration
PSF	point spread function
RMSE	root-mean-square error
SNR	signal-to-noise ratio
SWIR	short wave infrared
TNT	Trinitrotoluene
TOA	top-of-atmosphere
USGS	United States Geological Survey
ZKI	Zentrum für satellitengestützte Kriseninformation

1 Introduction and motivation

The presented thesis is an analysis of routine gas flaring observed from space using infrared remote sensing satellite imagery. The thesis is structured as follows:

Chapter 1 describes gas flaring, its technologies and impact on the environment. Moreover, international activities towards limiting routine gas flaring processes are described, as well as possibilities of monitoring them, especially from space. At the end of the chapter, the research purpose and research focus are described.

Chapter 2 provides an overview of history of infrared remote sensing, remote sensing of high temperature events and remote sensing of gas flaring. The most important aspects of a sensor for gas flaring analyses are analysed in detail. A group of sensors is compared with respect to the above-mentioned features, in order to derive the best sensor for gas flaring parametrisation.

Chapter 3 describes the theory of signal processing chain in an infrared camera, lists and describes parameters of a gas flare flame relevant for remote sensing analyses and describes the procedure of image processing used to derive flame radiance, which is further used to calculate flow of flared gas. A method for calculating flow of flared gas is presented.

In **Chapter 4** the results of the conducted analyses are presented. First, a description of the experiments conducted is given, and results of the introductory experiments are presented, giving an overview on the general conditions for calculating gas flow from infrared (IR) imagery. In the next step, the model is used with imagery of industrial gas flares in two study areas, to prove the feasibility of the model to work with different sensors. Results from both sensors are compared for both study areas. Next, the results obtained are compared with results published by Caseiro *et al.* 2019. At the end of the chapter, sources of uncertainty are described.

Chapter 5 discusses the results and conclusions of comparison from previous chapter. The model proposed is analysed in detail, describing its pro's and con's. Special focus is laid on sensor parameters and design. Next steps for gas flaring research and further development and application of the method are described.

In the whole text, all illustrations are prepared by the author of this dissertation, unless stated otherwise in an according caption.

Abstract and conclusions of the chapter

Routine gas flaring is a process of burning natural gas, produced as a side-product of crude oil production and refinement. Flaring the associated gas is not the only solution for disposing of this product. There are multiple ways, in which this natural gas can be used instead of flaring it, but it can also be injected back into the rock formations, where it came from.

Gas flaring has a huge environmental impact from local to local scale. The process contributes to climate change and moreover causes health problems for people living in the neighbourhood of gas flaring activities. Monitoring and limiting gas flaring is an important subject for the international community. Many international organisations, such as World Bank, have conducted activities towards limiting routine gas flaring.

Monitoring of gas flaring can be done using remote sensing techniques. In this thesis, a model for parametrisation of gas flares using infrared remote sensing satellite imagery, is proposed. The focus of this thesis is twofold. First, sensor features and sensor design are considered in depth and the proposed method is adapted to the given sensor features. Second, the gas burning process and the corresponding flare flame is analysed in detail. The flame parameters are analysed and described, basing on the conducted experiments. Using the results from the field experiments, a method is proposed that allows calculating flow of the flared gas from satellite mid-wave infrared imagery. The method was developed using an experimental series and physical measurements of a gas flare.

1.1 What is gas flaring

In the broadest sense, flaring can be defined as a chemical process of high temperature oxidation reaction that burns combustible components, mostly hydrocarbons, or waste gases from industrial operations (Cheremisinoff 2013). The applications for flaring in the industry are numerous, starting from burning waste gases, managing waste streams from coal gasification plants, as support in testing of rocket engines, in maintenance of nuclear power plants, ammonia fertilizer plants, heavy water plants, starting the reactors in polymerisation facilities and more (Cheremisinoff 2013). Gas flaring is a general term, describing burning off the so-called associated gas, either to dispose of unwanted side products or as a means to ensure safety of the installation (Ghadyanlou & Vatani 2015). The so-called routine gas flaring (which is disposing of unwanted side products) is an often applied solution, especially in the oil industry. World Bank provides a more precise definition, which differentiates routine flaring from safety-related flaring: "Routine flaring of gas at oil production facilities is flaring during normal oil production operations in the absence of sufficient facilities or amenable geology to re-inject the produced gas, utilize it on-site, or dispatch it to a market" (World Bank 2016). The amounts of routinely flared gas are very high, they are often the majority of overall flaring. In Cameroon, for instance, routine flaring in 2017 is 100% of the flaring in total, according to World Bank (World Bank n.d.(b)). The proportion of flared gas can also change from day to day, as can be seen in Figure 1.

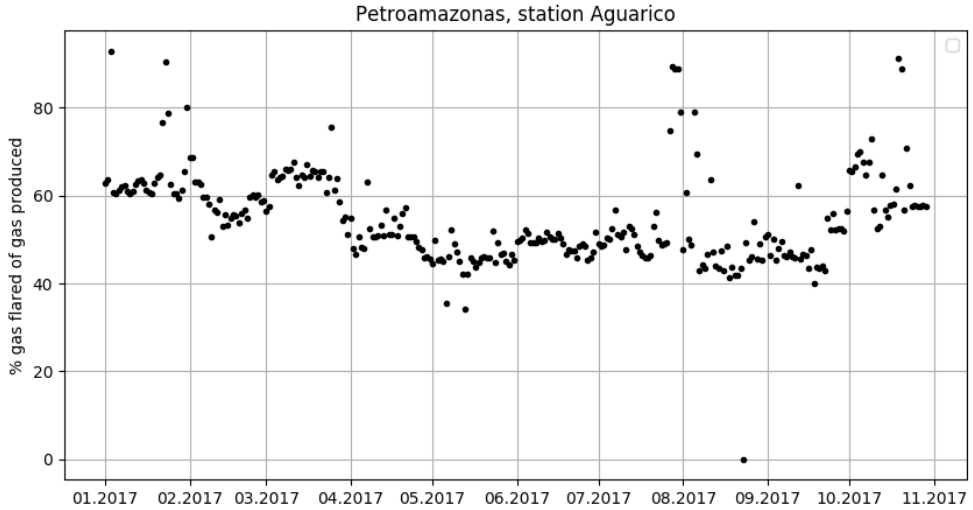

Figure 1: Flared gas as a percent of totally daily produced gas, in an example station: Aguarico. Data acquired from Petroamazonas EP.

Although in some cases flaring is inevitable due to safety reasons (Ghadyanlou & Vatani 2015; Zolfaghari *et al.* 2017), it is often possible to be reduced to minimum, by cutting off the routine flaring (Bjorndalen *et al.* 2005), which would be of advantage for the natural environment, local inhabitants and global climate. A more detailed analysis of consequences of gas flaring is provided in the section 1.3.

The presented dissertation focuses on monitoring the routine flaring. To avoid misunderstandings, henceforward the term gas flaring will be used to describe the routine gas flaring, understood as burning off the associated gas extracted as a side product during crude oil production.

In 2018, according to the World Bank, a total of 145 billion m^3 of natural gas was flared. Within last 5 years, this amount was relatively stable, with 2.3 billion m^3 standard deviation. The top 5 countries responsible for 55% of all the gas flared in 2018 were: Russia, Iraq, Iran, USA and Algeria. All of these countries increased the amount of total flared gas between 2014

and 2018[1]. There is however also a positive development: with a constant increase in a number of barrels produced per day since 1996, the amount of gas flared remains at a relatively stable level after a slight reduction between 2005 and 2010.

The gas, which is being flared, very often consists of at least 95% methane. Its exact constituents, nevertheless, can be numerous and diverse, and differ from region to region, but also even from station to station. As a side-product, this natural gas is not homogenised and its usage usually requires some purification. For the purpose of this research and modelling, the flared gas is assumed to be purely methane. This assumption is relatively safe (because the other components are usually only a small part of the overall mixture) and indispensable (because it is not possible to account for all the diverse mixtures that exist).

The associated gas does not necessarily need to be flared, there are alternative solutions. The gas can be processed and further utilized as an energy source. The processing required consists of removing water, CO_2 and natural gas liquids, such as hydrogen sulphide and hydrocarbons other than methane, e.g. propane. After such pre-processing, the gas can be further sent through pipelines, and sold. Alternatively, it is possible to produce electrical energy directly from the associated gas (without or with minimal pre-processing), which is then supplied to the electrical network. Another solution is to compress the pre-processed associated gas and sell it on the markets. The compression increases the energy density of gas and makes it more profitable on the market. Such gas can be used as car fuel or as an energy supply for power plants and domestic gas users. The last option is called gas-to-liquids, in which the associated gas is converted into a so-called syncrude (synthetic crude oil) or diesel after only little pre-processing and injected into an oil pipeline. More details on possibilities and requirements for using the associated gas can be found in the World Bank reports[2]

All the above-mentioned possibilities to use the associated gas can also be economically profitable. Studies suggest that the amount of the gas flared in Nigeria corresponds to loss of 2.5 billion US dollars per year (Collins & Oshodi 2010).With some investments into the infrastructure, the further selling of the gas or its processing products could bring additional profit to the economy.

1.2 Flaring technology

Websites providing an overview of technological and engineering aspects of gas flaring, such as "www.globalspec.com", describe some examples of different gas flare types. These include ground flares (enclosed design or equipped with an open pit), pit flares (equipped with burn pits), elevated flares (where the waste gas is transported to the top of the stack with a pipe or a vertical chimney and combusted), air assisted flares (in which the gas is premixed with air, enabling smokeless and most efficient combustion with the highest temperatures) and steam assisted flares (which use steam to increase the combustion efficiency, typically also smokeless and efficient)[3]. Apart from that, gas flares can be installed separately, in groups of stacks or even groups of multiple-nozzle flares together (see Figure 2).

[1]World Bank n.d.(a) `https://www.worldbank.org/en/programs/gasflaringreduction#7`

[2]World Bank 2018; Tractebel Engineering S.A. 2015; World Bank 2015.

[3]Engineering 360 n.d. `https://www.globalspec.com/learnmore/manufacturing_process_equipment/air_quality/gas_flares`

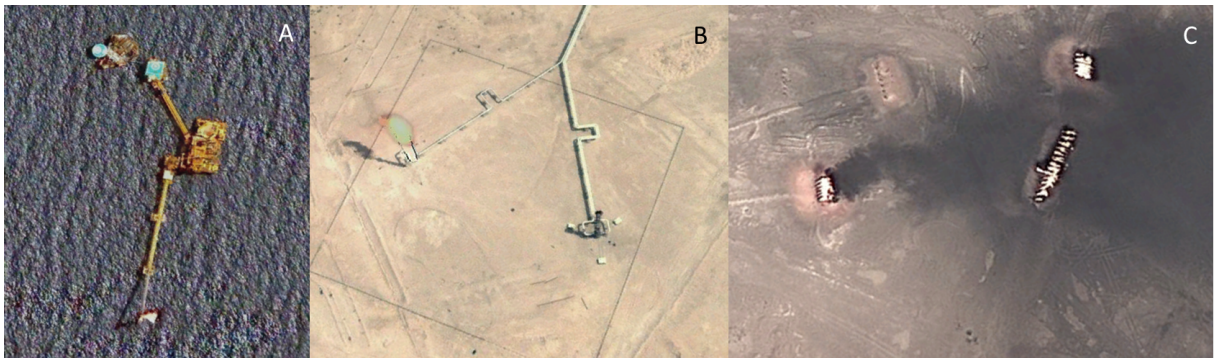

Figure 2: Examples of gas flares. A: gas flare on a sea platform (Source: *Google Earth: High Resolution World Imagery,* Maxar technologies, image taken on 10.06.2004), B: elevated individual stacks (Source: *Google Earth: High Resolution World Imagery,* Maxar Technologies, image taken on 15.05.2005), C: ground flares with open pits and multiple nozzles (Source: *Google Earth: High Resolution World Imagery,* Maxar Technologies, image taken on 01.09.2010).

All the different flare types have different characteristics, and hence, also different combustion conditions. If gas in a flare is premixed with sufficient amount of air before ignition, the combustion efficiency is higher, combustion temperature can reach its optimum and the number of combustion products are reduced. In a complete combustion reaction, the reaction products are H_2O and CO_2 only. The complete combustion reaction for methane is:

$$CH_4 + 2O_2 \rightarrow CO_2 + 2H_2O \tag{1}$$

The optimal combustion process, however, rarely takes place. Usually the combustion reaction is incomplete, and its product list becomes longer: starting from soot (C) and carbon monoxide (CO), it can also contain unburned pyrolysis products and partially oxidized compounds, which can be harmful for human health. Also, if combustion efficiency is low, some gas will be released into the atmosphere as in the venting process. A more detailed description of the combustion process taking place in flares can be found in Section 3.5. Leahey *et al.* 2001 state that the average efficiency of the flares is between 61% and 75%. In their research, they also provided a list of 61 combustion products measured on a specific site. Such flaring conditions lead to a smoky, harmful combustion such as can be seen in Figure 3.

Figure 3: Gas flare on an elevated stack. Due to incomplete combustion, significant amount of soot is being released in the form of smoke. Image source: Wikipedia Commons (Carter n.d.).

It is important to note that the combustion in gas flares can be almost constant over time, but can also be very variable. The flaring can be reduced or turned off, which is important to consider for modelling purposes (see Figure 4).

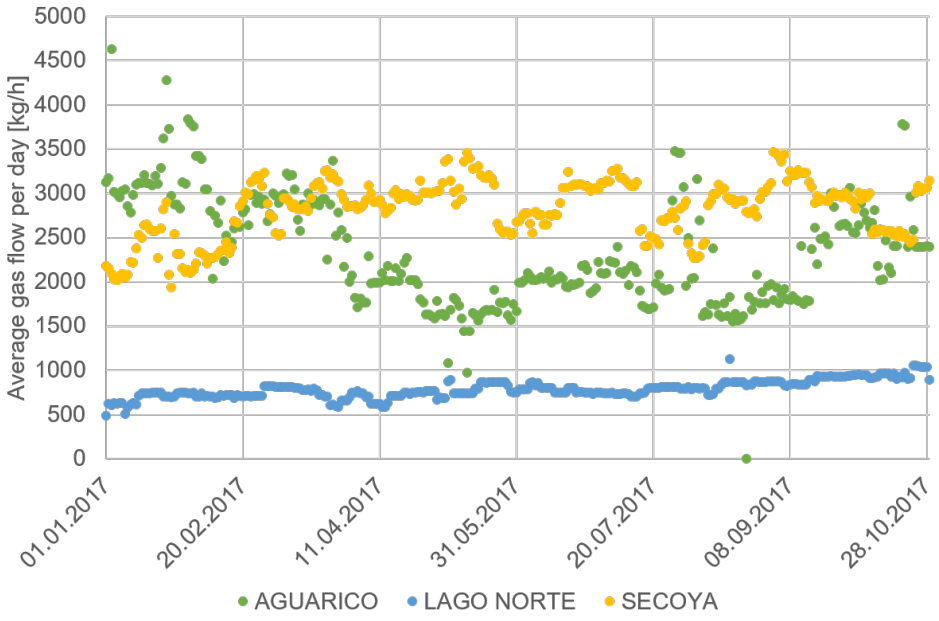

Figure 4: Daily average gas flow, an example of three flaring stations. Data acquired from Petroamazonas EP.

1.3 Environmental consequences of gas flaring

According to the Netherlands Environmental Assessment Agency, continuous gas flaring contributes to as much as 1% of the whole CO_2 yearly emission to the atmosphere (Olivier *et al.* 2012). As mentioned before, due to the often too low combustion efficiency, the CO_2 is not the only component which is released. Other components, such as methane, are even more harmful and have an even stronger impact on climate change. These immense amounts of the greenhouse gases, which are released during the flaring process, make gas flaring a significant contribution to the anthropogenic global warming effect (Ismail & Umukoro 2012).

Moreover, greenhouse gas emissions to the atmosphere are not the only negative impact factors on the natural environment. The list of other products of gas combustion in the surroundings of the flares contains sulphur dioxide (SO_2), multiple nitrogen oxides (NO_x), hydrogen sulphide (H_2S), volatile organic compounds, other hydrocarbons and heavy metals (Anejionu *et al.* 2015b). If analysing the effects of flaring on the local scale, the results are even more concerning. Ismail & Umukoro 2012 reviewed multiple research reports and articles on gas flaring consequences of local scale. They state that the amount of air pollutants in the vicinity of flaring stations contributes to a significant increase in lung diseases such as asthma and bronchitis. Other researchers found that flaring can also cause skin problems (Collins & Oshodi 2010). Some products of inefficient combustion are carcinogenic, and increased leukaemia cases have been noted in Nigeria are a result of gas flaring (Argo 2002). Furthermore, people suffer also indirectly from gas flaring. Agricultural yields are reduced due to constant air pollution, acidification of soil and water, and extinction of soil bacteria. Corrosion of the metal rooftops has also been noticed as a consequence of proximity of a flare (Ismail & Umukoro 2012; Anejionu *et al.* 2015b).

Obviously, the natural environment suffers as well: the heat stress connected to constant energy release has been connected to soil bacteria extinction and changes in the biotopes. Another effect is a decrease of plants bloom and fruit amount. Acidic rainfalls cause damage to the plants also in further distances than direct proximity of the flares (Ismail & Umukoro 2012; Anejionu *et al.* 2015b).

Last, but not least, the constant heat and noise emission is also a problem. Gas flares are often very close to housing areas, as can be seen in Figure 5, and according to the research and modelling done by Ismail & Fagbenla 2009 and other researchers cited in this paper, heat flux from the flare can even affect areas as far as 200 m distance from the stack.

More details on the environmental consequences of gas flaring, their modelling and results can be found in Anejionu *et al.* 2015b; Ismail & Umukoro 2012; Olivier *et al.* 2012; Leahey *et al.* 2001.

Figure 5: Gas flares in direct proximity of housing and agricultural production (Source: *Google Earth: High Resolution World Imagery,* Maxar technologies, image taken on 15.05.2005).

1.4 Global interests

Due to the huge environmental implications of the gas flaring process, a number of international organisations initiated joint actions against the routine gas flaring. An example of such an organisation is the Global Gas Flaring Reduction Partnership, initiated by the World Bank. The aim of the initiative is to increase the use of the associated gas, instead of flaring it. As the home page of the partnership states, "GGFR works to increase use of natural gas associated with oil production by helping remove technical and regulatory barriers to flaring reduction, conducting research, disseminating best practices, and developing country-specific gas flaring reduction programs"[4]. There are 16 governmental partners in the GGFR, including countries like Kuwait and Iraq, as well as regions such as Alberta (Canada). Furthermore, 13 companies belong to the group, such as BP, Shell and Kuwait Oil Company. The last sector of the partnership comprises 3 international organisations and institutions: European Union, World Bank and European Bank for Reconstruction and Development. The companies aim to end routine flaring of associated gas by 2030 and achieve an interim objective of 80% between 2010 and 2020, which some companies (e.g. Total) achieved already[5]. Among the information and resources provided by the GGFR are definitions, guidelines on measurement and technological possibilities for processing of the associated gas and its further usage.

Another important initiative of the World Bank is the "Zero Routine Flaring by 2030" scheme[6]. The partners in this initiative agree to eliminate routine flaring of associated gas by 2030. This initiative has altogether 32 governmental participants, 37 oil companies and 15 development institutions.

One of the most important purposes of all the initiatives is to support monitoring activities of the flaring process. The National Centers for Environmental Information National Oceanic and Atmospheric Administration (NOAA) provide a database with gas flaring information. The

[4] *Global Gas Flaring Reduction Partnership:* `https://www.worldbank.org/en/programs/gasflaringreduction#1`

[5] ibidem

[6] Zero Routine Flaring by 2030 `https://www.worldbank.org/en/programs/zero-routine-flaring-by-2030`

project was sponsored in 2012-2015 by the NOAA Joint Polar Satellite System proving ground program and GGFR providing a global map of gas flaring sites with parameters such as energy, flaring temperature and partly even flared gas volume[7]. Data is available for the period between March 2014 and December 2017, however a note on the website states that the results are to be considered as preliminary. Moreover, calculations of global gas flaring volumes have been published as a World Bank report for the years 1995-2006 and later an improved version for 1995-2009 followed. These global estimates have been made using the Defence Meteorological Satellite Program (DMSP) and details can be found in Elvidge *et al.* 2007; Elvidge *et al.* 2009b; Elvidge *et al.* 2009a.

However, legislative changes and decisions are mostly made on national levels. Many countries lack specific regulations on gas flaring and emissions related to it (Gerner n.d.). Some countries, such as Nigeria, set national limits not only for overall emission, but also for gas flare emissions specifically. The support of specific combustion technologies and practices, flaring locations, heat and noise regulation and other measures can be treated as other instances of regulating flaring. In some cases, the so-called environmental licences can be required to authorize flaring. Many regions require accurate reporting on flaring and venting, e.g. Alberta, Canada emphasises the need to report accurate measurements of flared and vented gas done with flare meters. These regulations in general are highly diverse in various countries and lack a common basis allowing comparisons and accurate overall analysis on a global scale.

1.5 Monitoring possibilities

Global monitoring of gas flaring is a crucial requirement to introduce regulations for gas flaring reduction. The knowledge on how much gas is being flared, locations of the flaring stations and their parameters is, however, not easy to obtain. Oil companies are registered in different countries and, consequently, are subject to variable regulations on reporting flaring processes. The reports are based on different time periods, units, and definitions, therefore unification of the data becomes an indispensable step, before starting any analysis. Local conflicts, corruption, and wars also cause additional complications for data reporting, as well as archiving. All the above-mentioned issues indicate a need for an objective data source for monitoring the gas flaring process globally, on a regular basis, independent of companies' and countries' internal regulations. This can be all provided by infrared satellite imagery.

Optical satellite sensors typically image in the visual spectral wavelengths, using light reflected from the objects on Earth's surface. Infrared sensors, however, record photons not only reflected from the objects, but also photons emitted by those objects (in longer infrared wavelengths). This group of sensors can be of particular use in gas flaring analysis, because gas flare flames emit significant amounts of energy, which can be recorded by these sensors.

The major challenge in this case is the ratio of the gas flare size to the sensor's pixel footprint area. Due to technological issues, spatial resolution of the infrared sensors typically is not smaller than 100 m ground sampling distance (GSD, corresponding to the distance, a pixel records radiation from on the ground in its instantaneous field-of-view (IFOV)), and therefore $10000\,\mathrm{m}^2$ area. Gas flares, however, usually have a flame area nearer to $30\,\mathrm{m}^2$. This makes the hot-spot-background ratio minuscule. Hence, high spatial resolution is an important factor when analysing gas flares.

The abundance of technological developments leads to diversity in systems and technologies used in different sensors. An overview of different satellite sensors that can be used, and a detailed description of their features crucial for the gas flaring analysis can be found in Section 2.3. It is advisable to consider the individual sensor's characteristics, when using the imagery for remote sensing purposes, and use tailored algorithms for deriving complicated quantitative parameters from the imagery.

[7]National Centers for Environmental Information National Oceanic and Atmospheric Administration n.d. `https://www.ngdc.noaa.gov/eog/viirs/download_viirs_flares_only.html`

1.6 Research purpose

The presented research aims to calculate gas flow from satellite infrared imagery. This is a highly complex subject, due to two aspects. First, the characterisation of a flame is difficult, and its radiative features as yet, are not well described in remote sensing literature. This leads to the first research question: what is the relation between the gas flow flared, and radiance recorded by a sensor? Second, the radiance image of a flare is influenced by the design of the sensor and pre-processing of the data products. This can lead to inaccuracies in analyses or even some sort of biasing, if this influence is not accounted for.

The development of the sensor science and modern IR sensor design, has resulted in the production of a wide variety of sensors, designs and products available for gas flaring research. In this dissertation, specific sensor parameters and features are investigated, and it is proposed to consider these features for the development of tailored algorithms. Therefore, one of the research questions is: what is the optimal sensor system for gas flaring parametrisation?

Gas flares are parametrised using two sensor systems, BIROS from the German Aerospace Center FireBIRD mission and NASA's VIIRS, to prove that the model developed is feasible to use with different sensor systems and provide similar results. Due to the fact that this research has been conducted within the frameworks of the FireBIRD project at the Institute for Optical Sensor Systems of the German Aerospace Center, where the BIROS sensor and its predecessors were designed and built, it was possible to accurately characterise the BIROS sensor, its design and imaging mode and analyse all the pre-processing steps, necessary to fully understand all the sensor related effects influencing the accuracy of the gas flaring parameters derived from the imagery.

As for the first aspect, several issues are also addressed in this dissertation. Until now, the research in gas flaring parametrisation was based on some kind of reference data containing information about the flared gas amount. Often, this reference data was bought or obtained from business partners or administration. The reference data available from administration, typically does not contain direct information of the flared gas per station in a given time window, but rather on gas production and sales, which allows indirect calculation of flaring in a broader time window (such as a day or a week). Oil companies do not always invest effort in reporting the gas flared, and if so it is rather reporting on broader time windows, for administrative reasons. A satellite image, however, is a recording of an instantaneous combustion of gas in the extremely narrow time window of the integrating time, which is shorter than a second. Therefore, the available algorithm includes a significant amount of uncertainty, due to reference data not accounting for the variability of the gas flow. In the presented research, the proposed model bases on an experiment, which ensures the highest accuracy of the reference data. Additionally, in the recent research publications, the properties of the flame have often been neglected, and the gas flares were considered spherical black bodies. For a better understanding of the physical flame parameters influencing the signal recorded in the image, the proposed method bases on an experimental series describing the parameters of the flame in multiple scales: from the ground, from an aerial survey, and from a satellite. Basing the proposed method on an experimental series allows the most accurate parametrisation of the variables included, and therefore deriving the most transparent algorithm, based on physical variables measured, and known sensor features. Lastly, the sources of uncertainty of the model are analysed.

2 Remote sensing of gas flaring

In the following chapter, an introduction to the history of IR remote sensing is presented. Remote sensing of gas flaring originates in the fire remote sensing. Research in remote sensing of gas flaring can be divided into three groups basing on the purpose of the research. These groups are: (1) detecting and locating gas flares, (2) estimating gas flaring parameters, such as fire temperature, area, and fire radiative power (FRP), and (3) calculating the flared gas volume. One of the most popular methods for parametrising gas flares is the bi-spectral method (proposed by Dozier 1981), which originates in vegetation fire remote sensing. This method has been adapted for the analysis of gas flares i.a. by Elvidge *et al.* 2016, which allowed the creation of a global gas flaring database, updated until the end of 2017. The majority of the publications concerning calculating the amount of gas flared bases on linear models, where some kind of satellite image product represents the measured variable, and reported information on gas flared amount are used as reference data to calibrate the model. However, several research publications suggest that in order to calculate the flared gas volume, one needs a specialised model including the properties of the combustion process.

In the second part of the chapter, a group of sensors is compared, with respect to the properties crucial for gas flaring analysis. The features important for remote sensing of gas flaring are: spectral wavelength sensed, dynamic range, and spatial resolution. BIROS, VIIRS, SLSTR, LANDSAT-8, MODIS and MSI sensors are characterised and data from these sensors is analysed, in order to reveal two sensors which are the best feasible for gas flaring analysis. Among this group of sensors, BIROS and VIIRS have the best characteristics for this purpose, due to relatively high spatial resolution, high dynamic range and adjustments toward avoiding saturation, and spectral bands in the most suitable wavelength ranges. At the end of the chapter, features of a hypothetical, optimal sensor for gas flaring research are proposed.

2.1 The historical evolution of remote sensing research on gas flaring

IR imaging for remote sensing was initiated approximately a century ago, in the context of research for military purposes during the World War I. After S.P. Langley invented a bolometer sensitive to thermal spectral wavelengths in 1880, IR cameras were increasingly employed for tactical purposes and installed on balloons and aircraft; they were even mounted on pigeons. During the World War I, both sides of the conflict used thermal imaging to recognise people. A rapid development in the thermal remote sensing was triggered off by the invention of a detector element during the World War II. Furthermore, the global conflict brought one other significant change: the requirement of specialised personnel was recognised and addressed: staff trained for the acquisition and interpretation of aerial imagery (also thermal) was employed by the armies.

During the Cold War, the first scientific and environment-related research was conducted by R. Colwell (Colwell *et al.* 1956). A number of U.S. companies (e.g. Texas Instruments Inc.) developed thermal sensors, which were primarily installed on aircraft. Thermal imagery, however, remained classified and unreachable for the broad public until around the 1960s. Oil companies turned out to become the first major clients of thermal imagery after the data became public. The NASA project Television IR Operational Satellite of 1960 initiated the era of infrared sensors in space. Even though this particular sensor had an operational life of several weeks, its descendants appeared numerous and in rapid succession, enabling broader scientific research and widening public interest in thermal imagery. One of the first scientifically oriented missions equipped with a thermal infrared sensor was the Heat Capacity Mapping Mission, launched in 1978. The mission focused on geological issues. During the same year, NASA's Nimbus 7 was launched with a payload that included thermal spectral bands for the monitoring of the sea-surface temperature. Currently, according to the CEOS database, there are 37 sensor types in

space recording in mid-wave IR (MWIR) spectral range and around 45 in long-wave IR (LWIR)[8]. Further reading about the history of remote sensing and thermal remote sensing can be found in Jensen 2007; Madry 2013; Campbell & Wynne 2011.

Applications of thermal remote sensing are numerous, and include, apart from the military, vegetation analyses, sea-surface-temperature observation and more. One of the most important applications of infrared data is fire remote sensing. Vegetation fires, especially in remote and scarcely populated areas, are often detected late and can also be extremely difficult to extinguish. The forest fires in Siberia in the summer of 2019, which altogether covered an area of 2.6 million hectares and took over a month to extinguish, provide an expressive example of such a vegetation fire. In such crisis situation, infrared satellite data can be used for mapping fire areas and estimating their severity. Using such maps can help the fire fighting teams in orientation and planning the extinguishing. Maps of fire areas are produced and can be used already: the DLR initiative Center for Satellite Based Crisis Information (ZKI) provides maps of fires from satellite and aerial imagery. For example, the images of the Lübtheen fire in July 2019 were taken almost at the same time as some experiments for the presented thesis were conducted. The resulting map presented in Figure 6, provides information for the local firefighters and authorities, both to help to extinguish the fire and assessing the losses.

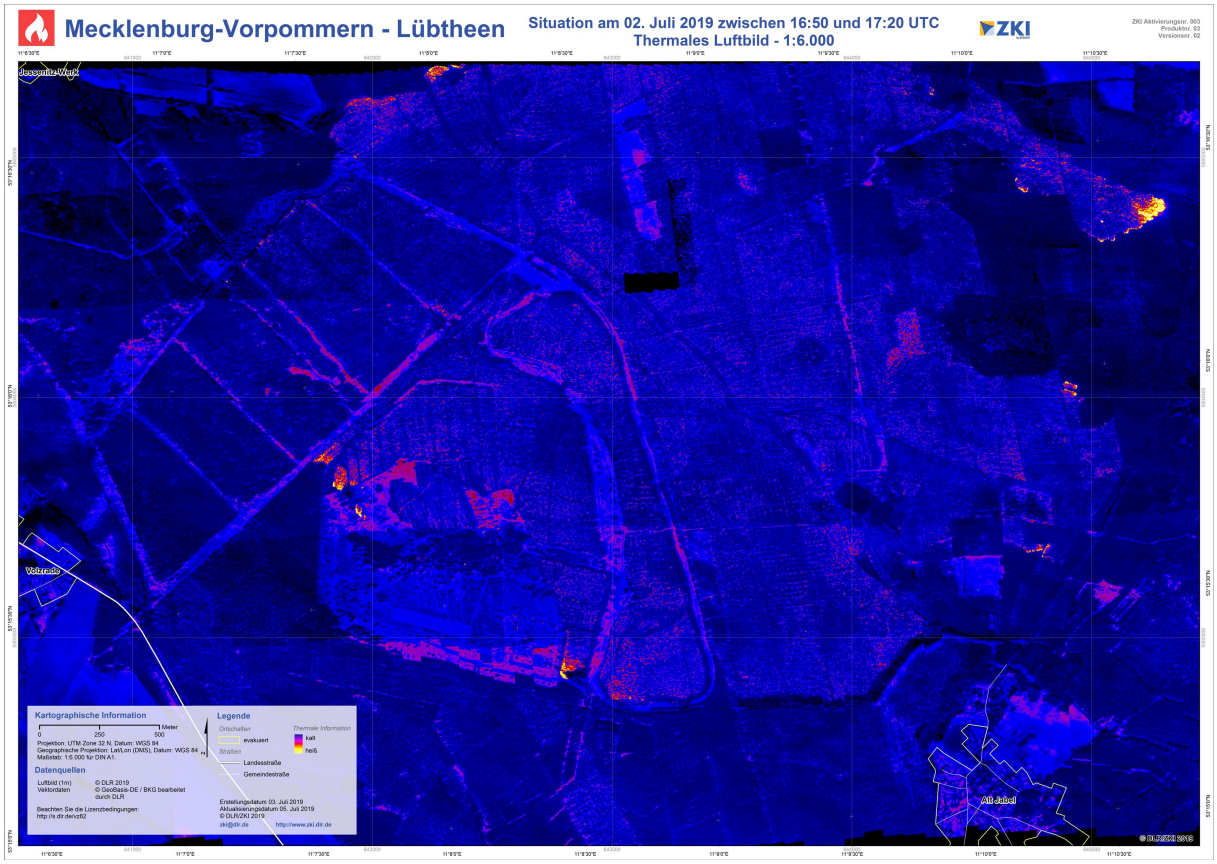

Figure 6: The ZKI map of the Lübtheen fire, created using aerial imagery and cameras, which were also used for experiments in the presented dissertation. Copyright: ZKI/DLR.

A typical vegetation fire, such as a grass fire, releases approximately 18 MJ energy per kilogram of burned dry fuel, as stated by Trollope *et al.* 2002, although this value increases with the fuel load per ha and decreases with increasing moisture of the fuel. Such an extreme energy release can be recorded by a satellite sensor quite accurately, even though the amount of radiation reaching the sensor is already decreased due to fuel and water content vaporisation,

[8] *The CEOS database* `http://database.eohandbook.com/index.aspx`

atmospheric absorption and imperfect emissivity of the source. According to Wooster *et al.* 2013, typical vegetation fire temperatures are 1000 K for an active flame and 600 K for a smouldering flame.

In the last decades, a number of algorithms for fire remote sensing was developed. These algorithms are used to estimate the fire radiative power (FRP), fire area, burned area, and fire temperature using data from different sensors, and different methodologies. One of the most important algorithms for fire analysis is the so-called bi-spectral method proposed by Dozier, which was later developed and adjusted for different satellite sensors. The bi-spectral method bases on an assumption that the pixel radiance value is a mixture of signals from the fire and from the background. Both radiating objects (fire and background) are assumed to radiate like black bodies. The strength of a signal of both objects is proportional to the ratio between the area of the object and the area of a pixel footprint on the ground. Therefore, a signal recorded in a pixel is a sum of the Planck curves of both objects, including their area proportions, as illustrated in Figure 7. The dashed lines illustrate the parts of the signal coming from the fire (orange) and from the background (green). The resulting pixel signal is a sum value, taking into account the proportions of the fire area and background area. In an image, only the radiance values recorded in gives spectral bands can be measured. In case of BIROS, two spectral bands in IR sensor are present: MWIR and LWIR (in Figure 7 presented as red point markers). It is important to note that this method is cluster-based. This means that the information illustrated in Figure 7 are spread over several pixels and need to be integrated, in order to avoid information loss. Additional information (e.g. on the background temperature) can be taken from the surrounding pixels, which typically contain only signal from the background.

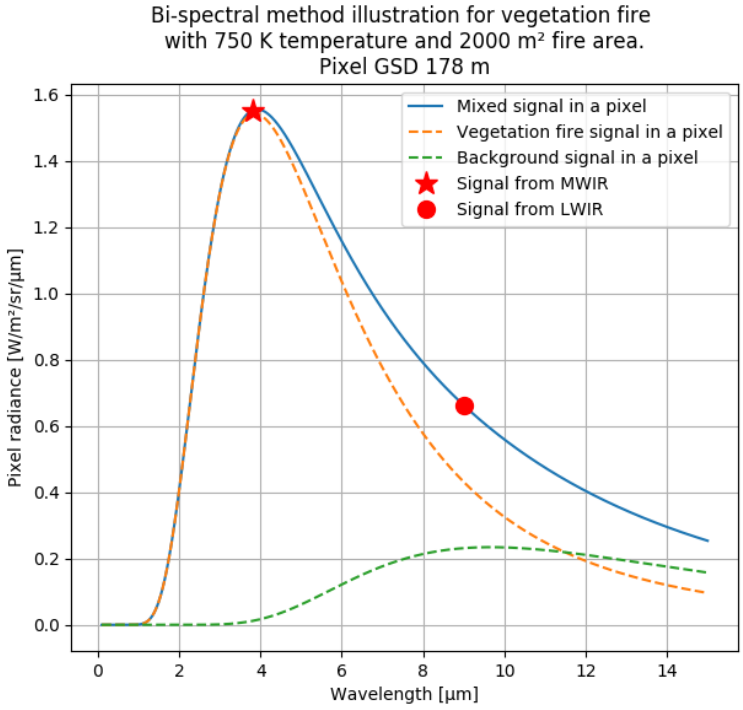

Figure 7: Bi-spectral method illustration for a hypothetical vegetation fire.

Zhukov *et al.* 2006 adapted the algorithm for the FireBIRD precursor: the BIRD sensor system. The development included, amongst other things, a method of separating false-alarm pixels from sun glint and is adapted to the geometric characteristics of the FireBIRD sensors, containing information of the point spread function (PSF) of the system.

Another group of the active fire algorithms bases on brightness temperature, calculated from the radiance values using Planck's function. Such algorithms assume that the brightness

temperatures calculated for both the MWIR and LWIR spectral bands should be similar, as long as no fire is present within the pixel. The threshold of difference between the two brightness temperature values basing on two spectral bands informs of the presence of the fire. A weakness of such algorithms is the fact that a difference in the brightness temperature can also be caused by sun glint effects (Wooster *et al.* 2012).

Fire detection algorithms sometimes base on fixed thresholds estimated for a particular geographic area (e.g. using data from the Advanced Very-High-Resolution Radiometer (AVHRR) satellite instrument as in Flannigan & Haar 1986). Changing seasons, which cause changes in the radiation, and the fact, that the fixed thresholds can only be applied for the same specific geographic area, are a weak spot of this group of algorithms.

Contextual active fire detection algorithms apply the method of a fixed threshold on fire pixels and add additional thresholding on the surroundings to detect false alarms (Wooster *et al.* 2013). The latest algorithms base also on statistical information on potential fire pixels and clusters or derived feature-based information as an addition to contextual thresholding, such as in Zhukov *et al.* 2006; Wooster *et al.* 2012.

2.2 Remote sensing techniques for gas flaring research

A very specific type of fire is a gas flare flame. The first detection of gas flares from space was realised in 1978 by Croft using DMSP and LANDSAT Multispectral Scanner System sensors (Croft 1978). Later on, gas flares were also identified in the AVHRR imagery by Matson & Dozier 1981. Remote sensing techniques have evolved strongly since then, and so has their contribution to the gas flaring analysis. With the designing and construction of new infrared sensors, the research opportunities have substantially widened. Research in the remote sensing of gas flaring concentrates on four major purposes:

1. Detecting and locating flares (e.g. Casadio *et al.* 2012b; Anejionu *et al.* 2014; Anejionu *et al.* 2015a; Chowdhury *et al.* 2014)

2. Estimating flaring parameters, such as flaring temperature (e.g. Casadio *et al.* 2012b; Elvidge *et al.* 2009b; Anejionu *et al.* 2014; Anejionu *et al.* 2015a; Elvidge *et al.* 2011; Elvidge *et al.* 2013; Elvidge *et al.* 2016; Casadio *et al.* 2012a)

3. Estimating flared gas volumes (e.g. Elvidge *et al.* 2009b; Anejionu *et al.* 2015a; Elvidge *et al.* 2011; Caseiro *et al.* 2019)

4. Assessing the environmental consequences of flaring (e.g. Anejionu *et al.* 2015b; Haus *et al.* 1998).

2.2.1 Detecting and locating gas flares

The detection of gas flares is a derivative of lessons learned from the research on fire remote sensing. Initially, the detection of gas flares from space developed from fire detection algorithms. Anejionu *et al.* 2014 describe four major categories of algorithms used for fire detection, which can also be used for gas flare detection. The first category consists of single band algorithms, such as the one developed by Malingreau & Tucker 1988 for mid-infrared AVHRR band 3 (3.75 µm). However, such algorithms require a specialised sensor, because the data is otherwise often saturated. Band 3 in AVHRR was not designed for fire recognition and therefore, it saturates already at a brightness temperature of around 325 K. The second category bases on multiple spectral bands, typically all from the infrared spectrum. Such algorithms combine thresholds from one or multiple bands and derive information from multiple bands to detect fire. Contextual algorithms are another category of algorithms used for fire detection. This approach allows the dynamic adaptation of thresholds depending on local conditions from surrounding pixels. Such an algorithm was used for MODIS active fire detection (Giglio *et al.* 2003). The last class of

algorithms are subpixel fire detection algorithms, which focus on fires of smaller sizes (of less than the sensor's ground sampling distance, GSD). The principle is derived from the assumption that the pixel contains signal from the fire as well as from the background. These algorithms often also use multiple bands for solving the equations, such as in the bi-spectral method. Nowadays, the applied techniques usually mix at least two of the above-mentioned classes, e.g. as in the fire algorithm developed by Zhukov *et al.* 2006 and implemented on data from modern FireBIRD satellites, TET-1 and BIROS.

Casadio *et al.* 2012b applied a single band thresholding together with contextual interpretation (temporal persistence of hot signal and presence of industrial infrastructure) to globally detect gas flares for the period 1991-2009, using the Along Track Scanning Radiometer (ATSR). The weakness of the algorithm, as stated by Anejionu *et al.* 2014, is the coarse spatial resolution, making it difficult to detect flares in a more detailed way. In another study, Casadio *et al.* 2012a, detected gas flares in the North Sea by using ATSR data in combination with the Synthetic Aperture Radar (SAR). They analysed the development of gas flaring between 1991 and 2010.

More recently, gas flaring research was also conducted using sensors with higher spatial resolution, such as the LANDSAT series. Anejionu *et al.* 2014 used LANDSAT data to detect and locate gas flares and obtained 87% user's accuracy and RMSE of location ± 24 m. Chowdhury *et al.* 2014 also developed a method for LANDSAT-8 data for detecting flares. In this work, accuracy was tested manually by comparing the detected locations to high resolution imagery from Google Maps and Bing Maps, as well as flaring reports.

Examples of other works on detecting gas flares are: Elvidge *et al.* 2013 with thresholding on short-wave IR (SWIR) spectral band, Caseiro *et al.* 2018, where the authors used contextual thresholding to detect flares, and Fisher & Wooster 2018, who used multiband thresholding for LANDSAT-8 OLI sensor and single band thresholding for MODIS and VIIRS sensors.

2.2.2 Parametrising gas flares and calculating flared gas volume

The methods for calculation of gas flaring parameters from remote sensing imagery can be divided into two groups, basing on the approach used. The first approach can be understood as a black-box approach. In this case, some kind of product, derived from satellite imagery, is used to fit a model (mostly a linear model) on reference data. This approach is used in the vast majority of all attempts to parametrise gas flares. The second approach is to consider the parameters of the combustion process. There are only a few publications, which use this approach, mostly because estimating the parameters of combustion is highly complex and often requires a specialised experimental series.

In 2007, the first attempt of mapping gas flares and deriving their parameters on a global scale was made by Elvidge *et al.* 2007 using the DMSP sensor. The amount of flared gas was calculated in billion cubic meters (BCM) using a linear model fitted on reference data from GGFR and the sum of lights measured by the sensor. The overall accuracy of the model was calculated to be around ± 1.6 BCM. However, the validation of the map highlighted some issues: the imagery for the mapping could only be taken by night (in order to avoid errors due to the solar reflection), city lights were often interpreted as gas flares, and the very high radiation of the flares often led to saturation in the pixels, which made it impossible to derive any precise parameters from this value (Anejionu *et al.* 2015a; Anejionu *et al.* 2014; Elvidge *et al.* 2007; Elvidge *et al.* 2009b). The database was later improved and extended to 2008 (Elvidge *et al.* 2009a). The accuracy of the inter-calibration of the data used was improved in the second edition, and more attention was given to off-shore flares and saturated pixels. The publication proposed methods for the reconstruction of saturated pixels, which applies to around 15% of the data.

The MODIS sensor was used in different research analyses (e.g. Anejionu *et al.* 2015a; Elvidge *et al.* 2009a; Elvidge *et al.* 2011) with varying results. Gallegos *et al.* 2007 correlated

the reported flared gas volume with MODIS thermal anomaly detections, and stated that some reference gas flares with known flared gas volumes were not detectable. The authors discouraged the further use of MODIS data for gas flaring research. Furthermore, Elvidge *et al.* 2011 attempted calculated flaring volumes using MODIS image data and the methodology developed in Elvidge *et al.* 2007 and concluded that MOD14 fire data is insufficient for this purpose. The authors, however, also developed a technique for MODIS fire products which yielded a reasonable detectability of gas flares and a potential for higher volume estimation accuracy.

Anejionu *et al.* 2015a used the MODIS sensor to detect gas flares and calculate flared volumes. The authors developed MODET (MODIS Flare Detection Technique) and MOVET (MODIS Flare Volume Estimation Technique) algorithms, which used thresholding and high pass filtering for flare detection and fitting a linear model on statistical measures of flare radiance for calculating flared volume. Using these methods, 90.7% of flares were detected correctly and the estimated error of flared gas volume was on average 0.058 BCM.

Casadio *et al.* 2012a, apart from detecting flares, also analysed a possibility to estimate gas flaring parameters, such as the rate of heat released from gas combustion within the flame, and combustion efficiency, as in Beychok 2005[9]. The calculations in the study remain purely theoretical, but the authors conclude that it is possible to calculate the above-mentioned parameters.

A significant work on mapping gas flares and deriving flaring parameters was carried out by NOAA Earth Observation Group, using VIIRS data. Their effort yielded a global database of gas flares, including flaring parameters[10]. The potential of VIIRS sensor for analysing gas flares was described in Elvidge *et al.* 2013; Elvidge *et al.* 2016 and Elvidge *et al.* 2017.

Elvidge *et al.* 2016 calculated the flared gas volume per year for individual flaring sites in BCM. For the estimation of flared gas volume, reference data set acquired from Cedigaz was used[11]. It is important to know, that the Cedigaz database only includes flared gas volumes at oil fields and can thus contain a bias related to flaring non-associated gas and flaring at gas condensate fields, which were not included (Elvidge *et al.* 2016). The accuracy of the calculated flared gas volume was reported to be ± 9.5%. The authors noted the following shortcomings of VIIRS data:

1. It is not possible to derive flaring parameters for small flares,
2. In case of rarely active flares, the temporal sampling of the sensor is not frequent enough,
3. Due to a very wide field-of-view, some flares may be located at high viewing angles in the image. This leads to inaccuracies in detecting flaring parameters.

The accuracy of flared gas estimations from the VIIRS sensor was tested by Brandt 2020. The author found that 80.8% of flare estimates lie within 0.5 orders of magnitude of reported volumes. Additionally, the author stated that a systematic bias occurs in smaller flares and the relative error ratios are also higher in case of smaller flares.

Zhang *et al.* 2015 proposed a physical based method basing on physical properties of methane (heating value), combustion efficiency, proportion of energy released in form of radiation, and ratio of the total surface area of the flare, which emits radiation, to the satellite-sensing cross-section area. In the model proposed, the authors use an adapted bi-spectral method to derive flaring parameters: fire temperature and fire area. The adaption of the bi-spectral method included considering the emissivity of the flare and of the background, as well as atmospheric transmittance. For gas volume calculation, following Equation (2) was used:

[9]Unfortunately, the original publication of Beychok 2005, which was self-published online, is not accessible anymore

[10]available at `https://www.ngdc.noaa.gov/eog/viirs/download_global_flare.html`

[11]for further information, see `https://demo.cedigaz.org/`

$$r_{CH_4} = \frac{\alpha}{C \cdot F} \cdot \frac{f_e \cdot A \cdot \sigma \cdot T^4}{E_{out}} \tag{2}$$

where:

r_{CH_4}	methane consumption [mol/s]
α	ratio of the total surface area of the flare to the satellite sensing cross-section area [1]
C	combustion efficiency [1]
F	efficiency factor of the total reaction energy emitted as radiation [1]
f_e	effective fractional area of the flare [1]
A	area of the pixel containing the flare [m^2]
σ	Stefan-Boltzmann constant [$W/m^2/K^4$]
T	absolute temperature of a flare [K]
E_{out}	total energy output of the gas burning reaction [J/mol]

The values of the parameters F, C, and α were assumed. To obtain flare parameters (f_e and T), a non-linear equation is solved for a pixel with a flare, and a neighbouring pixel without a flare. Parameter A is dependent on sensing parameters. The total energy output of the burning reaction E_{out} was assumed to be the lower heating value of methane. The obtained results correlate with the reference data on $R^2 = 0.75$ with mean relative error of -0.5 million cubic meters per day [MCM/day]. The authors compared their results with the VIIRS NightFire algorithm and state that their results bring a significant accuracy improvement, with respect to the reference data. The correlation of the results calculated with the VIIRS NightFire algorithm and the reference data is only $R^2 = 0.37$ and $R^2 = 0.26$ respectively, for the first and the second processing version of the NightFire product, and the mean relative error -0.73 MCM/day and 7.63 MCM/day. In this study, a sensitivity analysis regarding atmospheric correction is conducted, which concludes that an atmospheric correction improves the accuracy around 10%. Another interesting subject of discussion is the influence of wind. The analysis conducted by Zhang *et al.* 2015 suggests that there is no significant co-variation between the calculated amount of gas flared and wind speed.

Caseiro *et al.* 2018 slightly changed and adapted the method developed by Elvidge *et al.* 2013 for VIIRS data, to apply to SLSTR data. The main difference to Elvidge *et al.* 2013 was using clusters of pixels for deriving gas flare parameters instead of single pixels. This change in the methodology accounts for the differences in the results: first, SLSTR detected less gas flares than VIIRS, because the SLSTR algorithms aggregate neighbouring pixels into a single cluster, and second, the derived gas flaring temperature was systematically lower than the one from VIIRS database. The authors derived flaring temperature, area, and FRP to describe gas flares.

In another study, Caseiro *et al.* 2019 calculated flare parameters, including flared gas volume per year, by using a method developed by Elvidge *et al.* 2013, again with adaptions of the methodology as in Caseiro *et al.* 2018. In this case, the flared gas volume was calculated basing on the persistence of a hot-spot, derived from the number of observations in SLSTR data. The yearly global flaring volume estimated by Caseiro *et al.* 2019 was around 10% lower than the one reported by Elvidge *et al.* 2016.

Other studies, which used the method developed for the VIIRS database, are those by Lagutin *et al.* 2020, and by Sharma *et al.* 2017, where the results were compared to those obtained from MODIS data.

Until now, LANDSAT imagery, which has a potential for achieving a higher accuracy in parametrising gas flares due to its higher spatial resolution, was mainly used to detect, identify and locate flares, but not to derive gas flaring parameters. An exception to this, is the study of Peremitina *et al.* 2018, where flared gas volumes have been estimated with LANDSAT-8 data of Western Siberia by using a regression model. In this research, reference data from official reports

of the Department of Subsoil Use and Natural Resources of the Khanty-Mansiysk Autonomus Okrug was used. The author fitted a linear model on the number of identified flares, using flared gas volume per quarter of a year as a reference. The relative error of their estimation was 40%. Quantitative analysis of radiance values was not included into the methodology in this study.

Among gas flaring researchers in remote sensing, there is also a discussion on how the combustion process influences the accuracy of derived gas flaring parameters. For instance, Kumar *et al.* 2020 analysed the influence of smoke on FRP estimations. The authors stated that the presence of dark, sooty smoke can lower the detection rates of gas flares and cause an underestimation of FRP values, especially in emergency flaring. However, the estimations with MWIR spectral band were less influenced by smoke as the estimations with SWIR bands. This result suggests that the calculation of gas flaring parameters may be more beneficial using MWIR bands instead of SWIR, despite the Planck curve of a gas flare peaking in the SWIR range.

2.2.3 Summary of methods applied

As can be concluded from the studies described above, the approaches to calculate flared gas volume can be divided into two groups: approaches based on regression modelling, and modelling flaring radiation using physical properties. In the first case, a linear model is fitted using reported flaring volume as reference data and different independent variables, e.g. radiance or radiance derivatives (such as FRP) (e.g. Elvidge *et al.* 2016), statistical measures of flare radiance (e.g. Anejionu *et al.* 2015a), the sum of lights (e.g. Elvidge *et al.* 2007) or even the number of flare detections over time (e.g. Peremitina *et al.* 2018; Elvidge *et al.* 2013; Caseiro *et al.* 2019). Calculating flared gas volume based on a linear model is a more straightforward approach, and is easier to apply, but contains a considerable possibility of a bias, due to errors in reference data, undersampling, not taking radiance values into consideration, or not taking radiative properties of a flame into consideration.

The second approach is to calculate the radiated energy of a flare, by modelling the combustion process. This approach is proposed by Casadio *et al.* 2012a and Zhang *et al.* 2015. Modelling combustion is a highly complex subject, requiring a deeper understanding of the physics of combustion and all the variables influencing it. Zhang *et al.* 2015 made an attempt at this, by using assumed values of the parameters of combustion, derived from other research publications.

Within those two approaches, there are also different methods with respect to what type of data should be used, what flare parameters should be considered, and in what way they should be calculated.

In most of the studies described above, radiance (or its derivatives, e.g. statistical measures of hot-spot radiance) is used as a measured variable (Elvidge *et al.* 2016; Elvidge *et al.* 2013; Zhang *et al.* 2015; Fisher & Wooster 2018; Anejionu *et al.* 2015a). In some studies, other variables are used, e.g. sum of light, or number of detections in a given time window (e.g. Caseiro *et al.* 2019; Elvidge *et al.* 2007; Elvidge *et al.* 2009a; Peremitina *et al.* 2018).

The VIIRS gas flaring database is created using a multi-band approach based on Planck curve fitting (Elvidge *et al.* 2016), which allows calculating fire area and fire temperature. Also, Zhang *et al.* 2015 derive the same fire parameters with an adapted bi-spectral method. Fisher & Wooster 2018 state, however, that these parameters are irrelevant for gas volume calculation. Instead, the authors list a number of advantages for using a MWIR-based single band algorithm for deriving FRP instead of a multi-band approach. The authors state that using only one band is beneficial in gas flaring analysis, because it allows avoiding errors due to spatial misregistrations between the spectral bands. Apart from that, the use of a single MWIR band allows to avoid the stronger noise in LWIR spectral bands. Also, this approach is beneficial in case of targets with low intensity or small spatial coverage with respect to the pixel area.

Another aspect, visible in this chapter, is that a group of sensors can be used for studying gas flares. The feasibility of these sensors for gas flaring research is often disputed (e.g. whether

it is possible to detect weaker flares in daytime with the VIIRS sensor in Chowdhury *et al.* 2014, whether MODIS data should be used for the parametrisation of gas flares in Elvidge *et al.* 2011 and Gallegos *et al.* 2007, etc.).

Therefore, the author of this dissertation decided to conduct a comparison of data from a group of sensors and their features with respect to their feasibility for gas flaring research, which is presented in the next section.

Lastly, parametrisation of gas flares can be done using daytime, as well as nighttime imagery. However, using nighttime imagery has several important advantages over the daytime imagery:

1. In shorter infrared wavelengths, some parts of solar reflection contribute to the overall signal recorded in the daytime imagery. This is the case, e.g. in MWIR spectral bands. Deriving flare signal from a pixel including not only background radiation, but also background solar reflection is more challenging, than in pixels with only background radiation (as in nighttime images). More on influence of solar reflection in the images can be found in 5.7.

2. Solar radiation causes warming up of the surfaces. A warmed up background surface may be more challenging to subtract from the flare signal than a cold one, due to a weaker contrast between the hotspot and the background.

3. In some cases, sun glint may appear. In such case, a very bright spot in the image (imitating a real hot-spot) may be mistaken with a gas flare.

Researchers have attempted to use nighttime imagery for gas flare parametrisation in several studies, e.g. Elvidge *et al.* 2013; Casadio *et al.* 2012b, but some studies on daytime images appeared as well (e.g. Chowdhury *et al.* 2014).

2.3 Opportunities for gas flaring research

The recent development in technology enabled the design and production of a group of sensors that can be used for gas flaring analyses. These sensors differ in design and optical features. In this chapter, six satellite sensors are compared, with respect to the most relevant features for gas flaring analyses.

The sensors taken into consideration are:

1. BIROS, Bispectral InfraRed Optical System, from German Aerospace Center mission FireBIRD. The sensors in FireBIRD mission were designed for detection and analyses of high temperature events (HTE) and was used for such analyses since the launch (e.g. Plank *et al.* 2016; Klein *et al.* 2017; Fischer *et al.* 2017; Plank *et al.* 2017; Lorenz *et al.* 2018; Frauenberger *et al.* 2018; Halle *et al.* 2018; Fischer *et al.* 2018; Plank *et al.* 2019). BIROS is a pushbroom sensor with special adjustments towards avoiding saturation in HTE. The sensor is equipped with two spectral bands in IR: MWIR (3.4-4.2 µm) and LWIR (8.6-9.4 µm) and three in VIS-NIR region: green (0.46-0.56 µm), red (0.565-0.725 µm) and NIR (0.79-0.93 µm). The VIS-NIR bands detector is a charge-coupled device (CCD), and the MWIR-LWIR detector is a Mercury-Cadmium-Telluride (HgCdTe). One very important feature of the sensor is the fact that the detectors are aligned in a staggered array. This means that even though the sampling distance is in fact around 350 m, the final products are recalculated to 175 m, due to partially overlapping pixels. This feature also leads to redundant recording of each point in the image. BIROS has an orbit of around 500 km altitude.

2. LANDSAT-8, the eighth satellite in the USGS/NOAA LANDSAT series. LANDSAT-8 is equipped with 11 spectral bands in two sensors: OLI (Operational Land Imager) and TIRS (Thermal InfraRed Sensor). LANDSAT series provides data for scientific research of Land-Use-Land-Cover and multiple other purposes, continuously since 1972. LANDSAT-8 is a

pushbroom sensor, with silicon PIN detectors for bands 1-5 and 8 and HgCdTe for bands 6, 7 and 9 (recording in SWIR and LWIR spectral range). Bands relevant for gas flaring analyses are B6 (further related to as SWIR1) (1.57- 1.65 µm) and B7 (further related to as SWIR2) (2.11- 2.29 µm) and bands relevant for background temperature estimation: B10 (10.6- 11.2 µm) and B11 (11.5- 12.5 µm) LANDSAT-8 has an orbit of 709 km altitude. A complete description of the sensors can be found on the sensor's website[12]. LANDSAT-8 was used in the analyses of gas flaring and fires in several studies so far (e.g. Schroeder *et al.* 2016; Mallinis *et al.* 2018; Song *et al.* 2015; Kumar & Roy 2018; Kochergin *et al.* 2017; Anejionu *et al.* 2014; Chowdhury *et al.* 2014; Kumar *et al.* 2020; Sofan *et al.* 2020; Lee & Small 2019; Fisher & Wooster 2018).

3. VIIRS, Visible Infrared Imaging Radiometer Suite, is a whiskbroom scanning radiometer, created by the Rayethon company and operated by NOAA and NASA for scientific purposes, especially for weather, vegetation and Land-Use-Land-Cover analyses. The sensor is equipped with 22 spectral bands in two spatial resolutions (moderate: 750 for the "M" bands and imaging: 375 for the "I" bands). SWIR, MWIR and LWIR bands of the sensor dispose of HgCdTe detectors. Bands relevant for gas flaring analyses are M10 (1.58-1.64 µm), M11 (2.23- 2.28 µm), M12 (3.61- 3.79 µm),M13 (3.97- 4.13), I3 (1.58- 1.64 µm) and I4 (3.55- 3.93 µm). Another group of bands is relevant to determine the background temperature: M14 (8.4- 8.7 µm), M15 (10.26- 11.26 µm), M16 (11.54- 12.49 µm) and I5 (10.5- 12.4 µm). VIIRS has an orbit of 829 km altitude. It is the most frequently used sensor in gas flaring research. For instance, this sensor was used by, e.g. Elvidge *et al.* 2011; Elvidge *et al.* 2016; Baugh 2015; Faruolo *et al.* 2020; Brandt 2020; Facchinelli *et al.* 2020; Zhang *et al.* 2015.

4. MODIS, Moderate Resolution Imaging Spectroradiometer, operated by NOAA. MODIS was launched already in 1999, and was technically replaced by VIIRS, even though it remains operational. MODIS is a whiskbroom scanner, imaging in 36 spectral bands in three different spatial resolutions. Bands relevant for gas flaring are B6 (1.628-1.652 µm), B7 (2.105-2.155 µm), B20 (3.66-3.84 µm), B21 (3.929-3.989 µm), B22 (3.929-3.989 µm), B23 (4.02-4.08 µm) and for background signal analysis B29 (8.4-8.7 µm), B30 (9.58-9.88 µm), B31 (10.78-11.28 µm) and B32 (11.77-12.27 µm). The detector type for the bands interesting for gas flaring analysis is also HgCdTe. MODIS operates from a 705 km orbit. MODIS was used in gas flaring research in e.g. Anejionu *et al.* 2014; Sharma *et al.* 2017; Anejionu *et al.* 2015a; Anejionu *et al.* 2013; Fisher & Wooster 2018; Faruolo *et al.* 2018.

5. Sentinel-3 SLSTR, Sea and Land Surface Temperature Radiometer. SLSTR is one of the two sensors (together with OLCI, Ocean and Land Colour Instrument) of the Sentinel-3 mission. It belongs to the ESA Copernicus (previously GMES, Global Monitoring for Environment and Security) programme and is operated by Eumetsat. Its primary objective is to provide data for sea surface temperature and analyses. Spectral bands relevant for gas flaring are S5 (1.58-1.64 µm) and S6 (2.23-2.28 µm), S7 and F1 (3.54-3.94 µm) and S8 (10.47-11.24 µm), S9 and F2 (11.57-12.48 µm) relevant for background analysis. SLSTR detectors are photovoltaic and photoconductive HgCdTe. The sensor operates from an 800-830 km orbit. The data from SLSTR were used in gas flaring research by Caseiro *et al.* 2018; Caseiro *et al.* 2019; Fisher & Wooster 2019.

6. Sentinel-2 MSI, MultiSpectral Instrument. There are two satellites carrying the MSI sensor: Sentinel-2A and Sentinel-2B. The sensors in these two satellites differ slightly in recorded spectral ranges (see details in Appendix A). Operated by Eumetsat, the sensor was designed and built by Airbus. The applications for the data are land monitoring, maritime monitoring, emergency management and security. This sensor is equipped with 13

[12] `landsat.gsfc.nasa.gov/landsat-8/`

spectral bands, of which B11 (≈1.6 µm) and B12 (≈2.2 µm) are relevant for gas flaring[13]. The GSD of these two bands is 20 m, which is the lowest number of all analysed sensors. The SWIR bands have a HgCdTe detector. Until now, there are no publications on gas flaring with data delivered by Sentinel-2 MSI, but high spatial resolution and the presence of spectral bands in the SWIR region prove a potential for this purpose.

A detailed comparison of the sensors, listed above, can be found in Appendix A. In order to validate the sensor's feasibility for gas flaring research, the following aspects need to be taken into account:

1. spectral wavelength sensed,
2. dynamic range of the sensor,
3. spatial resolution, i.e. GSD,
4. temporal resolution, i.e. how often the sensor is able to image the same spot on Earth.

These parameters will be discussed in detail within the following sections.

2.3.1 Spectral wavelength sensed

A gas flame is a strong luminous radiation source. Most studies consider flames to be black bodies (e.g. Elvidge *et al.* 2007), some other treat them as grey bodies proving that flame emissivity is dependent on different parameters, such as flame depth (see: Johnston *et al.* 2014 for further details). In any case, the radiation of a gas flame is formed mainly by Planck's law, rather than special spectral features. Therefore, the choice of the spectral bands for gas flare analyses mainly depends on the flame temperature and atmospheric windows.

Gas flaring researchers do not exactly agree on the temperature of the flares. Fisher & Wooster 2018 state that using SWIR wavelengths is probably more accurate for flares of over 1500 K. Elvidge *et al.* 2016 state as well, that the best wavelength for sensing gas flares is rather SWIR, and their estimation of flaring temperature is as high as 1800 K.

In an attempt to parametrise gas flares in the North Sea, Casadio *et al.* 2012a estimated the temperature of the recorded flares. They calculated the modal value for all the results to be ≈1300 K with a standard deviation of 100 K. However, it is important to note that in this research, the emissivity of the flame was not considered. Including this parameter (with value $\varepsilon = 0.8$) would increase the flaring temperature to around 1400 K.

Division & Leahey 1985 found the average radiation temperature of a flame in field test to be around 1300 K, but a deviation to even 1150 K was noted during wind gusts.

The suggestions on the temperature of gas flaring vary mainly between 1200 K and 1800 K. The most suitable wavelength for analyses consequently varies between 2.4 µm and 1.6 µm.

[13]The exact wavelengths for each band are slightly different for each of the two satellites equipped with MSI sensor. For S2A the B11 band is 1.568-1.659 µm and B12 is 2.115-2.290 µm, whereas for S2B the wavelengths are 1.563-1.657 µm for the B11 band and 2.093-2.278 µm for the B12 band.

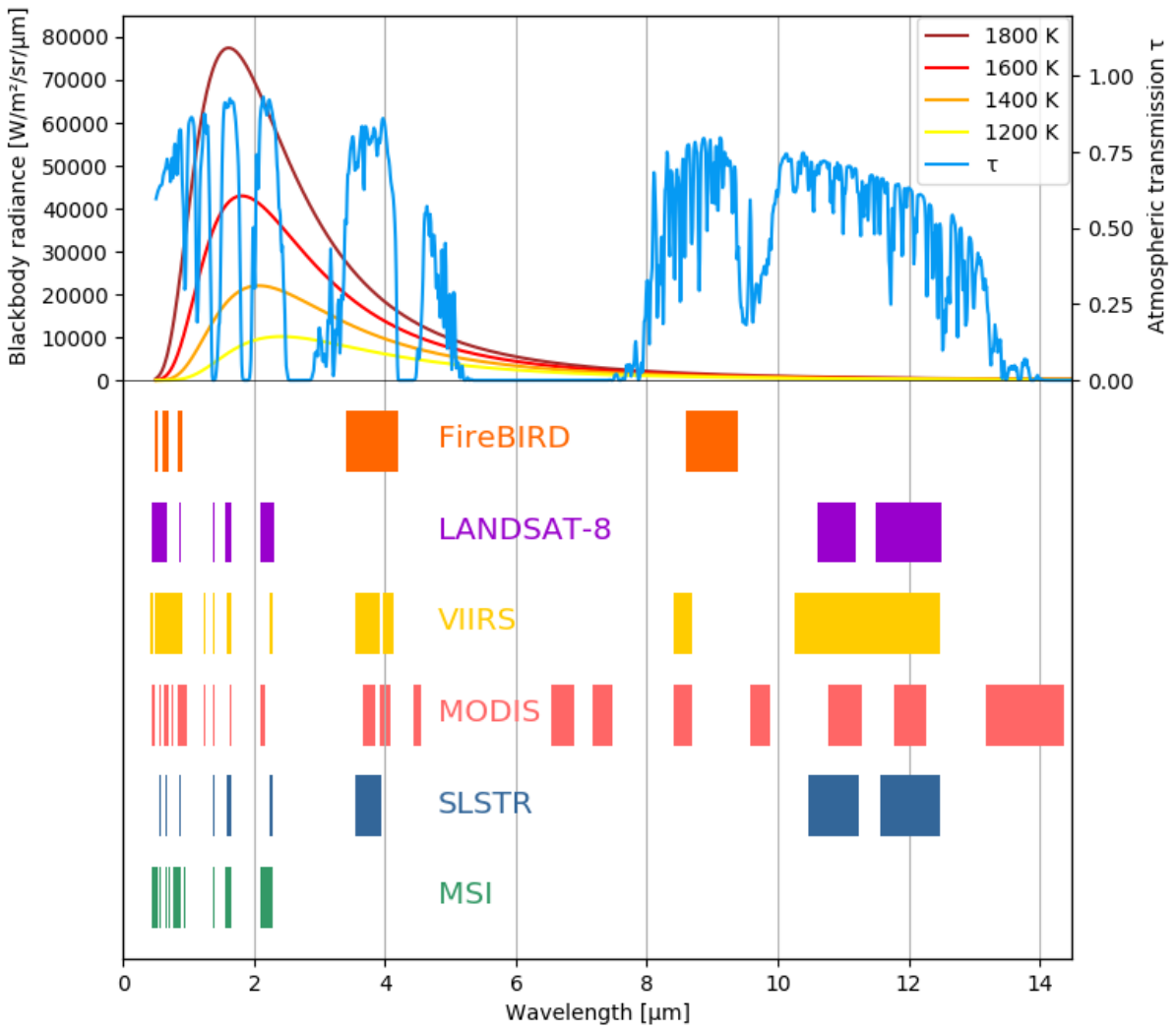

Figure 8: Spectral bands of available sensors in comparison to typical flare (Planck) curves and atmospheric windows. The transmittance of the atmosphere is depicted with the blue line. Graphic adapted from Soszyńska 2017.

As can be seen in Figure 8, there are two atmospheric windows in this range: 1.45 - 1.75 µm and 2.00 - 2.45 µm. In these two windows, almost all the compared sensors (apart from FireBIRD) have spectral bands.

Most of the compared sensors have very narrow spectral bands in the SWIR region and broader bands in the MWIR region. Apart from MSI, all sensors also have at least one spectral band in the LWIR region. For parametrisation of the flame itself, the LWIR region is not very helpful, however it can be used in calculating the background signal.

There is, however, one certain aspect of sensing in SWIR rather than in other, longer wavelengths, which leads to uncertainty in the analysis. As Schott 2007 states, the shorter the wavelength, the bigger the proportion of reflected light in the overall radiation of the object. This means that if imaging in daytime (as most of the sensors with SWIR bands do), the recorded signal is a mixture of light radiated by the flame, light reflected by the flare infrastructure (which mostly consists of metal) and light reflected by the background (e.g. sand or water, etc.), apart from the flare radiation. This issue is smaller in MWIR wavelengths, because the proportion of the reflected light is a lot smaller than the radiated light. In SWIR wavelengths, the amount of reflected light is also very specific with respect to the infrastructure and materials used in the

flaring set-up, e.g. the albedo of the surface. This means that each flare depicted in a SWIR image can have a different bias, possibly causing a significant decrease in overall accuracy of the analysis. Therefore, it is advisable to use data from both the SWIR and the MWIR spectral range for gas flaring analyses.

2.3.2 Dynamic range

For gas flaring research, it is crucial to design the sensor in a way that it is able to record very high temperatures as well as low (normal) temperatures of the background, and to avoid saturation. This can be done e.g. by adjusting the integrating time or adding a high temperature mode. Saturation causes errors in the analysis, because the pixel values do not behave linearly with growing energy. If an image is saturated, part of the energy is not recorded and parameters, such as FRP and gas flow, will have huge errors. In some cases, even pixels with low-end saturation occur (see Figure 9). The origin of this behaviour is not exactly clear.

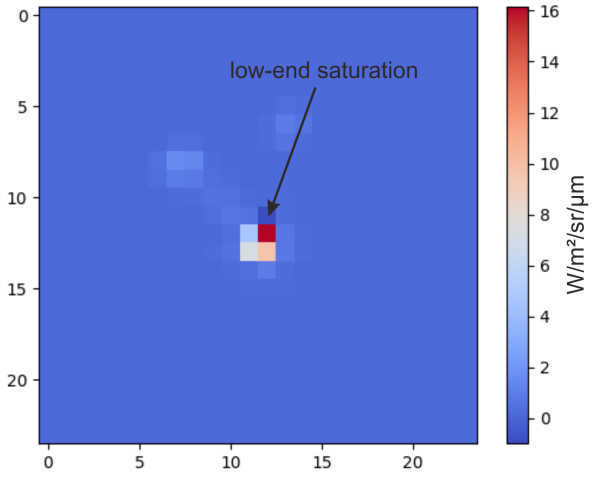

Figure 9: Upper-end and low-end saturation in LANDSAT 8 imagery (SWIR2 band).

In case of the LANDSAT-8 OLI sensor (which includes two SWIR spectral bands), the images of the gas flares are usually saturated. Figure 10 presents the possible energy loss due to the saturation in the LANDSAT-8 image. An integral of the blue line (here a simplified two-dimensional version is presented) would be the real radiance of the flare, but the saturation allows integrating only the red line of the real image profile. This can cause an underestimation of the flare radiation of even two magnitudes.

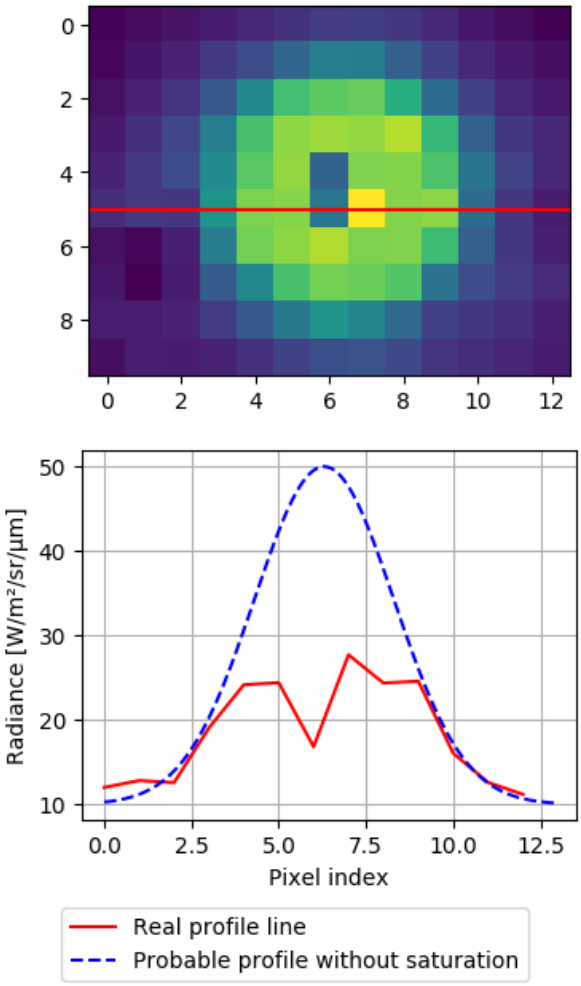

Figure 10: A saturated LANDSAT-8 image, with a flare (above). Profile of the saturated flare signal in the LANDSAT-8 image, and a probable real profile.

A quick calculation allows seeing what values could be theoretically recorded by the LANDSAT-8 sensor.

Table 1: Calculation of pixel radiance in SWIR bands of LANDSAT 8. Due to the PSF effects, this value can be divided into several neighbouring pixels.

	SWIR1 1.57- 1.65µm	SWIR2 2.11- 2.29µm
Blackbody radiance L [W/m²/sr/µm]		
Background 300 K	1.48E-06	7.88E-04
Gas flare 1600 K	4.16E+04	3.94E+04
Area A [m²]		
Background 300 K	880	880
Gas flare 1600 K	20	20
Emissivity ε [1]		
Background 300 K	0.96	0.96
Gas flare 1600 K	1	1
Spectral range $\Delta\lambda$ [µm]	0.08	0.18
Atmospheric transmission $\tau_{(\lambda)}$ [1]	0.97	0.97
Radiant flux $\Phi = L \cdot A \cdot \Delta\lambda \cdot \varepsilon \cdot 2\pi$ [W]		
Background 300 K	6.30E-04	7.53E-01
Gas flare 1600 K	4.18E+05	8.92E+05
Overall power in pixel $E = \Phi_{\text{bkg}} + \Phi_f$ [W]	4.18E+05	8.92E+05
Top-of-Atmosphere (TOA) pixel radiance $L_{\text{px}} = E/(A_{\text{bkg}} + A_f)/2\pi/\Delta\lambda$ [W/m²/sr/µm]	897.26	850.33

Morfitt *et al.* 2015 state that the saturation limit in SWIR bands of LANDSAT-8 are 71.3 W/m²/sr/µm for SWIR1 and 24.2 W/m²/sr/µm for SWIR2. The calculated values depicted in Table 1 obviously exceed these limits.

To assess the suitability of LANDSAT-8 data for gas flare parametrisation, a set of 10 scenes over the Persian Gulf region was analysed with respect to upper-end and low-end saturation. The results of this analysis are presented in Table 2 below. As can be seen, only three images did not have any upper-end saturation at all. At the same time, all the analysed images did exhibit low-end saturation. Moreover, in 5 cases, all the identified flares exhibited low-end saturation.

Table 2: Analysis of saturated pixels in LANDSAT-8 scenes of Persian Gulf.

Datum	Number of flares identified	Upper-end saturation	Low-end saturation
14.07.2018	31	7	27
02.10.2018	15	1	14
21.12.2018	14	0	14
06.01.2019	30	9	24
11.03.2019	30	11	26
27.03.2019	12	0	12
14.05.2019	11	2	11
03.09.2019	12	1	12
19.09.2019	11	3	11
14.04.2020	13	0	11

Due to the fact, that the origins of the low-end saturation are not entirely understood, it is rather untrustworthy to ignore this phenomenon and use the imagery for gas flares parametrisation.

The following sensors have certain adjustments towards avoiding saturation by high temperatures:

1. VIIRS, which has low- or high-gain settings for the M13 band, depending on the radiance level. The documentation states that it saturates with temperatures above 659 K (Schroeder & Giglio 2017).

2. BIROS, which has an automatic Hot-Area-Mode for high temperature events in both IR spectral bands.

3. MODIS band 21 (3.929 - 3.989 µm) has an increased dynamic range avoiding saturation in order to be used for analyses of the high temperature events. However, this spectral band is noisier as the band 22 (which has the same spectral wavelength, but not the increased dynamic range) (Anejionu *et al.* 2015a).

4. The Sentinel-3 bands F1 and F2 (active fire bands) have an increased dynamic range (in comparison to S7 and S8, which are based on the same detectors).

The limits of saturation for the listed sensors can be found in Appendix A and detailed calculations for a theoretical gas flare signal for the relevant bands of these sensors can be found in Appendix B. These calculations allow the conclusion that only BIROS, VIIRS and SLSTR can be used for the parametrisation of gas flares without the risk of saturated data.

2.3.3 Spatial resolution

The spatial resolution is considered one of the most important aspects for the accuracy of gas flaring analysis. As mentioned above, gas flares are very small sources of radiation, in comparison to GSD of a thermal IR sensor. Typically, sensors record radiation from an area limited by a square, whose edges have the dimension of the GSD. Let us assume a gas flare of 20 m^2 and 1300 K, recorded in a pixel.

Table 3: Proportion of a 20 m^2 flare flame in a theoretical pixel.

GSD	GSD^2	Proportion of an area of 20 m^2 in a whole pixel (GSD^2)
50	2500	8.00E-03
100	10000	2.00E-03
200	40000	5.00E-04
500	250000	8.00E-05
1000	1000000	2.00E-05

As can be seen from Table 3, the ratio between the flare signal and the background signal in a pixel is extremely low, causing practical difficulties for analyses. In theory, if we take a BIROS MWIR pixel as an example, we get 0.5 $W/m^2/sr/µm$ radiance in a pure "background" pixel with 300 K temperature and 3.0 $W/m^2/sr/µm$ radiance in a mixed pixel with a 20 m^2 flame of 1600 K (assuming black body radiation). Practically, the gas flare signal is blurred over neighbouring pixels. This process is depicted in Figure 13 and described in Section 3.1.

The GSD is a product of detector dimensions and telescope strength. The size of an IR detector is constrained in production due to the fact that it should not be below the wavelength, in which it is recording. This could cause a reduction in signal recording and a higher Signal-to-Noise Ratio (SNR). Henceforth, the bigger the pixel size, the stronger, bigger and more expensive the telescope required to obtain a higher spatial resolution. Small satellites are rarely equipped with very strong telescopes. Most of the GSDs of modern thermal satellite sensors vary between 1000 m and 60 m. A GSD comparison of the seven compared sensors is presented in Figure 11.

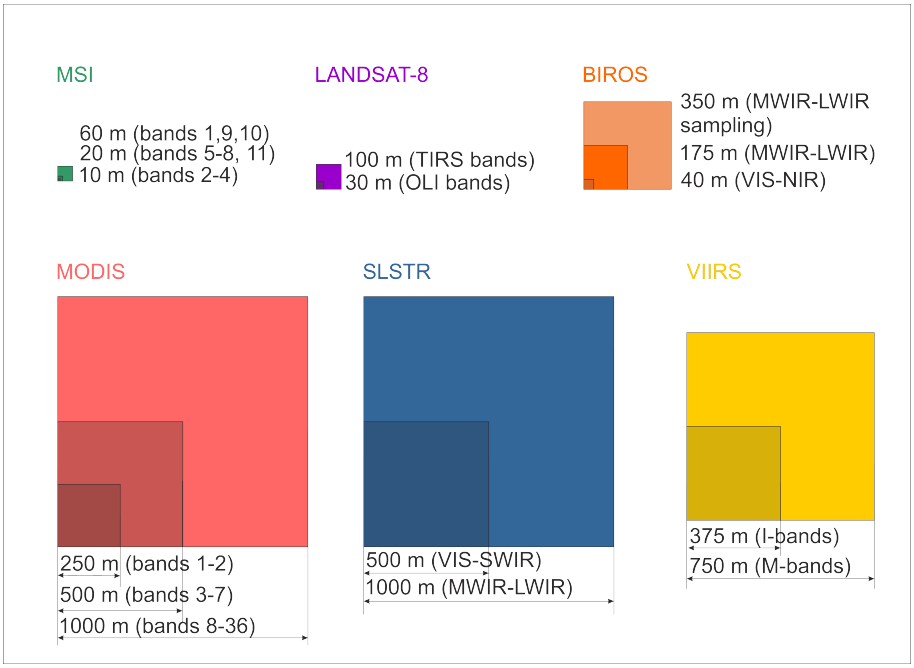

Figure 11: GSD at nadir comparison of different sensors. Graphic adapted from Soszyńska 2017.

The Sentinel-2 MSI sensor disposes of the highest spatial resolution of the six compared sensors. The spatial resolution of the LANDSAT 8 imagery is 30 m for SWIR1 and SWIR2 spectral bands and 100 m for thermal bands. The third-highest spatial resolution comes in BIROS (350 m for MWIR and LWIR bands) and, very close to that, VIIRS I-bands (375 m). The SWIR bands of SLSTR sensor have GSD of 500 m. The M-bands of VIIRS have relatively low spatial resolution, with 750 m GSD. Lastly, the relevant MODIS bands, and the MWIR and LWIR bands of SLSTR have GSD of 1000 m. A graphic illustration of this comparison is depicted in Figure 12.

A low GSD value causes that a very small source of radiation, such as a gas flare comprises a relatively higher proportion of a pixel, than in case of GSD values of 1000 m. Therefore, fewer gas flares will be detected in the imagery of high GSD in comparison to imagery of low GSD. An Eumetsat study shows, that only 56% of gas flares can be detected by the SWIR bands *Copernicus Sentinel-3 NRT Fire Radiative Power (FRP) – Radiant heating & threat monitoring of fires, gas flares, and volcanoes* of SLSTR, although the band covers the theoretical peak wavelength of a gas flare Planck curve.

A comparison of detection of gas flares in imagery of SLSTR and BIROS is presented below in Figure 12. In the SLSTR image on the right, the gas flares show radiance values which barely exceed the radiance values of the background. Moreover, a significantly smaller number of flares can be identified. At the same time, on the BIROS image (on the left) gas flares can easily be recognised, and their radiance values strongly exceed the background values. It is worth noting that these two datasets have been chosen in a way that the time of sensing of the two images is as close as possible to each other. In this case, the time gap between the SLSTR and the BIROS image is almost exactly two hours. In the SLSTR image only 13 gas flares can surely be detected (above the noise level), whereas in the BIROS image the number of detectable flares is 32.

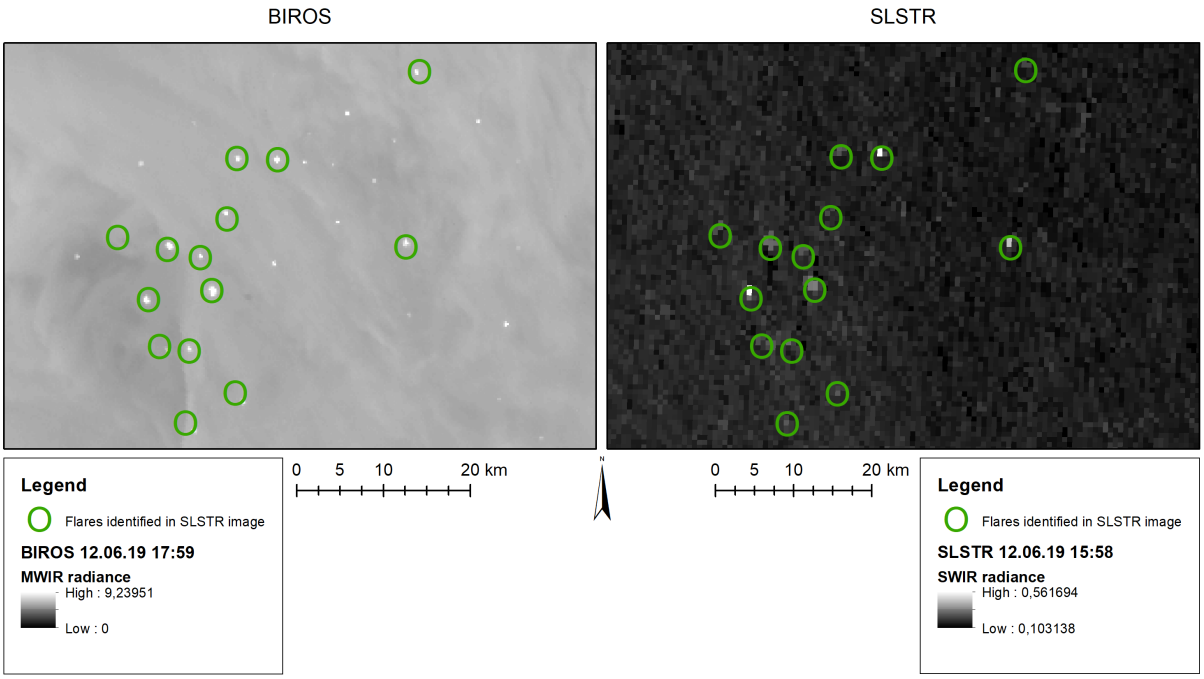

Figure 12: A comparison of the number of gas flares which can be detected by SLSTR with gas flares visible in a BIROS mission.

Taking the GSD of a sensor into consideration, it is important to know the design of the sensor and how exactly the pre-processing of the final image products works. For instance, the BIROS sensor is a push-broom system with two staggered arrays of detectors for MWIR and LWIR spectral bands. The actual GSD of the sensor, calculated from the physical size of a detector unit (or the instantaneous field-of-view, IFOV), focal length and imaging height is actually around 350 m and due to staggering, the images are resampled to around 180 m GSD.

This feature does not have a significant influence for some applications, however, it is extremely important for calculating the energy of a subpixel source, because the number of photons comes from a source and its background at the same time and is averaged over the real GSD to acquire radiance units ($W/m^2/sr/\mu m$). All of this happens in the pre-processing of the image products.

Another important consequence of recording with staggered arrays is that a hot-spot is recorded redundantly. This happens, because each of the arrays records the hot-spot once and in post-processing the pixels from both arrays are used to create the end product, i.e. the radiance image. This mechanism is described in Section 3.1 and has led to the introduction of an additional variable in the method called "sampling factor" s.

2.3.4 Optimal sensor features for gas flaring research

A perfect sensor for gas flaring analysis should be equipped with three spectral bands in the SWIR, MWIR and LWIR ranges, to record the flares and derive the flaring parameters, e.g. using an adapted version of the bi-spectral method. Additionally, it would be advisable to include high-spatial resolution bands in VIS-NIR ranges, to estimate the geometry of the flame more accurately.

To distinguish the flaring signal from the sunlight reflection in SWIR bands, it is particularly important that the sensor should operate and record during the night as well as in daytime

A crucial feature for gas flaring analysis is an adjustment of the sensor's dynamic range to avoid saturation, such as an additional setting of integrating time for high temperature events.

In order to record small gas flares and to distinguish gas flares which are located near each other, the higher the spatial resolution of the sensor, the better the results. It would be advisable to design a sensor with a GSD of around 100 m. The VIS-NIR bands should be able to sense with a GSD of around 5 m, in order to resolve the flame geometry more accurately.

Finally, it is important to maximise the SNR value (or minimise the Noise Equivalent Temperature Difference (NEDT) value), therefore cooled photon detectors (such as HgCdTe), calibrated for both high and low temperatures, would provide the best results in the IR bands. A comparison of the SNR values for the analysed group of sensors can be found in Appendix A.

Due to all these demands, two out of six sensors have been chosen for further analysis. Six criteria have been developed for the comparison:

1. Visibility of gas flares in the imagery,
2. Number of visible flares,
3. Saturation in signal,
4. Spectral bands in SWIR, MWIR and LWIR range,
5. GSD of the sensor,
6. Scientific relevance.

The BIROS sensor detects all the gas flares (from the prepared geodatabase, created using photo-interpretation of high resolution imagery), the gas flares are well distinguishable from the background and not saturated. The GSD is the third highest in the compared group. BIROS is equipped with spectral bands in the MWIR and LWIR spectral range, however the sensor has no band in SWIR. BIROS has not been used for the parametrisation of gas flares yet, but has often been used to characterise fire events.

LANDSAT-8's high spatial resolution allows to detect all the flares in the study area, the flares are well visible and distinguishable from the background signal. The flare signal is, however, saturated in many cases, as shown in Table 2, with upper-end saturation as well as low-end saturation present in all images. LANDSAT-8 is equipped with two spectral bands in the SWIR spectral range, two in LWIR, and none in MWIR. In gas flaring research, LANDSAT-8 imagery has been used so far to detect flares, rather than to parametrise them.

VIIRS, can be compared twofold. In its moderate spatial resolution bands (the "M" bands), only few gas flares are visible (around a half of gas flares, which are visible in the imaging "I" bands). A primary analysis proved no saturation in "M" and "I" bands of the sensor, even though the calculations in Appendix B suggest the possibility of saturation in case of bigger flames. Both "M" and "I" bands record in SWIR, MWIR and LWIR spectral bands. The VIIRS sensor is most frequently used in gas flaring literature, mostly due to a very active research group organised by Christopher Elvidge in NOAA/USGS.

The MODIS sensor is the oldest of the compared sensors. Its noise is the highest among all the compared sensors due to ageing of hardware, and numerous image artefacts are visible. Therefore, only few gas flares in the study area are visible in the imagery and distinguishable from the background signal. MODIS is equipped with multiple spectral bands in the SWIR, MWIR and LWIR region, which would make this sensor potentially very suitable for the gas flaring research. There are several publications in remote sensing of gas flaring, both in detection and in parametrisation of gas flares.

Sentinel-3 SLSTR reveals some potential for gas flaring research. Some, but not all gas flares are visible in SLSTR imagery as can be seen in Figure 12. The signal of gas flares does not exhibit saturation. SLSTR has spectral bands in the SWIR, MWIR and LWIR regions, and additionally the so-called "fire" bands in the MWIR and LWIR region. The sensor has bands in moderate and coarse spatial resolution (500 m for VIS-SWIR bands and 1000 m for

MWIR-LWIR and "fire" bands). This spatial resolution causes that gas flares in the study area are barely visible in "fire" bands and only partly visible in the SWIR bands. The potential of SLSTR for gas flaring parametrisation has been explored in several research publications.

The MSI sensor from Sentinel-2 has a very high spatial resolution and the flares are well visible in the imagery. Nevertheless, the signal is almost always saturated, ruling out an accurate parametrisation. Moreover, this sensor is equipped with spectral bands only in the SWIR spectral range, which makes the calculation of the background signal difficult. Until now, the potential of the MSI sensor for gas flaring research remains unexplored, even though in many aspects the sensor appears feasible for this purpose, especially for detecting flares.

Concluding, the following two sensors, turn out to be the best choice for the parametrisation of gas flares in the presented research: BIROS, due to its high dynamic range and relatively high spatial resolution, and VIIRS, or, to be precise, the VIIRS "I" bands, due to spectral bands in the most appropriate spectral range and relatively high spatial resolution.

3 From fire on the ground to an infrared image

The following chapter contains the methodology of the research conducted. First, theoretical background on image formation in an IR camera is described, and an example IR satellite image of gas flares is analysed. In the next section, a model for gas flow calculation using satellite IR imagery is presented. The model brings together variables of a gas flare flame and parameters of a satellite sensor recording it. It allows calculating gas flow using flame radiance recorded by a satellite sensor, which needs to be derived from the image products. The method for calculating the flame radiance, including subtraction of the background signal, is presented in Section 3.3. Next, a group of parameters including recording conditions (e.g. atmospheric transmittance), and sensor parameters is analysed. Finally, flame parameters are analysed in Section 3.5. These are the parameters influencing the amount of energy radiated during the combustion, which can be potentially recorded by a satellite sensor.

3.1 Formation of an IR image in the camera

In this chapter, different sensors are described. A sensor, in this work, is understood as a complete camera system. A thermal sensor is a sensor recording in long-wave infrared (also called thermal infrared). Although the definition of thermal infrared spectral range is defined differently by different researchers, it typically consists of wavelengths between 7 and 20 µm. Spectral bands in other parts of IR spectrum are often used, e.g. in MWIR or in SWIR spectral ranges. A detector is a part of a sensor that transforms the incoming radiation into electric charges. The design of a sensor, with all its features, determines the quality of the signal read and consequently the accuracy of products further derived from the imagery. Therefore, it is crucial, to understand the sensor design and operation, to avoid inserting any systematic error into the end product.

There are two types of detectors, used in IR remote sensing: photon detectors and thermal detectors. As all the sensors described in Section 2.3 are photon detectors, this chapter focuses on this type of detector. Photon detectors are detectors, in which the absorbed electromagnetic radiation is transformed into an electric charge distribution in a semiconductor. This is done by changing the free carrier concentration, a process called "internal photo-electrical effect" (Vollmer & Möllmann 2017). Infrared photon detectors need to be cooled (typically to around 70-80 K), to reduce the thermal noise of the detector.

As light enters the front lens of a sensor, it is filtered on its way to the detector. This happens, as a side effect due to imperfect transmittance of the lenses, and on purpose due to spectral filters, installed for allowing only a part of the electromagnetic spectrum to reach the detector. Each detector type is sensitive to a certain spectral interval only, which needs to be in accordance with the spectral filters used. Once a photon reaches a detector, it will be transformed to an electric charge with a probability described by the quantum efficiency of a detector.

To model the number of photo-electrons generated per given radiation sensed, one could use the following equation (Säuberlich 2018):

$$n_e = \frac{\pi}{4F^2 + 1} \cdot A_{\text{pix}} \cdot t_{\text{int}} \int_{\lambda_0}^{\lambda_1} \left(\frac{\lambda}{h \cdot c} \cdot L(\lambda) \cdot \tau_{\text{system}}(\lambda) \cdot q(\lambda) \right) d\lambda \quad (3)$$

where:

n_e	number of generated electrons [1]
F	F-number of the optics, defined as the ratio between focal length and aperture diameter [1]
A_{pix}	detector unit area [m^2]
t_{int}	integrating time, defined as time in which detectors record incident radiation [s]
λ	wavelength [m]
$\lambda_0 ... \lambda_1$	spectral interval delimited by bandpass filters [m]
h	Planck constant [J·s]
c	speed of light [m/s]
$L(\lambda)$	spectral radiance [W/m^2/sr/µm]
τ_{system}	combined spectral transmittance of the optics and bandpass filters [1]. Attention: in further chapters the variable τ is used for transmittance of the atmosphere.
q	quantum efficiency of the detector material [1]

Using the Equation (3), the number of electrons generated in a detector can be calculated. The sum of the electric charges, coming from recording of photons in a given integration time, will be transcribed to a digital number (DN), also known as grey value, of a pixel.

In order to interpret a DN as a radiance value, a calibration is required. For IR photon detectors, the calibration is usually performed right before the image acquisition, by measuring an internally installed reference black body, e.g. in case of BIROS: a cover in front of the optical system. The internal black body heats up, and the recorded signals are compared to the expected radiation, derived from the temperature of the calibration black body, which is additionally monitored with temperature sensors installed on it. This allows the calculation of a radiance value for each DN value, which is typically done using a linear model. This conversion to radiance values is done for each pixel in the image, with its specific model, derived during the calibration. The calibration procedure allows also calculating the SNR value for each scene, by dividing the standard deviation of the recorded radiance by its mean.

The spatial resolution of a sensor, depends on its detector unit size (also known as pixel pitch) and properties of the optical system: focal length and modulation transfer function (MTF). The NEDT is dependent on the detector area – the larger the detector area, the lower the NEDT (Rogalski & Chrzanowski 2014). However, the pixel pitch of thermal detectors should not drop below the size of the wavelength sensed, in order not to lose on sensitivity. This results in a trade-off between the sensor's thermal sensitivity and its spatial resolution. Typically, the pixel pitch is constructed at least twice as large as the wavelength sensed, for instance the BIROS pixel pitch is 17 µm for MWIR (3.4-4.2 µm) and LWIR (8.6-9.4 µm).

The image is usually slightly blurred. This has several reasons. The first is the diffraction effect. Another reason is the intentionally introduced defocus of the optics, in order to avoid aliasing effects[14]. Lastly, the blur of the optics may be caused by a non-diffraction-limited optical design. The overall blur, which results from all the above-mentioned effects, can be described by the PSF of a system. The PSF describes the response of an optical system to a point. In blurred optics, the image of a point is spread over several neighbouring pixels (Figure 13). The extent of this spreading is described by the PSF, a measure typically used to describe the quality

[14] Aliasing is an effect that maps signals of different frequencies to the same output frequency (Wikipedia contributors 2020). It causes an artefact in an image. These artefacts are very hard to remove, and they decrease the accuracy of products derived from an affected image. Therefore, a typical procedure to avoid aliasing in an imaging system, is to design the optical system to blur slightly, i.e. to suppress spatial frequencies in the image above the detector's Nyquist frequency.

of a sensor. According to Reulke & Eckardt 2013, the optimal width (σ) of the PSF should be around 0.7 px.

As can be seen in Figure 13, the radiation initially coming from a point source is spread over several pixels.

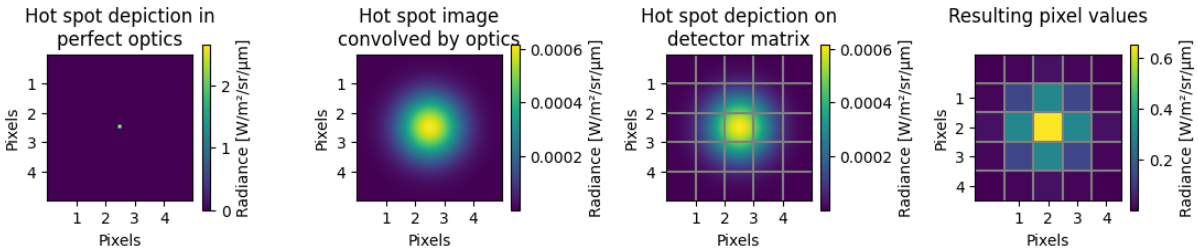

Figure 13: Illustration of the convolution of a point source, such as a gas flare, by the PSF. For illustration purposes, the spatial resolution of the two plots in the middle was increased 35 times.

As can be seen in Figure 13, the radiation initially coming from a point source is spread over several pixels. To calculate the overall radiation of a point source, e.g. a gas flare, recorded in an image, it is necessary to deconvolve the image with the PSF. This approach may be approximated as an integration or summing over all affected pixels, with subsequent background radiance subtraction. This issue is addressed in detail in Section 3.3.

As mentioned before, the spatial resolution of thermal sensors is far coarser than the spatial resolution of those sensing in the visible spectral range. Hence, in order to maintain the sensor sensitivity and nevertheless achieve a higher spatial resolution, several approaches can be followed. One solution is to use stronger, and thus typically heavier, optics. Doing this, however, increases the cost of the project, especially the launch. Another solution is to use staggered detector arrays. Staggered detector arrays are two independent detector lines placed adjacent on the long edge, as in a detector matrix, but with a half pixel shift in the direction of the line. In an image product such as BIROS products, the pixels from both arrays are placed alternating. An illustration of this process can be found in Figure 14.

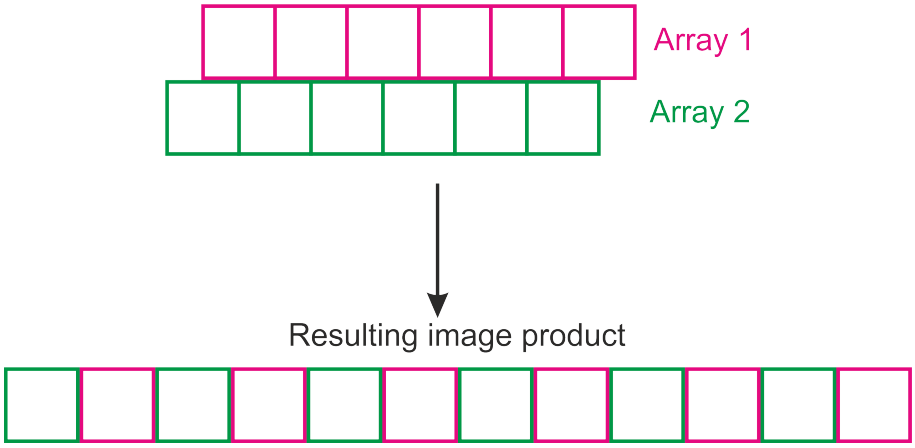

Figure 14: Staggered arrays and resulting recorded image.

Using staggered arrays increases the spatial sampling frequency. As Reulke *et al.* 2006 state, the sampling limit, or Nyquist frequency, for a single array is $\frac{1}{2 \cdot \delta_{\text{pix}}}$ (where δ_{pix} is the detector size), whereas for a staggered array it doubles to $2 \cdot \frac{1}{2 \cdot \delta_{\text{pix}}} = \frac{1}{\delta_{\text{pix}}}$. This causes an increase of sampling frequency in the cross-track direction. To achieve a corresponding increase in the

flight direction, the sampling speed must be doubled. In this way, the sampling frequency is doubled in both directions. However, this also means that each point on the ground is sampled redundantly.

The redundancy has no particular effect in cases, where pixels cover a homogeneous area, because the radiant flux recorded in a pixel is divided by GSD^2, spectral range and solid angle recorded, resulting in pixel radiances in $W/m^2/sr/\mu m$.

All algorithms operating on more than one pixel will be affected. The approach presented in this work is such an algorithm. In case of a recorded hot-spot, the redundancy has a significant effect, because radiation of the hot-spot is recorded four times. This effect is illustrated in Figure 15.

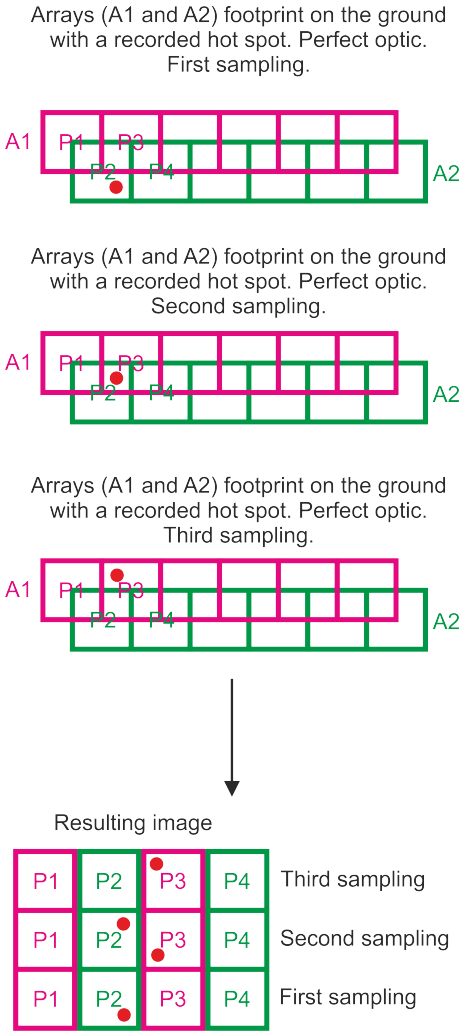

Figure 15: Effect of staggering on an image with a point source of radiation (such as a gas flare) in case of perfect optics (no PSF).

Figure 15 illustrates staggering in case of perfect optics. Such ideal optics, however, do not exist. A more realistic representation can be found in Figure 16. It takes into account the blur of the optical system, so the radiation of a flare is spread over multiple pixels. Additionally, the scene is over-sampled due to staggering and a doubled sampling speed.

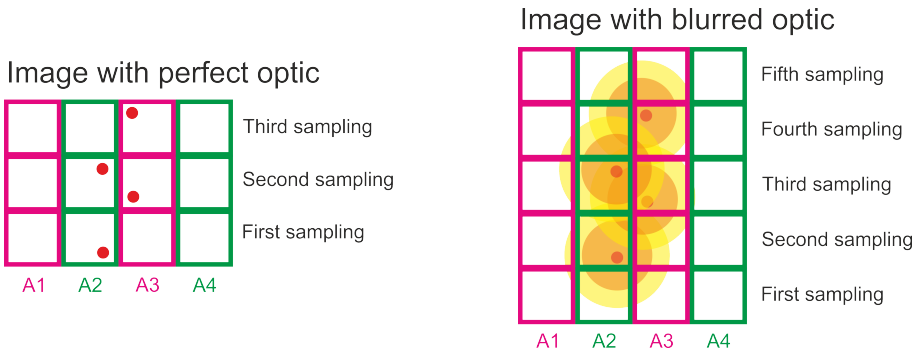

Figure 16: Staggering and PSF effects on an image.

In order to account for this effect, one can either consider the image pixel area to be four times smaller than the GSD^2, or introduce a factor correcting the redundancy, which is applied to a sum of hot-spot radiance. To avoid confusion between the image pixel area and the GSD^2, the author of this dissertation considers introducing an additional factor a more elegant solution to address the redundancy. In this work, the term GSD^2 is understood as a physical property of a sensor, and is defined as:

$$\mathrm{GSD}^2 = \left(\frac{\delta_{\mathrm{pix}_x}}{f} \cdot H\right) \cdot \left(\frac{\delta_{\mathrm{pix}_y}}{f} \cdot H\right) \tag{4}$$

where:

GSD^2	Ground sampling area [m^2]
δ_{pix_x}	Pixel pitch in x direction[m]
δ_{pix_y}	Pixel pitch in y direction[m]
f	Focal length [m]
H	Orbit height [m]

Processing satellite data of gas flares needs to be done considering all the applicable effects (blur of the image, redundant recording due to staggered arrays). Additionally, due to the fact that the terrain, on which a gas flare is located, is rarely homogeneous, a careful modelling of the background signal needs to be done.

Figure 17 presents two satellite image fragments of a gas flare and its surrounding environment. In the left fragment, the flare is not active, i.e. no flame is recorded.

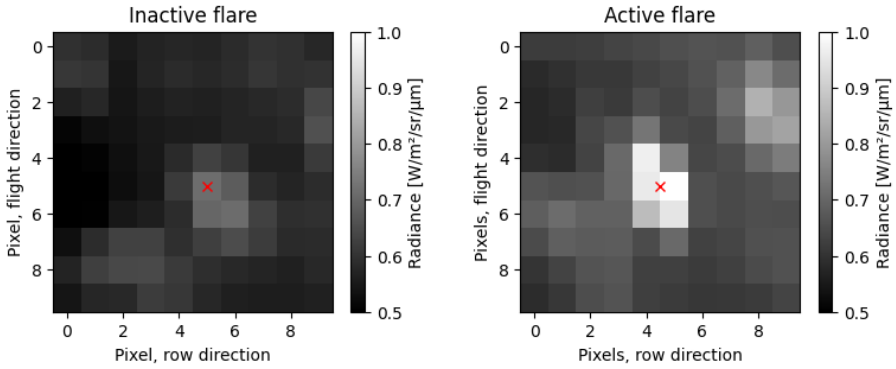

Figure 17: Satellite image fragments of a flare. On the left, a satellite image without a flame can be seen. On the right, the gas flare is active. The flare position is marked with a red cross.

In the fragment on the right, the flare is active and visible. As can be seen, in both left and right satellite image fragments, a group of pixels around the flare (marked with a red cross) has stronger radiation than the surroundings. This is because the flare is placed on a fire test site cut out of the forest. In the image fragment on the right, it is hard to distinguish the blurred signal of the flare, from the signal of the fire test site (which is blurred as well, but its radiance is much lower than the flare signal). A non-homogeneous scene, such as in Figure 17, is typical and contains a mixture of radiation from the flame itself, buildings, roads and other infrastructure in the direct vicinity as well as from vegetation and soil surrounding it.

Let us consider a satellite scene with multiple gas flares, such as in Figure 18.

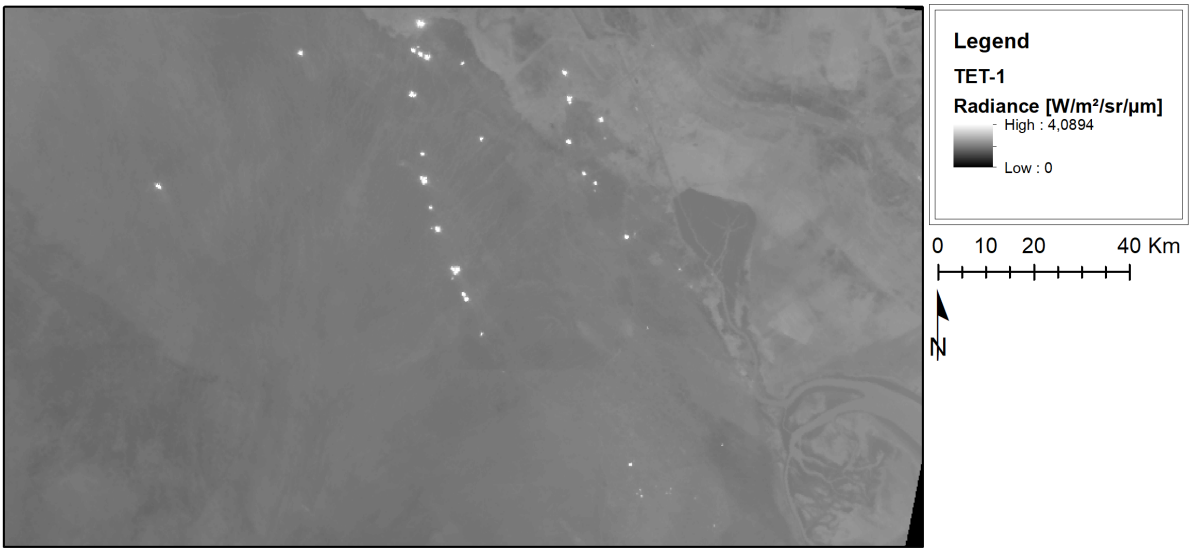

Figure 18: TET-1 (precursor of BIROS) scene of Kuwait in MWIR (12.05.2016).

The line of bright spots in the upper central part of the image is a group of gas flares, often multiple direct next to each other, leading to formation of larger spots. For a simplified analysis, let us assume a homogeneous background with radiance equal to the median of radiances of the flare neighbourhood. For each flare, a 10x10 pixels window around the flare is chosen and the background radiance (here, the median of the image fragment) is subtracted. After subtracting the background radiance and masking invalid values (smaller than 0.01 $W/m^2/sr/\mu m$), the remaining radiance values are summed to obtain the flare radiance. The flare radiance values are presented in Figure 19.

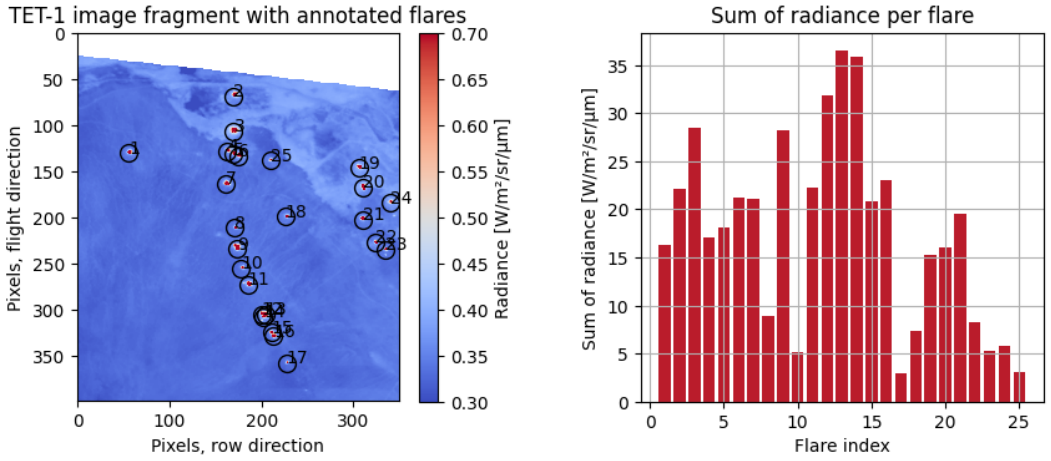

Figure 19: TET-1 image fragment with annotated gas flares and sum of radiance per flare.

As can be seen in Figure 19, the radiance values are strongly varying. The literature on remote sensing of gas flaring does not name any direct relation between flare radiance and instantaneous gas flow flared. As the purpose of this research is, to calculate instantaneous gas flow values for the flares, a new method needed to be developed, and the relation between gas flow and flare radiance needed to be investigated. This was done by conducting an experimental series, described in the Section 4.1.

3.2 Model for calculating flared gas flow from IR satellite imagery

The model for calculating the instantaneous gas flow values from IR satellite imagery, which is the central point of this research, is presented below in Eq. (11).

The following parameters are used in the model:

$\mathrm{LHV}_{\mathrm{fuel}}$	calorific value of the fuel [J/kg]
$\dot{m}$	mass flow of the fuel [kg/s]
T	temperature of combustion [K]
$\chi(T)$	combustion efficiency [1]
$\rho(T)$	proportion of energy radiated to the overall energy released during combustion [1]
4π	full sphere [sr]
$\tau(\lambda)$	atmospheric transmission [1]
$\psi(\lambda, \Delta\lambda, T)$	proportion of the energy radiated in the sensor spectral band with respect to the complete black body radiation of a given temperature [1]
GSD^2	ground sampling area of one pixel [m^2]
$\Delta\lambda$	bandwidth of a sensor spectral band [µm]
s	sampling factor [1]
$L_{\mathrm{at\,sensor}}$	spectral radiance of a gas flare flame recorded by a sensor [$\mathrm{W/sr/m}^2/\mu\mathrm{m}$]

The first part of the model describes the flame. Parameters of the flame are described in detail in Section 3.5.

The amount of energy released in the combustion of gas E_{flame} is estimated by multiplying the calorific value of the fuel $\mathrm{LHV}_{\mathrm{fuel}}$ with the amount of the fuel burned m. In most cases, the combustion in gas flares is not complete. This means that the amount of energy released during combustion is reduced by a factor called combustion efficiency $\chi(T)$:

$$E_{\text{flame}} = m \cdot \text{LHV}_{\text{fuel}} \cdot \chi(T) \tag{5}$$

It is also possible to write the equation above for gas flow $\dot{m}$ instead of a certain mass of gas m. In this case, the quantity energy E_{flame} will become power P_{flame}, but the other variables and their values remain the same:

$$P_{\text{flame}} = \dot{m} \cdot \text{LHV}_{\text{fuel}} \cdot \chi(T) \tag{6}$$

Only a part $\rho(T)$ of the whole energy released during combustion is radiated. A flame does not radiate like a black body, but like a grey body (Johnston *et al.* 2014), this is expressed by the emissivity of the flame ε. The flare is assumed to radiate homogeneously over the complete sphere of 4π sr. Therefore, the total radiant intensity of a gas flame I_{flame} [W/sr] can be calculated with the following Equation:

$$I_{\text{flame}} = \frac{P_{\text{flame}} \cdot \rho(T)}{4\pi \text{ sr}} = I_{blackbody} \cdot \varepsilon \tag{7}$$

The radiation of a flame, before being recorded by a satellite sensor, propagates through a medium – the atmosphere. The atmosphere absorbs a part of the propagating radiation and reflects another part. The factor, which describes the remaining fraction of the radiation that reaches a sensor, is called transmittance τ. The at-sensor radiant intensity $I_{\text{at sensor}}$ [W/sr] is calculated as follows:

$$I_{\text{at sensor}} = I_{\text{flame}} \cdot \tau \tag{8}$$

The way from the combustion source to the satellite sensor, with all its parameters is illustrated in Figure 20.

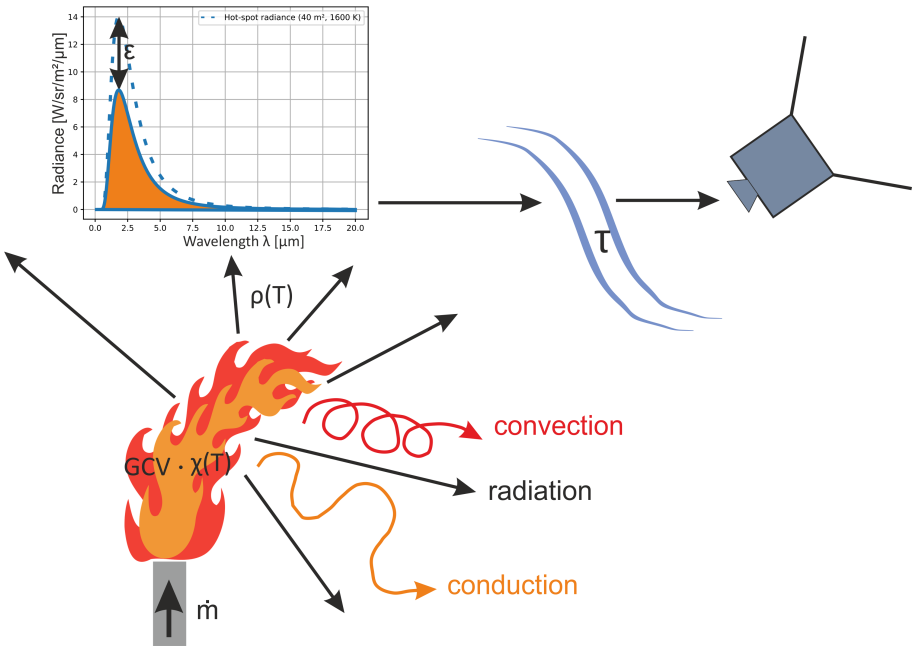

Figure 20: Illustration of the energy path from combustion source to the sensor.

A satellite sensor typically records only a part of the whole radiation spectrum, limited by a band pass filter. Therefore, a part of the total at-sensor radiant intensity is filtered and cannot be recorded. The radiation of a flame is assumed to be a grey body radiation. Therefore, the parameter representing the band pass filter and reducing the radiation coming to the detector to the recorded part $\psi(\lambda, \Delta\lambda, T)$ is calculated using a Planck curve.

So far, the radiant intensity [W/sr] arriving at the sensor is modelled. An IR satellite image is typically given in the unit of radiances [W/sr/m²/µm]. Two sensor features need to be considered, in order to normalise to sensor-independent values: A sensor collects radiation from an area on the ground of GSD^2. Only the radiation from a certain band of sensitivity with a bandwidth of $\Delta\lambda$ is recorded by a sensor. The radiation recorded is treated, as it was homogeneous over a whole pixel and the complete spectrum, and therefore, the transform from radiant intensity to radiances is achieved by dividing by GSD^2 and $\Delta\lambda$. The above described process is illustrated in Figure 21.

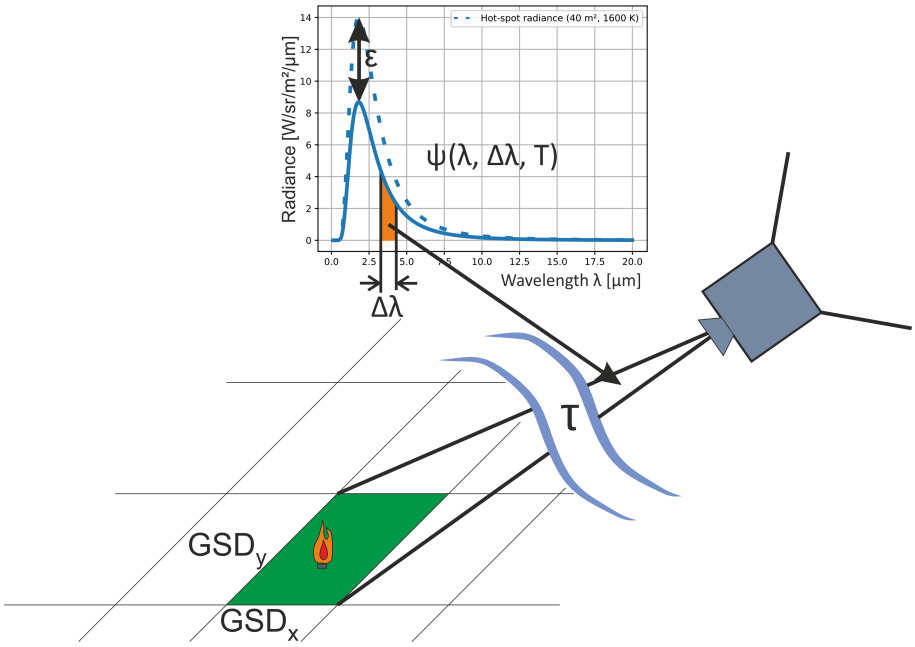

Figure 21: Sensing of a gas flare with a sensor.

Lastly, if the detector arrays in a sensor are staggered or samples are taken in shorter intervals than the dwell time, the radiance of a target on ground is recorded redundantly. To account for this redundancy, a correction parameter s is introduced. The radiance of a flame $L_{\text{at sensor}}$ [W/sr/m²/µm], as recorded in a satellite image, can be calculated as:

$$L_{\text{at sensor}} = \frac{I_{\text{at sensor}} \cdot \psi(\lambda, \Delta\lambda, T)}{\mathrm{GSD}^2 \cdot \Delta\lambda \cdot s} \tag{9}$$

Or in an alternative representation:

$$L_{\text{at sensor}} = \dot{m} \cdot \frac{\mathrm{LHV}_{\text{fuel}} \cdot \chi(T) \cdot \rho(T)}{4\pi\ \text{sr}} \cdot \tau \cdot \frac{\psi(\lambda, \Delta\lambda, T)}{\mathrm{GSD}^2 \cdot \Delta\lambda \cdot s} \tag{10}$$

If Equation (10) is solved for $\dot{m}$, it is possible to derive gas flow values from the radiance of a flame recorded by a satellite sensor $L_{\text{at sensor}}$. In this case, the equation looks as follows:

$$\dot{m} = L_{\text{at sensor}} \cdot \frac{4\pi\ \text{sr}}{\mathrm{LHV}_{\text{fuel}} \cdot \chi(T) \cdot \rho(T)} \cdot \frac{1}{\tau} \cdot \frac{\mathrm{GSD}^2 \cdot \Delta\lambda \cdot s}{\psi(\lambda, \Delta\lambda, T)} \tag{11}$$

Using Equation (11), gas flow values for the experimental series were calculated from the BIROS imagery. Additionally, in order to prove the feasibility of the model to work with data from different sensors with comparable results, gas flow values for two study areas were calculated from BIROS and VIIRS satellite imagery. In Tables below, a list of parameters with their values used for calculation of gas flow values from satellite images of BIROS and VIIRS is

presented. For BIROS in Table 4. There are two sets of parameters for VIIRS sensor. The first are parameters for the I4 band, presented in Table 5. And lastly, parameters for VIIRS I3 band are presented in Table 6.

Table 4: A list of parameters and their values used for gas flow calculation from BIROS imagery

Parameter	**Value**	**Unit**	**Note**
LHV_{fuel}	50.0	MJ/kg	for methane
	46.4	MJ/kg	for propane
χ	0.90	1	1200 K for methane
ρ	0.07	1	
τ	0.70	1	Mid-latitude summer
	0.74	1	Mid-latitude winter
	0.75	1	US Standard
ψ	0.1448	1	for 1200 K
	0.1069	1	for 1600 K
	0.0897	1	for 1800 K
	0.0626	1	for 2226 K
GSD	≈350	m	calculated for each pixel separately
$\Delta\lambda$	0.8	µm	
s	0.25	1	

Table 5: A list of parameters and their values used for gas flow calculation from VIIRS I4 imagery.

Parameter	**Value**	**Unit**	**Note**
LHV_{fuel}	50.0	MJ/kg	for methane
χ	0.90	1	1200 K for methane
ρ	0.07	1	
τ	0.78	1	Mid-latitude summer
	0.87	1	Mid-latitude winter
	0.84	1	US Standard
ψ	0.0723	1	for 1200 K
	0.0536	1	for 1600 K
	0.0451	1	for 1800 K
	0.0311	1	for 2226 K
GSD	≈375	m	calculated for each pixel separately
$\Delta\lambda$	0.38	µm	
s	1	1	

Table 6: A list of parameters and their values used for gas flow calculation from VIIRS I3 imagery.

Parameter	Value	Unit	Note
LHV_{fuel}	50.0	MJ/kg	for methane
	46.4	MJ/kg	for propane
χ	0.90	1	1200 K for methane
ρ	0.07	1	
τ	0.91	1	Mid-latitude summer
	0.92	1	Mid-latitude winter
	0.91	1	US Standard
ψ	0.0103	1	for 1200 K
	0.0211	1	for 1600 K
	0.0246	1	for 1800 K
	0.0275	1	for 2226 K
GSD	≈375	m	calculated for each pixel separately
$\Delta\lambda$	0.06	µm	
s	1	1	

3.3 Extraction of flame radiance $L_{\text{at sensor}}$

One of the most challenging parts of the methodology is deriving the flame radiance $L_{\text{at sensor}}$ from a satellite image, because a flare is very small in comparison to GSD², its radiation is mixed together with the background signal, and spread over multiple pixels. The workflow illustrating the process of flame radiance extraction is presented in Figure 22.

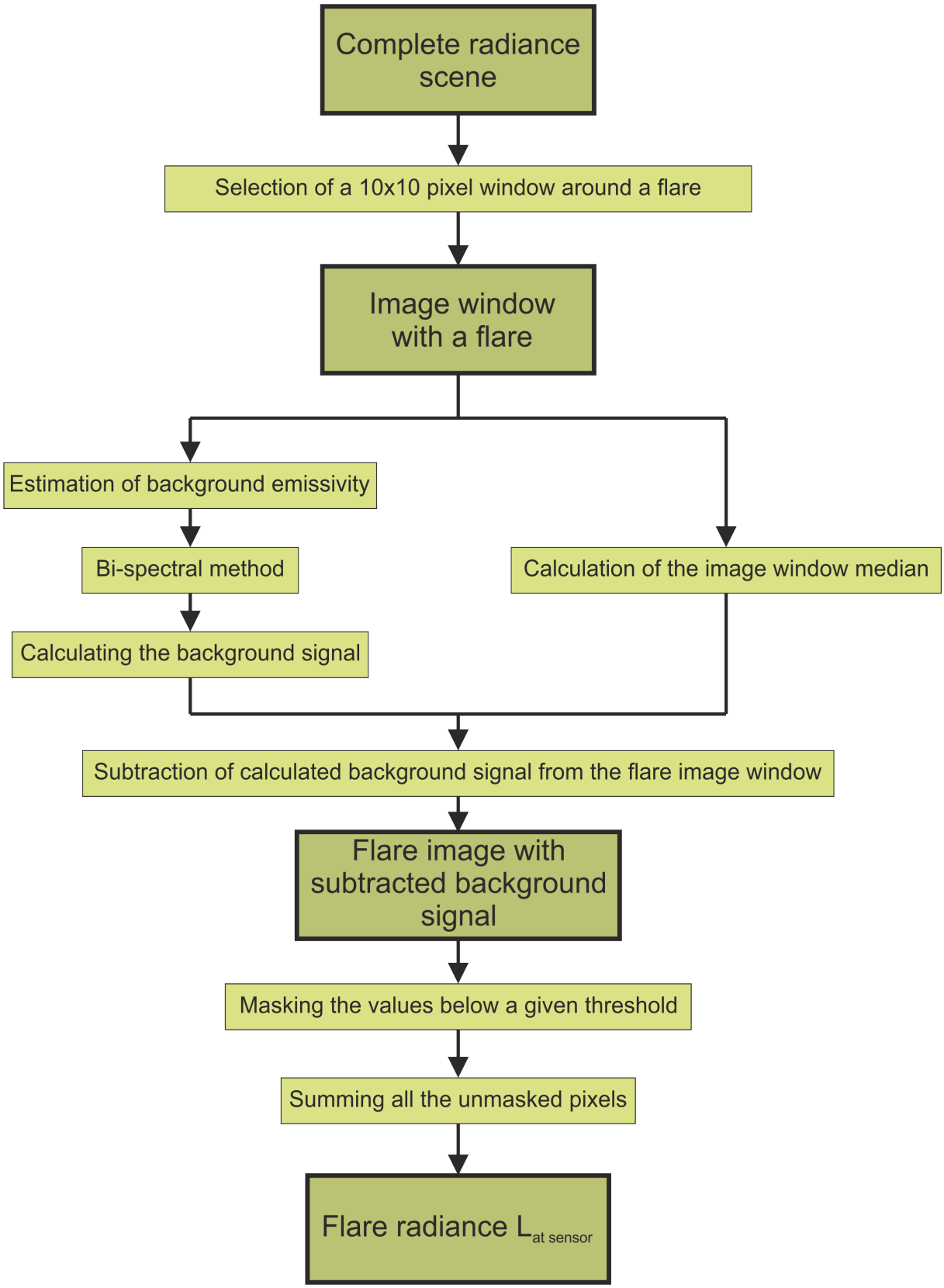

Figure 22: Workflow for calculating gas flare radiance from a satellite image.

As this research does not focus on identifying the gas flares automatically, the analysed gas flares were identified by photointerpretation of high-resolution imagery from LANDSAT, Google Earth and ArcGIS. The location and index of each flare were saved into a geodatabase. Using

their geo-coordinates, it was possible to locate them in the satellite images. After selecting a gas flare, a window of 10x10 pixels around the flare location was considered.

Each such image fragment contains both signals from a flare and from the background. In order to derive the radiance of a gas flare accurately, the background signal needs to be subtracted from the selected image fragment. The calculation of background signal was done in two different ways for different study areas. For the BAM TTS experiments and the study area of North Dakota, the bi-spectral method was applied. Using the bi-spectral method requires knowledge on the emissivity of the background ($\varepsilon_{\mathrm{bkg}}$). One approach for setting the parameter $\varepsilon_{\mathrm{bkg}}$, is to use the ASTER Global Emissivity Database. However, the emissivity data for the BAM TTS area with 100 m spatial resolution was updated only until the end of 2008, whereas the facilities were built quite recently and were continuously developed since.

Figure 23: An aerial image of the BAM TTS fire test site. Source: ArcGIS high resolution imagery.

An aerial image of the facility is presented in Figure 23. As can be seen, the BAM TTS fire test site is cut-out of the surrounding forest. The site itself is almost 200 m wide in its widest spot (along E-W axis) and 450 m long (along the N-S axis). The TTS contains buildings as well as other infrastructure, along with vegetation and sand.

The BIROS pixel-footprints are of very similar size (i.e. approximately 350 m x 350 m) as the TTS fire test site, hence, due to the blur of the pixels, the signal of the TTS can be spread over 3 pixels in row direction (i.e. width of the TTS), as can be seen in Figure 24. Therefore, the TTS is large enough, in comparison to BIROS GSD, to be detected and analysed in the BIROS images. For a comparison, an aerial image (the same as in Figure 23) is presented in the background of Figure 24.

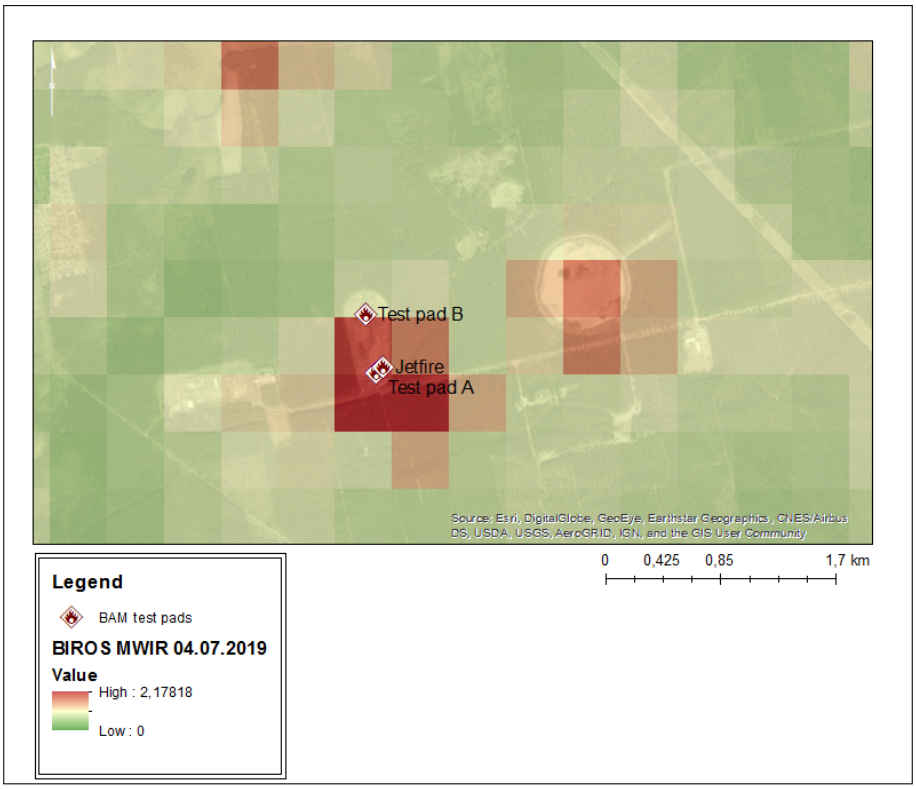

Figure 24: BIROS image from experiment 3 from 04.07.2019 on the background of high resolution imagery (source: ArcGIS high resolution imagery).

To calculate the background emissivity ε_{bkg} of the TTS (i.e. $\varepsilon_{\text{bkg}} = \varepsilon_{\text{TTS}}$), several BIROS images were analysed. This parameter was calculated using the night imagery of the TTS, due to lack of reflection of the sunlight in those images. The temperature for the emissivity calculation has been taken from the archive of the neighbouring weather station in Baruth.

The background emissivity was calculated as follows:

$$W := \text{window of 4x4 pixels around TTS} \tag{12}$$

$$I_W := \sum_{i \in W} \frac{L_i}{|W|} \cdot (A_{\text{forest}} + A_{\text{TTS}}) \tag{13}$$

$$I_W = \tau_{(\lambda)} \cdot L_{T_W} \cdot \varepsilon_{\text{forest}} \cdot A_{\text{forest}} + \tau_{(\lambda)} \cdot L_{T_W} \cdot \varepsilon_{\text{TTS}} \cdot A_{\text{TTS}} \tag{14}$$

$$\varepsilon_{\text{TTS}} = \frac{\frac{I_W}{\tau_{(\lambda)} \cdot L_{T_W}} - \varepsilon_{\text{forest}} \cdot A_{\text{forest}}}{A_{\text{TTS}}} \tag{15}$$

where:

I_W	spectral intensity of the window [W/sr/µm]
L_i	pixel radiance [W/m²/sr/µm]
A_{forest}	area of the forest inside the window [m^2]
A_{TTS}	area of the TTS [m^2]
L_{T_W}	black body radiance per given temperature and sensor's spectral band [W/m²/sr/µm]
$\varepsilon_{\text{forest}}$	forest emissivity, derived from ASTER Global Emissivity Database [1]
ε_{TTS}	emissivity of the TTS [1]
$\tau_{(\lambda)}$	atmospheric transmittance [1]

In the case of the North Dakota study area, the background emissivity value was derived from the ASTER Global Emissivity database. The analysis of the North Dakota study area in the archive of Google Earth exhibited no significant change in the land cover over the last two decades, so using the ASTER Global Emissivity database does not bring additional uncertainty, in contrast to the BAM TTS area.

The calculated (or derived from ASTER imagery) background emissivity parameter was used to calculate the background signal at the BAM TTS, as well as in North Dakota. In these two study areas, the bi-spectral method with a-priori assumptions on the fire temperature and fire size, as well as the calculated flame emissivity (see section 3.5.3 for details) was applied, to derive the temperature of the background. The next step was to calculate the black body radiance for the estimated background temperature and calculating the background signal, by multiplying the black body radiance with two parameters: atmospheric transmittance and calculated emissivity.

In case of Persian Gulf data, the bi-spectral method did not work accurately enough for the presented analysis. The background temperature estimated using the bi-spectral method was inconsistent, because radiance values from the MWIR band translated to higher temperatures than those from the LWIR band. For instance, the MWIR radiance for 13.11.2019 was 0.34 W/sr/m²/µm, which translates to 291.5 K and the LWIR radiance for the same data set was 7.86 W/sr/m²/µm, which translates to 288 K. The bi-spectral method estimated the sea temperature of 290 K for this window (MWIR radiance value of this temperature is 0.32 W/sr/m²/µm), each sea pixel was left with a remaining value of 0.02 W/sr/m²/µm after subtraction. The radiance values are summed over the whole window in the last step of processing, therefore such an error of background subtraction leads to an overestimation of the flare radiance of 2 W/sr/m²/µm, which translates to an overestimation of the gas flow of 9400 kg/h [15]. Therefore, for this study area, background signals were estimated by calculating the median over the sampling window.

[15] Further details on the sensitivity of the method to background estimation can be found in the Sections 4.3.4 and 5.

Now back to the data processing. Subsequently, after calculating the background signal for a given window (calculated either using the bi-spectral method or by calculating the median), it was subtracted from the selected window. All the remaining radiance values lower than a given threshold (e.g. for Persian Gulf the threshold was 0.001 W/sr/m²/µm, the value corresponds to roughly one standard deviation of the water signal in the Persian Gulf, in an example 10x10 window.) were treated as background noise and masked (see Figure 25).

As a result, a flare image, with subtracted background and masked pixels not belonging to the flare, was obtained.

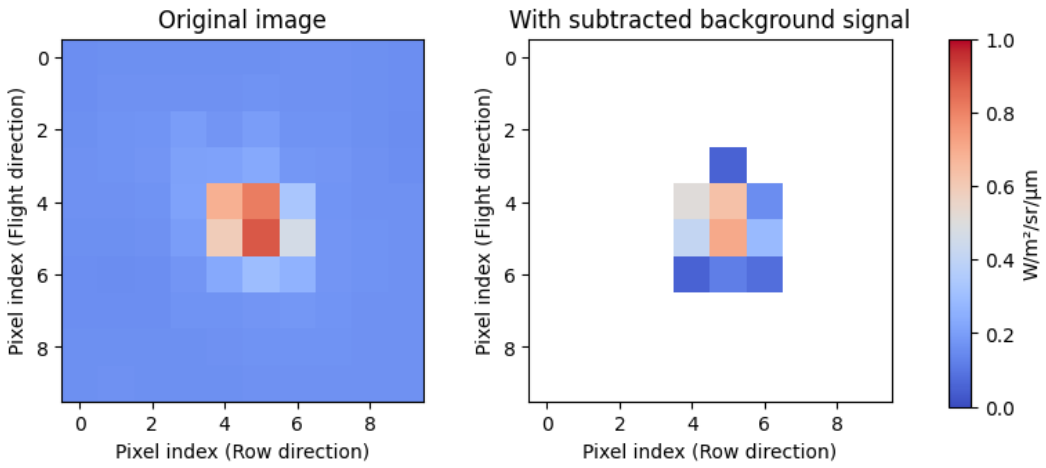

Figure 25: Illustration of image processing for flare radiance calculation. The sum over the unmasked pixels in the right image is considered the flare radiance.

Due to the blur of the optics, not only one pixel contains the whole flare radiation, but several pixels in the vicinity of the flare also contain parts of the signal (for more detailed information refer to Section 3.1). Therefore, the signal needed to be deconvolved to obtain the flare radiance. As an approximation of the deconvolution, the remaining unmasked pixels, which were assumed to contain the signal of the flare, were summed up. Thus, flare radiance $L_{\text{at sensor}}$ was calculated.

3.4 Parameters dependent on a sensor

In this section, parameters used in Equation (11) that are dependent on the sensor design or imaging features, are described.

These parameters are:

1. Atmospheric transmittance $\tau(\lambda)$
2. Proportion of the energy radiated in the sensor spectral band with respect to the complete black body radiation of a given temperature $\psi(\lambda, \Delta\lambda, T)$
3. Sampling factor s

Additionally, in the calculation of the gas flow, sensor parameters are used:

1. Ground sampling area GSD^2 of a pixel is calculated for each pixel individually, depending on the orbit height and the off-nadir angle of the line-of-sight.
2. Bandwidth of a sensor spectral band $\Delta\lambda$ is a parameter delimiting the wavelength recorded.

3.4.1 Atmospheric transmittance $\tau(\lambda)$

Atmospheric transmittance is a function of the wavelength and is additionally dependent on the area sensed, especially its climate. Modtran Web App lists six atmospheric models that are most typically used for remote sensing applications: Tropical, Mid-Latitude Summer, Mid-Latitude Winter, Sub-Arctic Summer, Sub-Arctic Winter, and US-Standard 1976.

An example atmospheric transmittance of the Mid-Latitude Summer model is illustrated in Figure 26. As can be seen, the transmittance for the highlighted spectral bands of BIROS and VIIRS is relatively high.

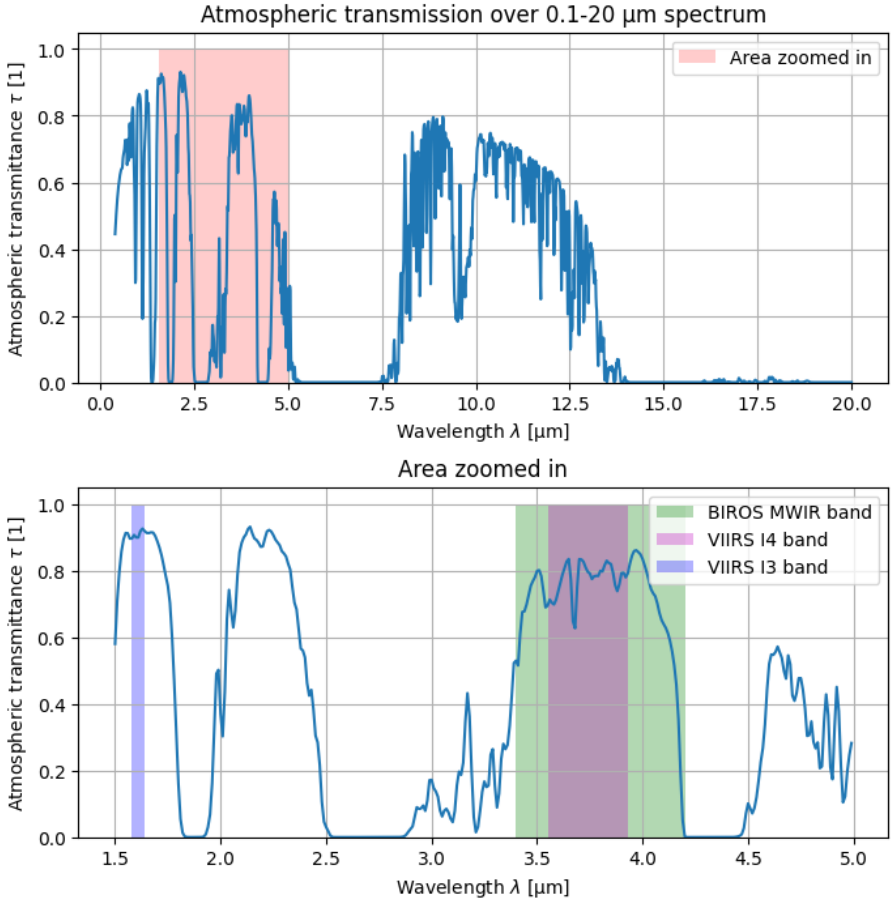

Figure 26: Atmospheric transmittance over the whole 0.1-20 µm spectrum, Mid-Latitude Summer model, with spectral band of BIROS and VIIRS ranges depicted.

The models for atmospheric corrections were chosen based on guidelines in Harris Geospatial 2009. For the calculation of gas flow values in the Persian Gulf, the value of $\tau_{(\lambda)}$ was derived from the atmospheric model Mid-Latitude Summer. For the North Dakota study, the value was derived from the Polar Winter model. The primary calculations for BAM TTS have been made with Mid-Latitude Summer and Mid-Latitude Winter, according to the season. A mean transmittance value for the whole spectral band was used as the value of parameter $\tau(\lambda)$.

3.4.2 Proportion of the energy radiated in the sensor spectral band $\psi(\lambda, \Delta\lambda, T)$

Since a flare is assumed to radiate like a grey body (i.e. the spectral distribution of the radiation is known), the fraction of this radiation that is recorded in a sensor's spectral band, can be derived easily. It is a function of three parameters: wavelength sensed, bandwidth, and temperature of combustion. Due to the fact that the emissivity factor ε does not influence the value

of $\psi(\lambda, \Delta\lambda, T)$, the calculation of this parameter is illustrated basing on black body radiation ($\varepsilon = 1$).

Calculating the parameter $\psi(\lambda, \Delta\lambda, T)$ requires integrating the area under the Planck curve for the given spectral interval, as illustrated in Figure 27.

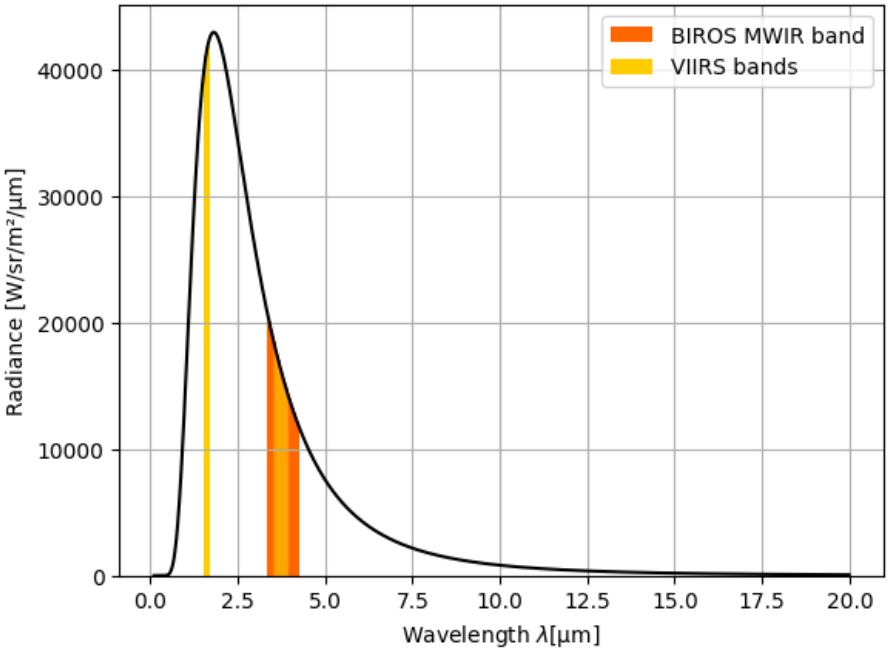

Figure 27: Black body radiance and spectral bands of BIROS and VIIRS.

The value of the parameter is a function of the temperature of combustion, as presented in Figure 28. The function presented in Figure 28 is different for each spectral band, depending on the wavelength, and bandwidth.

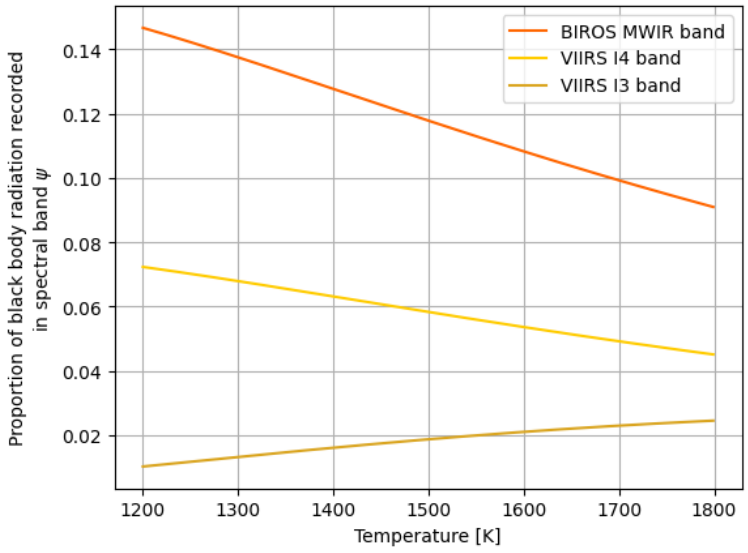

Figure 28: Dependency of $\psi(\lambda, \Delta\lambda, T)$ on temperature of combustion T for BIROS and VIIRS spectral bands.

The values of the parameter $\psi(\lambda, \Delta\lambda, T)$ as used in calculation of gas flow are presented in Table 7.

Table 7: Values of the parameter $\psi(\lambda, \Delta\lambda, T)$.

	1200 K	**1600 K**	**1800 K**	**2226 K**
BIROS MWIR band	0.1448	0.1069	0.0897	0.0626
VIIRS I4 band	0.0705	0.0523	0.0439	0.0311
VIIRS I3 band	0.0705	0.0523	0.0439	0.0275

3.4.3 The sampling factor s

A very important part of the calculation of flame radiance $L_{\text{at sensor}}$ is to address the potential redundancy in recording of the flare signal, due to spatial oversampling by staggering and temporal intervals between subsequent integrations. As presented in Figure 16, due to staggered detector arrays in the BIROS sensor, the hot-spot is recorded redundantly. To account for this effect, the sampling factor s was introduced. The factor's value was calculated to be 0.25 and proved correct using real image data for validation.

The validation of the sampling factor's value was done using imagery of gas flares, as illustrated on an example in Figure 29. A part of destaggered image with a gas flare was chosen. The processing steps for this analysis were the same as mentioned above and illustrated in Figure 22. This procedure was repeated for images from both single arrays of the same data set. The sum of radiances from an array image was divided by the sum of radiances from the destaggered image in both cases. Ideally, the result of this division should be exactly 0.5. The calculated values were 0.496 for one array and 0.504 for the other.

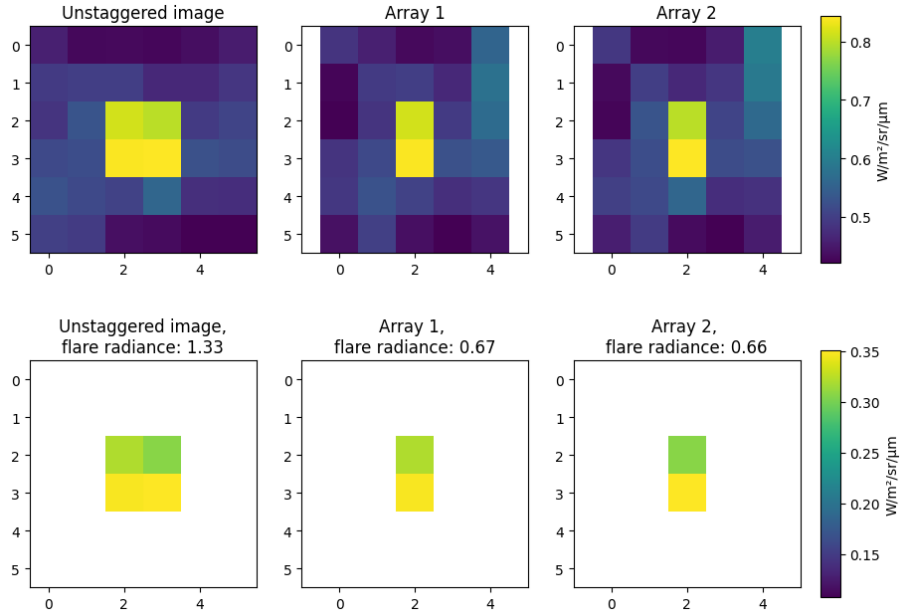

Figure 29: Radiation recorded in destaggered image and in both raw image arrays.

The next aspect to consider, was the sampling frequency and integration time. BIROS records with 24.220 ms time gap between each sampling. As the satellite moves along the orbit with 7600 m/s, which corresponds to approximately 7150 m/s ground speed, and thus, a new sampling happens roughly every 173 m. This is approximately a half of the sensor's GSD (which is dependent on orbit height, roll and pitch). This means that each point is sampled twice also in flight direction.

Therefore, the sampling factor value s was set to be 0.25.

3.5 A gas flare flame and its parameters

The term "gas flare" describes a group of gas burning facilities, using different technologies and set-ups. The most typical construction is an elevated flare, which consists of a vertical pipe delivering fuel to its top, where the fuel is ignited. In some cases, air is mixed into the fuel before ignition. However, there are many kinds of constructions, e.g. pool fires or flares having multiple nozzles. The difference is impossible to distinguish in imagery of the mentioned satellite sensors. Given the constraint of pixel size in thermal satellite sensors (and hence the constraint on GSD), all kinds of gas flares cover only a fraction of a pixel. Therefore, some simplifications and assumptions must be made: The first simplification in the model is that all the gas flares in the satellite imagery used for gas flow calculation, are considered single-flame flares with the same combustion conditions as the gas flare from test pad A used in the experiments. This assumption induces some uncertainty, because the variety of gas flaring set-ups is significant, and the set-up determines some flaring parameters.

The second simplification, made in the methodology, concerns the type of fuel that is flared. Due to the fact that the flared gas is a side-product of crude oil production, its exact composition depends on the oil field and hence differs from one place to another. The natural gas used in the industry is typically understood as a normalised, homogenised mixture, mainly consisting of methane. In reality, methane is the main ingredient of the gas mixture (up to 99%), but the proportion varies. The rest consists of different hydrocarbons in different proportions, varying from field to field. Within the method for gas flow calculation from satellite imagery, gas flared in the study areas was considered to be 100% methane. The properties of methane were included in the calculation (for further details see Section 3.5.4).

The experiments conducted for the purpose of this dissertation, were limited by the set-up used in the BAM facility, which uses only the commercially available propane-butane mixture (LPG: liquified petroleum gas). Due to the fact that butane is only a small part of the LPG mixture and that its proportion varies throughout the year, for simplification in the calculations in the method for the experimental series gas was assumed to be homogeneous propane. Also, the gas-air mixtures in all the analysed gas flares are assumed to be fuel rich, which means that there is more fuel than air in the mixture. This constraint is necessary, because the experiments conducted in the BAM facility allowed only such mixtures. The designed method allows calculating the released combustion energy for methane as well as for propane (and basically any other gaseous hydrocarbon), based on the a-priori known (or assumed) resulting temperature of the products.

The parameters of the flame influence the combustion process as can be seen in Eq. (11). The following sections describe these parameters, and the calculation of their values, in detail.

The described parameters are:

1. Gas mass flow ($\dot{m}$) – is the amount of gas burned in the facility per time unit. It influences the power of the combustion.

2. Projected flame area (A) – the area seen by the camera that contains the flame. This is a projection of the flame volume on a plane perpendicular to the line of sight of the camera, from the point of view of the camera (e.g. satellite sensor).

3. Combustion efficiency ($\chi(T)$) – the ratio of the energy released during combustion to the theoretical enthalpy of complete (stoichiometric) combustion Yuan *et al.* 2013.

4. Proportion of energy radiated ($\rho(T)$) – the ratio of energy emitted in form of radiation to the whole energy released during the combustion.

5. Flame emissivity (ε) – the ratio of the flame's radiation, per given temperature and wavelength to theoretical radiation of a blackbody of the same conditions, as a function of temperature and wavelength.

These variables and their values have been derived or measured during various experiments, or found in literature, and are explained in more detail in the next sections.

3.5.1 Gas mass flow $\dot{m}$

In order to estimate the gas flow flared, from satellite images, it was crucial for the experimental series to have accurate information on the gas flow at the moment when the satellite image was taken. The test pads of the BAM facility allow setting a different gas flow for each experiment. The theoretically maximal possible value to be released during the combustion is proportional to the amount of the fuel burned, by a factor called "calorific value" ($\mathrm{LHV_{fuel}}$), and can be calculated from the following equation:

$$P\,[W] = \mathrm{LHV_{fuel}}\,[J/kg] \cdot \dot{m}\,[kg/s] \tag{16}$$

where:

P	overall power released during combustion (theory) [W]
$\mathrm{LHV_{fuel}}$	calorific value of the fuel [J/kg]
$\dot{m}$	mass flow of the fuel [kg/s]

Gas flow influences directly the volume of the flame. In satellite or on-ground imagery, one cannot precisely estimate the volume, because of the lack of information on the third dimension (the depth) of the flame. Instead, for the purpose of this research, the projected flame area parameter A was analysed in conjunction with the flame depth dependent emissivity ε together as a geometric flame model.

3.5.2 Geometric flame model and flame depth d

If recorded from the side, the flame area is proportional to the gas flow, according to experimental results, as can be seen in Figure 30. This is the case, due to the fact that flame height is proportional to the gas flow (see Figure 34) and the flame width is vastly constant and given by the flare construction.

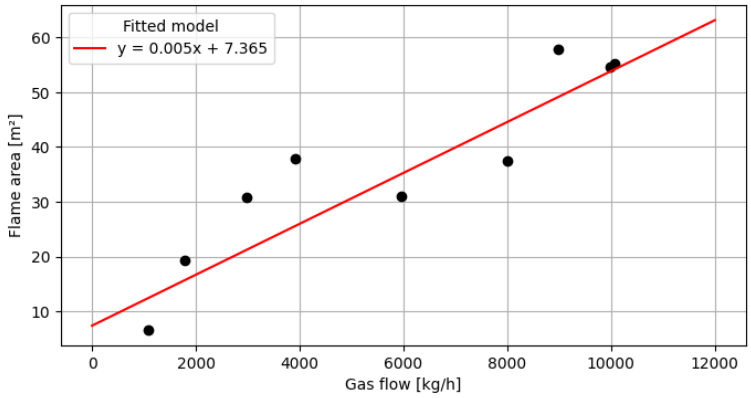

Figure 30: Relationship between flame area and gas flow, derived from the on-ground experiments.

When viewed from above, e.g. from a satellite or a plane, the projected flame area is mostly given by the construction of the flare. The gas flow dependent height cannot be observed geometrically. There may be an observable variation of the emissivity as a function of the flame depth, i.e. flame height, in this viewing geometry (see Section 3.5.3). In order to derive the relation between the gas flow and the flame area from a top view, imagery from the aerial survey was analysed. Even though, the distance between the camera and the flame is much smaller for aerial imagery than for the satellite, the perspective remains the same and therefore allows drawing conclusions on the flame area with the gas flow, as can be seen in Figure 31.

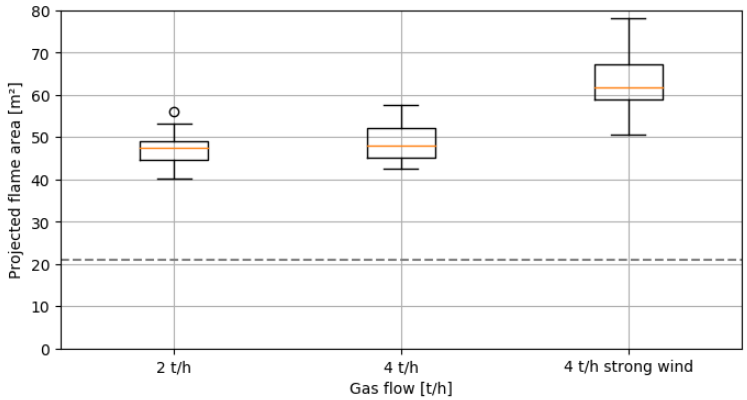

Figure 31: Relationship between the flame area and the gas flow, illustrated using box plots. The dashed grey line delineates the minimum flame area given by the construction of the flare.

The box plots in Figure 31, show the calculated flame area from three imaging series, recorded from the plane (Experiment 2). As can be seen, the projected flame area for the 4 t/h gas flow remained very similar to the projected flame area for the 2 t/h gas flow (plots on the left and in the middle). In these experiments, the gas flare is a so-called pool fire, consisting of multiple nozzles located in regular intervals. Therefore, in this case, there is a minimal flame area, limited by the experimental set-up. This minimal flame area is depicted in Figure 31 by the grey line.

Another important aspect is the high spread between the percentiles in case of the "4 t/h strong wind" box plot. During this flight, strong wind gusts were present in the second half of the survey. In Figure 32, the flame is shown from the side, giving an idea on the "growth" of the flame area recorded from the plane, during strong wind blasts. The wind has a strong influence on the projected flame area, because the typical cone of the flame gets bent, which makes the

flame, observed from the top perspective, significantly bigger. More detailed information on the wind influence of the flame can be found in Section 4.3.4.

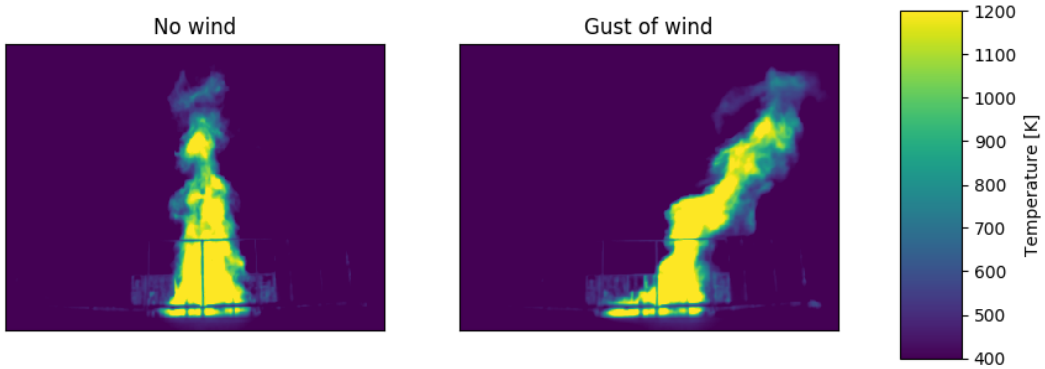

Figure 32: Side view of the flame with and without a wind gust.

Another significant effect on the projected flame area originates from the roll angle of the camera. In most cases, the larger the roll angle, the larger the projected flame area will be. This is due to the fact the flames are usually higher than they are wide. This is however not a general rule. In some cases, if the flame is rather low, there will be no (or little) apparent change in the projected flame area, even with a higher roll angle (Figure 33). The effect is also significantly higher for higher mass flows, because the projected top of the flame (A' in Figure 33 will appear further away from the flame basis; compare 1 with 3 and 2 with 4). Therefore, a geometric model of a flame was introduced. The presented geometric model of the flame allows calculating the flame area from the camera's perspective and, additionally, to calculate the deviation of the flame area due to wind gusts. As mentioned before, all the gas flares are assumed to have exactly the same set-up as the test pad A from the experimental series. The flame is assumed to be a pyramid with a base limited by the experimental set-up (see Figure 43): 4.2 m x 5.0 m.

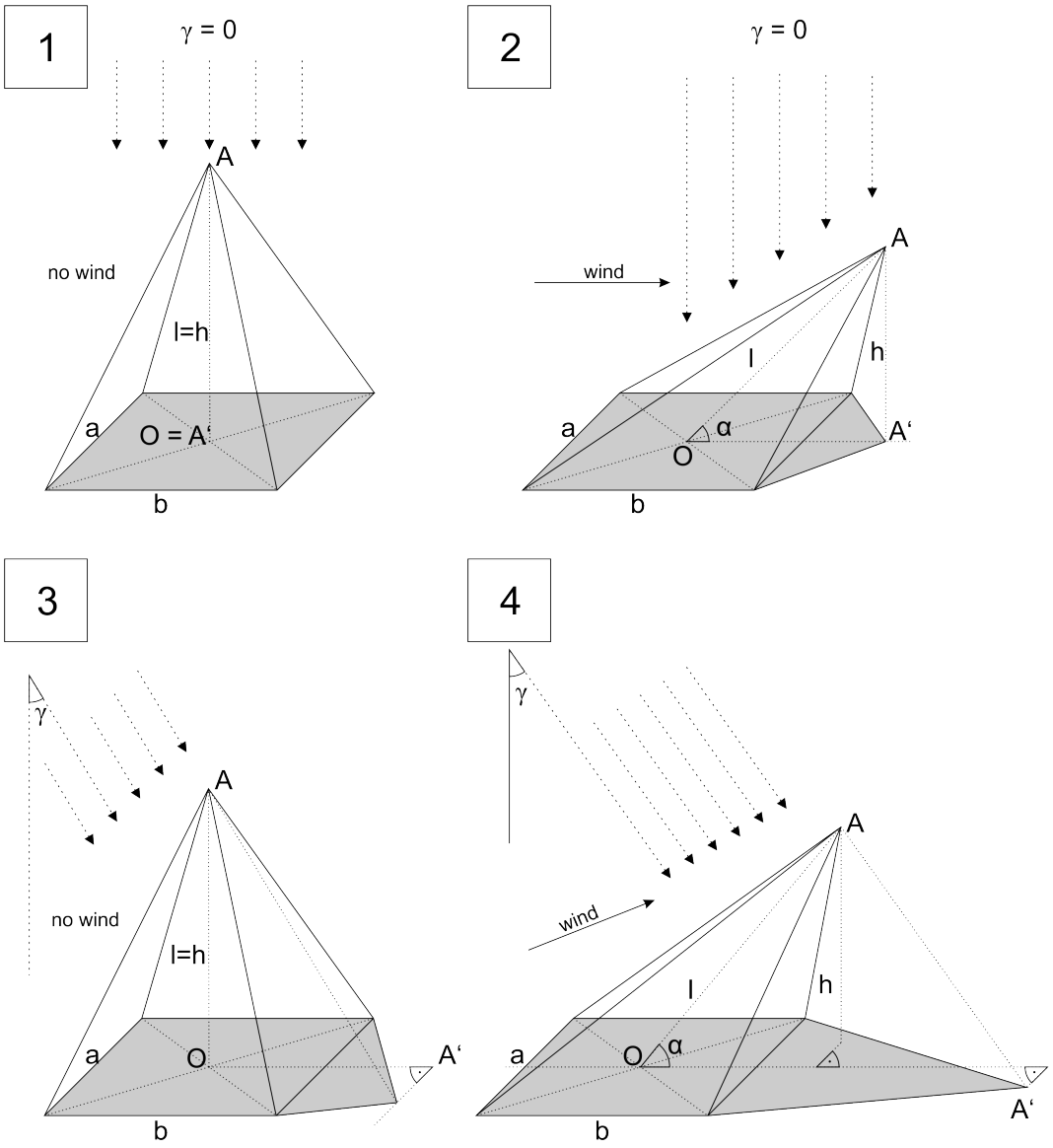

Figure 33: Modelling of flame geometry with two variables: angle (γ) between nadir, satellite and the gas flare position and flame deflection due to the wind (α).

The projection of point A on the ground (i.e. point A') together with the flame basis, delimits the projected flame area (grey surface in Figure 33). Case 1 represents no wind and a nadir perspective - in this case the projected flame area will be equal to the flame base area. Case 2 represents a nadir image of a flame with wind-caused flame deflection; the projected flame area will be bigger, due to the projection of the top, point A', laying outside the base. The same result is observed in the case 3, although the conditions are different: there is no wind, but the image is taken from a larger roll angle. Case 4 has the biggest change in the projected flame area with respect to the simplest case 1, because the wind and the roll angle of the camera both add to the projected flame area.

To sum up, the position of A' depends on four factors:

1. Flame height ($l = \overline{AO}$ in Figure 33),
2. the angle (γ) between the nadir line and line of sight to the gas flare (see Figure 35),
3. the azimuth of the wind deflection of the flame, i.e. the angle between the geographic North and the line $\overline{OA'}$, and
4. the deflection angle of the flame due to the wind gust (α).

A linear model to calculate the flame height l from a given gas flow, has been derived from the experiments (Figure 34) by least squares fitting. During the experiments, the flame has been recorded by various cameras (see Table 8). The flame height has been derived from on ground camera imagery, having the side perspective of the flame, and the known GSD value (calculated from the IFOV of the camera and the distance to the target). The fitted function is valid for gas flows of at least 1000 kg/h, the upper limit has not been calculated.

The proposed function (see Eq. (17) and Figure 34) assumes proportionality between gas flow and flame height. However, this proportionality only holds in case of no wind (Figure 34). More about the influence of the wind on the model accuracy can be found in Section 4.3.4.

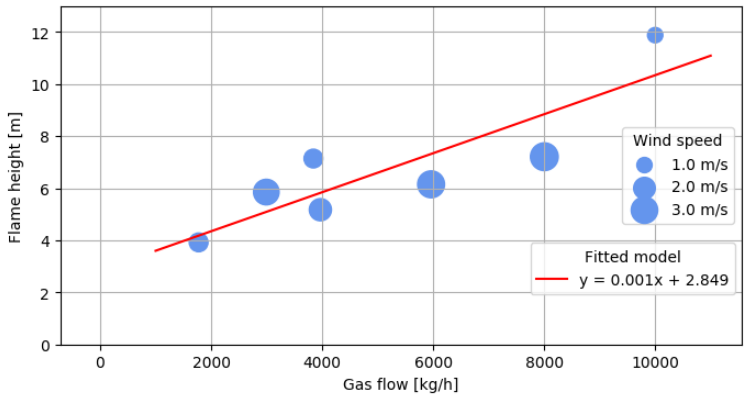

Figure 34: Relation between gas flow, flame height and wind speed.

As can be seen in Figure 34, wind does not influence the flame height in any distinct direction. The wind introduces a noise-like component to the data, as analysed by Soszynska *et al.* 2019.

$$l_{flame} = 0.001 \frac{\text{m}}{\text{kg/h}} \cdot \dot{m}\,\text{kg/h} + 2.849\,\text{m} \tag{17}$$

where:

$L_{\text{at sensor}}$	flame height [m]
$\dot{m}$	gas mass flow [kg/h].

To calculate γ, information about the satellite's roll angle (β) is required, as well as the position of the gas flare in the image coordinate system, in row-direction (X_{flare}). The relation between γ and β is depicted in Figure 35 and detailed in Eq. (18).

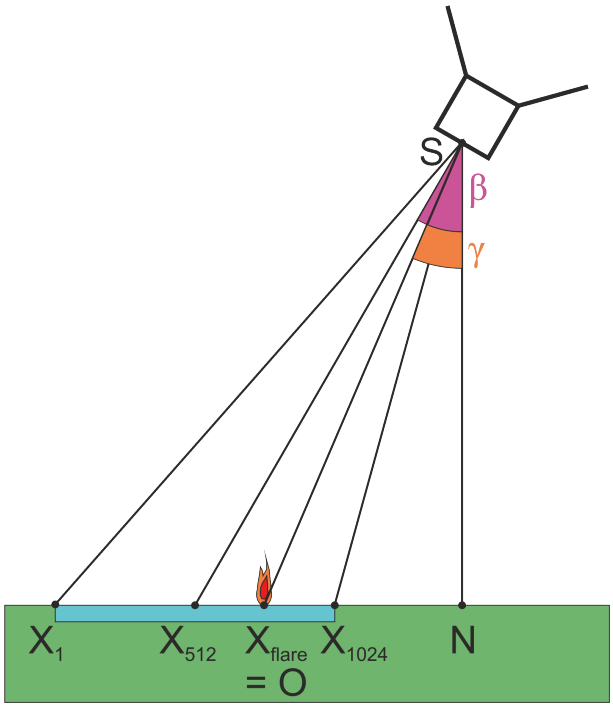

Figure 35: Depiction of roll angle of the satellite (β) and angle between nadir, satellite and the gas flare (γ).

The roll angle (β) is the angle between the ground sample in the middle of the image (ground sample at X_{512}), satellite (S) and ground sample at nadir ground sample at N), whereas γ takes the position of the gas flare in image coordinates (X_{flare}) into consideration.

$$\gamma = \beta - (X_{\text{flare}} - \frac{n_{\text{cols}}}{2}) \cdot \text{IFOV} \tag{18}$$

where:

γ	angle between nadir (N) and line of sight to the flare (X_{flare}) [°]
β	roll angle of the satellite; angle between nadir (N), satellite position (S) and the ground-sample of the middle pixel (X_{512}) [°]
X_{flare}	flare position in row direction in image coordinates [1]
n_{cols}	number of columns of the image (1024 in the example) [1]
IFOV	instantaneous field-of-view of the camera [°].

For the experiments, the wind azimuth and wind speed have been measured, and the cameras on ground allow to estimate the deflection angle of the flame. For further application of the model, no wind was assumed (hence the model without wind deflection, case 1 and 3).

The projection of point A onto the ground is calculated as the intersection of the satellite's line-of-sight and the plane containing the flame base (Figure 36). The model allows calculating the flame depth d from any given perspective, be it from a satellite, from a plane or from a ground-based position). It is calculated by intersecting the planes, representing the flame's sides, and the satellite's line-of-sight, in 10 cm resolution. For instance, the flame model for the experiment no. 6, conducted on 20.12.2019, looks as follows:

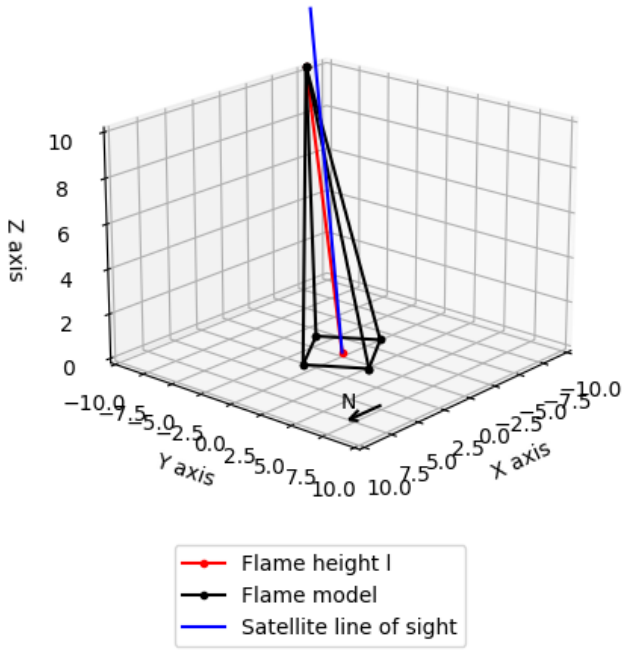

Figure 36: Flame model for the experiment conducted on 20.12.2019, with slight wind (0.9 m/s) coming from 323°.

The flame depth for the same experiment is depicted in Figure 37.

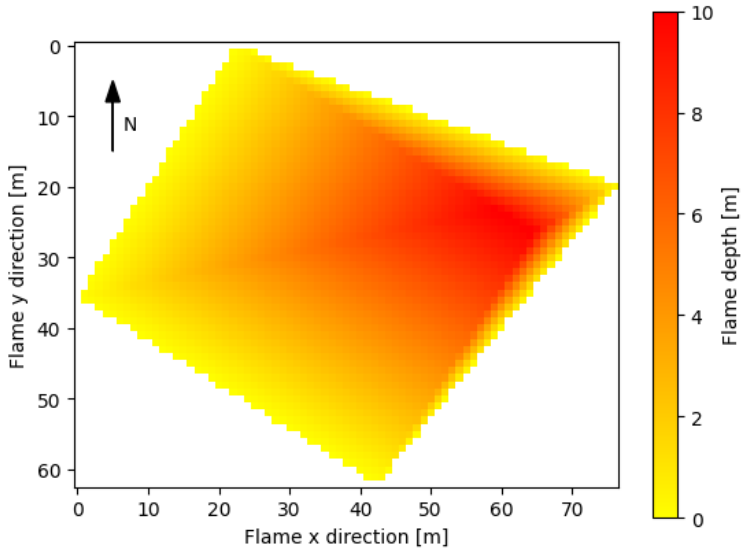

Figure 37: Projected flame area and flame depth for the experiment on 20.12.2019.

The flame depth further allows to calculate the flame emissivity.

3.5.3 Flame emissivity ε

Planck's law describes the density of electromagnetic spectrum per wavelength, which is radiated by a black body in its thermal equilibrium per given temperature. Emissivity of an object is defined as the ratio between the actual radiation of that object and radiation of a black body at

the same temperature. The emissivity of a black body is therefore 1 (or 100%). As black bodies are idealized and theoretical objects, flames, as all other real objects, are characterised with an emissivity value lower than 1. A body, with an emissivity which is lower than 1, but equal over all the wavelengths, is called a grey body.

A flame is a mixture of different species: reactants, products of combustion, and intermediate products of combustion (such as free radicals). Each of this species has its spectral characteristics, including emissivity. Some species do not radiate heat, such is the case for non-polar gases (e.g. O_2 and N_2) (Whitty 2014). The main part of radiation in the flame comes from polar gases (hydrocarbons, CO_2 and H_2O) and soot. The emissivity of different species may vary with temperature of the flame. Additionally, the emissivity of soot can vary, because soot particles with different forms are built in the flame[16].

Generally, the lower the air-feed in the flame, the more soot will be produced. In very sooty flames, the emissivity of a flame is almost the same as the soot emissivity.

However, the conditions, such as air-feed are very complex to determine, and in field experiments the conditions may vary, due to e.g. wind gusts, providing more air into the flame. It is, therefore, extremely complicated to calculate the emissivity for all the species in all the states found in the gas flame: a flame contains a diverse mixture of species, with varying proportions and temperatures, depending on the location in the flame (e.g. typically higher proportions of soot in the hotter centre of the flame).

In a satellite image, though, a flame is only a point source covering a very small portion of a pixel. Therefore, for the purpose of this research, a simplifying assumption has been made. It states that all the species contribute to an averaged "overall emissivity of the flame". Additionally, a grey body radiation is assumed. This assumption bases on research by Johnston et al., in which the authors tested a flame for its radiation properties and derived emissivity parameter, as a function of the flame's depth from the point of view of the camera (Johnston *et al.* 2014). The presented dissertation assumes the emissivity as calculated by Johnston and Wooster. The relation between flame depth and flame emissivity is presented in Figure 38.

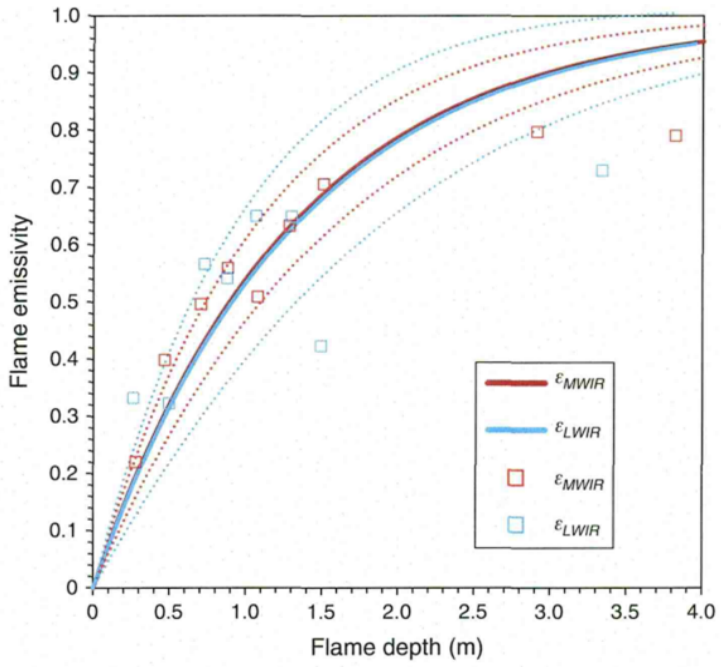

Figure 38: Emissivity as a function of flame depth. The dotted lines give the standard deviation of the measurements. Source: Johnston *et al.* 2014.

[16]More detailed information on soot radiative characteristics can be found in Dombrovsky 2011.

The relationship between the flame depth and the flame emissivity is described by the authors, using the following equation:

$$\varepsilon = 1 - e^{(-k \cdot d)} \tag{19}$$

where:

ε flame emissivity [1]
k extinction factor [m^{-1}],
for MWIR, $k_{MWIR} = 0.7769\,m^{-1}$ (with $R^2 = 0.90$) and
for LWIR, $k_{LWIR} = 0.7626\,m^{-1}$ (with $R^2 = 0.61$).
d flame depth [m]
Please note that the flame depth d used in Eq. (19) is called l in the publication of Johnston *et al.* 2014. Due to the fact that the variable l was already used with a different meaning in the presented dissertation, the author decided to use the letter d instead.

In the present work, the flame depth, calculated from the geometric flame model, allows calculating the flame emissivity as presented in Figure 38 and Eq. (19), which was further used to derive the flame radiance from the pixel radiance.

The emissivity distribution for two of the experiments are calculated according to Eq. (19), are presented in Figure 39.

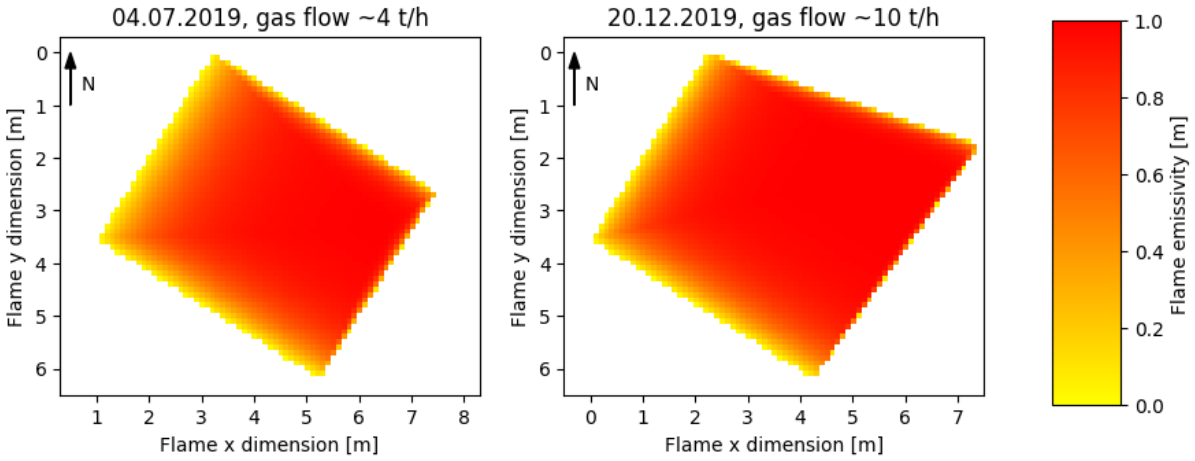

Figure 39: Emissivity values for two of the experiments, calculated from flame depth, according to Eq. (19). The emissivity values are calculated with $100\,cm^2$ resolution.

3.5.4 Combustion Efficiency $\chi(T)$

Combustion efficiency is a parameter describing the ratio between the energy released in combustion reaction and the theoretical maximum energy that can be released in combustion of a given species (which is described by the calorific value of the fuel, LHV_{fuel}). This parameter is a function of temperature, and many other combustion conditions. Mostly, it depends on the air-feed to the flame. The optimal amount of air mixed into the fuel in combustion results in very high temperature, near to the stoichiometric combutstion temperature. Too little, or too much air results in decreasing temperature of combustion.

The efficiency of gas flares should be very high, e.g. 98% (Ismail & Umukoro 2016), but several studies have shown that in reality, the efficiency can be as low as 62% (Strosher 2000).

Within the scopes of this research, the combustion efficiency for each flare could not be estimated. Therefore, the author decided to assume the parameter combustion efficiency to be 90%.

3.5.5 Proportion of energy radiated $\rho(T)$

Release of energy during the combustion occurs in several ways simultaneously. Energy can be released by heat conduction (e.g. into the ground, or, as in the case of the experiments – into the water tub). Another way, in which energy can be released, is convection: heat transfer due to the bulk movement of molecules. Furthermore, energy can be emitted in the form of radiation.

Radiation of an object is radiation of photons, depending on the object's temperature, surface, spectral properties and emissivity. In the case of a hydrocarbon flame, a homogeneous radiation over a complete sphere is assumed.

In order to calculate the gas flow from the radiation recorded in a satellite image, it is indispensable to know how much of the enthalpy of reaction is radiated in form of photons. Generally, the sootier the flame, the more energy will be emitted as radiation. The parameter $\rho(T)$ describes the ratio of energy released in the form of radiation to the enthalpy of reaction, for the purpose of this work.

The exact estimation of this parameter is however very complicated: e.g. $\rho(T)$ depends on the experimental set-up and fuel properties. Some researchers tried to characterise flames in terms of thermal radiation (e.g. Becker & Liang 1982; Brzustowski *et al.* 1975; Burgess *et al.* 1974). Often, however, the experimental set-ups were designed for laboratory scale experiments (such as in Becker & Liang 1982)

For the purpose of this research, the parameter $\rho(T)$ was fitted using the experimental aerial data from two surveys with two gas flow values. The best fitted value for both surveys was calculated and a mean of those values was calculated to obtain $\rho(T)$. The value has been found to be 0.07 (see Figure 40). This was done by using fixed values for all other parameters, and optimising the parameter $\rho(T)$ in the model described in Equation (11) based on the experimental data of gas flow measurements by minimising the mean average error (MAE) values.

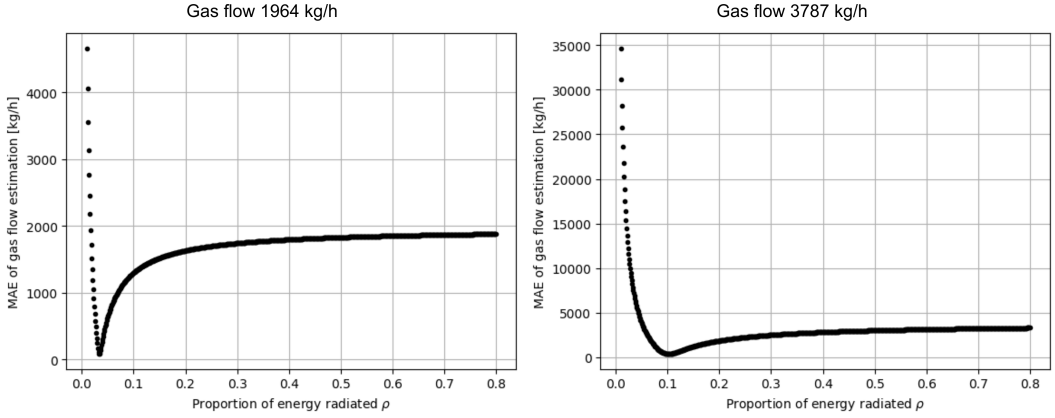

Figure 40: MAE of calculated gas flow as a function of $\rho(T)$ for two gas flow values.

The value $\rho(T) = 0.07$ is considered plausible, because the flames during the experimental series were not very sooty, as can be seen in Figure 41.

Figure 41: A documentation image from one of the experiments using the Test Pad A.

4 Calculation of gas flow from satellite imagery from BIROS and VIIRS sensors

In the following chapter, the results of gas flow calculation using satellite imagery are presented and validated. The first section is devoted to the experimental series conducted. The experimental set-up is described and an overview of experiments is given. The results of an experimental series is given, where the gas flare at the BAM TTS was recorded on the ground and from a plane. These experiments allowed to characterise the flame with respect to changing conditions, e.g. gas flow. One of the most important conclusions of these experiments is that neither flame temperature, nor flame area, changes proportionally to gas flow change. These conclusions raise major doubts about the usefulness of the bi-spectral method for the purpose of gas flares parametrisation. However, as the experimental series proves, there is a linear relation between the recorded radiation and the gas flow.

In the next section, a set of real gas flares in two study areas was considered. A calculation of gas flow was done, using imagery from two, previously chosen sensors: BIROS and VIIRS. Thus, the feasibility of the developed model to work with data from different sensors, was tested.

The section "Validation" (4.3.2) contains the results of different methods of validation of the obtained gas flow estimations. First, the experimental series is analysed. The estimated gas flow values for each experiment are compared to the measured values. The values correlate well, with Pearson's coefficient R^2=0.87. The RMSE and MAE of the gas flow estimation are 1387 kg/h and 1214 kg/h, respectively. Next, the gas flow calculations from two study areas from both sensors are compared. The calculated gas flow values from both sensors are fairly similar, and the correlation between the calculations is relatively high. In the next step, the gas flow calculations for the Persian Gulf study area are compared to calculations done using SLSTR data and method developed by Elvidge *et al.* 2016 and Caseiro *et al.* 2018. Also, in this comparison, the values from both methods are similar and the correlation between the values is high.

The last part of the chapter describes the sources of uncertainty, which can be quantified. An analysis is conducted for three sources of uncertainty: the accuracy of atmospheric correction, the accuracy of the background signal estimation and the flame temperature. The source of the highest uncertainty is the flame temperature.

4.1 Experiments conducted

In order to describe a gas flare flame and its optical properties, a series of experiments has been conducted. The primary purpose of the experiments was to test the suitability of the IR image data for gas flares parametrisation. This could be done by comparing the recorded radiance values of the gas flare, with the according gas flows. Secondly, the experiments served as a base to develop an algorithm for calculation of the instantaneous gas flow from satellite imagery of gas flares. Thirdly, a method to describe the properties of the gas flare (such as dependence of the flame geometry on the gas flow) was developed. This allowed to test the parameters, which are calculated with the bi-spectral method, against the measurements of these parameters with different gas flows. These properties were further included in the method to parametrise gas flares from satellite imagery.

4.1.1 Experimental set-up

The experiments were conducted between summer 2018 and winter 2019, in cooperation with the German Federal Institute of Material Testing and Research (German: Bundesanstalt für Meterialforschung und -prüfung, BAM), at its test site for technical safety (German: Testgelände Technische Sicherheit, TTS) in Horstwalde (Brandenburg, Germany).

The TTS is equipped with three flaring test pads, mainly used for testing material heat resistance. All the test pads are operated with LPG. The test pads allow for a controlled and quite constant gas flow during the experiments. Thermocouples can be installed optionally in the flame, to monitor the flame temperature. Additionally, there are meteorological stations measuring the weather conditions (air temperature, humidity, amount of rain, wind speed and direction) during the experiments.

The main experiments have been conducted using test pad A, presented in Figure 42.

Figure 42: Test pad A of the TTS.

The experimental set-up in the test pad A consists of a tub made of concrete, filled with water. The constantly circulating water prevents the heat radiation to disturb the mechanical stability of the test bench. Additional protection is provided by metal sheets hung around the test bench for protection against strong wind gusts. The test bench itself consists of a pipe ring equipped with nozzles, through which the liquid propane is sprayed into the air. The fuel vaporises a few centimetres away from the nozzle exit, where it is ignited by pilot burners. The test pad dimensions are presented in Figure 43.

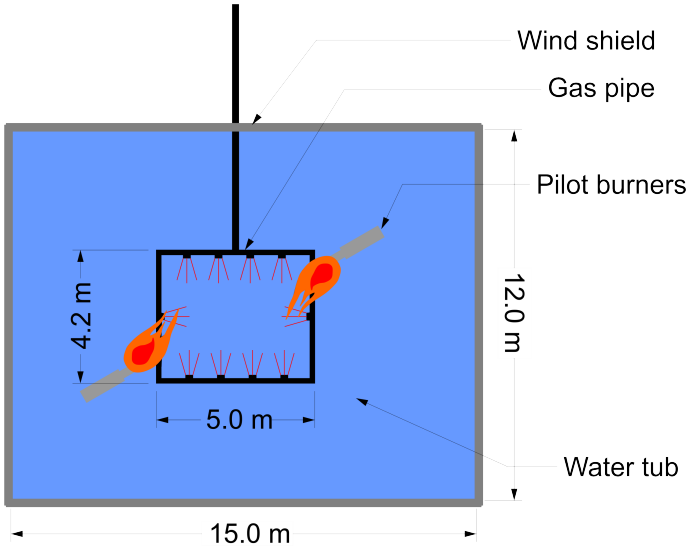

Figure 43: Test pad A scheme.

Some experiments were conducted on other test pads of the TTS. During the first experiments, the jet fire pad was used. The gas flow of the jet fire test pad is fixed to approximately 1000 kg/h and cannot be changed. The construction is equipped with a vaporiser (visible in Figure 44 bottom right), in which the liquid gas is vaporised and then sent to the main nozzle (on the left).

Figure 44: The jet fire test pad.

The third test pad, test pad B, was used only twice, because it was occupied by other experiments (Figure 45). This is the biggest and strongest test pad, built and operated analogously to the test pad A.

Figure 45: Test pad B. In the bottom right corner of the image, the camera set-up is visible.

4.1.2 Description of experiments

During the experiments, the gas flare was recorded by cameras on the ground, simultaneously with the satellite image. Additionally, in some experiments, the temperature of the flame was recorded using thermocouples installed in the flame. The on-ground measurements helped to

describe the flame radiation and flame dimensions, later used in the model. In two of the experiments, additionally to the camera on ground and satellite images, an aerial survey was conducted that provides a link between the on-ground measurements and the satellite imagery.

The MWHT camera, which was used on the ground and in the aerial survey was chosen and set up, so that it resembles the MWIR camera from the BIROS payload, as much as possible. The other cameras have been used as a back-up, and were chosen among the available cameras of the institute. Altogether, three cameras were used for the on ground measurements; their specification can be found in Table 8. Two of those cameras were also used for the aerial survey. The cameras used for the on-ground measurements and the aerial survey have been characterised in a laboratory.

Table 8: Cameras used in the experiments.

Camera	MWHT	VCHD	Optris PI
Camera name	ImagerIR 8300	VarioCam HD	Optris PI 450
Sensor type	InSb (indium antimonide) Cooled photon detector	Uncooled microbolometer	Uncooled microbolometer
Focal length	25 mm	30 mm	8 mm
F-number	2.0	1.0	0.9
Field-of-View (FOV)	21.7°x 17.5°	32.4°x 24.6°	53.0°x 38.0°
Pixel pitch	15 µm	17 µm	17 µm
Wavelength	3.4 - 4.2 µm	7.5 - 14.0 µm	8.0 - 14.0 µm
Number of pixels	640x512	1024x768	288x382

The main experimental series consisted of six measurements, during which a satellite image was taken (Table 9). Five out of six experiments were conducted using the Test Pad A, with different gas flows each time. The intention was first to determine, which minimal gas flow value could be recorder and interpreted as a visible hot-spot in a BIROS image, and secondly to analyse the relationship between the radiance in the satellite image and the gas flow value measured in the test pad. After the first experiment (on 16.07.18), it was proven that the jet fire with 1000 kg/h gas flow yields too little radiance, to be visible in the satellite image. Therefore, the next two experiments (2, 3) were conducted with 4 t/h gas flow: the first time (Experiment 2) to verify the visibility in the satellite image, the second time (Experiment 3) to prove consistency in the signal recording. By analysing the satellite images with the same gas flow, the effects of a cirrostratus cloud, unfortunately covering the flare in the second experiment, could be studied. The last three experiments (4, 5, 6) were conducted successfully with three different gas flows: 3000 kg/h, 6000 kg/h and 10000 kg/h. In all those cases, the gas flare was well visible in the satellite image (the spot in the centre of the images, see Figure 46). During the experiments, weather conditions and a set of ground temperatures were measured, which allowed an exact modelling of the background signal.

Table 9: List of the experiments with satellite images of the flame.

Exp. no	Datum	Gas flow	Cameras used	Note
1	16.07.2018	1 t/h	Optris PI VCHD	Fire not visible in the satellite image
2	26.06.2019	4 t/h	Optris PI VCHD MWHT	Fire visible in the satellite image, aerial survey, VCHD and MWHT in aerial survey
3	04.07.2019	4 t/h	Optris PI VCHD MWHT	Fire visible in the satellite image, aerial survey, VCHD and MWHT in aerial survey
4	24.07.2019	3 t/h	Optris PI VCHD MWHT	Fire visible in the satellite image
5	22.08.2019	6 t/h	Optris PI MWHT	Fire visible in the satellite image
6	20.12.2019	10 t/h	Optris PI VCHD MWHT	Fire visible in the satellite image

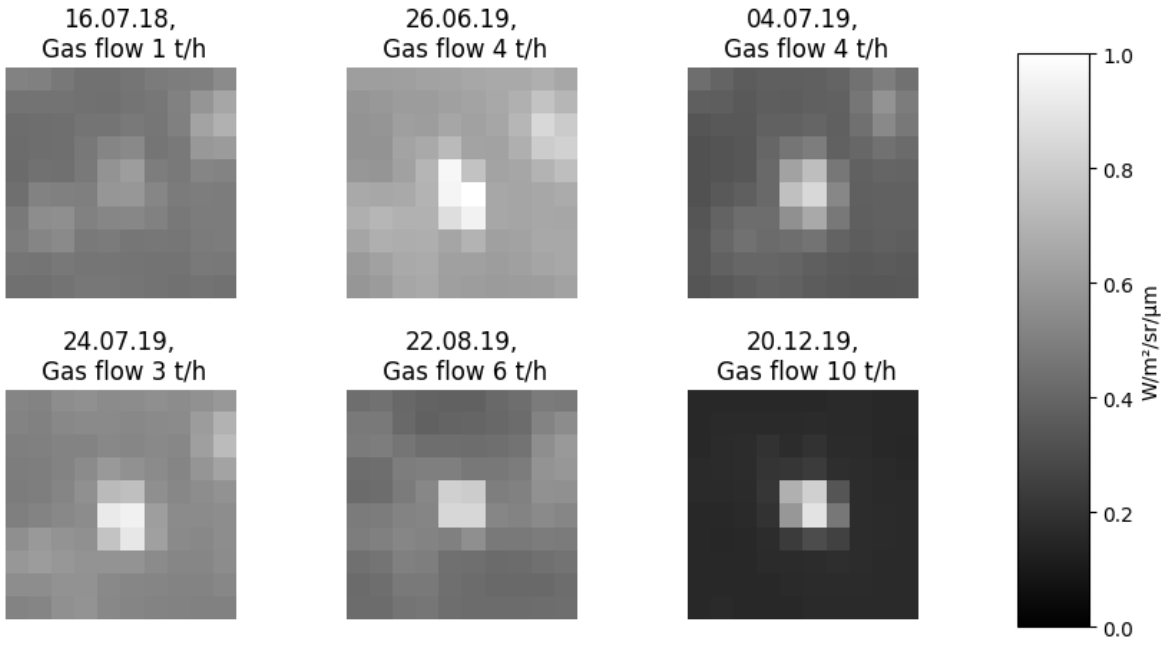

Figure 46: Extracts (10x10 pixels) of the satellite images of the six main experiments, MWIR channel.

Apart from the main experiments listed in Table 9, several additional experiments were conducted. The first series of experiments was not successful, because the flare was not visible (or distinguishable from the background) in the satellite image. Although inconvenient, the data from the cameras recording on ground was used to derive information on the flame characteristics, and the dependence of the flame geometry on the gas flow. Additionally, the influence of wind gusts on the flame were observed and analysed (for further details, see Soszynska *et al.* 2019). Due to the fact that the first experiments, which did not result in a usable satellite image, were one of the very first, they were also used to help design the further experiments, by

providing information on the settling time required to stabilize the gas flow. Results of these additional experiments can be found in Soszynska *et al.* 2019 and Soszynska *et al.* 2020.

4.1.3 Results of the on ground experiments

One of the most important purposes for the experimental series was to determine the relation between the gas flow and the radiation recorded in the camera. The relation was tested using the imagery recorded on the ground. The cameras used for the on ground experiments deliver images of temperature. These temperature values were calculated into spectral radiance values, according to Planck's law. All pixels, which only contained signal from the background, were masked, and the remaining pixels were summed for each image. In the last step, the sum of radiance per image was multiplied by GSD^2, wavelength interval of the spectral band and 4 π, to obtain radiant flux [W]. The correlation of the spectral flux per image with the gas flow measured was tested, as presented in Figure 47.

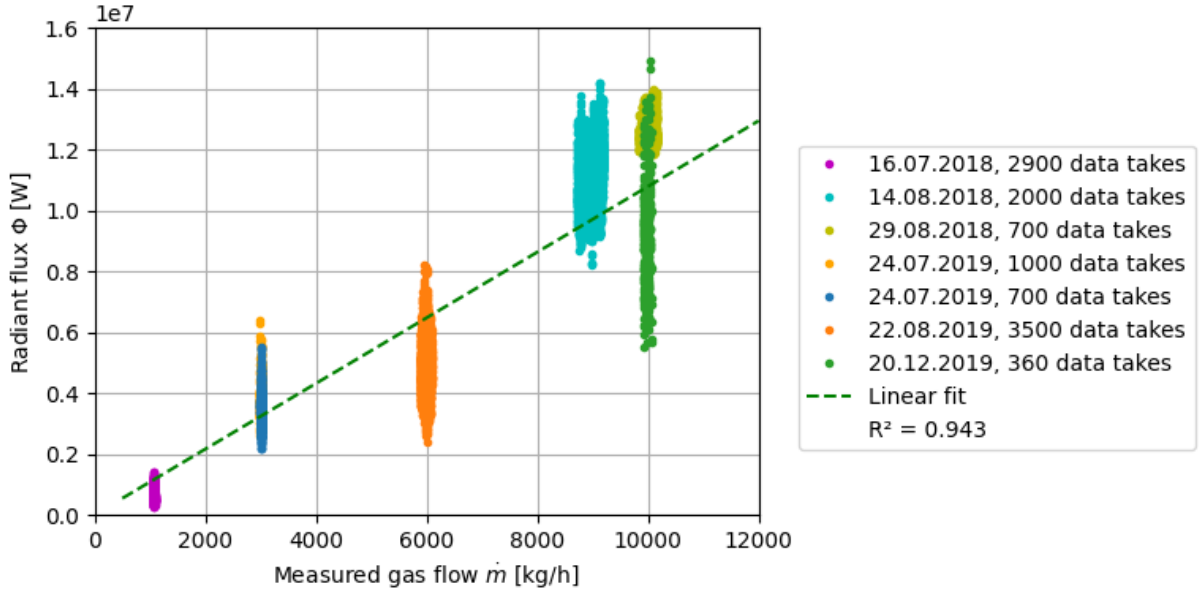

Figure 47: Relation between the measured gas flow and the radiant flux derived from imagery recorded on ground.

As can be seen, the correlation between the spectral flux derived from the imagery and the measured gas flow is very high. This high correlation means that it is plausible to use the radiation recorded in the camera to calculate the gas flow.

Additionally, the dispersion of the radiation, recorded during stable gas flow, could be analysed. For this analysis, the aerial survey data was used, in order to provide the similarity of the perspective to the satellite. Let us consider the data from the experiment from 04.07.19. The Figure 48 below presents the radiant flux recorded during the time when the gas flow was stable.

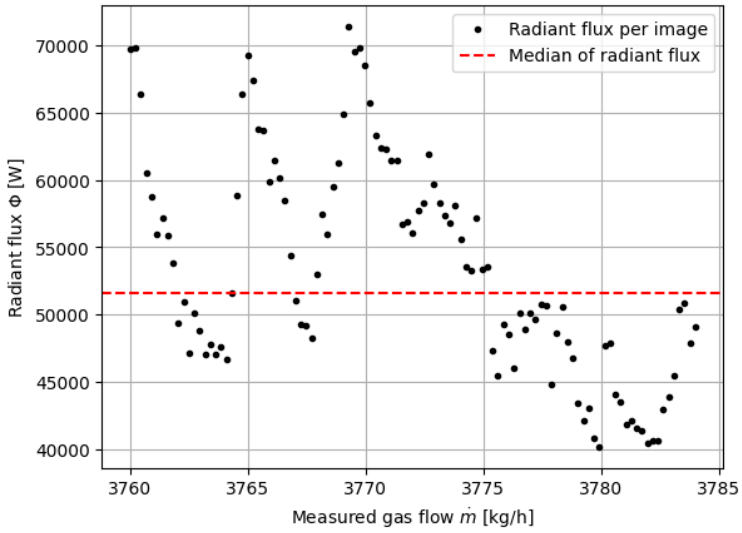

Figure 48: Radiant flux recorded during the experiment conducted on 04.07.19, in relation to the recorded gas flow. Each data point represents radiant flux derived from one image.

As can be seen, the data points are strongly scattered over the plot. To quantify the scattering, the difference between the maximum and the minimum, was divided by the median; the resulting measure for all the aerial data sets as in Figure 47, are presented in Table 10.

Table 10: Dispersion of the radiant flux derived from the aerial imagery.

Flight height	**Gas flow**	**Wind speed**	**Deviation from median**
6000 ft	4 t/h	0.8 m/s	±61%
5000 ft	4 t/h	1.4 m/s	±35%
4000 ft	4 t/h	3.5 m/s	±29%
6000 ft	2 t/h	1.5 m/s	±29%
5000 ft	2 t/h	3.6 m/s	±43%
4000 ft	2 t/h	3.1 m/s	±12%

This means that even with a relatively stable gas flow, the recorded radiation is still extremely variable. This result leads to a very important conclusion for the parametrisation of gas flares from satellite imagery. As can be seen, the radiance sensed by a sensor varies strongly, and the uncertainty of the gas flow calculation from the radiance variation only is as high as ± 61%.

Due to the fact that the bi-spectral method is the most often used method for gas flares parametrisation, it was important to analyse the parameters, which this method allows calculating. From Figure 31 we know already that the projected area of the flame does not change significantly with the changing gas flow. Moreover, wind gusts seem to influence the projected flame area very strongly. The second parameter derived from the bi-spectral method is the flame temperature. The primary analysis on this subject was published in Soszynska *et al.* 2019. Following Figure 49 is cited from this publication. The flame temperature presented in Figure 49 below is an average over 5 thermocouples distributed inside the flame.

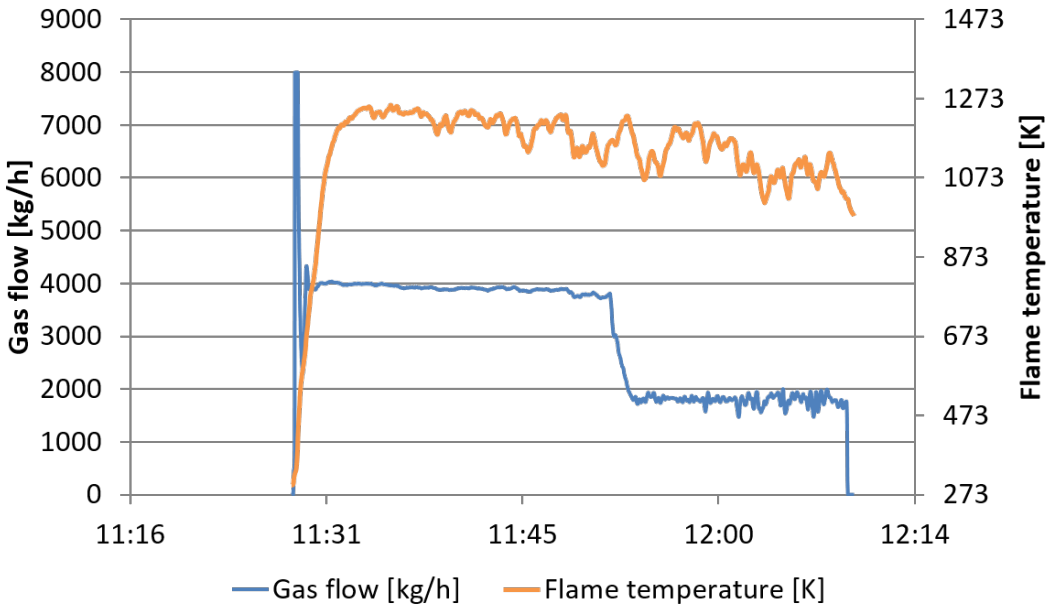

Figure 49: Measurements of gas flow and flame temperature, during the experiment on 04.07.19. Source: Soszynska *et al.* 2019.

As can be seen, there is a drift of the temperature visible, most probably coming from the fact that the water circulating in the tub of the test pad A got increasingly warmer and started to vaporise. However, there is no sudden change in the flame temperature during the time when the gas flow was halved. This result proves that the temperature of the flame is not directly dependent on the gas flow. The temperature rather depends on other combustion conditions, e.g. air-feed.

These results raise strong doubts against using the bi-spectral method (which derived the fire temperature and fire area from the satellite images) for gas flaring parametrisation. Using radiance values instead of temperature values provides a better solution, because the temperature values are interpretations of radiance, basing on assumptions, which may not be true. Therefore, in the presented dissertation the flame radiance $L_{\text{at sensor}}$ was used for this purpose, and the bi-spectral method was used in an adapted version, only to provide information on the background signal.

4.2 Application studies

One of the most important features of the model proposed, was the consideration of the sensing parameters. By considering these parameters, the model should be feasible to be used with different kinds of satellite data, coming from different sensors, with similar results. In order to test this ability, real gas flares from two study areas were considered. Gas flow for the flares in the study areas was calculated from the imagery from two sensors: BIROS and VIIRS. The results of this calculation is presented in following sections.

4.2.1 Study areas

Two study areas were investigated: Persian Gulf and North Dakota.

The first study area is a part of the Persian Gulf between Qatar and Iran. This study area has been chosen due to the simplicity of the background signal. Gas flares in this region are placed on the platforms surrounded by water. The homogeneity of the background allows reducing uncertainties related to otherwise complex modelling of the background signal. In this

region, a geodatabase of gas flares was created, based on photo-interpretation of high-resolution imagery from the LANDSAT-8 panchromatic band (15 m GSD). The database contains 34 gas flares with their exact geolocation (see Figure 50).

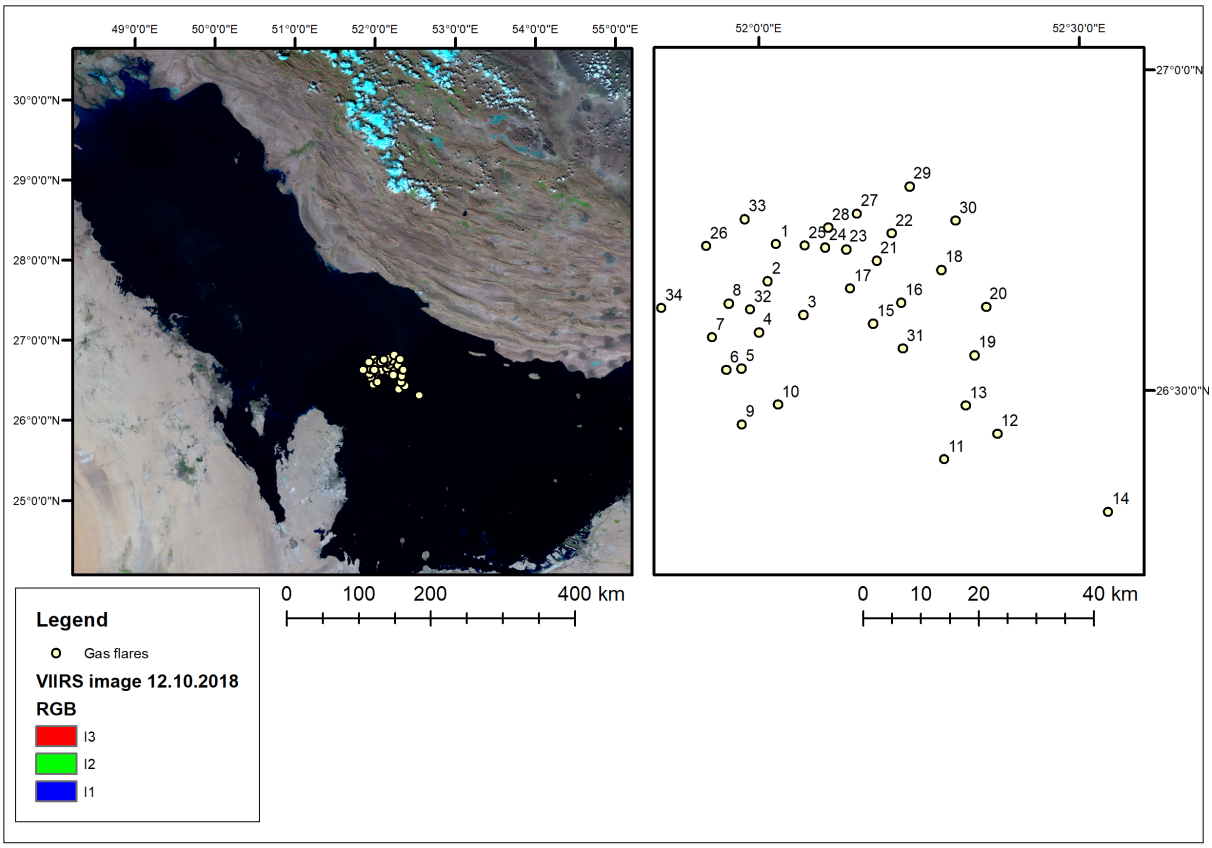

Figure 50: Study area in the Persian Gulf, in comparison to the whole Persian Gulf (on the left) and detailed overview of the gas flares in the database with their ID numbers (on the right).

For the gas flow calculation in this study area, 32 BIROS data sets have been used, recorded between July 2018 and November 2019. Only cloud free imagery has been chosen for the analysis.

For comparison, 10 VIIRS data sets of the Persian Gulf have been selected, recorded between October 2018 and November 2019.

The second study area is a part of North Dakota, referred to as Bakken field (Figure 51). This region has been chosen, due to huge number of gas flares in it, and low temperatures in winter. This area is one of the largest oil production fields in the US, with one of the largest developments in the past 40 years (Zhang *et al.* 2015). The region produces over 10% of the overall US oil production (Zhang *et al.* 2015).

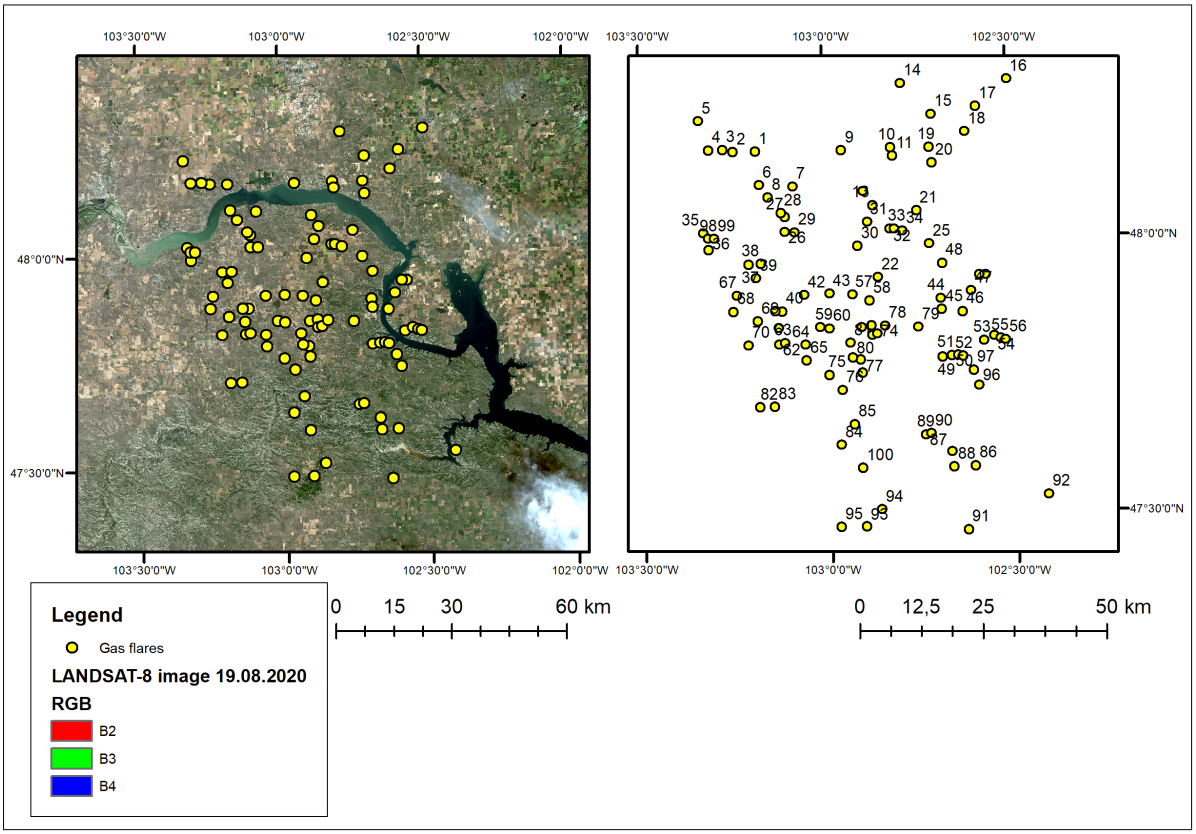

Figure 51: Study area in North Dakota (on the left) and detailed overview of the gas flares in the database with their ID numbers (on the right).

For this region, only winter imagery has been analysed. This approach allowed to derive some information on suitability of the algorithm for parametrising gas flares in low temperature areas, and feasibility of the analysed sensors for the same purpose, their dynamic range and saturation performance.

In this case, one BIROS image from 10.12.2018 03:54 and one VIIRS image from 10.12.2018 08:24 were used. The small-time gap of four hours make the weather conditions very similar for both data sets (the air temperature was 262 K for the BIROS image and 263 K for the VIIRS image, according to the weather archive). Also, both images have very similar light conditions, because both images are recorded during nighttime.

4.2.2 Data selection and processing

Images used for calculation of gas flow have been chosen based on the following criteria:

1. The image is cloud-free or clouds do not cover gas flares.
2. The time gap between BIROS and VIIRS image is less than 2 days.
3. The gas flares are located in the centre of VIIRS image.

VIIRS is a whiskbroom sensor with a very wide imaging swath. The most off-nadir parts of the image have a higher GSD, which can be even double of the GSD at nadir. Giglio & Kendall 2001 suggest that retrieval errors become very high, if a hot-spot consists of less than 0.5% of a pixel area. In case, when GSD at the edges of an image doubles, the proportion of flare signal to background signal becomes disadvantageous for deriving gas flaring parameters.

Apart from that, VIIRS as a whisk-broom sensor records areas, which are more than 30°off-nadir and located near the scan border, twice in subsequent scans. In georeferencing process, the original image is resampled. If a gas flare is recorded twice in subsequent scans, its signal in the georeferenced image consists of a mixture from both scans. The influence of this change has not yet been analysed with respect to gas flaring analysis, hence, the images, in which the study area would be geometrically changed have been excluded from the validation. The same constraints have been applied by, e.g. Zhang *et al.* 2015.

All the VIIRS images, used for gas flow calculation, have been selected, so that time gap between the VIIRS image and the according BIROS image is as small as possible.

For each sensor and each study area, four cases with different flame temperatures have been considered:

1. 1200 K
2. 1600 K
3. 1800 K
4. 2226 K

The temperature 1600 K was chosen as the most probable flame temperature of methane combustion. The temperature 1800 K is often found in the literature, as the probable flame temperature (e.g. Elvidge *et al.* 2016). The other temperatures, 1200 K and 2226 K allow to calculate the minimum and maximum gas flow, so to provide an estimate of the maximum possible gas flow error due to temperature uncertainties. The temperature of 1200 K is the minimal flaring temperature found in literature (e.g. Leahey *et al.* 2001), and 2226 K is the temperature of stoichiometric methane combustion.

When changing flaring temperature for the calculation, parameter proportion of radiation recorded in spectral band $\psi(\lambda, \Delta\lambda, T)$ need to be adjusted accordingly (as in Figure 28). In theory, also the parameters $c\chi(T)$ and $\rho(T)$ should be adjusted, however within the framework of this research it was not possible to estimate the dependency of ρ on the flaring temperature, therefore the value was estimated using the experimental imagery and assumed to be constant.

An important step before the actual analysis was to mask the invalid values. The calculated gas is considered invalid if it reaches a value below 1000 kg/h or above 100000 kg/h. The lower threshold has been set basing on results of the experimental series and the sensitivity of the BIROS sensor. In one of the experiments at the BAM TTS, gas flow was set to 1000 kg/h, and the fire was not visible in the satellite image. The BAM scenes were, in comparison to Persian Gulf scenes, very difficult to calculate the flare radiance due to a very variable background. Let us assume a gas flare recorded by BIROS sensor. In theory, radiation of a gas flare in a BIROS image should be 0.214 $W/m^2/sr/\mu m$. As the radiation of a flare is distributed over several pixels (due to blur of the optics, this value would increase the radiance of several pixels surrounding the flare, by the above-mentioned value, distributed as described in the PSF function. The assumed blur is illustrated in Figure 13. The radiation of a point source is distributed over around 9 pixels with a Gaussian shape. The maximum of this distribution is in the centre pixel, which records 0.245 of the flare radiation recorded by BIROS sensor. Therefore, the centre pixel would record $0.245 \cdot 0.214\,W/m^2/sr/\mu m$, so $0.05\,W/m^2/sr/\mu m$. The standard deviation of the Persian Gulf study area is around $0.017\,W/m^2/sr/\mu m$ and around 97% of all sea pixels are within one standard deviation from the mean. Therefore, a flare with a radiance value of $0.05\,W/m^2/sr/\mu m$, which is 2.9 times the standard deviation of the sea radiance, should be well distinguishable from the background in the Persian Gulf study area. This threshold should also apply for the North Dakota image, because the background radiance and its standard deviation in winter is very low (mean radiance is $0.09\,W/m^2/sr/\mu m$ with standard deviation of $0.008\,W/m^2/sr/\mu m$).

As for the upper threshold, in theory, only saturation can restrain the feasibility of a sensor to derive gas flaring parameters, but a detection should still be possible. A gas flare with gas flow of 100000 kg/h would cause an immensely large flame, which is rather improbable. The flame height for 100000 kg/h, calculated as in Section 3.5.2, would be 102.8 m. Additionally, such a gas flow would cause a release of energy greater than a ton of TNT explosion per hour. In the gas flaring database published by Elvidge *et al.* 2016, the highest gas volume for an individual flaring station was around 1 BCM, which calculates to 75000 kg/h gas flow on average. Due to the fact that calculations can contain errors (e.g. error of the model for summed gas flaring volumes for each country is 1.6 BCM), an additional safety buffer needed to be assumed. Hence, the author decided to set the upper threshold to 100000 kg/h.

4.2.3 BIROS results

Persian Gulf

The calculated gas flow values for each flare in the Persian Gulf study area are presented in Figure 52, on an example image from 13.11.2019. In this calculation, a flame temperature of 1600 K is assumed. Flares, in which the calculated gas flow does not reach the lower threshold of 1000 kg/h, are considered to be inactive.

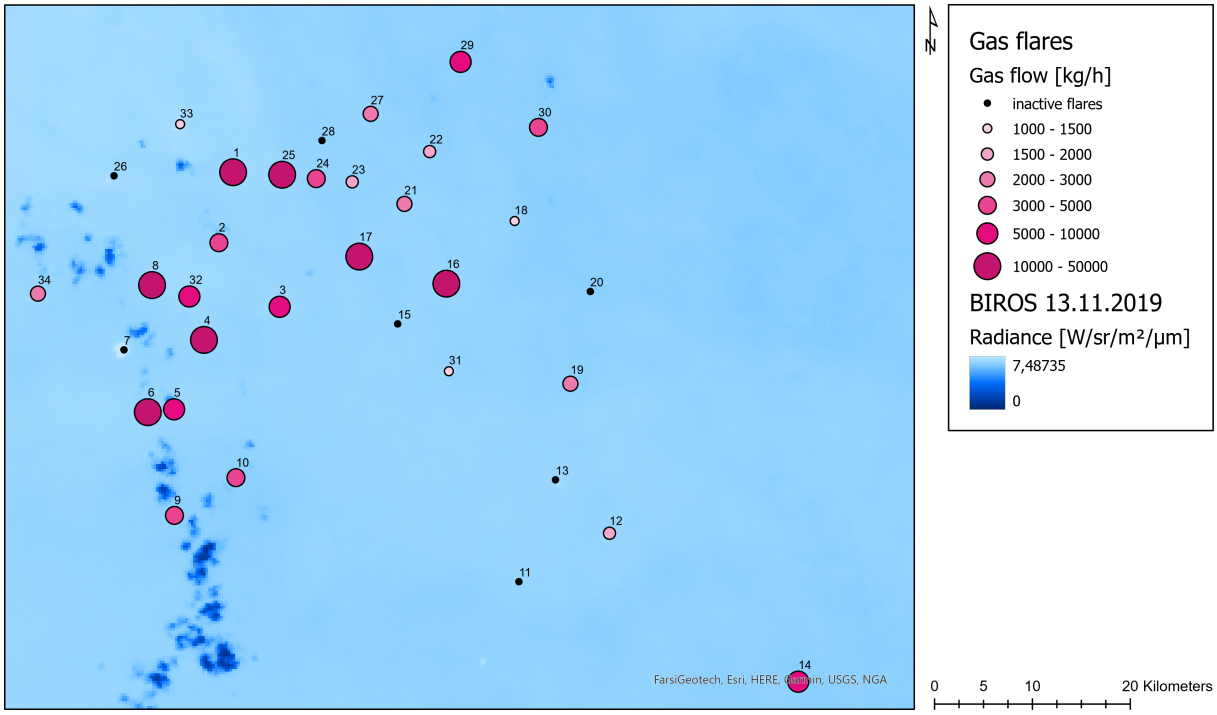

Figure 52: Example calculation of gas flow per flare in Persian Gulf, basing on BIROS MWIR image.

As can be seen, a significant number of gas flares are considered inactive (10). There is a strong variability in the calculated gas flow values. A group of 5 flares has gas flow exceeding 10000 kg/h, and at the same time 3 gas flares has gas flow between 1000 kg/h and 1500 kg/h.

For all the gas flares and all the dates, the distribution among the classes, as presented in Figure 52, is illustrated in Figure 53.

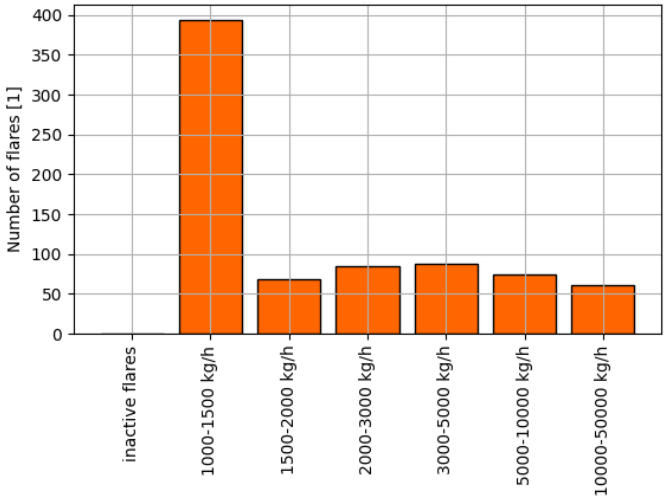

Figure 53: Distribution of calculated gas flow values among classes.

As can be seen, the distribution of calculated gas flow values is rather homogeneous among all the classes, apart from the "inactive flare" class. For a better overview of calculated gas flow values, an analysis of the time series per gas flare is an important step.

A time series for three gas flares is presented in Figure 54. In Figure 54 three gas flares are chosen, which have the most valid gas flow calculations from all the images. Thus, more valid conclusions on time series can be drawn.

As we know from Figure 4, the amount of gas flared may vary strongly from day to day. This variation is also visible in Figure 54, especially in case of Flare 4.

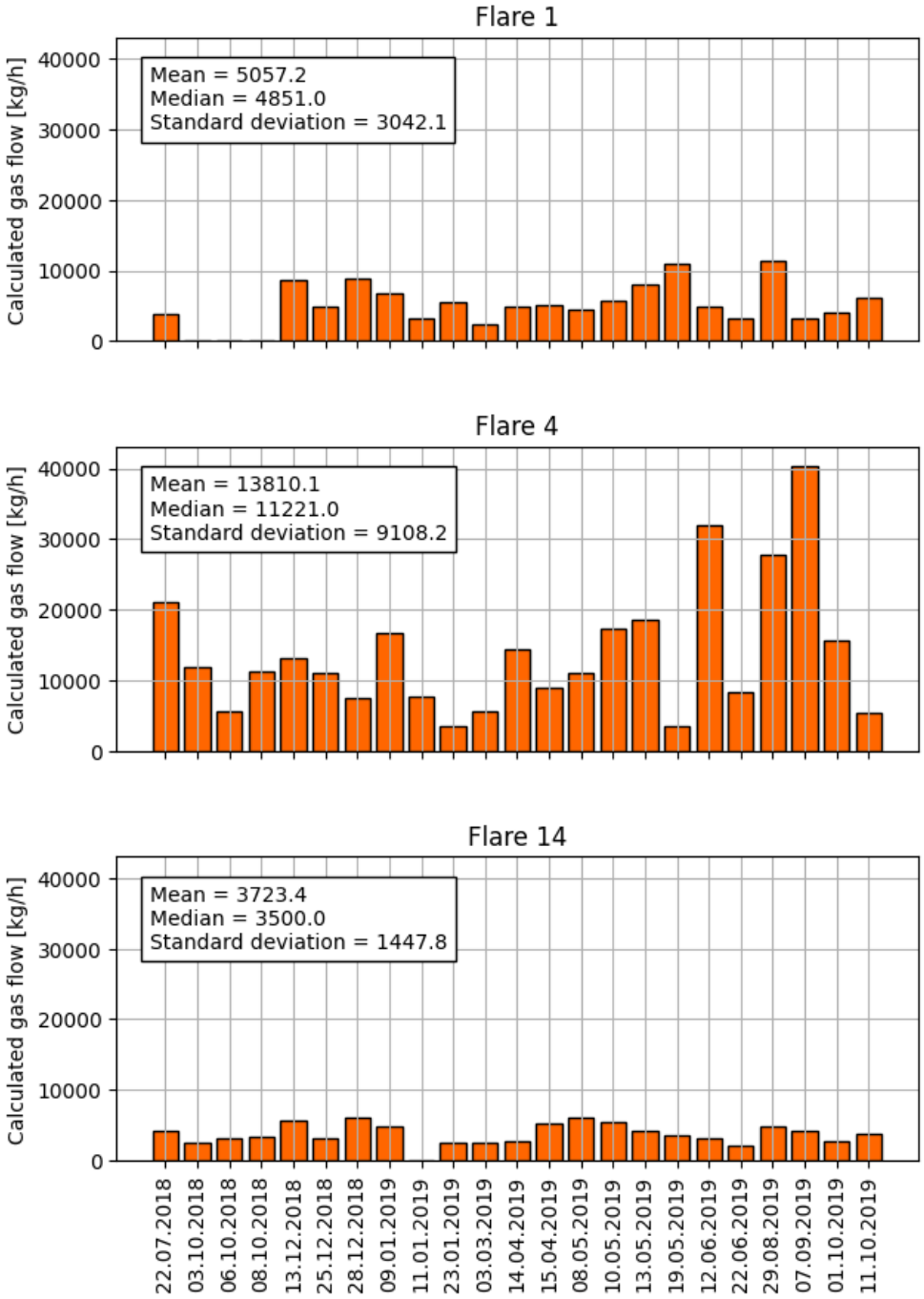

Figure 54: Gas flow calculated for flares with ID 4, 8 and 25 using BIROS imagery.

In case of the gas flare with ID 4, between July 2018 and May 2019, moderate variation in gas flow can be observed. On the other hand, in case of Flare 14, the variation between the dates is rather low. As can be seen in the boxes with statistical measures in Figure 54, the higher the mean, the higher the standard deviation. This tendency can be more clearly observed in Figure 55 presented below.

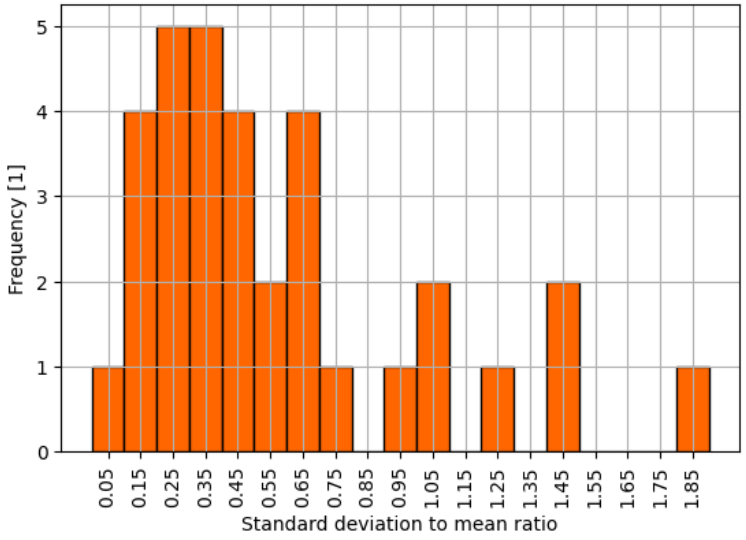

Figure 55: Histogram of standard deviation to mean ratio.

A majority of all calculated ratios presented in Figure 55 belong to the first classes with rather low ratio values. However, the frequency of the 0.65 class is not far from the peak. It seems that the ratios are concentrated in lower classes. In only six gas flares, the standard deviation is higher than the calculated mean. This confirms the statement that the standard deviation grows with the mean, which means that gas flares with typically higher gas flows also have stronger variation in the gas flow values. Consequently, it is safe to use mean or median values for calculating flared gas volume for a time period (e.g. a month). This approach is used in some research publications, such as Elvidge *et al.* 2016; Elvidge *et al.* 2007.

The long-term statistics for all flares are presented in Table 11 below.

Table 11: Statistical measures per flare, for all BIROS images, calculated for the temperature 1600 K.

Flare ID	Median	Mean	Max	Standard deviation
1	5255	6253	13719	2975
2	5973	7879	50499	9541
3	2183	2782	6219	1363
4	11866	15275	47053	11126
5	3816	5271	28122	5459
6	5946	12647	70736	18599
7	12472	21283	81060	21174
8	22620	24511	55783	13469
9	2137	6621	45573	12362
10	1670	4594	52830	11712
11	NA	NA	NA	NA
12	1227	1313	1660	313
13	1398	1486	2231	424
14	3916	4147	8512	1556
15	1261	1361	1718	219
16	4010	6504	47485	9271
17	2763	3315	10391	2153
18	1418	1775	3032	683
19	1864	2393	7768	1552
20	2428	2283	3012	761
21	1510	1671	2255	403
22	1218	1302	1595	219
23	1311	1678	4588	923
24	1908	2251	4821	984
25	7050	8641	24506	5255
26	1338	1357	1677	249
27	1720	1680	2246	419
28	25741	28144	57670	28401
29	3540	3801	6411	1286
30	1674	2179	6192	1326
31	1526	1462	1585	164
32	2184	2525	5429	1153
33	1202	1282	1693	287
34	1761	1806	2968	648

In Table 11 some flares have only NA as statistical measures. This happens, when all the calculated gas flow values for a given flare have been below the lower masking threshold 1000 kg/h, or above the upper masking threshold 100000 kg/h.

The standard deviation values in Table 11 sometimes are very high. This is plausible, remembering the strong variation of gas flow over a long time span, as presented in Figure 4. Additionally, the standard deviation values may be high if in a single case (or in very few cases) emergency flaring is recorded. The emergency flaring appears if e.g. pressure in the system builds up and needs to be released to maintain safety of the system. In such case, the gas flow values may be very high, typically for a short period of time.

Statistics over all the gas flares and all the images are presented in Table 12.

Table 12: Statistical measures of all gas flow values calculated from the BIROS imagery, for all the assumed temperatures.

	1200 K	**1600 K**	**1800 K**	**2226 K**
Median	2639	2969	3209	3962
Mean	5823	6498	7205	8699
Standard deviation	9816	10389	11997	13754
Max	94218	81060	96488	99680
NaN %	46	38	32	25

Generally, the hotter the flame temperature assumed, the higher the gas flow calculated (to be exact: mean and median of calculated gas flow). This happens due to the change of the Planck curve with increasing temperature: The hotter the black body, the further towards the shorter wavelengths the peak is, and hence, the higher the proportion $\psi(\lambda, \Delta\lambda, T)$ of overall radiation recorded in MWIR spectral region (the measured flame radiance $L_{\text{at sensor}}$ remains constant). Exceptions to this rule may appear if some values are masked, when higher temperature is assumed.

All the gas flow calculations from BIROS imagery of the Persian Gulf can be found in Appendix C.

North Dakota

As for North Dakota, the results are illustrated in the following map (Figure 56).

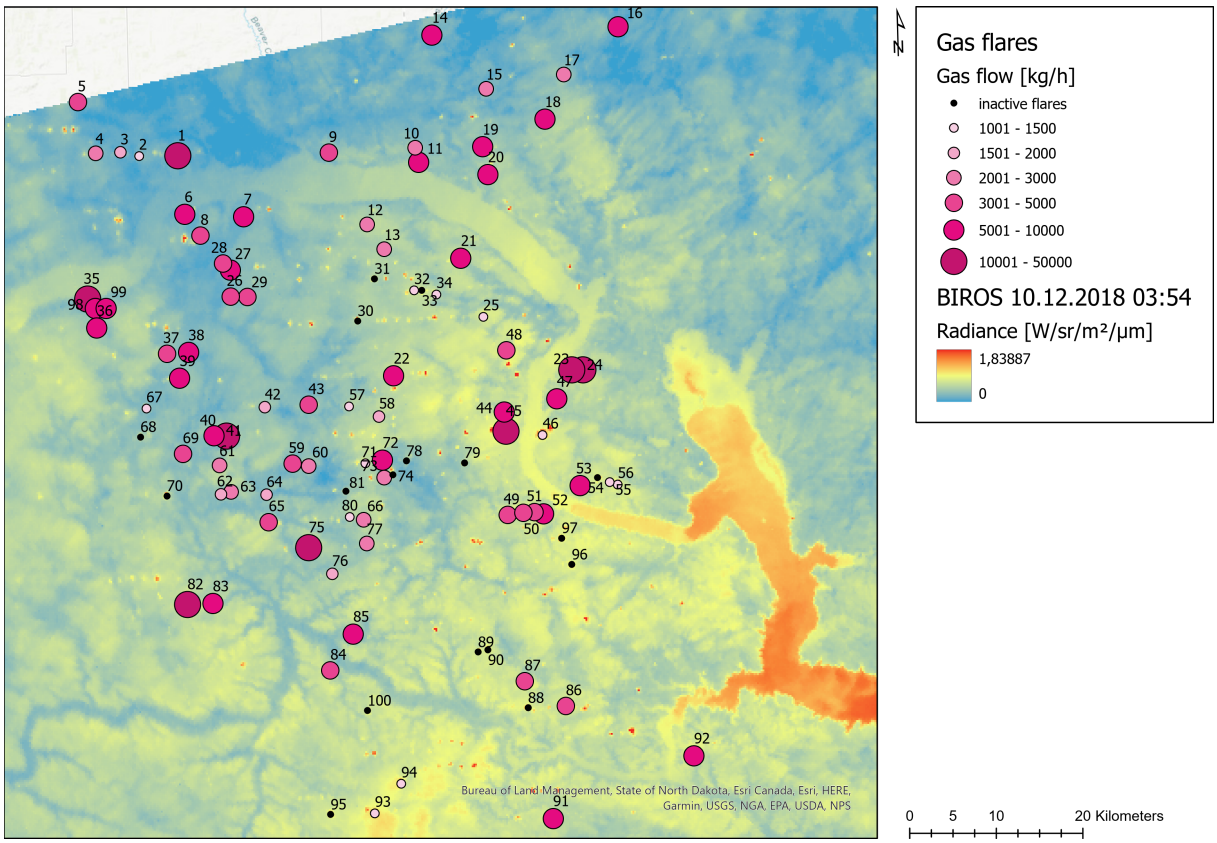

Figure 56: Calculated gas flow values in North Dakota, illustrated on the BIROS image from 10.12.2018, used for calculation.

Again, many gas flares are treated as inactive. The values are also quite variable, similar to those in the Persian Gulf. This is also visible in the histogram calculated for the classes as in Figure 56, presented in Figure 57.

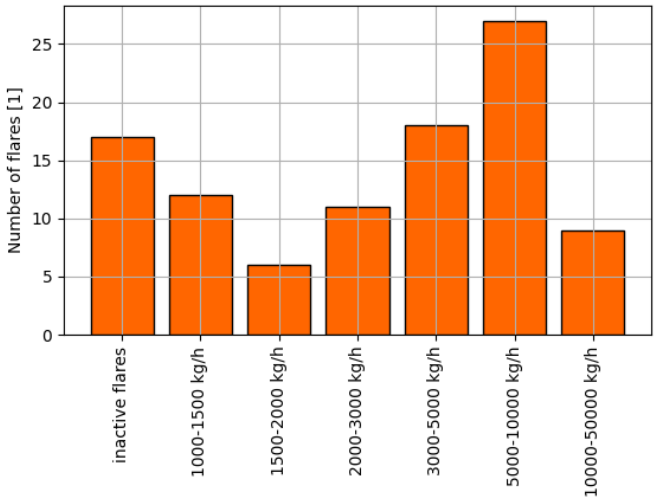

Figure 57: Distribution of calculated gas flow values among classes for, North Dakota study area.

The distribution of calculated gas flow values is similar to the normal distribution, except for the first class (inactive flares). This is different from in the Persian Gulf flares, where the distribution among the classes was rather homogeneous. The only similarity is the high number of inactive flares.

The gas flow values for all the gas flares are presented in Figure 58.

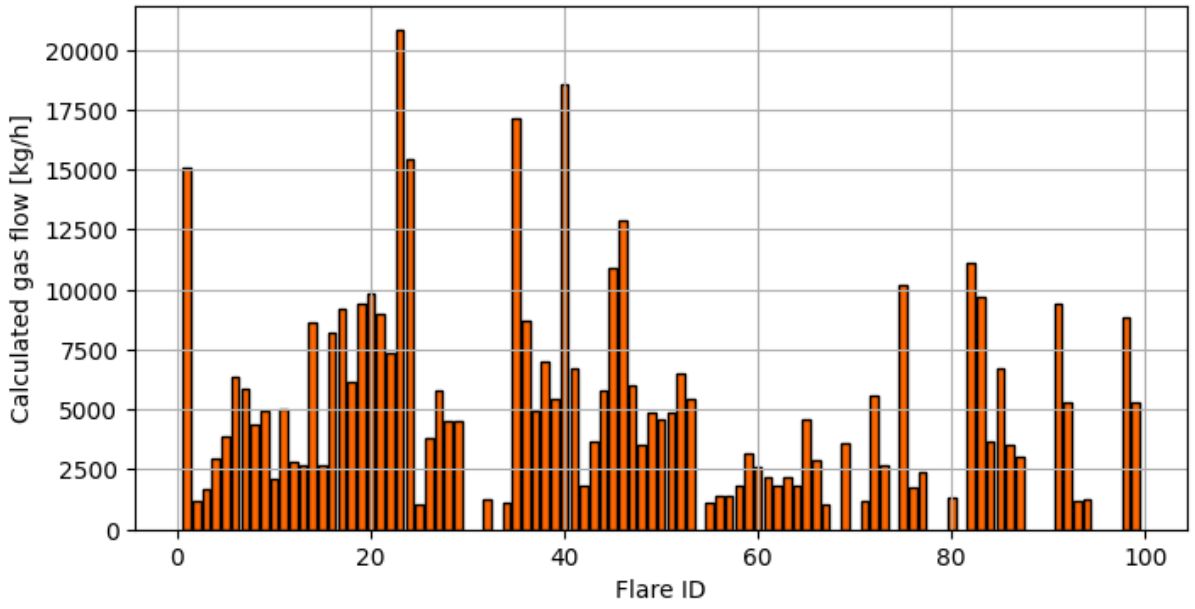

Figure 58: Gas flow values per flare in North Dakota calculated from BIROS MWIR imagery, for a temperature of 1600 K.

The gas flow values vary strongly from one flare to another. However, in some cases, two consecutive gas flares have very similar gas flow values (e.g. 28 and 29, as well as 56 and 57). This may happen, if the gas flares are located so close to each other, that the window used for calculation of the flame radiance $L_{\text{at sensor}}$ covers both flares. In North Dakota gas flares are sometimes located so near one to another that they are treated as a single hot-spot (see Figure 59).

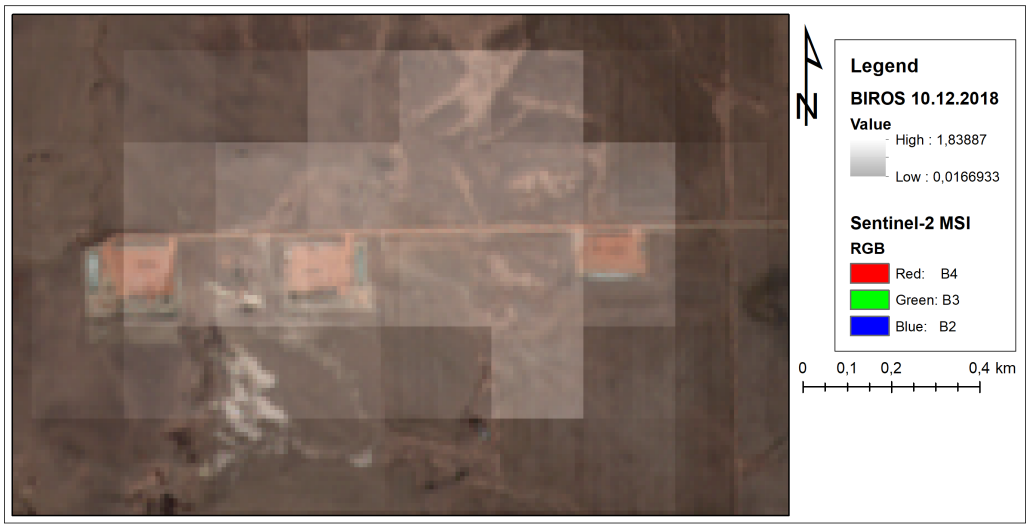

Figure 59: A single BIROS hot-spot covers multiple flaring sites.

The statistical measures of the calculated gas flow values for all flares are presented in Table 13.

Table 13: Statistical measures of gas flow values for all flares, calculated from BIROS imagery of North Dakota.

	1200 K	**1600 K**	**1800 K**	**2226 K**
Median	3652	4555	5412	6653
Mean	4462	5458	6432	8632
Standard deviation	3050	4188	4990	7293
Max	15355	20804	24764	35959
NaN %	27	17	16	8

Interestingly, the median gas flow values from the North Dakota study area are significantly higher than these from the Persian Gulf. In Persian Gulf more gas flares had exceptionally high values, which have an influence on mean, but not median. This observation is confirmed by comparing the maximum values of Persian Gulf and North Dakota: the North Dakota maximal values are much lower.

4.2.4 VIIRS results

In this section, results of gas flow calculations from VIIRS imagery are presented. Two of VIIRS spectral bands were used for this calculation: I4 (recording in MWIR spectral range) and I3 (recording in SWIR spectral range). Both of these bands have a GSD of 375 m. First, the gas flow values calculated from the I4 band are presented.

Persian Gulf results for I4 band

An example of gas flow calculation from VIIRS data from the 11.11.2019, is presented in Fig-

ure 60. Again, a flame temperature of 1600 K is assumed. Same as for the BIROS results, the calculated gas flow values below 1000 kg/h were treated as invalid (inactive flares).

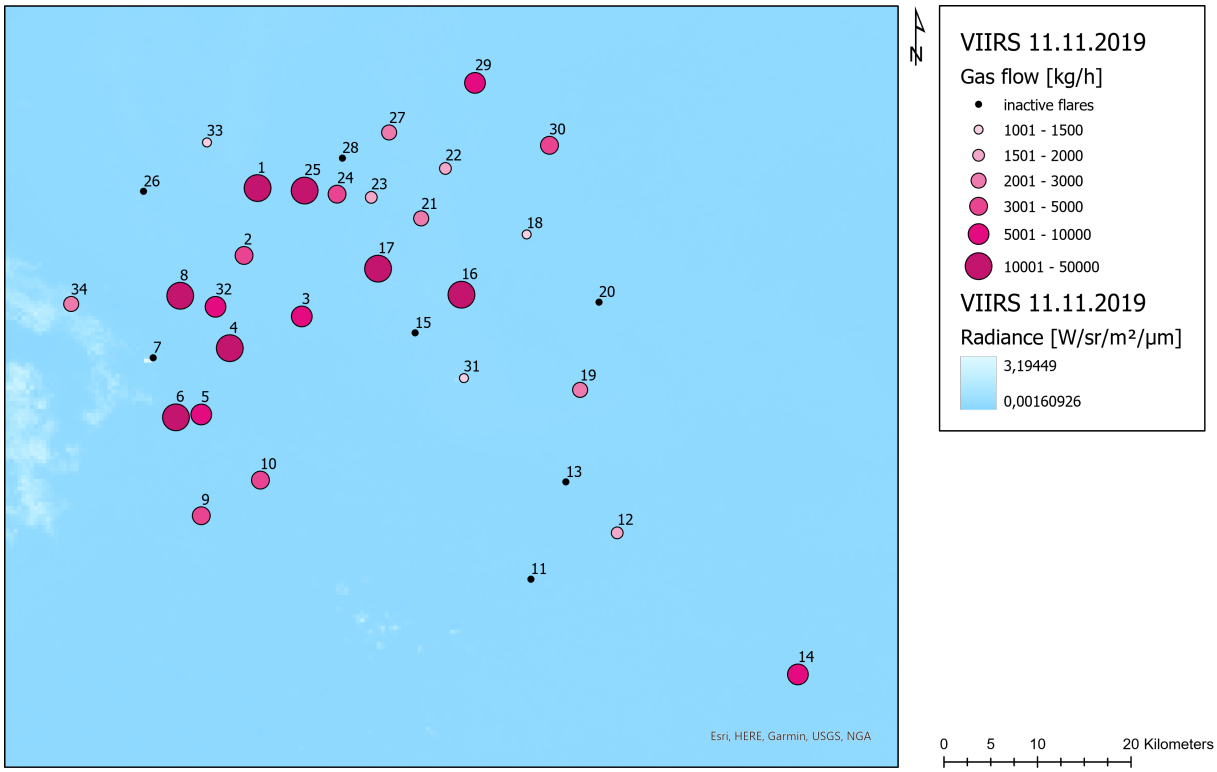

Figure 60: Example calculation of gas flow per flare in Persian Gulf from VIIRS I4 imagery.

In Figure 60, some gas flares (8) are marked as inactive. There are 5 gas flares with gas flow exceeding 10000 kg/h. The rest of the gas flares has rather moderate gas flow values.

The distribution of all the gas flow values among the classes, as in Figure 60, is presented in Figure 61.

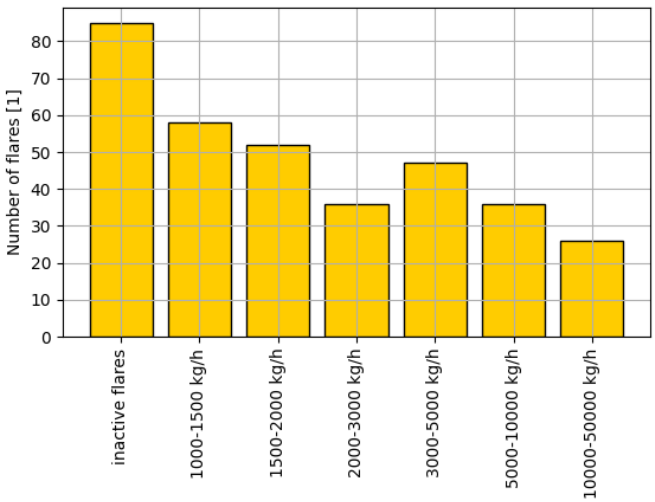

Figure 61: Distribution of gas flow values, calculated from VIIRS imagery, among classes.

The distribution of gas flow values calculated from VIIRS imagery is different from the distribution of classes calculated from BIROS imagery. The number of flares decreases from left to right, towards the highest gas flow values.

Analogously to Figure 54, a time series of gas flow values is presented in Figure 62 for the same gas flares.

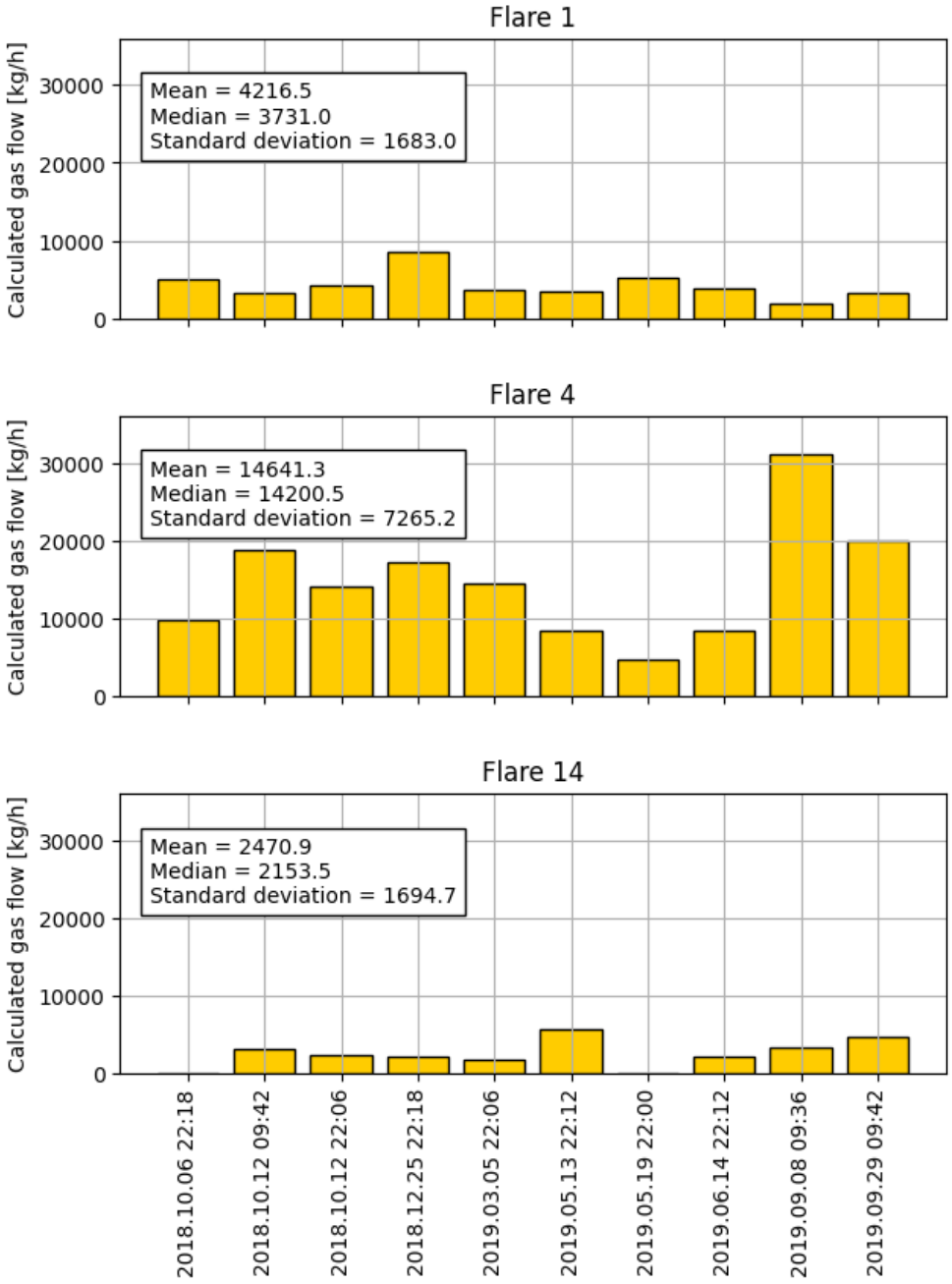

Figure 62: Gas flow values calculated for flares with ID 1, 4, 14 from VIIRS I4 imagery.

In case of flares 1 and 14 presented in Figure 62 the calculated gas flow is rather low. Flare 4, as in BIROS, has rather high gas flow values. The distribution of higher gas flow values throughout the year is also quite similar to the distribution calculated with BIROS data. In the next step, the analysis of distribution of standard deviation to mean ratio was conducted (Figure 63).

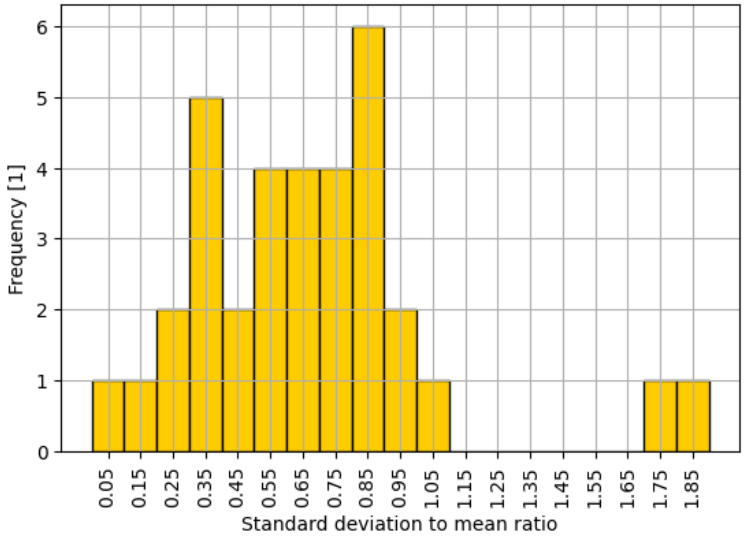

Figure 63: Histogram of standard deviation to mean ratio (calculated from VIIRS data).

This time, the distribution of standard deviation to mean ratio resembles more the normal distribution, with a peak at 0.85. Most of the gas flares have standard deviations of the gas flow values lower than the means. Only 3 gas flares have the opposite situation. It is important to note that only 10 VIIRS images were used for this analysis. It is possible that with more data takes, the histogram would be more similar to the one calculated from BIROS data in Figure 55.

The statistics of gas flow values for each flare throughout all the dates from VIIRS imagery are presented in Table 14.

Table 14: Statistical measures per flare, for all VIIRS images, calculated for temperature 1600 K.

Flare ID	Median	Mean	Max	Standard deviation
1	3766	4824	10893	2624
2	4388	5635	17185	4526
3	1829	2046	3041	614
4	13965	14320	31067	7343
5	4028	4824	16560	4309
6	4831	13708	39722	13143
7	9568	11520	27952	7879
8	16427	17595	36315	11855
9	1956	2328	4947	1332
10	1519	4125	23989	7461
11	1229	2515	6568	2243
12	2079	3710	7933	2752
13	1608	2621	6890	2079
14	3065	3086	5620	1297
15	1472	1700	3117	782
16	3515	4599	18471	4707
17	1927	2965	8087	2170
18	1753	2673	8299	2322
19	1845	2486	6405	1748
20	1545	2273	7135	1873
21	1369	1362	1640	319
22	1507	2089	6073	1774
23	2092	2570	4346	1661
24	1521	1649	2767	632
25	8575	7793	11682	2651
26	1530	1449	1688	284
27	1389	1422	2024	344
28	1745	4560	22386	7874
29	2748	2511	3484	801
30	1544	2220	5638	1453
31	1798	1897	3768	959
32	1997	2257	3864	755
33	1773	1773	1773	NA
34	3544	4672	10419	4339

In one case, the standard deviation for a flare is NA. This happens if a valid gas flow value was calculated only once in all the images. Mean values are typically higher than median values (38% higher on average). This is a result of several outliers with high gas flow values.

Statistics for all flares and all images, calculated for three temperature cases are presented in Table 15.

Table 15: Statistical measures for gas flow values calculated from VIIRS I4 imagery of Persian Gulf, for four flame temperatures.

	1200 K	1600 K	1800 K	2226 K
Median	2271	2334	2626	3336
Mean	4201	4957	5572	7460
Standard deviation	5002	6412	7459	10501
Max	29448	39722	47209	68461
NaN %	37	25	20	11

In Table 15, the mean values are around twice as high as the medians. The standard deviation values are also very high and are even higher than the mean values. This suggests that many outliers with exceptionally high gas flow values are present.

Further statistics on the flares calculated from VIIRS I4 imagery can be found in Appendix C.

North Dakota results for I4 band

In case of North Dakota, the following map (Figure 64) presents the gas flow values calculated from the VIIRS I4 imagery.

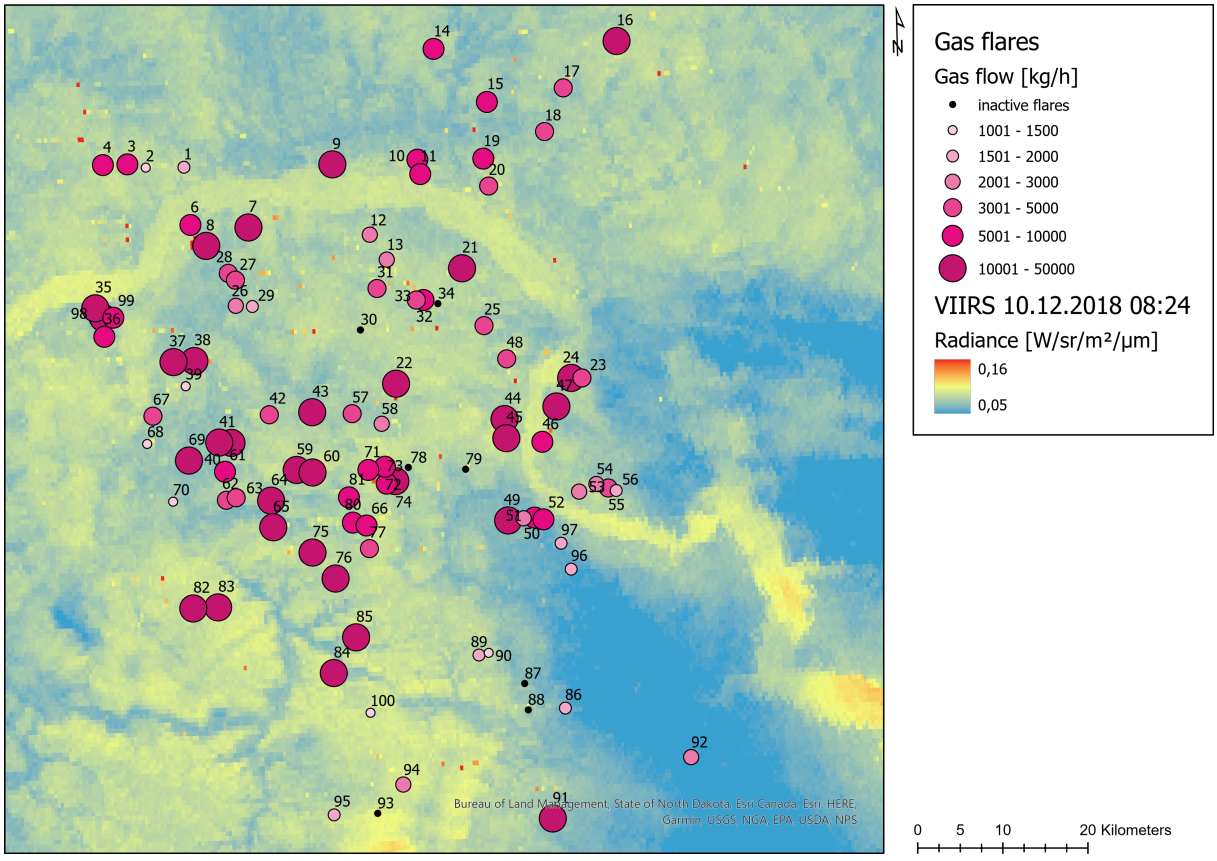

Figure 64: Gas flow values calculated from VIIRS I4 imagery of North Dakota.

As opposed to gas flow values calculated for Persian Gulf study area, the gas flow values presented in Figure 64 are higher. Only 7 gas flares are inactive in this case. In Figure 64, many calculated gas flow values belong to the highest class in the scale (10000 kg/h to 50000 kg/h).

The distribution of all values over classes can be seen in Figure 65.

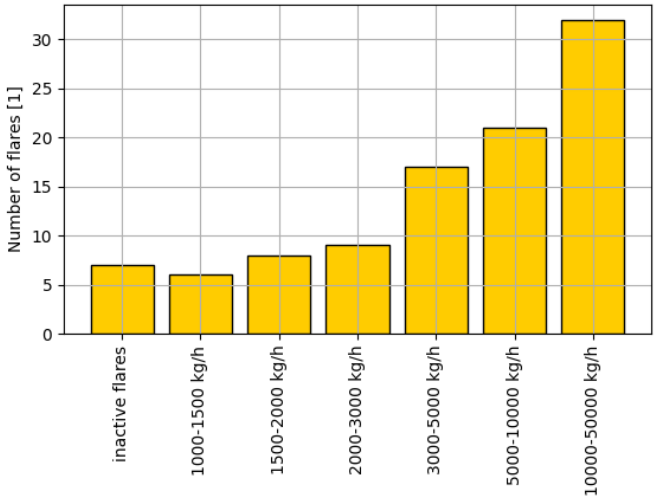

Figure 65: Distribution of gas flow values, calculated from VIIRS imagery of North Dakota, among classes.

As can be seen, the distribution among classes is different from the Persian Gulf area. The distribution is strongly concentrated in the higher gas flow classes.

The gas flow values per flare are presented in Figure 66.

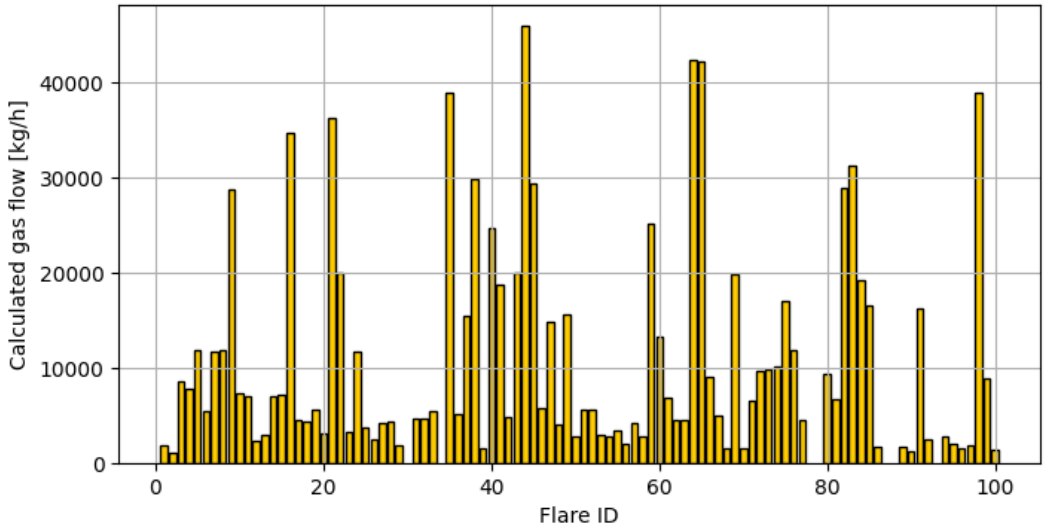

Figure 66: Gas flow values per flare calculated from VIIRS I4 imagery for temperature 1600 K.

The gas flow values vary very strongly. The variation seems to be even stronger than in the gas flow values calculated from BIROS images.

The statistical measures of gas flow values in North Dakota are presented in Table 16.

Table 16: Statistical measures for gas flow, calculated from VIIRS I4 imagery of North Dakota.

	1200 K	**1600 K**	**1800 K**	**2226 K**
Median	4890	5676	6733	9530
Mean	8388	10988	12806	17873
Standard deviation	8313	11176	13254	19134
Max	34070	45957	54618	79205
NaN %	10	7	5	1

The strong variability visible in Figure 66 is confirmed by high standard deviation values in Table 16. The mean and median are altogether significantly higher than the gas flow values in the Persian Gulf calculated from VIIRS imagery.

The presented results of gas flow calculation using the I4 band seem plausible and have similar values to those calculated using the BIROS data. This is however not the case for the gas flow values calculated using the I3 band.

Results from VIIRS I3 band

Although, in principle, the method presented should be applicable with SWIR spectral bands, the gas flow values estimated from the I3 band of VIIRS were not plausible. The calculated values are expected to be similar to those calculated with I4 band, but in reality they were approximately two magnitudes lower. To explain this situation, the radiance values of gas flares in I3 band were modelled, and compared with the real recorded values.

The theoretical values of radiation can be estimated twofold. The first method is to assume a pixel containing a black body (or grey body) of a certain area, and a homogeneous background. The calculation (such as in Table 17) comprises calculating spectral intensity of a gas flare flame I_{flame} by multiplying flame radiance $L_{\text{at sensor}}$ by flame area A_{flame} and flame emissivity $\varepsilon_{\text{flame}}$. The same procedure is then repeated for spectral intensity of background I_{bkg}. To calculate the radiance of a pixel with a gas flare, a sum over spectral intensities of the flare and background I_{flame} and I_{bkg} is divided by a sum of both areas A_{flame} and A_{bkg} (which corresponds to GSD^2 of a sensor).

Table 17: Pixel radiance calculation for a pixel with a gas flare, for VIIRS I3 band.

Flare			
Temperature	T_{flame}	1600	K
Spectral radiance	$L_{\text{at sensor}}$	41474	W/m^2/sr/µm
Area	A_{flame}	10	m^2
Emissivity	$\varepsilon_{\text{flame}}$	0.7	1
Spectral intensity	I_{flame}	2.90E+05	W/sr/µm
Background			
Temperature	T_{bkg}	300	K
Spectral radiance	L_{bkg}	1.27E-06	W/m^2/sr/µm
Area	A_{bkg}	140615	m^2
Emissivity	ε_{bkg}	0.96	1
Spectral intensity	I_{flame}	1.72E-01	W/sr/µm
Pixel			
Area	A_{pix}	140625	m^2
Spectral intensity	I_{pix}	2.90E+05	W/sr/µm
Spectral radiance	L_{pix}	2.06	W/m^2/sr/µm

It is important to note that the signal of the background is 6 magnitudes lower than the signal of the flame. However, it is important to note that this value consists of radiance values

only, not taking the solar reflection into account (which is significant in SWIR). As calculated in Table 17, the expected pixel radiance of a pixel with a gas flare is 2.06 $W/m^2/sr/\mu m$.

The second method is to solve Equation (11) for spectral radiance of a gas flare recorded by a sensor $L_{\text{at sensor}}$ assuming a given gas flow, e.g. 2000 kg/h. This method calculates the flare radiance only, without the background. Assuming a gas flow of 2000 kg/h, flare radiance would be 1.26 $W/m^2/sr/\mu m$.

Notably, the radiance calculated with the first method is 1.63 times the radiance calculated with the second method, this can be explained by the fact that a gas flare of 2000 kg/h does not necessarily need to have a projected flame area of 10 m^2.

If comparing the radiance values from I3 spectral band, e.g. from the image 14.06.2019, conclusions can be drawn. After masking all the sea pixels (using the histogram as a guideline), only flare pixels are left. Mean radiance value for the flare pixels is 0.07 $W/sr/m^2/\mu m$ without subtracting background radiation or reflection and 0.023 $W/sr/m^2/\mu m$ with the background signal subtracted, including reflection. Using the reversed Equation (11) as a guideline, flare radiances without background would translate into 145 kg/h gas flow. At the same time, in the same image in I4 band, the mean flare radiance is 0.63 $W/sr/m^2/\mu m$, which translates to 1826 kg/h. The maximal flare radiance (with subtracted background radiance) value in the I3 band is 0.30 $W/sr/m^2/\mu m$. This translates to 1893 kg/h. In I4 image, the maximal value is 2.27 $W/sr/m^2/\mu m$, which translates to 6579 kg/h.

The modelled radiance values for I3 band are significantly higher than the radiance values recorded in the I3 band. This difference may be explained if one of the parameters of the model differs from the assumed values. The parameter, which could be significantly different in MWIR and SWIR wavelengths, is the amount of radiation: ρ.

Fitting ρ on the values derived from I4 band and radiance recorded in I3 band, leads to a conclusion that in SWIR range it is significantly lower than in MWIR. If fitted on maximal values (0.3 $W/sr/m^2/\mu m$ in SWIR and 2.27 $W/sr/m^2/\mu m$ in MWIR), the ρ parameter for SWIR should be around 0.02. If fitted on mean values (0.023 $W/sr/m^2/\mu m$ in SWIR and 0.63 $W/sr/m^2/\mu m$ in MWIR), the ρ for SWIR should be around 0.006.

4.3 Validation

The validation of the results comprises four parts. The first and the most important one, is the validation of the gas flow values calculated from the imagery of the experimental series. This is the only absolute validation basing on the reference gas flow values measured during the experiments.

The second part of the validation was a comparison between the gas flow values calculated using BIROS and VIIRS data. This allowed to test whether the method proposed is applicable for different sensors with similar results.

In the third part, gas flow values calculated using BIROS data were compared to gas flow values calculated using SLSTR with a method published by Elvidge *et al.* 2016 adapted for the SLSTR by Caseiro *et al.* 2018. The method published by Elvidge *et al.* 2016 is often applied in gas flow research and was validated in different study areas.

Lastly, different sources of uncertainty influencing the accuracy of the gas flow calculation were analysed.

4.3.1 Gas flow calculation for the experimental series

The experiments conducted were used to test the accuracy of the model. For each of the satellite images from the experiment, gas flow was calculated and compared with the gas flow measured (see Figure 67).

The error bars presented in the plot were calculated by reducing and increasing the parameters ρ, and $\tau_{(\lambda)}$ 0.1 each. Additionally, the $L_{\text{at sensor}}$ was altered 10% to account for the

variability of the flame. The uncertainty level is very high, however given the complexity of the object modelled and the scarcity of measurements, from which the gas flow is derived, it seems reasonable to count with such uncertainties.

The gas flow values calculated with the model seem to be well in accordance with the measured gas flow values, except for one data set. The Pearson's coefficient of correlation is $R^2 = 0.90$.

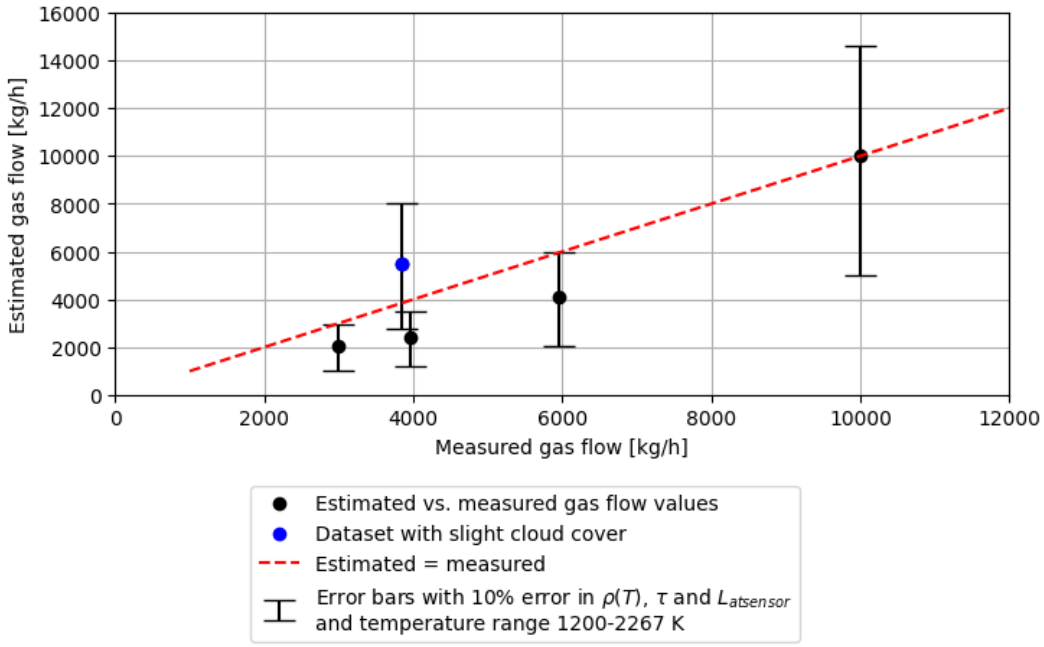

Figure 67: Model tested on 5 experiment data sets.

After a review of the documentation of the experiments, it was stated that this data set should rather be neglected, due to a partial cirrus cover over the TTS (see Figure 68), which causes some variation the radiance values measured by the satellite, especially in the LWIR band. Cloud cover seems to have a different influence on radiance recorded in MWIR and in LWIR ranges. Radiance values in LWIR are dimmed stronger than in MWIR; this causes an underestimation of background signal, which is subtracted from the image. Therefore, too much radiance is assigned to come from the gas flare, and hence, the gas flow is overestimated. More on this subject can be found in Section 4.3.4. RMSE values for all the estimations in Figure 67 is 1387 kg/h and for cloud free data: 1315 kg/h. MAE values are accordingly 1214 kg/h for all data and 1106 kg/h for cloud free data.

If the data point coming from the experiment with the cloud influence is left out, the other data point seem to be systematically below the x=y line. This would suggest a bias in the parameters. In this case, the most probable biased parameter is $\rho(T)$, because its values was fitted using the aerial data from one of the experiments, and assumed to be constant, whereas in reality the value of this parameter is a function of different combustion conditions (e.g. air feed).

Figure 68: Sky during the experiment on 04.07.2019.

Therefore, instead of the cloudy satellite image, data from aerial survey from the same day (04.07.2019, experiment 3) and with the same gas flow has been used. The plane flew below the cloud cover, so its influence should be accounted for.

The data has been processed analogously to the satellite data, with adjusted parameter $\tau_{(\lambda)}$, accounting for the distance between the camera and the flare, and perspective of the camera with respect to the flare.

The calculated values of the gas flow from aerial imagery can be seen in Figure 69. The calculated gas flow varies strongly between 4690 kg/h and 2926 kg/h, with standard deviation of 485 kg/h. Mean (3715 kg/h) and median (3615 kg/h) values, however, are quite close to the measured gas flow of 3878 kg/h. For the model accuracy testing the median value was taken, because median is less sensitive to strong variation in the test group, coming e.g. from wind gusts.

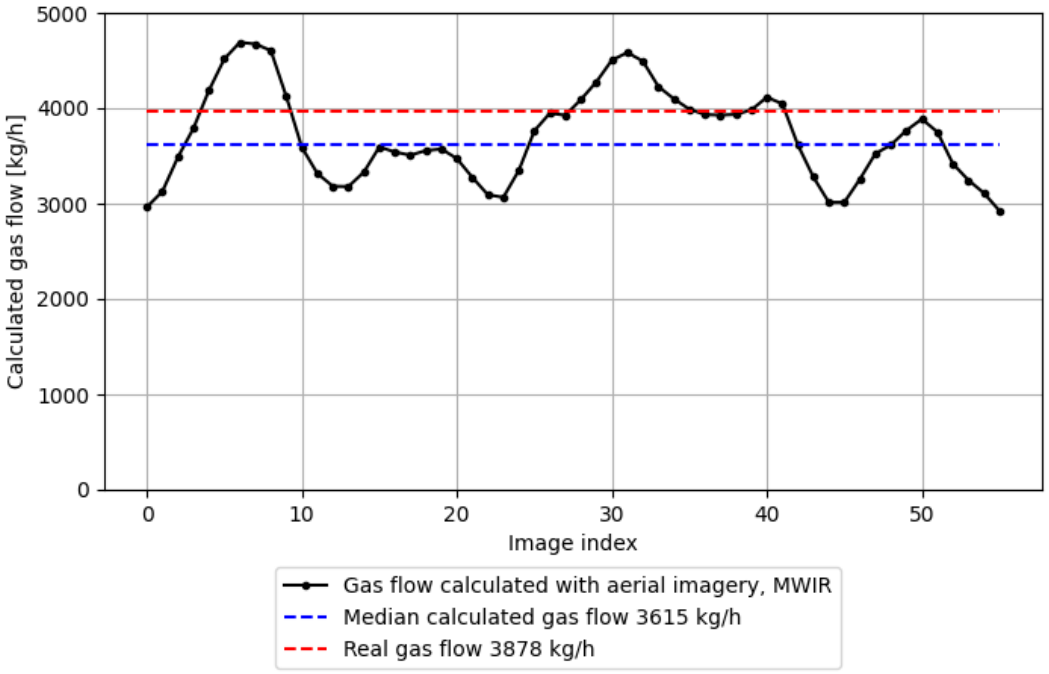

Figure 69: Gas flow calculated using MWHT camera.

The comparison of gas calculation with cloud-free satellite imagery and data from the aerial survey, with measured gas flow is presented in Figure 70. If using the cloud-free data and data from aerial survey, the RMSE value of the gas calculation is 1257 kg/h, and MAE 1007 kg/h. The values are slightly lower than the values calculated for the satellite-originating points only.

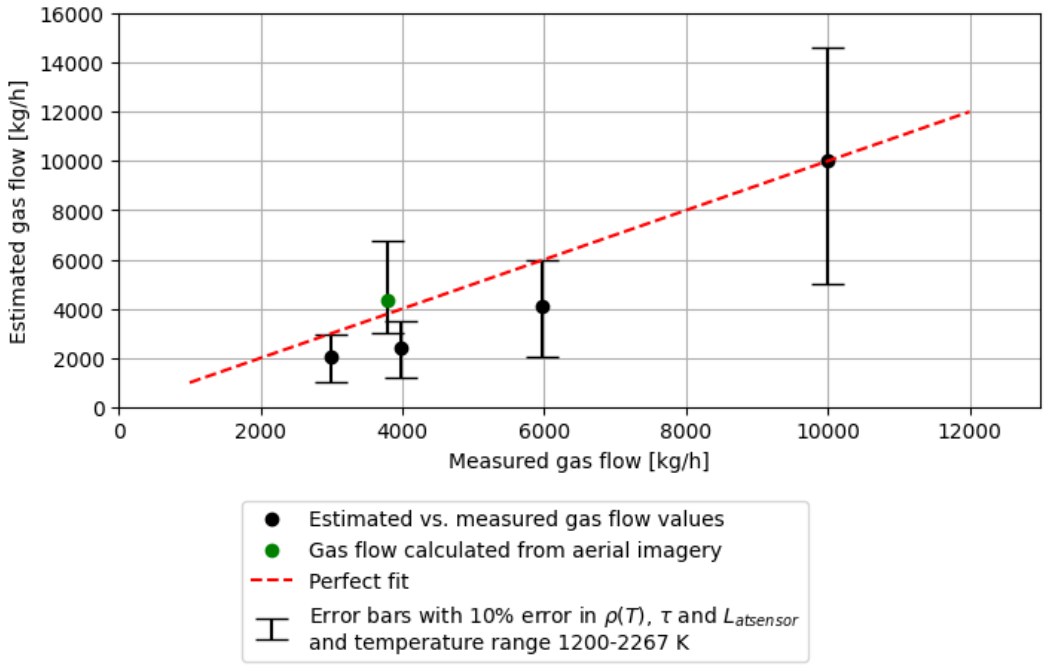

Figure 70: Model tested on experimental data, including data from the aerial survey.

4.3.2 Comparison between BIROS and VIIRS gas flow calculation

In this section, a comparison between the results, calculated with BIROS and with VIIRS data I4 band, is presented.

Since the GSD of the evaluated spectral bands of both sensors is similar, it is an important step, to compare the detection rate for both sensors (Table 18). For this comparison, only gas flow values below 1000 kg/h have been masked. Values exceeding 100000 kg/h, which are masked for statistical comparison of gas flow values, have been treated as valid detections.

Table 18: Detection rates in Persian Gulf and North Dakota for both sensors.

	BIROS	**VIIRS**
Mean detections per data take in Persian Gulf	18.1	25.5
Fraction of flares detected in Persian Gulf to all gas flares in database	62%	75%
Detections in North Dakota	83	93
Fraction of flares detected in North Dakota to all gas flares in the database	83%	93%

Notably, the VIIRS sensor records significantly more gas flares as active as BIROS, in both the Persian Gulf and North Dakota. The difference in detection rates is partly explained by time gap between the sensing, because some gas flares may be active during one recording and not active during the other. Also, the BIROS images are significantly smaller than the VIIRS images and sometimes only a part of the study area was recorded (e.g. Figure 56). In such case, the BIROS images will obviously record less gas flares than VIIRS. Nonetheless, a tendency is clear.

The statistics for the Persian Gulf study area, for both sensors and temperature 1600 K are presented in Table 19 below.

Table 19: Statistical measures for both sensors for Persian Gulf study area.

	BIROS	**VIIRS**	**VIIRS:BIROS ratio**
Median	2969	2334	79%
Mean	6498	4957	76%
Standard deviation	10389	6412	62%
Max	81060	39722	49%
NaN %	38	25	66%

The difference between average and median calculated gas flow is rather low: -21% points difference in mean and -24% points difference in median. The standard deviation is significantly higher in gas flow values calculated from BIROS data than in those from VIIRS data.

Similar comparison was made for North Dakota study area (Table 20).

Table 20: Statistical measures for both sensors for North Dakota study area.

	BIROS	**VIIRS**	**VIIRS:BIROS ratio**
Median	4555	5676	125%
Mean	5458	10988	201%
Standard deviation	3050	11176	267%
Max	20804	45957	221%
NaN %	17	7	41%

The first thing to notice from Table 20 is that the tendency here is reversed: the gas flow values calculated from BIROS data are lower than those from VIIRS data. In the study area of North Dakota, the gas flow values of the VIIRS results are in median 1.3 of the BIROS results. Also, the maximal calculated gas flow value is over twice as high in VIIRS results as in BIROS results. The standard deviation of calculated gas flow in VIIRS results is significantly higher as well.

For the North Dakota study area, only one data take was analysed for each sensor. The time gap between the image capture of each sensor is rather small: around 4 hours. It may be worth noting that both data sets were recorded during the local night: BIROS around 10 p.m. (09.12.2018) and VIIRS around 2 a.m. local time (CST), (10.12.2018).

The next step is to see, whether the calculated unique gas flow values, calculated with both sensors, correlate. This analysis for Persian Gulf data takes is presented in Figure 71. In this figure, some dates are marked red. These are the data sets, which were recorded within 5 hours time gap between both sensors. The black dates mark the data set, in which the time gap between images is higher. The dates written in Figure 71 are the dates of BIROS image capture.

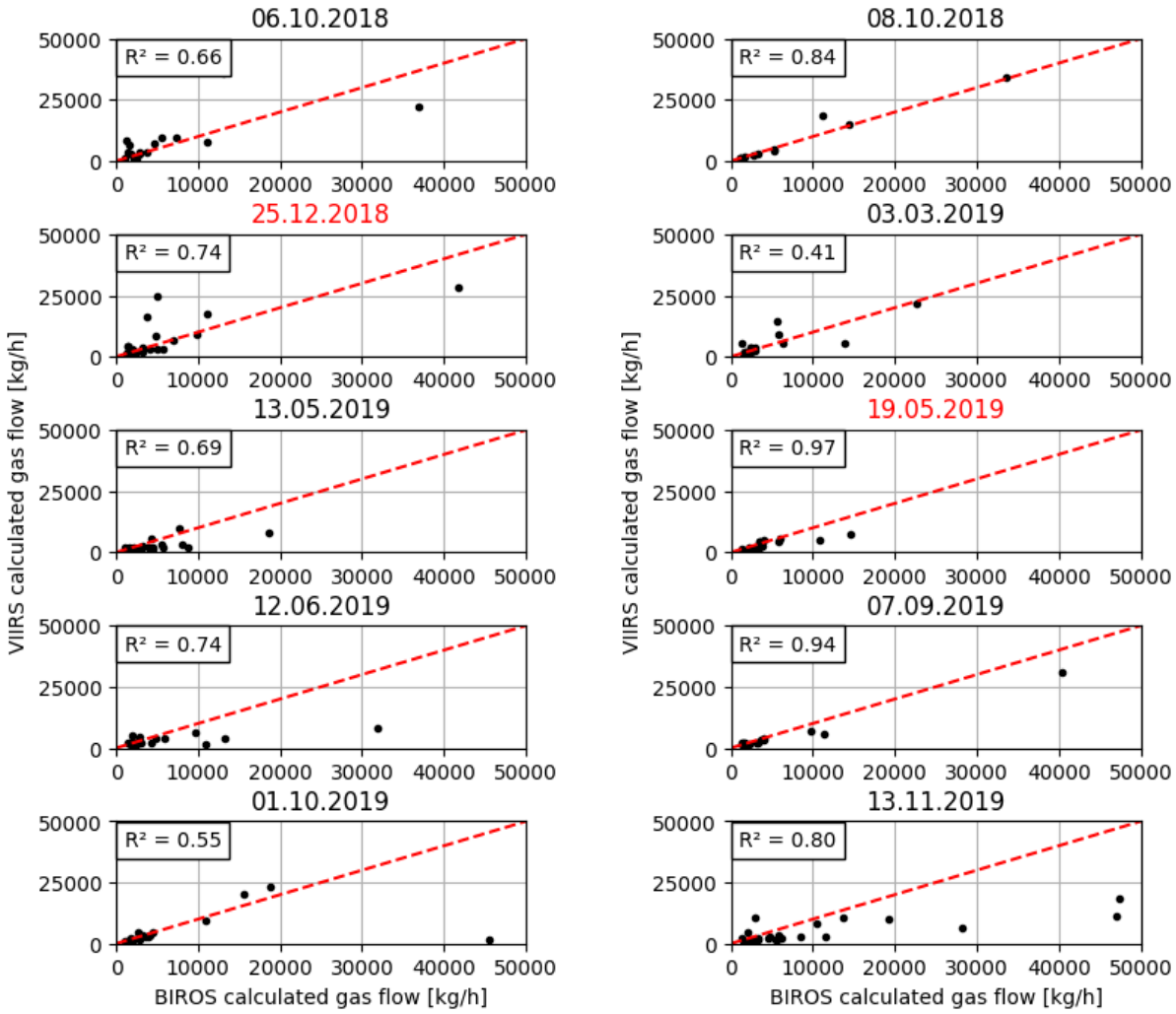

Figure 71: Correlation between the two data sets for each datum-pair. Dates, in which both sensors recorded gas flares during exacts same day, have been marked red. The dashed red line indicates the perfect correlation (x=y line).

For both sensors, several gas flow values were calculated to be below 1000 kg/h, therefore a number of data points was masked. Due to the fact that some flares are masked in either one of the sensors, in Figure 71 only data points were compared, if they were valid for both sensors. This resulted in a strong reduction of the number of points used for this analysis.

The correlation between the data sets seems to be quite high. However, the R^2 values are sometimes surprisingly low. The reason for that is that the Pearson's coefficient is quite sensitive to outliers. For instance, let us analyse the plot for 1.10.2019, at the bottom left of the Figure 71. The Pearson's coefficient for all the data points is quite low. However, if the single outlier (45573 kg/h gas flow calculated from BIROS data and 1270 kg/h calculated from VIIRS data) is left out, the Pearson's coefficient is 0.98. Therefore, to analyse the correlation per datum of both data sets, the following measure was calculated:

$$\text{median ratio difference} = \text{median}\left(\left|\frac{\dot{m}_{\text{VIIRS}}}{\dot{m}_{\text{BIROS}}} - 1\right|\right) \tag{20}$$

where:

$\dot{m}_{\text{VIIRS}}$ Gas flow value calculated from VIIRS data
$\dot{m}_{\text{BIROS}}$ Gas flow value calculated from BIROS data

This measure was calculated for each datum separately and the results are plotted in Figure 72. Usually, the median ratio difference is quite low, mostly up to around 20%. Notably, none of the median difference ratios is above 50%. This means that the difference between the gas flow values calculated from both sensors' images is usually rather low.

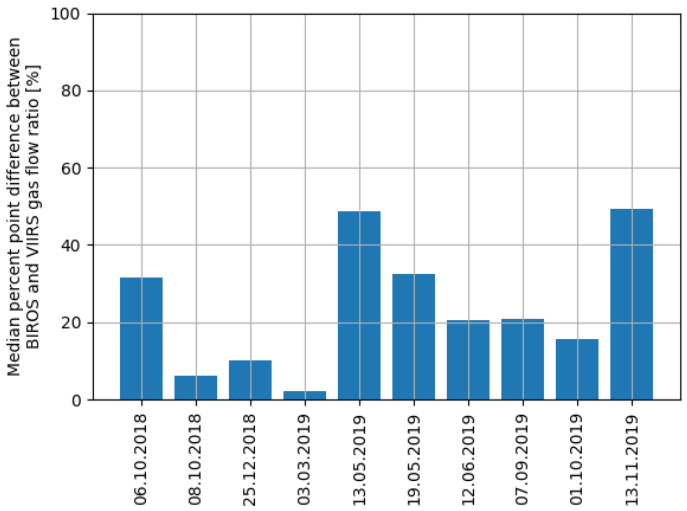

Figure 72: Median ratio difference between gas flow values calculated from VIIRS and from BIROS data, per datum.

As for North Dakota, the correlation between the calculated gas flow from both sensors' images is presented in Figure 73.

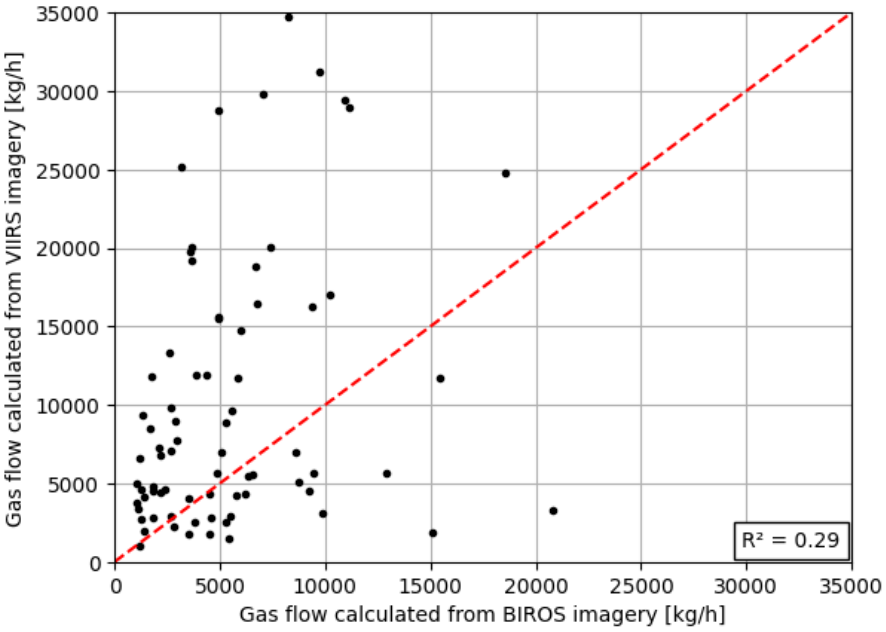

Figure 73: Correlation between gas flow values calculated from BIROS and VIIRS imagery of North Dakota. The red dashed line depicts the perfect correlation (x=y).

Pearson's coefficient calculated for gas flow values from BIROS and VIIRS images of North Dakota suggest very poor correlation between the data sets. In Figure 73, the data points are rather randomly distributed, and very few points lie in vicinity of the red line, depicting the perfect correlation (x=y). This is rather surprising, given the small time-gap between the images.

In the next step, means and medians for each flare have been calculated for both sensors and all data sets of Persian Gulf and then compared. Due to the fact that only one data set was used for North Dakota, this analysis could not be made for this study area. The results for Persian Gulf are presented in Figure 74.

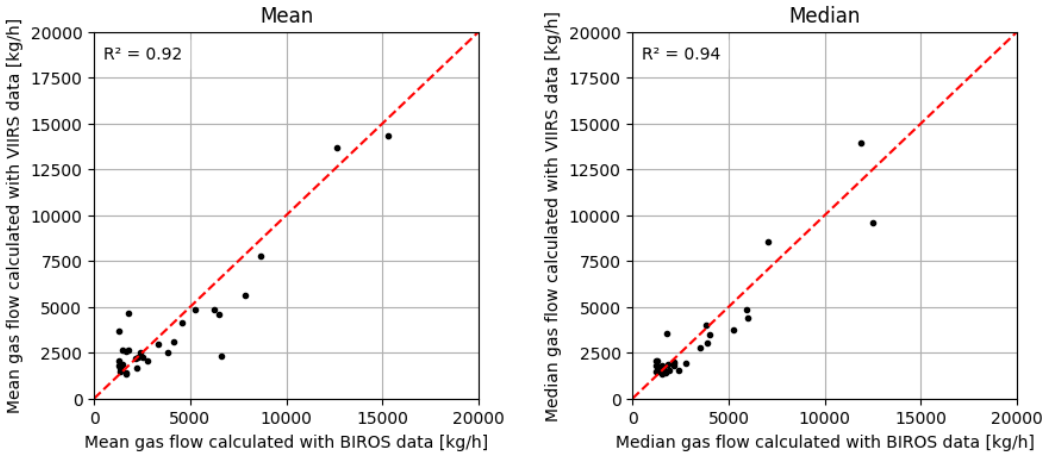

Figure 74: Correlation between sensor results: mean and median values per flare. The red dashed lines depict the perfect fit (x=y). The R^2 are calculated without the outlier.

Both median and mean seem to correlate well.

The median gas flow values are also given in Table 21. The third column contains the ratio of VIIRS median to BIROS median. In almost half of all cases, the difference between the

calculated gas flows with imagery from both sensors is less than 20% points, whereas only in 2 cases, the difference exceeds 70% points. The mean median ratio is 91%, which proves an excellent accordance between the data sets.

Table 21: Median of gas flow values calculated from BIROS and VIIRS imagery, and ratio of the medians.

Flare ID	BIROS	VIIRS	VIIRS:BIROS ratio
1	5255	3766	72%
2	5973	4388	73%
3	2183	1829	84%
4	11866	13965	118%
5	3816	4028	106%
6	5946	4831	81%
7	12472	9568	77%
8	22620	16427	73%
9	2137	1956	92%
10	1670	1519	91%
11	NA	1229	NA
12	1227	2079	169%
13	1398	1608	115%
14	3916	3065	78%
15	1261	1472	117%
16	4010	3515	88%
17	2763	1927	70%
18	1418	1753	124%
19	1864	1845	99%
20	2428	1545	64%
21	1510	1369	91%
22	1218	1507	124%
23	1311	2092	160%
24	1908	1521	80%
25	7050	8575	122%
26	1338	1530	114%
27	1720	1389	81%
28	25741	1745	7%
29	3540	2748	78%
30	1674	1544	92%
31	1526	1798	118%
32	2184	1997	91%
33	1202	1773	148%
34	1761	3544	201%

4.3.3 Comparison with other methods

To validate the method proposed in the presented dissertation, gas flow values, calculated from BIROS imagery, were compared to the values calculated from SLSTR imagery using a method published by Caseiro *et al.* 2019 and Elvidge *et al.* 2016. For this purpose, Alexandre Caseiro processed a set of SLSTR images of Persian Gulf, from 2018 and 2019 as in Caseiro *et al.* 2019, to provide a basis for validation. The processed data consisted of 839 data points (where each data point is a single sensing of a gas flare), recorded over 161 days, between 21.10.2018 and 06.09.2019. A group of 10 dates was chosen for further analysis, in which gas flares were recorded

by BIROS and SLSTR on the same day. Data provided by A. Caseiro contained FRP [MW], fire area [m²], and fire temperature [K] as well as geo-coordinates for each according flare. From these parameters, flared gas volumes per year could be calculated using an equation proposed by Elvidge *et al.* 2016:

$$V = F \cdot A^{0.7} \cdot T^4 \cdot \sigma \tag{21}$$

where:

V	Flared gas volume per year $[\frac{\mathrm{m}^3}{\mathrm{annum}}]$
F	Empirical factor introduced by Elvidge *et al.* 2016, equal to 0.0273 $[\frac{\mathrm{m}^{3.6}}{\mathrm{W}}]$
A	Fire area $[\mathrm{m}^2]$
T	Fire temperature [K]
σ	Stefan-Boltzmann constant, equal to 5.670373 · 1e-8 $[\frac{\mathrm{W}}{\mathrm{m}^2 \cdot \mathrm{K}^4}]$

From there, one can calculate the instantaneous gas mass flow as presented in the Eq. (22).

$$\dot{m} = \frac{V \cdot d_{\mathrm{gas}}}{C} \tag{22}$$

where:

d_{gas}	Density of a gas (in this case methane, equal to 0.657 $[\mathrm{kg/m}^3]$)
C	Conversion factor from years to hours [h/annum]

In this method, the relation between fire temperature, fire area and calculated gas flow is not linear. To analyse this method, theoretical gas flow values with varying temperature and area were calculated (Figure 75).

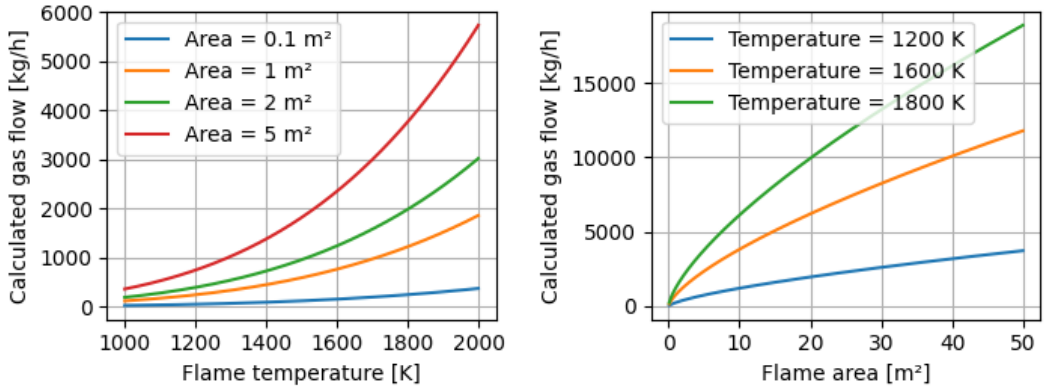

Figure 75: Influence of changing fire temperature and fire area on gas flow calculated with the model introduced by Elvidge *et al.* 2016. In the plot on the left, fire area is constant. In the plot on the right, the fire temperature is constant.

The median of the calculated fire area from SLSTR data is $3\,\mathrm{m}^2$. Therefore, the area values in the left plot are chosen to be realistic values around the median. In the right plot, the temperature values were chosen so that they match the calculations made for the BIROS sensor.

As can be seen in Figure 75, the gas flow values change very fast with changing fire area, and slower with changing temperature. To quantify this, derivatives for two cases will be considered. First, a constant fire area of $3\,\mathrm{m}^2$ is assumed and the fire temperature varies. The average derivative for this function is 3.77 kg/h. In the second case, a constant fire temperature of

1600 K is assumed, and the fire area varies. In this case, the average derivative for the function is 23.42 kg/h. This shows that the method proposed by Elvidge *et al.* 2016 is very sensitive to changes of the calculated fire area, and hence the accuracy of this parameter is crucial.

The first step to compare the results from both methods was again to compare the detection rate. To calculate the detection rate (presented in Table 22), the same method as for the comparison with VIIRS was applied. The dates used for comparison are different as those used for comparison with VIIRS. The dates were chosen, so that data sets from both sensors are as close as possible to each other. For comparison, 10 data sets were chosen from both sensors. All the data sets chosen for comparison are recorded on the same day. Moreover, 5 of the data sets are recorded within one hour time gap, and one data set with just over an hour time gap, together these data sets make a majority of all the analysed data sets.

Table 22: Detection rates for SLSTR and BIROS.

	BIROS	**SLSTR**
Mean detections per data take	22.7	4.7
All detections	73%	14%

In this calculation, the detection rate for BIROS is different from the one presented in Table 18, because the dates analysed were not the same. The number of valid gas flow values calculated with BIROS data is significantly higher than those calculated with SLSTR data. This may be due to the difference in both sensors' GSD: the GSD of SLSTR is almost three times larger than the GSD of BIROS.

The next step was, to calculate statistics for both data sets.

Table 23: Statistics of gas flow values calculated from BIROS and SLSTR data sets.

	BIROS	**SLSTR**	**SLSTR:BIROS ratio**
Mean	5891	4438	75%
Median	2943	2368	80%
Standard deviation	9012	3979	44%
Min	1000	1006	101%
Max	70736	16575	23%

As Table 23 presents, the difference between the median and mean in both data sets is rather low. The standard deviation is significantly higher in the gas flow values calculated from BIROS data, and so is the maximal value.

Next, correlation between the calculated values was tested. The individual gas flow values calculated from both sensors' imagery, presented in Figure 76, seem to correlate well. There is no apparent difference in correlation of gas flow values calculated from data sets recorded with a very short time gap, and gas flow values calculated from data sets with higher time gap.

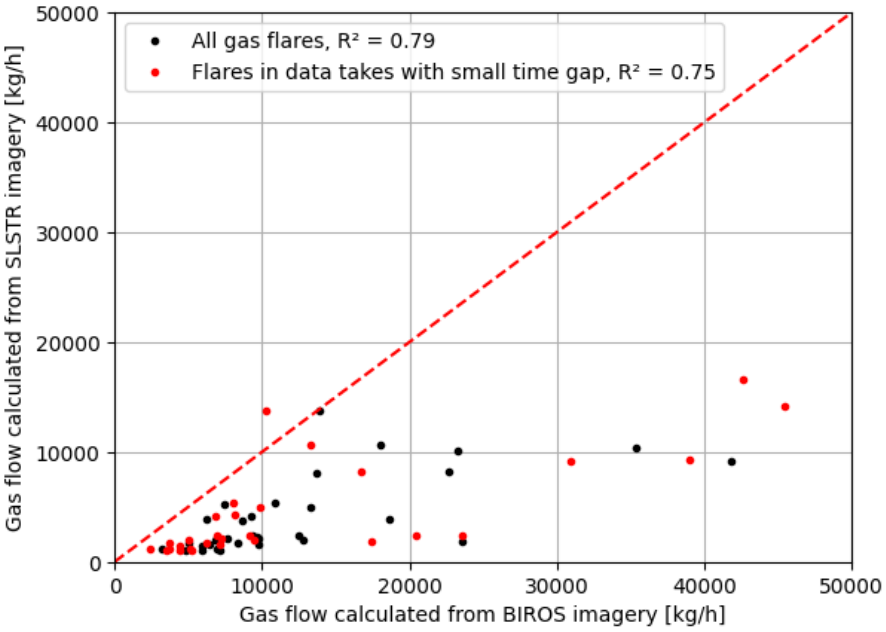

Figure 76: Gas flow values of individual flares, calculated from BIROS and SLSTR imagery. Red dots depict gas flows from data takes with very small time-gap between the recordings. The red dashed line depicts the perfect correlation (x=y).

Generally, gas flow values calculated from BIROS imagery are significantly higher than those calculated from SLSTR imagery. If a linear model is fitted on all the data points in Figure 76 (with gas flows calculated from SLSTR data as the dependent variable), the slope of the model is 0.27.

The correlation between the means and medians for each flare was calculated as well (see Figure 77).

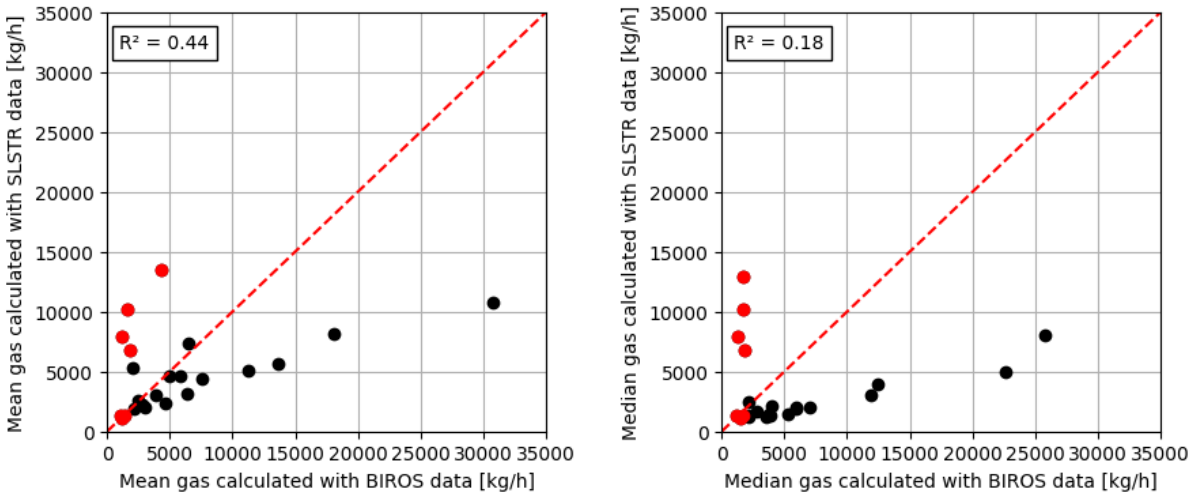

Figure 77: Correlation between means (on the left) and medians (on the right) calculated from SLSTR and BIROS data, for each flare. The red line depicts the perfect correlation (x=y). Red dots mark points, which were calculated from fewer than 5 measurements.

This time, all the recorded gas flares from both data sets, so not only the values from the 10 common dates, were used. This was done, because there are very little data points in the 10 common dates, and therefore, the statistical validity of such a small data set could be

questionable. Due to the fact that the SLSTR data and BIROS data have been recorded within a common time span, it was valid to take all the dates into account this time, instead only those from matching dates.

Both mean and median correlation is rather poor in Figure 77. However, the outlying points are the ones, which were calculated from up to 4 gas flow values (the red points). In this case, these points are very susceptible to outlying gas flow values, e.g. from emergency flaring. If all the data points in Figure 77, which are based on fewer than 4 data points (marked red in the plot) are left out, the Pearson's coefficient becomes very high: 0.94 for medians and 0.86 for mean values. If a linear model is fitted, with gas flow values calculated from SLSTR data as dependent variable, the slope of the model is 0.24 and offset 726 kg/h.

Table 24 below presents the median values for individual flares with a SLSTR:BIROS median ratio for each flare. In the last column, the number of points used for the median calculation in SLSTR, is presented. Gas flares, of which the median was calculated with very few data points, are marked red. The mean SLSTR:BIROS median ratio is 143%. However, this values is strongly influenced by the outlying points. If these points are left out, the mean ratio is 43%, which corresponds to the tendency observed in Figure 77.

Table 24: Median of gas flow values derived from BIROS and SLSTR imagery (only gas flares detected in both data sets), ratio between the medians per flare, and number of SLSTR data points used to calculate the median.

Flare ID	BIROS	SLSTR	SLSTR:BIROS ratio	Number of points
1	5255	1436	27%	39
2	5973	2065	35%	58
3	2183	1328	61%	12
4	11866	3053	26%	111
5	3816	1448	38%	31
6	5946	1865	31%	50
7	12472	3981	32%	95
8	22620	5001	22%	101
9	2137	2424	113%	8
10	1670	12867	770%	4
14	3916	1331	34%	15
15	1261	7956	631%	2
16	4010	2148	54%	34
17	2763	1698	61%	26
19	1864	6809	365%	1
22	1218	1334	110%	1
25	7050	2044	29%	74
27	1720	1345	78%	1
28	25741	7981	31%	13
29	3540	1254	35%	22
31	1526	1153	76%	1
32	2184	1218	56%	13
34	1761	10178	578%	1

To summarise, the gas flow values calculated with the method developed in the presented dissertation are generally higher than the values calculated with the method developed by Elvidge *et al.* 2016 and Caseiro *et al.* 2018. There is, however, a significant correlation between the datasets. The statistical measures seem to be similar, which seems to be a coincidence given the

tendency presented in Figure 77. This may be a result of a significant proportion of outlying, very high values in the SLSTR dataset.

4.3.4 Sources of uncertainty

There are multiple sources that influence the accuracy of the calculated gas flow. The main discussion on those influences can be found in Section 5. In some cases, uncertainty can be quantified, in other cases not. For the cases, in which the influence on accuracy could be quantified, calculations are presented below. The sources of uncertainty analysed in this section are divided into three groups: atmospheric effects, accuracy of subtracting the background signal from the flare signal and flame temperature. The other sources of uncertainty are discussed in Section 5.

First, let us consider the influence of the atmospheric correction accuracy on the accuracy of the gas flow calculation.

Atmosphere

For the purpose of this research a simple atmospheric correction, using a factor, was applied. Within the frameworks of this research, it was not possible to use a more advanced algorithm. However, it is important to note that applying a not-optimal atmospheric transmittance factor is a strong source of uncertainty.

The atmospheric transmittance factor is used in two crucial aspects of the applied method: calculating the flame radiance $L_{\text{at sensor}}$, and calculating gas flow $\dot{m}$ (Eq. (11)) from the flame radiance $L_{\text{at sensor}}$. The influence of $\tau_{(\lambda)}$ in calculation of gas flow is relatively straightforward.

Let us assume a recorded flame radiance $L_{\text{at sensor}}$ of 0.5 W/sr/m²/µm (which corresponds to around 2350 kg/h gas flow, if using standard parameters as in Table 4). The parameter $\tau_{(\lambda)}$ is varied between 0.50 and 0.99. For each $\tau_{(\lambda)}$ value, a gas flow is calculated (Figure 78).

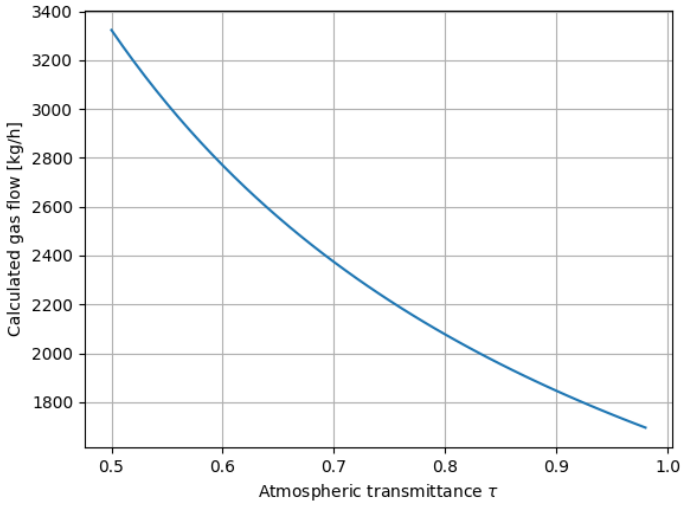

Figure 78: Gas flow calculated for radiance 0.5 W/sr/m²/µm, with varying $\tau_{(\lambda)}$ value.

The mean derivative of the function presented in Figure 78 is -34 kg/h, which means that with each 1% point difference in parameter $\tau_{(\lambda)}$, the calculated gas flow changes by -34 kg/h.

However, the influence of the accuracy of atmospheric transmittance is not limited to the above-mentioned effect. The main influence of the accuracy of the τ parameter is in calculating the flame radiance $L_{\text{at sensor}}$. This influence is very challenging to quantify. Depending on the type and homogeneity of the background of the flare, this effect may be stronger or weaker.

Depending on the $\tau_{(\lambda)}$, the signal to-be-subtracted will be higher or lower, and therefore may cause an over- or underestimation of $L_{\text{at sensor}}$.

Modelling this source of uncertainty may be done in a very theoretical way, by modelling a homogeneous background and a gas flare. The conclusions from such an analysis, are however only valid for the modelled situation. In order to provide an overview on the magnitude of this source of uncertainty, the experimental data was analysed. First, gas flow was calculated for each of the experiments with the optimal $\tau_{(\lambda)}$ value, and subsequently the calculation was repeated for an altered $\tau_{(\lambda)}$, changed 1% point. The difference between the gas flow values calculated for both cases provides a piece of information on the uncertainty coming from the atmospheric correction accuracy. The results of the analysis are presented in Table 25 below.

Table 25: Calculation of error in gas flow due to 0.01 error in $\tau_{(\lambda)}$.

	$\boldsymbol{\tau}_{\textbf{real}}$	**Gas flow** $\dot{m}$	$\boldsymbol{\tau - 0.01}$	**Gas flow** $\dot{m}$ **calculated for wrong** $\boldsymbol{\tau}$	$\Delta\dot{m}$ **[kg/h]**	$\Delta\dot{m}$ **[%]**
26.06.2019	0.68	2093	0.67	1763	420	16%
04.07.2019	0.68	5242	0.67	4981	280	5%
24.07.2019	0.69	1879	0.68	1712	259	9%
22.08.2019	0.69	3948	0.68	3840	137	3%
20.12.2019	0.75	9902	0.74	9871	26	0%

As can be seen in Table 25, the absolute and the relative error in gas flow varies strongly from experiment to experiment. The values are quite confusing, because they do not correlate with the correct gas flow. To explain this, the relative error was tested for correlation with variables measured during the experiments: pyrometer measurement of the ground, and air temperature. There seem to be a weak correlation with the pyrometer measurements (Pearson's coefficient 0.62), and stronger correlation with the air temperature (0.80). However, the tested population is so small, that the conclusions should be treated with caution. Nonetheless, the analysis presented in Table 25 proves that the inaccurate assumption of atmospheric transmittance may cause as much as 16% error in gas flow calculation.

Background signal calculation

The second significant source of uncertainty is the calculation of the background signal. The accuracy of calculating the background radiance is crucial for the accuracy of the gas flow calculation, because, as mentioned in previous sections, each under- or overestimation of the background, causes directly an over- or underestimation of the flare radiation (and consequently gas flow).

One of the most important steps of the validation was to test the accuracy of bi-spectral method in the background signal estimation. This could be done using the imagery from experiments, because apart from satellite imagery, additional measurements were made (e.g. on weather conditions, and radiation of the background surfaces). The bi-spectral method was validated using pyrometer measurements of the ground as a reference, taken during the experiments. In the bi-spectral method, the temperature of the background was estimated from the satellite imagery, using radiance values from both spectral bands. In this particular case, the bi-spectral method was adapted for the gas flare analysis: the fire temperature and fire area were given a priori. The estimated background temperature was compared to the measurements from the pyrometer during the experiments (Table 26).

Table 26: Validation of the bi-spectral method applied to satellite imagery with pyrometer measurements. The mean error of the temperature estimation is 8.8 K.

Exp. no.	**Datum**	**Temperature measured by pyrometer [K]**	**Temperature estimated using bi-spectral method [K]**	**Temperature difference [K]**
2	26.06.2019	314.3	325.0	10.7
3	04.07.2019	304.7	311.4	6.7
4	24.07.2019	311.1	321.0	9.9
5	22.08.2019	305.2	313.0	7.8

As can be seen, the bi-spectral method overestimates the temperature on average of 8.8 K. However, one also needs to consider the solar reflection, which influences the temperature estimation in bi-spectral method, because solar radiation is partially recorded in MWIR spectral bands.

In order to estimate the amount of reflected light in the MWIR band, daytime and nighttime imagery of the TTS without fire have been compared to the amount of the expected radiation, which is calculated based on the assumption that the measured air temperature is the same as the ground temperature. Additionally, the same parameters of the background emissivity ε and atmospheric transmission $\tau_{(\lambda)}$ have been used for this comparison. The expected radiance of the background L_{theory} is calculated according to Planck's law extended by emissivity and atmospheric transmission as follows:

$$L_{\text{theory}} = \frac{2hc^2}{\lambda^5} \cdot \frac{1}{e^{\frac{hc}{\lambda k_B T}} - 1} \cdot \varepsilon \cdot \tau_{(\lambda)} \tag{23}$$

where:

L_{theory}	expected radiance of the TTS surface [W/m^2/sr/m]
h	Planck's constant [J·s]
c	speed of light [m/s]
λ	wavelength [m]
k_B	Boltzmann constant [J/K]
T	temperature of the body [K]
ε	emissivity of the body [1]
$\tau_{(\lambda)}$	atmospheric transmission [1]

For a daylight image without a flare, the radiance of the reflected sunlight $L_{\text{reflected}}$ is assumed to be the difference between the measured and the expected radiance. $L_{\text{reflected}} := L_{\text{measured}} - L_{\text{theory}}$ The proportion r of the reflected light with respect to the expected radiance then calculates as:

$$r := \frac{L_{\text{reflected}}}{L_{\text{theory}}} = \frac{L_{\text{measured}} - L_{\text{theory}}}{L_{\text{theory}}} = \left(\frac{L_{\text{measured}}}{L_{\text{theory}}} - 1 \right) \cdot 100\% \tag{24}$$

Further, the amount of reflected light (r) in the measurements is calculated as a ratio between the measurements and the theory (Eq.(25)). In a data take recorded in daylight, the amount of reflected light should be greater than 0%. In a night image, this amount should oscillate around 0%.

$$r = \left(\frac{L_{\text{measured}}}{L_{\text{theory}}} - 1 \right) \cdot 100\% \tag{25}$$

where:

r	reflected light as percentage of the theoretical signal [%]
L_{measured}	measured radiance [W/m^2/sr/m]
L_{theory}	theoretical radiance [W/m^2/sr/m]

As a control measure, the same calculation was repeated with nighttime imagery. In this case, the expectation is that the ratio r should be around 0 %, which would support validity of the theoretical model. The results are presented in Table 27.

Table 27: Amount of reflected light in images of the BAM TTS without fire. The average value of r for the daytime images is 42% (with a standard deviation of 12.3%) and for the nighttime the average is 2%.

Datum	**Daytime** r [%]	**Datum**	**Nighttime** r [%]
06.06.2019	65	25.06.2019	0
11.06.2019	27	14.10.2019	5
25.06.2019	51	28.11.2015	8
14.10.2019	23	02.09.2016	-5
03.08.2018	40	16.09.2016	2
29.08.2018	43		
05.06.2019	38		
15.08.2015	44		
01.04.2016	42		

As can be seen, in daylight, the reflected light in the MWIR spectral band is typically around 42% of the whole signal, whereas in nighttime imagery, the 2% value can be treated as an error of estimation (coming e.g. from temperature difference between the weather station and the TTS).

The analysis conducted proved that the reflected light contributes to the total signal with 0.19 W/m^2/sr/µm, which translates to approximately 8 K. This value is very similar to the mean error of background temperature estimation in bi-spectral method in the imagery from the experimental series. This means that it is safe to accept the overestimation of the background signal in bi-spectral method, because the calculated value contains both the radiation and the reflection as well. It is however important to note that the above-mentioned amount of reflected light is only valid for the TTS area. Different background surfaces have different reflectance values, and therefore, without an analysis, such as presented above, it is impossible to assess the amount of reflected light in a pixel. However, if using the bi-spectral method for calculating background signal, or calculating the median of a given window, the reflected light should be accounted for. Hence, it is advisable to use one of those methods for background signal calculation (instead of e.g. using a priori knowledge on background temperature), in order to avoid uncertainties coming from the reflected light recorded.

Nevertheless, the inaccuracies in calculating the background signal come not only due to reflected light, but also due to the structure of the background. For instance, let us recall Figure 24, illustrating the BAM TTS. The TTS is cut out of the forest, and its dimensions are small enough, so that its signal may be confused with the flame signal. In the study area of Persian Gulf, the flame signal is practically indistinguishable from the signal of the drilling platform, the flare is located on. Without accurate measurements of the flare location without an active flame (such as used for the experimental series), it is practically impossible to differentiate

the flame signal from the signal coming from its direct vicinity. Nevertheless, for BIROS, each additional 0.01 W/m²/sr/µm added to the flame radiance, translates to an additional 47 kg/h added to the gas flow. The error is different for each sensor, because the parameters such as GSD, ψ and $\Delta\lambda$ are sensor specific (or band specific) and they influence the calculated gas flow. The standard deviation of water radiance in the Persian Gulf (calculated on an example image from 19.05.2019) is 0.016 W/m²/sr/µm. Interpreting this as flare radiance translates into a gas flow of 75 kg/h. These values seem rather small, but it is important to remember that such an error may occur in each of the analysed pixels in a given window. If considering a 10x10 pixel window, the error in the gas flow becomes very high. Obviously, if the background signal is overestimated, the calculated gas flow will be underestimated.

Flame temperature

The last source of uncertainty, which could be analysed quantitatively, is the flame temperature estimation. Varying the assumed flame temperature between 1200 K and 2226 K will cause variations in the calculated gas flow, because the parameter proportion of radiation recorded in MWIR $\psi(\lambda, \Delta\lambda, T)$ has to be adjusted according to the temperature. Theoretically, the proportion of energy radiated ρ changes as well. Unfortunately, it was not possible to determine this change, within the frameworks of this research.

In order to estimate the uncertainty, the gas flow was calculated for three cases:

1. Flame temperature of 1200 K, proportion of radiation recorded in MWIR spectral range $\psi(\lambda, \Delta\lambda, T)$ 14.7%.
2. Flame temperature of 1600 K, and proportion of radiation recorded in MWIR spectral range $\psi(\lambda, \Delta\lambda, T)$ 10.8%.
3. Flame temperature of 1800 K, and proportion of radiation recorded in MWIR spectral range $\psi(\lambda, \Delta\lambda, T)$ 9.1%.
4. Flame temperature of 2226 K, and proportion of radiation recorded in MWIR spectral range $\psi(\lambda, \Delta\lambda, T)$ 6.3%.

The model for gas flow calculation from satellite imagery (Eq. (11)) is a linear one. For illustration, a theoretical flare recorded at nadir by BIROS sensor was considered. In Figure 79, gas flow $\dot{m}$ as a function of recorded flame radiance $L_{\text{at sensor}}$ is presented for three cases, differing with temperature of combustion T.

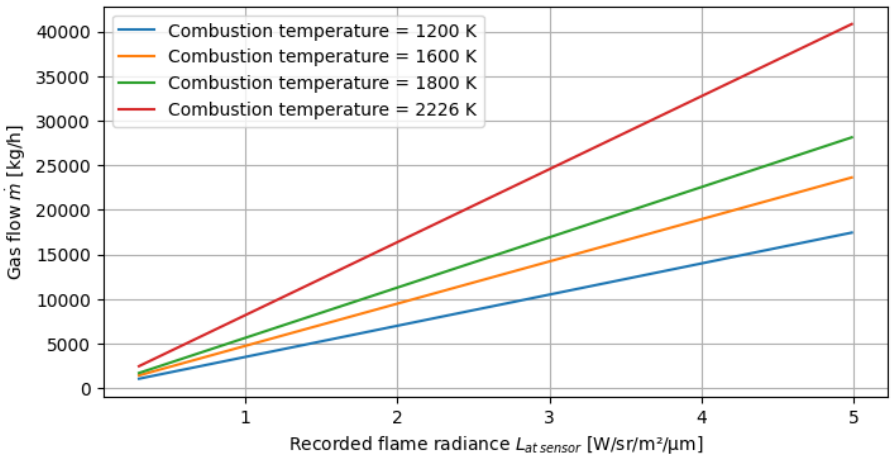

Figure 79: Gas flow $\dot{m}$ as a function of flame radiance recorded by sensor $L_{\text{at sensor}}$ for four temperature cases.

The relative difference between gas flow calculated for temperature 1200 K and calculated for temperature 2226 K with respect to the former is 42%. Naturally, the absolute difference grows with the radiance recorded. The absolute difference as a function of radiance recorded by a sensor $L_{\text{at sensor}}$ is presented in Figure 80.

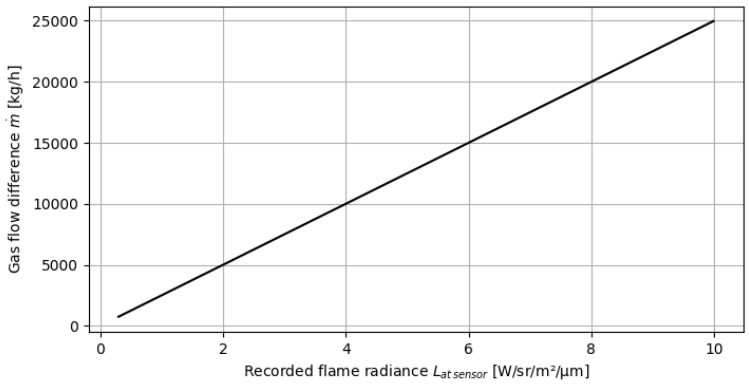

Figure 80: Absolute difference between gas flow $\dot{m}$ calculated for temperature 1200 K and for temperature 2226 K, as a function of radiance recorded by a sensor $L_{\text{at sensor}}$.

As can be seen in Figure 80, the uncertainty becomes very significant with high radiance values (ergo - high gas flow values). For a gas flow calculated from the BIROS imagery of Persian Gulf ($\approx$ 2639 kg/h calculated for temperature 1200 K) the maximal error due to false temperature estimation is 1108 kg/h. In the same calculation for mean gas flow in North Dakota ($\approx$ 3652 kg/h calculated for temperature 1200 K), the maximal error is 1533 kg/h. The false temperature estimation is so far the most significant source of uncertainty. Due to the fact that the assumptions on combustion temperature differ strongly between the researchers, this uncertainty remains an open challenge for the future research. While analysing the calculated gas flow values, one needs to consider the uncertainty, therefore it is safe to assume that the gas flow values calculated for temperature 2226 K are the maximal values, or the worst case scenario.

5 Discussion

The following chapter summarises the most important conclusions of the research conducted. The first section analyses the research on gas flaring, especially the usage of the bi-spectral method for gas flaring parametrisation. The two parameters, which are calculated using the bi-spectral method, the fire area and the fire temperature, are not changed with the gas flow change, as proved in the experimental series. Additionally, the gas flame radiation is dependent on the flaring set-up, especially the air-feed into the gas mixture. The combustion conditions are not considered in the bi-spectral method, but the model proposed in this dissertation addresses this niche.

The next sections are devoted to the assessment of the model proposed. The accuracy of the model is analysed. Given the level of uncertainty dealt with, the accuracy of the model seems relatively high. One of the most important aspects of the model proposed was to account for the sensor (and sensing) parameters, which allows using the model with data from different sensors, with equal results; the fulfilment of this requirement is analysed, by assessing the results obtained by applying the model on data from two sensors: BIROS and VIIRS.

A comparison of the results obtained, with gas flow values calculated with another method, is assessed in the next section. This leads to the assessment of the model proposed, and listing its shortcomings and advantages.

A significant part of the research was devoted to the comparison of 6 sensors, which can potentially be used for the gas flaring analysis. This allowed to derive a set of sensor features, important for the gas flares parametrisation. These parameters are described in the next section.

The last parts of the chapter describe the sources of uncertainty in the calculation of gas flow, using satellite imagery, and the possible future research and development of the model proposed.

5.1 Analysis of the bi-spectral method with respect to the results of the experiments conducted

The research publications within the subject of parametrising gas flares often base on algorithms developed for vegetation fires (Anejionu *et al.* 2014). The algorithm, most often used for this purpose, is the bi-spectral method, developed by Dozier 1981. It usually bases on two measurements, in the MWIR and LWIR spectral ranges. The bi-spectral method allows calculation of the fire temperature and fire area, from which the FRP is calculated. This method has been used to characterise gas flares e.g. in Elvidge *et al.* 2016 to create a global database using VIIRS data[17]. However, in the last years, publications appear, which suggest considering the physical properties of a flame in flare parametrisation, and basing on the combustion modelling[18].

There are several arguments for using the more physical-based approach as opposed to using the parameters derived from the bi-spectral method and reference data to fit a linear model. First is the uncertainty in the calculation of the flame area from the satellite imagery. The area of a gas flare recorded by a satellite or an aerial sensor is a projection of the flame on the ground. This projection is dependent on the sensor's position with respect to the flame, and on wind gusts, which change the flame geometry instantaneously. The experiments conducted prove that the projected flame area from the satellite's perspective does not change proportionally to the gas flow. It is rather dependent on wind gusts, but this dependence is also not linear (Soszynska *et al.* 2019). The analysis of the data from the aerial survey allowed to calculate the projected flame area of the gas flare to be around $40\,\mathrm{m}^2$, with no change apparent between gas flow of $2000\,\mathrm{kg/h}$ and $4000\,\mathrm{kg/h}$.

[17] Other research publications basing on this method are e.g.: Fisher & Wooster 2018; Fisher & Wooster 2019; Caseiro *et al.* 2018; Caseiro *et al.* 2019; Elvidge *et al.* 2011

[18] Examples of these publications are: Beychok 2005; Casadio *et al.* 2012a and Zhang *et al.* 2015

Another argument for using physics-based algorithms for gas flaring parametrisation, is the dependency of the radiated heat on the flaring set-up, e.g. the amount of the air mixed into the fuel. Flames, in which an air-rich mixture is burned, typically have very high temperatures and produce very little soot. Instead, the majority of the produced particles will be water vapour and carbon dioxide. Both these substances have rather low emissivity values in comparison to soot. This means that paradoxically the flares with very high temperatures (so around 2200 K) may be barely visible in a satellite image, due to the small soot amount, and hence, the small proportion of radiation.

The actual conditions in the flaring stations remain largely unknown. There have been attempts to estimate the flaring temperature, however, there is no exact consensus on this subject; the suggestions vary between 1200 K and 1800 K. The measurements made directly in the flame, during the experimental series, proved no influence of gas flow change on the flame temperature. This raises serious doubts against using the parameters flame temperature and flame area for the purpose of gas flow calculation.

The method proposed in this dissertation addresses both above-mentioned issues: the independence of the flaring temperature on the gas flow, and the independence of the flame area on the gas flow. A correct estimation of the flame geometry from a satellite image with GSD of over 100 m is very challenging, and the estimation is subject to very high uncertainty. The geometric flame model developed in this dissertation was used ultimately to estimate the emissivity of the flame. Generally, the method proposed is independent of the flame area.

As for the temperature estimation, the results in this work are calculated for four flaring temperatures: 1200 K, which is considered a minimum, 1600 K, which is considered to be the most probable value, 1800 K, which is a value often found in the literature, and 2226 K considered to be the maximum value (where the combustion is stoichiometric). The parameter "proportion of the energy radiated in the sensor spectral band" (ψ) was adapted accordingly to the temperature values. This approach allows to calculate the most probable value and a possible error range.

The author of this dissertation decided not to conduct the temperature estimation using the bi-spectral method. In the bi-spectral method, the flame area and flame temperature partly compensate each other. The values of fire area, calculated by Alexandre Caseiro from the SLSTR data, were somewhat unrealistic. The majority of the calculated values was lower than $2\,\mathrm{m}^2$ and the median was $3\,\mathrm{m}^2$. Such a small fire area corresponded to gas flows of around 4000 kg/h, which seems highly unrealistic. In the experimental series, such gas flows were used, and the projected flame area calculated from the aerial imagery was around $50\,\mathrm{m}^2$, so over a magnitude higher than the median value calculated from SLSTR data. On the other hand, the gas flow values calculated from SLSTR data by Alexandre Caseiro, using these two parameters, are realistic and very similar to those calculated using the method presented in this dissertation. It appears that both methods work with similar effects, although the parameters derived using the bi-spectral method should not provide a basis for gas flow calculation.

The fact that the gas flow values, calculated using the unrealistic values of the flame area, were realistic, leads to a conclusion that the parameters calculated using the bi-spectral method (fire temperature and fire area) are products of a more complex set of parameters, which lead eventually to a correct result. For instance, these "product" parameters might contain information on combustion efficiency, proportion of the energy radiated and emissivity. This hypothesis seems reasonable, because the sensor records a part of the energy of the flame, which is already reduced by these parameters. In order to test this hypothesis, an experimental series should be conducted. The experiments should be conducted with a flare in a possibly homogeneous background, to model the background signal with the highest possible accuracy. Additionally, the experiments should take place during the nighttime, to exclude the influence of the solar reflection on the background signal. The temperature of the flame should be measured as a reference for temperature estimation with the bi-spectral method, and some measurements of

the flame area should be conducted. Afterwards, it would be possible to develop an adaption of the bi-spectral method for the purpose of gas flares characterisation. This would allow to calculate the flame temperature, which is crucial for an accurate estimation of the gas flow.

5.2 Accuracy of the model proposed

One of the issues with calculating gas flow from satellite imagery is validating the accuracy of the method. In most of the remote sensing research on gas flares, the authors use some kind of the reference data on flared gas volume, obtained from external sources, e.g.local administration. For instance, Elvidge *et al.* 2016 used the Cedigaz database. Using the reported gas volumes as a reference brings some uncertainty with it. First, the information on gas flared is typically given as an amount of gas flared per day. This does not reflect variations in gas flow on the timescale of the integration time of a satellite. Second, there are many flare types with different set-ups, resulting in different flaring conditions. The differences between the set-ups (accounting, for instance, for the difference in the flaring temperature), are not reported. Therefore, a method calibrated on such reference data uses an "average" over all flare types and all gas flow values over the day. A satellite sensor measurement, however, is a recording of an instantaneous state; an integration time is typically in the order of few milliseconds or even below. Hence, it is impossible to address every condition and difference, using reported data as a reference.

The situation is, however, completely different in case of an experimental series. In this case, it is possible to validate the method directly using the measurements of the gas flow, and the flaring conditions are known. The accuracy measures presented in Section 4.3.1 are actually the only absolutely reliable validation results. The RMSE and MAE values (1387 kg/h and 1214 kg/h respectively) can be interpreted as relatively low, considering the dealt with level of uncertainty. The fact that only one measurement is used to derive a property of a system as complex as gas combustion, causes that the uncertainty of the calculation becomes very significant. For instance, the radiant flux, derived from the aerial imagery of the flare with constant gas flow, varied as much as ±65%. This means that even the radiance measured varies very strongly, increasing the level of uncertainty of the calculation.

If analysing Figure 67, (which compares the estimated gas flow values with the measured, for the experimental series), and leaving out one point from the cloudy data set, the distribution of the other points suggests a possible bias in the parameters. The most probably inaccurate parameter is the proportion of energy radiated $\rho(T)$. The value of this parameter was derived from the aerial experiments, and assumed to be constant. In reality, however, the value of the parameter is a function of the flaring temperature, and so, it is a derivative of the flaring conditions. Characterising the value of this parameter with respect to changing gas flow and other flaring conditions would be beneficial for the accuracy of the model developed in this dissertation.

5.3 Feasibility of the model to work with data from different sensors

One of the main purposes of the research was to develop a model for calculating gas flow from IR imagery, in which the parameters of sensing and the features of the sensor are accounted for. Thus, the model would be feasible to work with data from different sensors and potentially from different wavelengths. Due to the fact that the experimental series was conducted with the satellite imagery only from the BIROS sensor, it was important to test, whether applying the method developed on the data from other sensors yields similar results.

This feature of the model was tested already, when the data from aerial survey was used to calculate gas flow. The results were very promising, although a significant variation in the results was present. The variation in the calculated gas flow from the aerial imagery can be explained by the variation of the flame itself, which is very strong on its own, and even stronger under the influence of wind gusts. The main examination of the feasibility of the model to work

with data from different sensors, however, could be done by analysing the calculated gas flow values from another satellite sensor. By comparing a group of sensors: their parameters and the data sensed, a sensor for this examination was selected: the VIIRS sensor, which was already used for gas flaring parametrisation in multiple research publications.

The comparison with the gas flow values calculated with VIIRS I4 band brings promising results. The mean and median gas flow values for all flares and dates are similar (see Tables 28 and 29), except the mean values in North Dakota. However, the median value is more reliable, because several outliers with very high gas flows are present in all data sets. In this case, the median values in North Dakota also differ stronger than those in Persian Gulf, but given the fact that only one pair of data sets was compared, this difference cannot be treated as a tendency.

Table 28: Mean values of calculated gas flow for BIROS and VIIRS.

	BIROS	**VIIRS**
Persian Gulf	6498 kg/h	4957 kg/h
North Dakota	5458 kg/h	10988 kg/h

Table 29: Median values of calculated gas flow for BIROS and VIIRS.

	BIROS	**VIIRS**
Persian Gulf	2969 kg/h	2334 kg/h
North Dakota	4555 kg/h	6733 kg/h

Another important aspect is the correlation of the calculated gas flow values from both sensors (see Figures 71 and 74). The correlation between medians for single flares in Persian Gulf in both sensors is very high. Moreover, the correlation between individual gas flow values for the same study area, is very high as well, especially considering the time gap between the recordings by both sensors.

As for the North Dakota study area, the correlation between the calculated individual gas flow values from both sensors is rather poor. Interestingly, the images of this study area by both sensors, were taken only 4 hours apart, under very similar weather conditions. In this case, the gas flow values calculated from BIROS data are significantly lower than the values calculated from VIIRS data. This is an interesting result, which may be coming from the difference in sensitivity of the sensors, because the radiance values of the background were very low, due to very cold surface temperature. A further evaluation, with a larger number of similar data sets under similar conditions, would be advisable.

Processing data from the SWIR spectral band of VIIRS, I3, with the developed method, yielded interesting results. The radiance values in the I3 images yielded gas flow values around 2 magnitudes lower than expected, although the same gas flares sensed with the I4 band, yielded reasonable gas flow values. In theory, due to the location of the peak of the Planck curve for the temperatures similar to those of gas flares around 2 µm, the SWIR range should be perfect for the gas flares parametrisation. Researchers, e.g. Fisher & Wooster 2018 state that using the SWIR imagery for gas flaring parametrisation is more accurate than using the MWIR imagery. However, the research conducted for the presented dissertation proves that the radiation of gas flares in these wavelengths is significantly lower than expected. Due to the fact that the solar reflection is still recorded in the SWIR bands, a significant part of the recorded radiance is, in fact, the solar reflection. For the normal temperature, a radiance without the solar reflection of 8.16E-04 W/sr/m²/µm is expected. The spectral radiance of the background sensed in the image is, on average, 0.034 W/sr/m²/µm, which means that 97.6% of the recorded signal is the solar reflection.

On the other hand, the radiance values of the gas flares are approximately two magnitudes below the expected values. A gas flare with a radiance of 2.27 W/sr/m²/µm recorded in the

I4 spectral band has a gas flow of 6579 kg/h. In the I3 band, however, the same flare has a radiance of 0.3 W/sr/m^2/µm, which translates into 1893 kg/h gas flow. It is important to note, that very similar radiance values are also recorded in the LANDSAT-8 SWIR bands, which excludes an issue with the VIIRS sensor. Obviously, the method proposed, cannot be used with the SWIR spectral bands, unless some adaptions of are made. It is possible that a flame, which radiates like a grey body in MWIR and LWIR spectral ranges, does not maintain the same emissivity in the SWIR spectral range. Possibly, the radiance of the species in the flame in the SWIR range is strongly influenced by some spectral features deviating from a grey body radiation. Assuming that there is a difference in the emissivity in the SWIR, MWIR and LWIR spectral bands, it is possible to estimate the emissivity of a flame in the SWIR range, using a reversed Equation (11) and assuming gas flow value derived from the MWIR band. A possible emissivity deviation in the SWIR spectral range is an important issue and should be addressed in the future, possibly by conducting an experimental series with a gas flare recorded in all the above-mentioned spectral ranges. In such case, an additional parameter could be introduced to the model, or the parameter "proportion of the energy radiated" (ρ) could be adjusted.

5.4 Comparison of the results obtained with results from another method

A very important part of the validation was the comparison of the obtained results with results calculated with another method. An established and often used method for calculating the amount of gas flared, is the NightFire algorithm, a method developed by Elvidge *et al.* 2016, which was used to create a global database of gas flares. It is worth noting that the method, with which data for comparison was calculated (proposed by Elvidge *et al.* 2016), was validated at least twice on two different study areas. In the validation conducted by Zhang *et al.* 2015, the NightFire algorithm achieved worse results than the physics-based model proposed by the authors. The validation was done using reference data of Bakken Field, the same study area as used in the presented dissertation.

Unfortunately, a comparison with the flared gas amounts from the gas flares database developed as in Elvidge *et al.* 2016, was not possible. The gas flaring data calculated with VIIRS NightFire algorithm was updated until December 2017, and the data used for the analysis in the presented dissertation was sensed between mid 2018 and the end of 2019. Additionally, in a part of the VIIRS NightFire gas flares database, the gas volume is not calculated. Hence, the main information source remaining, was the article (Elvidge *et al.* 2016), where information on accuracy of results is given. Unfortunately, the accuracy of the calculation is only given as confidence intervals for the countries or flare types, but not for the individual flaring sites, which would allow a comparison with the method presented in this dissertation. Therefore, a validation with an adaption of the NightFire algorithm for SLSTR data, was performed.

The comparison with the SLSTR data was conducted using gas flare parameters derived from the SLSTR data by Alexandre Caseiro, as in Caseiro *et al.* 2019, for the area of Persian Gulf. Data from the same time span as the BIROS imagery, used in the presented research, was used. From the gas flare parameters, the author of the presented dissertation calculated the instantaneous gas flow values, and conducted the comparison with the gas flow values calculated with the method developed. The comparison of the results obtained from both methods is very promising. The mean and median values of the gas flow calculated from the imagery of BIROS and SLSTR are close to each other, as can be seen in Table 30.

Table 30: Mean and median gas flow values calculated using BIROS and SLSTR data.

	BIROS	**SLSTR**
Median	2943 kg/h	2368 kg/h
Mean	5891 kg/h	4438 kg/h

Moreover, the median and mean values for each flare correlate significantly ($R^2 = 0.94$ for the medians and 0.86 for the means)[19].

5.5 Analysis of the method proposed

The method proposed allows to calculate the gas flow flared, using the satellite IR imagery. The flame, which is the subject of the analysis, is extremely variable on its own, and additionally can be strongly influenced by wind. The level of uncertainty is therefore very high in the measured flame radiance already. Additionally, the parameter of the flame are estimated with some uncertainty as well. The flaring set-up determines the combustion conditions and, consequently, the parameters of the flame. This means that each flaring set-up will have its own conditions with according values of the flame parameters, such as proportion of energy radiated, combustion efficiency, and emissivity of the flame. Consequently, the same gas flow value may be a result of different parameter values combination. Therefore, each parameter, of which the value is assumed instead of derived from the data, adds to the uncertainty of the calculation. On the other hand, there is only one measurement available. All this means that the uncertainty dealt with is extremely high. A possible solution is to use measurements from multiple bands, e.g. from MWIR and SWIR bands. This, however, proved impossible for the current state of research, because the recorded radiance values in the SWIR band are not in accordance with the radiance values from the MWIR band. As long as this issue remains unresolved, the method can be applied with the measurement from one band only.

The method proposed allows to calculate the most probable gas flow value as well as confidence intervals, derived by calculating the gas flow for different temperatures. The most probable gas flow value is assumed to be the one for temperature 1600 K. This is a strong simplification. A development of the method to include a temperature estimation is possible, but most requires additional analysis. The author of the dissertation chose not to include the temperature estimation, because the development of an accurate method (e.g. adaption of the bi-spectral method) would exceed the time frameworks of this research. Instead, the model as it is, can be developed by adding the temperature estimation to achieve more accurate results.

As mentioned before, each parameter, of which the value is assumed, adds to the overall uncertainty of the model. For instance, the parameter "proportion of energy radiated" $\rho(T)$ was assumed to be the value fitted on the imagery from the experimental series. This value was used for all the gas flares parametrised: not only at the BAM TTS, but in the Persian Gulf and in North Dakota as well. This is a strong simplification, possibly leading to errors. The proportion of energy radiated is dependent on the flaring set-up and the amount of air in the fuel-air mixture. Therefore, the parameter $\rho(T)$ might vary strongly from flare to flare. In case of the combustion efficiency $\chi(T)$, which is also dependent on air-fuel ratio, the parameter value could be derived using the temperature measurements, from the existing combustion models. It is possible, that a similar relation between the fire temperature and proportion of energy radiated $\rho(T)$ is also present. To estimate this parameter more accurately, an experimental series, in well-known conditions of a laboratory, needs to be conducted and analysed.

[19]The mean and median values which were calculated on less than 5 data points were left out, due to a high sensitivity to outlying values. Outliers with exceptionally high gas flow values appear in both data sets from time to time. It seems that such gas flow values may be cases of emergency flaring, which take place seldom and for only a short time. In such cases, sensors recording not simultaneously, cannot record the same gas flow. The conclusion that the high gas flows are an exception, is confirmed by a fact that the correlation for individual gas flares and dates is high for most of the cases ($R^2 = 0.75$)

To recapitulate, the analysis of the method proposed in the presented dissertation, reveals the following weaknesses:

1. The method does not work with the SWIR spectral bands,
2. It does not allow a precise temperature estimation for each flare, which would allow to adjust the proportion of the radiation recorded in the sensor's spectral band (ψ) accordingly,
3. It assumes the values of the parameter $\rho(T)$ (proportion of energy radiated) a-priori, basing on the results from the experiments conducted.

Solving these issues was not possible to include in the presented thesis, but a development of the method, to overcome the listed weaknesses, is possible in the future.

It is however also important to mention the strengths of the presented model as well. The most important feature of the method presented, is that it is an algorithm tailored specifically for the gas flaring analysis, considering the conditions of the gas combustion process. The parameters of the gas combustion process are considered, i.e. the combustion efficiency and proportion of energy radiated. This means, that the method is also adjustable to different kinds of gases and different flaring set-ups.

In the algorithm, the sensor properties and imaging parameters are taken into account. Consequently, the model can be used with different satellite sensors and, in principle, with different wavelengths of sensing. The results have been validated for spectral bands sensing in MWIR, of different sensors. The results calculated from the MWIR spectral bands of two different sensors seem to be in very good accordance. As for the SWIR spectral bands, adjustments need to be done, in order to calculate valid gas flow values.

Due to the fact, that the flaring temperature estimation from the satellite imagery remains an open challenge for the remote sensing community, the gas flow values derived using the method presented, are calculated for four different temperature values. Apart from calculating the most probable gas flow values, this allows to determine a possible error due to the temperature estimation, or the minimum and maximum values of the gas flow.

Lastly, the accuracy of the method proposed has been validated experimentally. The RMSE and MAE values (1315 kg/h and 1106 kg/h accordingly) are relatively low, considering the variability of the conditions influencing the energy release rate, e.g. wind gusts. Additionally, the validation with gas flow calculations using a different method, proved also a high correlation of the results.

5.6 Sensor features

In Chapter 2.3, different sensors have been compared, with respect to the features important for remote sensing of gas flaring. A group of six sensors has been chosen, basing on number of publications in remote sensing of gas flaring, and suggestions in literature concerning the sensor features. The parameters of a sensor, which were analysed are: spatial resolution, spectral ranges sensed, and adjustments towards limiting saturation. The sensors compared were: BIROS, LANDSAT-8, VIIRS, MODIS, SLSTR and MSI.

In the course of the research, data from those sensors was compared, to test how many gas flares can be detected, and whether the signal of recorded gas flares is saturated. In the data from the sensors with the highest spatial resolution, MSI and LANDSAT-8, the gas flares were easily detectable, but the signal of most of the flares was saturated. In the data from the sensors with lower spatial resolution, such as MODIS and SLSTR, significantly less gas flares can be detected. Two last sensors, BIROS and VIIRS, provided satisfactory results, because all the gas flares were visible in the imagery, and the signal of the flares was not saturated. However, from the VIIRS sensor, only I-bands (with higher spatial resolution as M-bands) provide results comparable with BIROS. Therefore, two sensors have been chosen for further analysis: BIROS and VIIRS (I-bands).

Fisher & Wooster 2018 suggest using the SWIR spectral bands for gas flares parametrisation, rather than MWIR bands, because the peak wavelength of the assumed flaring temperature is located in the SWIR spectral range. The VIIRS sensor does have spectral bands in SWIR range, contrary to BIROS, which senses in MWIR and LWIR ranges (apart from VIS-NIR ranges).

VIIRS has another advantage over BIROS sensor: the high revisit time (12 hours) allows much more frequent imaging of gas flares. However, the large FOV of the VIIRS sensor, causes that the GSD in the zones 2 and 3 of the image is significantly higher than at nadir. Towards the edges of the image, GSD can even double, which is disadvantageous for detecting gas flares and deriving flaring parameters, because the area ratio between the hot-spot and the background becomes minuscule. Zhang *et al.* 2015 suggest to use only the middle part of the VIIRS image to avoid bias. If using only the middle of the image, the revisit time of the sensor decreases strongly.

Another important aspect of the gas flaring analysis, is the wavelength sensed. The VIIRS sensor has spectral bands in the SWIR as well as MWIR range. The method proposed was applied using two spectral bands, I3 (sensing in SWIR) and I4 (sensing in MWIR). The gas flow values calculated from I3 data are, however, completely incorrect, differing about two magnitudes from gas flow values calculated from I4 band (from the same image). This proves, that some adjustments in the method need to be done, in order to calculate gas flow also from SWIR data.

From the above described analysis, the features of a perfect sensor for gas flaring analysis can be derived. The sensor specialised for gas flaring analysis needs to have a relatively high spatial resolution (of around 350 m GSD and below) in order to resolve the signal of small flares as well as the larger ones. Such an optimal sensor needs to sense in the SWIR and MWIR spectral ranges, as well as in the LWIR range, which is used for background signal calculation. A high dynamic range and adjustments towards limiting saturation are required, e.g. such as the hot-area-mode in the BIROS sensor.

The cooled HgCdTe detectors seem to be sensitive enough to record gas flares properly. This type of detector usually has a high SNR, which is a very important aspect. Due to the fact that the gas flares are so small in comparison to the GSD of the thermal sensors, the analysis is particularly sensitive to noise. A redundancy in sensing due to staggered arrays (as in BIROS), is advantageous for this aspect, because the values can be averaged and therefore, the noise influence is minimised.

In order to monitor gas flares and derive their gas flared volume per month (or year) globally, it would be beneficial to have a group, or a constellation of sensors, with a rather lower FOV. This would allow to achieve a high sensing frequency, without decreasing the accuracy of the calculation, due to the low area ratio, between the hot-spot and the background.

Additionally, it would be beneficial to determine the geometry of the flame. This could be achieved, if high-resolution bands in VIS-NIR spectral ranges were added to the sensor system. The GSD of these bands should be optimally around 5 m, to allow calculating the flame size accurately.

Lastly, it is important that the sensor (or a group of sensors) would be operated at night as well as during the day, since gas flares are operated often all the time, and the night imagery is free of solar reflection, which increases the accuracy of background signal estimation.

5.7 Sources of uncertainty

Calculating gas flow using basically two measurements of a huge square of land, containing, among other things, a flare, is a highly complex subject, with multiple sources contributing to the uncertainty of the calculation.

The sources of uncertainty can be divided into those coming from the combustion conditions, the atmospheric effects and conditions, the recording conditions, and the sensor related effects.

5.7.1 Combustion conditions

Combustion of the natural gas is a complex process, highly dependent on the flaring set-up. One of the most important aspects of the set-up is the air feed to the flame. For instance, if a significant amount of air is premixed into the fuel before ignition, the combustion will be highly efficient. Thus, the temperature of the flame will be very high, and water vapour and carbon dioxide will dominate the products' list. These products have relatively low emissivity values. Therefore, the radiation of the flame will be relatively low.

In case of a low air-feed in the flame, the situation will be different. The fuel-rich mixture produces significant amounts of soot, and the combustion will this time have a lower temperature: in extreme cases even 1000 K lower than in the stoichiometric combustion. Soot produced in the flame has a high emissivity value, which means that the flame radiation will be altogether relatively higher. This brings practical problems for the gas flares parametrisation from the satellite imagery, because there is no information on the flaring set-up, which can be included as a-priori information to the modelling.

The described factors cause that a gas flame is an object extremely challenging to describe, taking all its properties into consideration. Therefore, assumptions and simplifications must be made, like those in the presented dissertation. Such assumptions can lead to significant errors, but as long as the parameters are not analysed in a specially designed experimental series, the magnitude of this error remains unknown.

5.7.2 Atmosphere

As for the atmospheric conditions, one of the most significant sources of uncertainty is the wind. During the experimental series, the flame was recorded also during wind blasts. A wind blast changes the geometry of the flame: the flame is pushed and tilted by the wind, and consequently, the emissivity changes. Zhang *et al.* 2015 mention some effects of the wind and state, that combustion efficiency changes in a wind blast. This can happen, e.g. because additional air is being fed, which can increase the efficiency of the flaring and the temperature in consequence. However, Zhang *et al.* 2015 state that combustion efficiency can be lowered by a wind blast. It is safe to presume that both effects can take place, depending on the flaring set-up, wind speed, etc. Analysis of the wind effects on the flare radiant flux, derived from IR camera measurements on the ground, was published in Soszynska *et al.* 2019. The authors state that the standard deviation of the recorded integrated radiance increases 70% during moderate wind blasts of up to 8 m/s. There is no quantitative analysis on the influence of a wind blast on the flame tilt. However, a geometric model introduced in Sections 3.5.2 and 3.5.3 allowed to estimate the tilt and from there the influence of the tilt on emissivity, by using the documentation of the experiments conducted.

For instance, assuming a gas flare with 10000 kg/h gas flow, in case of no wind, the overall (mean) emissivity of the flame will be 0.83. If a wind blast tilts the flame to 30°, the emissivity will reduce to 0.75, but if a strong wind tilts the flame to 60°, the emissivity reduces to 0.54, which is an almost 35% change. If unaccounted for, the 30° tilting can result in even 1000 kg/h underestimation and the 60° tilt translates to 3200 kg/h underestimation, which is over 30%.

However, wind is not the only factor contributing to the uncertainty. Another very important condition is the cloud cover. Even though thick clouds are quite easy to distinguish and mask, the thin cirrus layers are not always well visible in the satellite imagery. During one of the experiments at the BAM TTS, the satellite scene was covered with a thin cirrus cloud (see Figure 68). The cloud cover was very thin and hard to identify in the according satellite image, therefore difficult to detect altogether, without an a-priori knowledge from the experiment. Using this image for the gas flow calculation, however, lead to an overestimation of gas flow of around 2000 kg/h. This was the case, where the estimated background temperature was estimated the

lowest (see Table 26[20]). As underestimation of the background temperature leads to subtraction of too little radiance from a scene fragment, therefore, the radiance assigned to the flare was estimated too high, resulting in overestimation of the gas flow.

The cloud cover, even if very slight, is a significant source of uncertainty. To avoid the additional uncertainty in the calculations, the imagery with cloud cover should be excluded from the analysis.

The last factor, influencing the accuracy of gas flow calculation, in this group, is the atmospheric transmittance. The accuracy of the atmospheric transmittance is most important in the calculation of the flame radiance. As described in Section 4.3.4, an error in the atmospheric transmittance as small as 1% point may cause even 15% error in the gas estimation. It seems that the magnitude of the error is a function of background radiation, but the correlation was conducted using very few data points, and should be, therefore, treated with caution.

5.7.3 Sensing and sensor parameters

Another group of sources of uncertainty are the sensing parameters. One example is the time of day. The amount of the reflected light along the electromagnetic spectrum is not everywhere the same. In shorter wavelengths (especially in the visible spectrum), the amount of energy reflected is very high, whereas the light emitted by a source is negligible in these wavelengths (for object of normal temperature, so 300 K). In the LWIR region, the situation is the other way around: the emitted light from an object is very high, and the reflected light is negligible. The SWIR and MWIR regions, therefore, contain a mixture of light reflected and emitted from an object. In the MWIR region, the amount of reflected light should be approximately as high, as the emitted, whereas in SWIR, the tendency will be strongly towards the reflected light (Schott 2007). Therefore, the estimation of flame parameters is far more complex in daylight than in the night. Zhukov *et al.* 2006 made some analysis on the minimal proportion of a hot-spot area in a pixel, per given temperature and background radiance. The minimal proportion for a hot-spot of 1000 K is higher in case of daylight images, and is around $1.2 \cdot 10^{-4}$ and in case of night images reduces to $4.5 \cdot 10^{-5}$, so 2.7 times less.

The daylight conditions can also cause difficulties in calculating the background temperature, which is a crucial pre-processing step for calculating the amount of flared gas. The bi-spectral method, which is used for the background temperature estimation, usually seems to include the reflected light in the calculation. However, the background temperature estimations for the Persian Gulf study area did not bring satisfactory results: the temperature was estimated too low, because the LWIR estimation was significantly below the MWIR estimation. Most probably the reason was the reflected light from the water surface, visible in the MWIR band.

The influence of the reflected light on the overall accuracy is not quite clear and should be considered, especially in cases, where no information on the background temperature is available, or when the bi-spectral method does not provide reasonable results. In some cases, a more accurate solution is to calculate the median value over a given window, instead of modelling the background signal, using the estimated background temperature.

Apart from the light conditions, the type of background of a flare influences the accuracy of the gas flow calculation. For instance, as mentioned before, in the Persian Gulf study area, the gas flares were located on platforms surrounded by water. As water absorbs radiation, a huge water body, such as a sea, has a huge heat capacity. Therefore, the radiation is not simply radiated back, due to constant movement of water. This may potentially lead to errors in the gas flow estimation, as Elvidge *et al.* 2009a state. However, without a proper set of reference

[20] Although in comparison to the pyrometer measurements the estimated temperature is too high, the estimation using the bi-spectral method contains the reflected light already. As calculated in Section 4.3.4, the amount of reflected light typically causes an 8 K overestimation in the background temperature calculation with the bi-spectral method, which means that the temperature including the solar reflection was in this case underestimated.

data for gas flares located on water, the quantitative analysis of this kind of error remains an open issue.

The opposite effect will take place in case of highly reflective surfaces. For instance, surfaces, such as bright sand, may reflect a significant portion of energy, which will be recorded by a satellite sensor. In such case, a sensor records also the energy radiated primarily in other directions, although a homogeneous radiation over a sphere is assumed. This would lead to an overestimation of the gas flow value. Again, the magnitude of the error due to reflective background remains unknown.

Apart from the type of the background, also the background temperature may have significant influence on the accuracy of gas flow calculation. The mean measured radiance for an example image of Kuwait (16.07.2016) was 1.38 $W/sr/m^2/\mu m$, which translates to 55°C brightness temperature. Similar radiance will be radiated by a flare with around 6500 kg/h gas flow. A small gas flare of 1000 kg/h, will radiate around 0.22 $W/sr/m^2/\mu m$, which is approximately 3 times the standard deviation of radiance (which is 0.07 $W/sr/m^2/\mu m$ for the sand area in this image). Thus, additional radiance in the height of 2 standard deviations, added to the flare signal, will cause an overestimation of 660 kg/h. In comparison to other sources of uncertainty, this influence seems to be relatively low, as long as the background of the flare remains homogeneous.

The roll angle of the sensor is also one of the conditions, which possibly influence the accuracy of the calculation. With increasing roll angle, the GSD per pixel increases as well, consequently, a decrease in hot-spot proportion in a pixel is observed. Let us assume a BIROS image with a 30°roll angle. The pixel furthermost from nadir will have a GSD of 525 m, therefore GSD^2 - 275625 m^2. A 30 m^2 gas flare flame will comprise $1.1 \cdot 10^{-4}$ of a pixel, which is almost exactly on the limit of minimal proportion of a hot-spot in daylight, described by Zhukov *et al.* 2006. In case of a sensor with a larger GSD, the proportion will decrease, and may become too low, to characterise the flare correctly.

Another possible source of uncertainty is noise in the imagery. Since the Equation (11) is a linear one, the influence of noise on accuracy of gas flow calculation can be calculated using the SNR value. With an SNR value of 100, an error of 1% will be introduced due to noise. The higher the SNR value, the lower the influence of noise on gas flow calculation accuracy. Sensor noise seems to be a rather weak uncertainty source, in comparison with other factors. Noise can also be reduced, e.g. by averaging a multiple recording. Therefore, a redundancy in sensing decreases noise in the image.

As can be seen, the calculation of gas flow using satellite imagery is a highly complex issue, with multiple sources contributing to the uncertainty of the calculation. Even though some of these sources may work against each other, it is also possible that multiple sources will add up to a significant error. In some cases, the error can be estimated, in other the current state of knowledge is insufficient to estimate the influence.

5.8 Future work

In the presented research, a method for calculation of gas flow from satellite data is proposed. Within the frameworks of this research, not all aspects of the flaring process could have been analysed. It is advisable, to continue studying this subject and further develop the method proposed.

One of the parameters crucial for an accurate estimation of the gas flow is the proportion of energy radiated $\rho(T)$. The value of this parameter is only assumed in this dissertation, because a correct estimation would require a separate study and a specialised experimental set-up, which was not possible for this dissertation. Nevertheless, for future studies and applications, it would be beneficial to further study this parameter.

The method proposed, could be further developed by adding a temperature estimation into the workflow. Possibly, an adaption of the bi-spectral method, including the parameters of

combustion, could be used for this purpose. This would allow calculating other combustion parameters, for each flare individually, which would increase the accuracy of the calculation.

Another important development of the method would be to calculate the ρ parameter for the SWIR spectral range. This, however, requires a dedicated research regarding the spectral response of a gas flame in this spectral range. Several researchers. e.g. Fisher & Wooster 2018, suggest that the SWIR spectral range is the most proper for gas flare parameters estimation. Therefore, it is advisable to study the emissivity of a gas flame in this spectral range.

In the presented study, a minimal detectable gas flow of 1000 kg/h is assumed, and all the values below this threshold are treated as invalid. This threshold value is based on a theoretical calculation of flare radiance in comparison with standard deviation of background signal. Additionally, in one of the experiments, the gas flow was set to 1000 kg/h. The satellite image from this experiment shows that the gas flare is not distinguishable from the background. However, in this case the combustion was highly efficient and, hence, the flame radiated weaker, thus it is possible that a less efficient combustion with such gas flow would be detectable. Additionally, the accuracy of the background radiation estimation has a strong influence on the gas flow calculation accuracy. It is therefore advisable, to further analyse this influence. Aspects, which should be considered are: the background temperature, the background type, and the solar reflection. Such analysis could provide information on minimal detectable gas flow with respect to all the above-mentioned aspects.

Lastly, a further validation of the results would be advisable. In the presented dissertation, a comparison with gas flow values calculated with a method proposed by Elvidge *et al.* 2016, is conducted only for a group of 35 gas flares in the Persian Gulf. This comparison should be developed in a separate study, focusing on aspects, such as influence of background type and temperature, on the correlation of gas flow results from both methods. Additionally, a comparison of both methods on images, where the time gap between the images from both sensors is as small as possible, would be very informative on the feasibility of both sensors for gas flaring analysis.

The method proposed has a potential for global mapping of gas flaring. It would be strongly advisable to globally monitor gas flares using the model developed, optimally with a constellation of sensors, which are able to map the Earth daily or almost daily. Using the method proposed, with such imagery, would provide a good information basis for further reduction of routine gas flaring.

6 Bibliography

1. Colwell, R. *et al.* Determining the prevalence of certain cereal crop diseases by means of aerial photography. *Hilgardia* **26,** 223–286 (1956).
2. Burgess, D, Hertzberg, M, Afgan, N & Beer, J. Heat transfer in flames. *Scripta Book Co* **413** (1974).
3. Brzustowski, T., Gollahalli, S., Gupta, M., Kaptein, M & Sullivan, H. Radiant heating from flares. *ASME paper,* 4 (1975).
4. Croft, T. A. Nighttime images of the earth from space. *Scientific American* **239,** 86–101 (1978).
5. Dozier, J. A method for satellite identification of surface temperature fields of subpixel resolution. *Remote Sensing of environment* **11,** 221–229 (1981).
6. Matson, M. & Dozier, J. Identification of subresolution high temperature sources using a thermal IR sensor. *Photogrammetric Engineering and Remote Sensing* **47,** 1311–1318 (1981).
7. Becker, H. & Liang, D. Total emission of soot and thermal radiation by free turbulent diffusion flames. *Combustion and Flame* **44,** 305–318 (1982).
8. Division, A. A. E. R. M. & Leahey, D. *A preliminary study of the chemical composition and combustion efficiency of a sour gas flare* (Alberta Environment, Environmental Protection Services, Research Management . . ., 1985).
9. Flannigan, M. D. & Haar, T. V. Forest fire monitoring using NOAA satellite AVHRR. *Canadian Journal of Forest Research* **16,** 975–982 (1986).
10. Malingreau, J.-P. & Tucker, C. J. Large-scale deforestation in the southeastern Amazon basin of Brazil. *Ambio,* 49–55 (1988).
11. Haus, R., Wilkinson, R., Heland, J. & Schäfer, K. Remote sensing of gas emissions on natural gas flares. *Pure and Applied Optics: Journal of the European Optical Society Part A* **7,** 853 (1998).
12. Strosher, M. T. Characterization of emissions from diffusion flare systems. *Journal of the Air & Waste Management Association* **50,** 1723–1733 (2000).
13. Giglio, L. & Kendall, J. D. Application of the Dozier retrieval to wildfire characterization: a sensitivity analysis. *Remote Sensing of Environment* **77,** 34–49 (2001).
14. Leahey, D. M., Preston, K. & Strosher, M. Theoretical and observational assessments of flare efficiencies. *Journal of the Air & Waste Management Association* **51,** 1610–1616 (2001).
15. Argo, J. Unhealthy effects of upstream oil and gas flaring. *A report prepared for Save Our Seas and Shores (SOSS) for presentation before the Public Review Commission Into Effects of Potential Oil and Gas Exploration, Drilling Activities Within Licenses* **236,** 236 (2002).
16. Trollope, W., Trollope, L. & Hartnett, D. Fire behaviour a key factor in the fire ecology of African grasslands and savannas. *Forest Fire Research and Wildland Fire Safety, Millpress, Rotterdam* (2002).
17. Giglio, L., Descloitres, J., Justice, C. O. & Kaufman, Y. J. An enhanced contextual fire detection algorithm for MODIS. *Remote sensing of environment* **87,** 273–282 (2003).
18. Beychok, M. R. *Fundamentals of stack gas dispersion* (MR Beychok, 2005).
19. Bjorndalen, N, Mustafiz, S, Rahman, M. & Islam, M. No-flare design: converting waste to value addition. *Energy sources* **27,** 371–380 (2005).

20. Reulke, R., Becker, S., Haala, N. & Tempelmann, U. Determination and improvement of spatial resolution of the CCD-line-scanner system ADS40. *ISPRS Journal of Photogrammetry and Remote Sensing* **60,** 81–90 (2006).

21. Zhukov, B, Lorenz, E, Oertel, D, Wooster, M & Roberts, G. Spaceborne detection and characterization of fires during the bi-spectral infrared detection (BIRD) experimental small satellite mission (2001–2004). *Remote sensing of Environment* **100,** 29–51 (2006).

22. Elvidge, C. D. *et al.* A twelve year record of national and global gas flaring volumes estimated using satellite data. *Boulder, CO, NOAA National Geophysical Data Center* (2007).

23. Gallegos, S, Ryan, R., Baud, R & Bloemker, J. MODIS products to improve the monitoring of gas flaring from offshore oil and gas facilities. *Final Report to NASA* (2007).

24. Jensen, J. R. *Remote sensing of the environment: an earth resource perspective* (Pearson Prentice Hall: Upper Saddle River, 2007).

25. Schott, J. R. *Remote sensing: the image chain approach* (Oxford University Press on Demand, 2007).

26. Elvidge, C. *et al.* Improving satellite data estimation of gas flaring volumes. *Year Two Final Report to the GGFR. Internet: http://s3. amazonaws. com/zanran_storage/www. ngdc. noaa. gov/ContentPages/15507168. pdf* (2009).

27. Elvidge, C. *et al.* A fifteen year record of global natural gas flaring derived from satellite data. *Energies* **2,** 595–622 (2009).

28. Harris Geospatial. Atmospheric Correction Module: QUAC and Flaash User Guide v. 4.7. *ITT Visual Information Solutions Inc.: Boulder, CO, USA* (2009).

29. Ismail, O. & Fagbenla, R. Accurate safty zone detemination during gas flaring (2009).

30. Collins, C & Oshodi, O. Improper Abandonment of Oil. *Nigerians in America* (2010).

31. Campbell, J. B. & Wynne, R. H. *Introduction to remote sensing* (Guilford Press, 2011).

32. Dombrovsky, L. *Radiative properties of soot particles* 2011.

33. Elvidge, C. D., Baugh, K. E., Ziskin, D., Anderson, S. & Ghosh, T. Estimation of gas flaring volumes using NASA MODIS fire detection products. *NOAA National Geophysical Data Center (NGDC), annual report* **8** (2011).

34. Casadio, S, Arino, O & Minchella, A. Use of ATSR and SAR measurements for the monitoring and characterisation of night-time gas flaring from off-shore platforms: The North Sea test case. *Remote sensing of environment* **123,** 175–186 (2012).

35. Casadio, S., Arino, O. & Serpe, D. Gas flaring monitoring from space using the ATSR instrument series. *Remote Sensing of Environment* **116,** 239–249 (2012).

36. Ismail, O. S. & Umukoro, G. E. Global impact of gas flaring (2012).

37. Olivier, J. G., Peters, J. A. & Janssens-Maenhout, G. Trends in global CO2 emissions 2014 report (2012).

38. Wooster, M., Perry, G. & Zoumas, A. Fire, drought and El Niño relationships on Borneo (Southeast Asia) in the pre-MODIS era (1980–2000). *Biogeosciences* **9,** 317–340 (2012).

39. Anejionu, C., Blackburn, A & Duncan, W. Remote Mapping of Gas Flares in the Niger Delta of Nigeria with MODIS imagery. *Lancaster University, Lancaster Environment Centre, United Kingdom* (2013).

40. Cheremisinoff, N. P. *Industrial gas flaring practices* (John Wiley & Sons, 2013).

41. Elvidge, C., Zhizhin, M., Hsu, F.-C. & Baugh, K. VIIRS nightfire: Satellite pyrometry at night. *Remote Sensing* **5,** 4423–4449 (2013).

42. Madry, S. Introduction and History of Space Remote Sensing. *Handbook of Satellite Applications,* 657–666 (2013).

43. Reulke, R. & Eckardt, A. *Image quality and image resolution* in *2013 Seventh International Conference on Sensing Technology (ICST)* (2013), 682–685.

44. Wooster, M. J. *et al.* in *Thermal Infrared Remote Sensing* 347–390 (Springer, 2013).

45. Yuan, M., Chen, B., Li, C., Zhang, J. & Lu, S. Analysis of the Combustion Efficiencies and Heat Release Rates of Pool Fires in Ceiling Vented Compartments. *Procedia Engineering* **62.** 9th Asia-Oceania Symposium on Fire Science and Technology, 275 –282. ISSN: 1877-7058. http://www.sciencedirect.com/science/article/pii/S1877705813012472 (2013).

46. Anejionu, O. C. D., Blackburn, G. A. & Whyatt, J. D. Satellite survey of gas flares: Development and application of a Landsat-based technique in the Niger Delta. *International journal of remote sensing* **35,** 1900–1925 (2014).

47. Chowdhury, S. *et al. Daytime gas flare detection using Landsat-8 multispectral data* in *2014 IEEE Geoscience and Remote Sensing Symposium* (2014), 258–261.

48. Johnston, J., Wooster, M. & Lynham, T. Experimental confirmation of the MWIR and LWIR grey body assumption for vegetation fire flame emissivity. *International Journal of Wildland Fire* **23,** 463–479 (2014).

49. Rogalski, A & Chrzanowski, K. Infrared devices and techniques (revision). *Metrology and Measurement Systems* **21** (2014).

50. Whitty, K. J. *Radiation:Multi-Surface Systems andRadiation with Participating Media (Gas Radiation)* Presentation from lectures published online, accessed 20.03.2020. 2014. https://my.eng.utah.edu/~whitty/chen3453/Lecture%2037%20-%20Radiation%20-%20Gas%20Radiation.pdf.

51. Anejionu, O. C., Blackburn, G. A. & Whyatt, J. D. Detecting gas flares and estimating flaring volumes at individual flow stations using MODIS data. *Remote Sensing of Environment* **158,** 81–94 (2015).

52. Anejionu, O. C., Whyatt, J. D., Blackburn, G. A. & Price, C. S. Contributions of gas flaring to a global air pollution hotspot: Spatial and temporal variations, impacts and alleviation. *Atmospheric Environment* **118,** 184–193 (2015).

53. Baugh, K. Characterization of Gas Flaring in North Dakota using the Satellite Data Product, VIIRS Nightfire. *AGUFM* **2015,** A23N–05 (2015).

54. Ghadyanlou, F. & Vatani, A. Flare-gas recovery methods for olefin plants. *Chemical Engineering* **122,** 66 (2015).

55. Morfitt, R. *et al.* Landsat-8 Operational Land Imager (OLI) radiometric performance on-orbit. *Remote Sensing* **7,** 2208–2237 (2015).

56. Song, Z. *et al.* Analysis of coal fire dynamics in the Wuda syncline impacted by fire-fighting activities based on in-situ observations and Landsat-8 remote sensing data. *International Journal of Coal Geology* **141,** 91–102 (2015).

57. Tractebel Engineering S.A. *CNG for commercialization of small volumes of associated gas (Vol.2) (English)* Washington D.C., 2015. http://documents.worldbank.org/curated/en/210571472125529218/CNG-for-commercialization-of-small-volumes-of-associated-gas.

58. World Bank. *Executive summary: comparison of mini/micro LNG and CNG for commercialization of small volumes of associated gas (English)* Washington D.C., 2015. http://documents.worldbank.org/curated/en/469561534950044964/GGFR-Technology-Overview-Utilization-of-Small-Scale-Associated-Gas.

59. Zhang, X., Scheving, B., Shoghli, B., Zygarlicke, C. & Wocken, C. Quantifying gas flaring CH4 consumption using VIIRS. *Remote Sensing* **7,** 9529–9541 (2015).

60. Elvidge, C., Zhizhin, M., Baugh, K., Hsu, F.-C. & Ghosh, T. Methods for global survey of natural gas flaring from visible infrared imaging radiometer suite data. *Energies* **9,** 14 (2016).

61. Ismail, O. S. & Umukoro, G. E. Modelling combustion reactions for gas flaring and its resulting emissions. *Journal of King Saud University-Engineering Sciences* **28,** 130–140 (2016).

62. Plank, S. *et al. Monitoring of active volcanoes by means of multi-sensor remote sensing – a case study of the 2014/15 Holuhraun fissure eruption* in *The 2nd Workshop on the Physics of Volcanoes* (2016). `https://elib.dlr.de/103310/`.

63. Schroeder, W. *et al.* Active fire detection using Landsat-8/OLI data. *Remote sensing of environment* **185,** 210–220 (2016).

64. World Bank. *Global gas flaring reduction partnership - gas flaring definitions (English).* Washington D.C., 2016. `http://documents.worldbank.org/curated/en/755071467695306362/Global-gas-flaring-reduction-partnership-gas-flaring-definitions`.

65. Elvidge, C. D., Baugh, K., Zhizhin, M., Hsu, F.-C. & Ghosh, T. *Supporting international efforts for detecting illegal fishing and GAS flaring using VIIRS* in *2017 IEEE International Geoscience and Remote Sensing Symposium (IGARSS)* (2017), 2802–2805.

66. Fischer, C. *et al. Wild Fire Mapping using FireBIRD Data* in *EARSel SIG 2017* (2017). `https://elib.dlr.de/133347/`.

67. Klein, D. *et al. The Use of DLR FireBIRD Mission Data for Hot Spot Detection and Fire Characterization* in *ISRSE 37* (2017). `https://elib.dlr.de/118489/`.

68. Kochergin, G., Kupriyanov, M. & Polishchuk, Y. M. The use of landsat 8 space images for rapid assessment of total flaring volumes of associated gas in the oil-producing territory. *Sovremennye problemy distantsionnogo zondirovaniya Zemli iz kosmosa* **14,** 47–55 (2017).

69. Plank, S. *et al. DLR's FireBird mission monitoring the 2014/15 Holuhraun fissure eruption* in *Physics of Volcanoes 2017* (2017). `https://elib.dlr.de/111464/`.

70. Schroeder, W. & Giglio, L. Visible Infrared Imaging Radiometer Suite (VIIRS) 750 m Active Fire Detection and Characterization Algorithm Theoretical Basis Document 1.0 (2017).

71. Sharma, A., Wang, J. & Lennartson, E. M. Intercomparison of MODIS and VIIRS fire products in Khanty-Mansiysk Russia: Implications for characterizing gas flaring from space. *Atmosphere* **8,** 95 (2017).

72. Soszyńska, A. *FireBIRD Mission Data for Gas Flaring Analysis* in *Pacific-Rim Symposium on Image and Video Technology* (2017), 369–381.

73. Vollmer, M. & Möllmann, K.-P. *Infrared thermal imaging: fundamentals, research and applications* (John Wiley & Sons, 2017).

74. Zolfaghari, M., Pirouzfar, V. & Sakhaeinia, H. Technical characterization and economic evaluation of recovery of flare gas in various gas-processing plants. *Energy* **124,** 481–491 (2017).

75. Caseiro, A. *et al.* A methodology for gas flaring detection and characterisation using SLSTR. *Remote Sens* **10,** 1118 (2018).

76. Faruolo, M., Lacava, T., Pergola, N. & Tramutoli, V. On the potential of the RST-FLARE algorithm for gas flaring characterization from space. *Sensors* **18,** 2466 (2018).

77. Fischer, C., Bucher, T., Säuberlich, T. & Halle, W. *FireBIRD- High Dynamic Range Thermal Infrared Satellite Systems for hot and cold temperature environments* in *15th International Circumpolar Remote Sensing Symposium (ICRSS)* (eds Guenther, F., Grosse, G. & Jones, B.) (Bibliothek Wissenschaftspark Albert Einstein, 2018), 41–41. https://elib.dlr.de/121814/.

78. Fisher, D. & Wooster, M. Shortwave IR Adaption of the Mid-Infrared Radiance Method of Fire Radiative Power (FRP) Retrieval for Assessing Industrial Gas Flaring Output. *Remote Sensing* **10,** 305 (2018).

79. Frauenberger, O. *et al. The DLR FireBIRD Mission - A Technological Experiment for Operational Wildfire Monitoring* in *52. Tschtenii Poswjaschennych Raßrabotke Nauchnogo Nasleduja i Raßwitiju Idei K. E. Ziolkowskogo* (eds Marow, M. & Abakumowa, N.) (Is-dwo Kasan, 2018), 10–21. https://elib.dlr.de/123922/.

80. Halle, W. *et al. FIREBIRD - small satellite for wild fire assessment* in *2018 IEEE International Geoscience and Remote Sensing Symposium (IGARSS)* (2018), 1–4. https://elib.dlr.de/121239/.

81. Kumar, S. S. & Roy, D. P. Global operational land imager Landsat-8 reflectance-based active fire detection algorithm. *International Journal of Digital Earth* **11,** 154–178 (2018).

82. Lorenz, E. *et al. Detection of High Temperature Events using FireBIRD Data* in *LVPE - Workshop on Land Product Validation and Evolution* (2018). https://elib.dlr.de/133349/.

83. Mallinis, G., Mitsopoulos, I. & Chrysafi, I. Evaluating and comparing Sentinel 2A and Landsat-8 Operational Land Imager (OLI) spectral indices for estimating fire severity in a Mediterranean pine ecosystem of Greece. *GIScience & Remote Sensing* **55,** 1–18 (2018).

84. Peremitina, T., Kochergin, G., Kupriyanov, M., Polishchuk, Y. & Yashchenko, I. *Remote monitoring of associated petroleum gas flaring in oilfields of Western Siberia* in *AIP Conference Proceedings* **2051** (2018), 020234.

85. Säuberlich, T. *Private communication* 2018.

86. World Bank. *GGFR Technology Overview - Utilization of Small-Scale Associated Gas (English)* Washington D.C., 2018. http://documents.worldbank.org/curated/en/469561534950044964/GGFR-Technology-Overview-Utilization-of-Small-Scale-Associated-Gas.

87. Caseiro, A., Gehrke, B., Rücker, G., Leimbach, D. & Kaiser, J. W. Gas flaring activity and black carbon emissions in 2017 derived from Sentinel-3A SLSTR. *Earth Syst. Sci. Data Discuss* **10** (2019).

88. Fisher, D. & Wooster, M. J. Multi-decade global gas flaring change inventoried using the ATSR-1, ATSR-2, AATSR and SLSTR data records. *Remote Sensing of Environment* **232,** 111298 (2019).

89. Lee, R. & Small, C. Detection and temperature estimation of gas flares with nocturnal Landsat OLI (2019).

90. Plank, S. M., Martinis, S. & Richter, R. *Thermal remote sensing of volcanoes by means of DLR's FireBIRD mission - a case study of the 2015 Villarrica Volcano eruption, Chile* in *ESA Living Planet Symposium 2019* (2019). https://elib.dlr.de/127482/.

91. Soszynska, A. *et al. Analysis of the gas flare flame with IR cameras* in *SPIE Remote Sensing 2019* (SPIE Digital Library, 2019). https://elib.dlr.de/129226/.

92. Brandt, A. R. Accuracy of satellite-derived estimates of flaring volume for offshore oil and gas operations in nine countries. *Environmental Research Communications* **2,** 051006 (2020).

93. Facchinelli, F. *et al.* Unburnable and Unleakable Carbon in Western Amazon: Using VIIRS Nightfire Data to Map Gas Flaring and Policy Compliance in the Yasuní Biosphere Reserve. *Sustainability* **12,** 58 (2020).

94. Faruolo, M., Lacava, T., Pergola, N. & Tramutoli, V. The VIIRS-Based RST-FLARE Configuration: The Val d'Agri Oil Center Gas Flaring Investigation in Between 2015–2019. *Remote Sensing* **12,** 819 (2020).

95. Kumar, S. S., Hult, J., Picotte, J. & Peterson, B. Potential Underestimation of Satellite Fire Radiative Power Retrievals over Gas Flares and Wildland Fires. *Remote Sensing* **12,** 238 (2020).

96. Lagutin, A. A., Mordvin, E. Y., Volkov, N. V. & Tuchina, N. V. *Estimation of Natural Gas Flaring Volume at the Western Siberia Flares using Satellite Night-Time Data in the Visible and Near-Infrared Range* in *CEUR Workshop Proceedings* **2534** (2020), 22–26.

97. Sofan, P., Bruce, D., Schroeder, W., Jones, E. & Marsden, J. Assessment of VIIRS 375 m active fire using tropical peatland combustion algorithm applied to Landsat-8 over Indonesia's peatlands. *International Journal of Digital Earth,* 1–22 (2020).

98. Soszynska, A. *et al. Challenges in Remote Sensing of Gas Flares using Infrared Aerial Imagery* in *40. Wissenschaftlich- Technische Jahrestagung der DGPF* **29** (2020). https://elib.dlr.de/134368/.

99. Wikipedia contributors. *Aliasing — Wikipedia, The Free Encyclopedia* Online; accessed 20-November-2020. 2020. https://en.wikipedia.org/wiki/Aliasing.

100. Carter, W. *Gas flare on top of a flare stack at Preemraff oil refinery, Lysekil, Sweden.* n.d. https://upload.wikimedia.org/wikipedia/commons/d/d6/Gas_flare_on_top_of_a_flare_stack_at_Preemraff_Lysekil_4.jpg.

101. CEOS. *The CEOS database* Accessed on 01.09.2020. http://database.eohandbook.com/index.aspx.

102. Chimot, J. *Copernicus Sentinel-3 NRT Fire Radiative Power (FRP) – Radiant heating & threat monitoring of fires, gas flares, and volcanoes* https://www.eumetsat.int/website/home/Data/ScienceActivities/OperationalAlgorithms/CopernicusSentinel3NRTFireRadiativePowerFRP/index.html#OVP.

103. Engineering 360. *Gas Flares Information* n.d. https://www.globalspec.com/learnmore/manufacturing_process_equipment/air_quality/gas_flares.

104. Gerner, F. Regulation of Associated Gas Flaring and Venting: A Global Overview and Lessons (n.d.).

105. *Google Earth: High Resolution World Imagery* earth.google.com/web/.

106. National Centers for Environmental Information National Oceanic and Atmospheric Administration. *VIIRS Nightfire (Flares Only Version)* https://www.ngdc.noaa.gov/eog/viirs/download_viirs_flares_only.html.

107. World Bank. *Gas flaring volumes, top 30 countries 2014-2018* n.d. https://www.worldbank.org/en/programs/gasflaringreduction#7.

108. World Bank. *Global Gas Flaring Reduction Partnership* https://www.worldbank.org/en/programs/gasflaringreduction#1.

109. World Bank. *Zero Routine Flaring by 2030* n.d. https://www.worldbank.org/en/programs/zero-routine-flaring-by-2030#5.

A Comparison of sensors

		BIROS	LANDSAT-8	VIIRS
Name		Bispectral InfraRed Optical Sensor	LDCM Landsat Data Continuity Mission	Visible Infrared Imaging Radiometer Suite
Operated by		DLR	NOAA/NASA	NOAA/NASA
Status		Operational	Operational	Operational
Orbit		500 km	705 km	829 km Within an orbit, the altitude varies from 828 km near 15° N to 856 km near the South Pole
Revisit time		5 days	16 days	12 hours
Spectral range		VIS NIR MWIR LWIR	VIS NIR SWIR LWIR	VIS NIR SWIR MWIR LWIR
Spectral bands relevant for gas flaring research	SWIR	----------	SWIR1 1.56-1.66 µm SWIR2 2.1-2.3 µm	M10 and I3 1.58 - 1.64 µm M11 2.23 - 2.28 µm
	MWIR	MWIR 3.4-4.2 µm	----------	I4 3.55-3.93 µm M12 3.61-3.79 µm M13 3.97-4.13 µm
	LWIR	LWIR 8.6-9.4 µm	TIR1 10.6-11.2µm TIR2 11.5-12.5 µm	M14 8.4-8.7 µm M15 10.26-11.26 µm I5 10.5-12.4 µm M16 11.54-12.49 µm
GSD		175 m (350 m)	100 m for TIR bands 30 m other	750 m for M-bands and 375 for I-bands
Sensor type		HgCdTe	Silicone PIN (bands 1-5, 9) and HgCdTe (other)	VIS/NIR - silicon PIN diodes SWIR/MWIR/LWIR PV HgCdTe
Imaging mode		Pushbroom	Pushbroom	Whiskbroom
Daytime/nighttime imagery		Daytime and nighttime	Daytime (all bands) and nighttime (only LWIR)	Daytime and nighttime
Special features		Staggered array		
SNR/NEΔT		TET-1 MWIR SNR 343.3 LWIR SNR 136.5	SWIR1 SNR 267 SWIR2 SNR 327 LWIR1 NEΔT at 240 K 0.8 K at 300 K 0.4 K at 360 K 0.3 K LWIR2 NEΔT at 240 K 0.7 K at 300 K 0.4 K at 360 K 0.3 K	M10 SNR 342 M11 SNR 10 M12 NEΔT 0.396 K M13 NEΔT at 300 K 0.1 K at 380 K 0.4 K M14 NEΔT at 270 K 0.091 K M15 NEΔT at 300 K 0.01 K M16 NEΔT at 300 K 0.072 K I4 NEΔT at 270 K 2.5K I5 NEΔT at 210 K 1.5 K
Cooling		Active stirling cooling for IR detector, 80-100 K	A mechanical, two-stage cryocooler for TIRS, 43 K	FPAs are housed inside their own dewars and will be cryogenically controlled at 82 K on-orbit using a three stage passive cooler.
Quantisation		14 bits	12 bits	12 bits
Field-of-View		19.6° VIS-NIR 19° IR	15°	112.56°
Swath		211 km VIS-NIR 178 km IR	185 km	3060 km
Saturation		Hot-Area-Mode	SWIR1 96 W/m²/sr/µm SWIR2 29 W/m²/sr/µm LWIR1 20.5 W/m²/sr/µm LWIR2 17.8 W/m²/sr/µm	I4 4 W/m²/sr/µm I5 24 W/m²/sr/µm M10, M11 1.31 (reflectance!) M12 4.5 W/m²/sr/µm M13 600 W/m²/sr/µm M14 24 W/m²/sr/µm M15 25 W/m²/sr/µm M16 22 W/m²/sr/µm
Gas flares in images		Well visible and suitable for analysis	Well visible, but saturated	Visible
Application in gas flares research until now		Detection and parametrisation	Detection	Detection and parametrisation

		MODIS	SLSTR	MSI
Name		Moderate Resolution Imaging Spectroradiometer	Sea and Land Surface Temperature Radiometer	MultiSpectral Instrument
Operated by		NOAA/NASA	Eumetsat	Eumetsat
Status		Operational, but replaced by VIIRS	Operational	Operational
Orbit		705 km	800-830 km	786 km
Revisit time		1-2 days	0.5 day (both satellites)	5 days (both satellites)
Spectral range		VIS NIR SWIR MWIR LWIR	VIS SWIR MWIR LWIR	VIS NIR SWIR
Spectral bands relevant for gas flaring research	SWIR	B6 1.628 - 1.652 µm B7 2.105 - 2.155 µm	S5 1.58-1.64 µm S6 2.23-2.28 µm	B11 1.568-1.659 (S2A) 1.563-1.657 (S2B) B12 2.115-2.290 (S2A) 2.093-2.278 (S2B)
	MWIR	B20 3.660 - 3.840 µm B21 3.929 - 3.989 µm B22 3.929 - 3.989 µm B23 4.020 - 4.080 µm	S7 and F1 3.54-3.94	----------
	LWIR	B29 8.400 - 8.700 µm B30 9.580 - 9.880 µm B31 10.780 - 11.280 µm B32 11.770 - 12.270 µm	S8 10.47-11.24 µm S9 and F2 11.57-12.48 µm	----------
GSD		250 m (bands 1–2) 500 m (bands 3–7) 1000 m (bands 8–36)	500 m (VIS-SWIR) 1000 m (MWIR-LWIR)	10 m (bands 2-4) 20 m (bands 5-8, 11, 12) 60 m (bands 1, 9, 10)
Sensor type		PIN photo-voltaic (PV) silicon hybrids for 0.4-1.0 µm HgCdTe PV detector hybrid for 1.2-10 µm photo-conductive (PC) detector for >10 µm	photovoltaic (3.74 µm) and photoconductive (10.85 ,12 µm) HgCdTe detectors custom photovoltaic (PV) silicon detectors for VIS-NIR	monolithic Complementary Metal Oxide Semiconductor (CMOS) detectors for VNIR (MCT) detectors hybridised on a CMOS read-out circuit for SWIR
Imaging mode		Whiskbroom	Whiskbroom	Pushbroom
Daytime/nighttime imagery		Daytime and nighttime	Daytime (all bands) and nighttime (only TIR)	Daytime
Special features				
SNR/NEΔT		B6 SNR 275 B7 SNR 110 B20 NEΔT 0.05 K B21 NEΔT 2 K B22 NEΔT 0.07 K B23 NEΔT 0.07 K B29 NEΔT 0.05 K B30 NEΔT 0.25 K B31 NEΔT 0.05 K B32 NEΔT 0.05 K	VIS-SWIR >20 MWIR NEΔT < 80 mK TIR NEΔT < 50 mK F1 NEΔT < 1 K F2 NEΔT < 0.5 K	S2A, S2B B11 SNR 158, 167 @4 $W/m^2/sr/µm$ B12 SNR 167, 171 @2 $W/m^2/sr/µm$
Cooling		Passive radiative cooler provides cooling to 83K for the 20 infrared spectral bands on two HgCdTe Focal Plane Assemblies (FPAs)	SWIR, and TIR channels are cooled	The SWIR focal plane is passively thermo-controlled at temperatures below 195 K
Quantisation		12 bits	10 bits	12 bits
Field-of-View		110°	68.5°	20.6°
Swath		2330 km cross track 10 km along track at nadir	1400 km nadir view 740 km along track view	290 km
Saturation			Increased dynamic range in F1 and F2 all S7 BTs above 305 K are known to present non-linear behaviour as the values are beyond the nominal limits of the detector and related radiometric calibration performance.	The saturation level of 255 digital counts correspond to a level of 3558 for L1C products or 2000 for L2A products (0.3558 and 0.2 in reflectance value respectively.
Gas flares in images		Little visible	Partly visible, but no saturation	Well visible, but saturated
Application in gas flares research until now		Detection and parametrisation	Detection and parametrisation	

BIROS

- Soszynska, Agnieszka und Fischer, Christian und Säuberlich, Thomas und Bucher, Tilman und Pless, Sebastian und Halle, Winfried und Borch, Jörg und Otremba, Frank und Reulke, Ralf (2020) Challenges in Remote Sensing of Gas Flares using Infrared Aerial Imagery. 40. Wissenschaftlich- Technische Jahrestagung der DGPF, Stuttgart. ISSN 0942-2870
- Soszynska, Agnieszka und Säuberlich, Thomas und Fischer, Christian und Borch, Jörg und Otremba, Frank und Reulke, Ralf (2019) Analysis of the gas flare flame with IR cameras. In: Proceedings of SPIE - The International Society for Optical Engineering. SPIE Digital Library. SPIE Remote Sensing 2019, Strasbourg.
- Soszynska, Agnieszka (2018) FireBIRD Mission Data for Gas Flaring Analysis. Lecture Notes in computer Science. Springer. ISBN 978-3-319-92752-7.
- Soszynska, Agnieszka und Fischer, Christian und Lorenz, Eckehard und Reulke, Ralf (2017) The Contribution of the Earth Observation to the Monitoring of Gas Flaring. 37th EARSeL Symposium 2017, 27.-30. Juni 2017, Prag, Tschechien
- Glasmann, Felix (in press) The FireBIRD Mission: Potential for the Detection of Gas Flaring. Master thesis at the University of Würzburg, Institute of Geography and Geology.
- Ruecker, Gernot, et al. "Detection and characterization of small hot fires: Comparing FireBird, BIRD, S-NPP VIIRS and MODIS capacities over gas flares." EGUGA (2016): EPSC2016-15092.

LANDSAT-8

- Schroeder, Wilfrid, et al. "Active fire detection using Landsat-8/OLI data." Remote sensing of environment 185 (2016): 210-220.
- Chowdhury, Subir, et al. "Daytime gas flare detection using Landsat-8 multispectral data." 2014 IEEE Geoscience and Remote Sensing Symposium. IEEE, 2014.
- Kochergin, G. A., M. A. Kupriyanov, and Yu M. Polishchuk. "The use of landsat 8 space images for rapid assessment of total flaring volumes of associated gas in the oil-producing territory." Sovremennye problemy distantsionnogo zondirovaniya Zemli iz kosmosa 14 (2017): 47-55.
- Liu, Yongxue, et al. "Automatic extraction of offshore platforms using time-series Landsat-8 Operational Land Imager data." Remote Sensing of Environment 175 (2016): 73-91.
- Anejionu, Obinna Chukwubuikem Diony, George Alan Blackburn, and J. Duncan Whyatt. "Satellite survey of gas flares: development and application of a Landsat-based technique in the Niger Delta." International Journal of Remote Sensing 35.5 (2014): 1900-1925.
- Sofan, Parwati, et al. "Assessment of VIIRS 375 m active fire using tropical peatland combustion algorithm applied to Landsat-8 over Indonesia's peatlands." International Journal of Digital Earth (2020): 1-22.
- Kumar, Sanath Sathyachandran, and David P. Roy. "Global operational land imager Landsat-8 reflectance-based active fire detection algorithm." International Journal of Digital Earth 11.2 (2018): 154-178.
- Lee, Ruiwen, and Christopher Small. "Detection and temperature estimation of gas flares with nocturnal Landsat OLI." (2019).
- Fisher, Daniel, and Martin J. Wooster. "Shortwave IR adaption of the mid-infrared radiance method of fire radiative power (FRP) retrieval for assessing industrial gas flaring output." Remote Sensing 10.2 (2018): 305.
- Peremitina, T. O., et al. "Remote monitoring of associated petroleum gas flaring in oilfields of Western Siberia." AIP Conference Proceedings. Vol. 2051. No. 1. AIP Publishing LLC, 2018.
- Zhizhin, M. N., et al. "Nightfire: Sub-pixel Pyrometry of Nighttime Combustion Sources with Suomi NPP and Landsat 8." AGUFM 2014 (2014): A51B-3044.
- Anejionu, Obinna CD. "Satellite Mapping of Gas Flares in the Niger Delta."

VIIRS

- Elvidge, Christopher D., et al. "Methods for global survey of natural gas flaring from visible infrared imaging radiometer suite data." Energies 9.1 (2016): 14.
- Fisher, Daniel, and Martin J. Wooster. "Shortwave IR adaption of the mid-infrared radiance method of fire radiative power (FRP) retrieval for assessing industrial gas flaring output." Remote Sensing 10.2 (2018): 305.
- Zhizhin, M. N., et al. "Nightfire: Sub-pixel Pyrometry of Nighttime Combustion Sources with Suomi NPP and Landsat 8." AGUFM 2014 (2014): A51B-3044.
- Faruolo, Mariapia, et al. "The VIIRS-Based RST-FLARE Configuration: The Val d'Agri Oil Center Gas Flaring Investigation in Between 2015–2019." Remote Sensing 12.5 (2020): 819.
- Brandt, Adam R. "Accuracy of satellite-derived estimates of flaring volume for offshore oil and gas operations in nine countries." Environmental Research Communications 2.5 (2020): 051006.
- Facchinelli, Francesco, et al. "Unburnable and Unleakable Carbon in Western Amazon: Using VIIRS Nightfire Data to Map Gas Flaring and Policy Compliance in the Yasuní Biosphere Reserve." Sustainability 12.1 (2020): 58.
- Mordvin, Egor Yu, Anatoly A. Lagutin, and Maksim S. Trishin. "Monitoring Of natural gas flaring in the territory of western Siberia with the use of the visible and near infrared channel readings of VIIRS/SNPP at night-Time." CEUR Workshop Proceedings. Vol. 2033. 2017.
- Lagutin, Anatoly A., et al. "Estimation of Natural Gas Flaring Volume at the Western Siberia Flares using Satellite Night-Time Data in the Visible and Near-Infrared Range." CEUR Workshop Proceedings. Vol. 2534. 2020.
- Elvidge, Christopher D., et al. "VIIRS night-time lights." International Journal of Remote Sensing 38.21 (2017): 5860-5879.
- Zhang, Xiaodong, et al. "Quantifying gas flaring CH4 consumption using VIIRS." Remote Sensing 7.8 (2015): 9529-9541.
- Sharma, Ambrish, Jun Wang, and Elizabeth M. Lennartson. "Intercomparison of MODIS and VIIRS fire products in Khanty-Mansiysk Russia: Implications for characterizing gas flaring from space." Atmosphere 8.6 (2017): 95.
- Elvidge, Christopher D., et al. "What is so great about nighttime VIIRS data for the detection and characterization of combustion sources." Proceedings of the Asia-Pacific Advanced Network 35.0 (2013): 33.
- Elvidge, Christopher D., et al. "Extending nighttime combustion source detection limits with short wavelength VIIRS data." Remote Sensing 11.4 (2019): 395.
- Polivka, Thomas N., et al. "Improving nocturnal fire detection with the VIIRS day–night band." IEEE Transactions on Geoscience and Remote Sensing 54.9 (2016): 5503-5519.
- Elvidge, Christopher D., et al. "Supporting international efforts for detecting illegal fishing and GAS flaring using VIIRS." 2017 IEEE International Geoscience and Remote Sensing Symposium (IGARSS). IEEE, 2017.
- Baugh, K. "Characterization of Gas Flaring in North Dakota using the Satellite Data Product, VIIRS Nightfire." AGUFM 2015 (2015): A23N-05.
- Franklin, Meredith, et al. "Characterizing flaring from unconventional oil and gas operations in south Texas using satellite observations." Environmental science & technology 53.4 (2019): 2220-2228.
- Ruecker, Gernot, et al. "Detection and characterization of small hot fires: Comparing FireBird, BIRD, S-NPP VIIRS and MODIS capacities over gas flares." EGUGA (2016): EPSC2016-15092.
- Sharma, Ambrish. "Evaluation of VIIRS Nightfire Product and Comparison with MODIS and VIIRS Active Fire Products in a Russian Gas Flaring Region." (2019).

MODIS

- Fisher, Daniel, and Martin J. Wooster. "Shortwave IR adaption of the mid-infrared radiance method of fire radiative power (FRP) retrieval for assessing industrial gas flaring output." Remote Sensing 10.2 (2018): 305.
- Faruolo, Mariapia, et al. "On the potential of the RST-FLARE algorithm for gas flaring characterization from space." Sensors 18.8 (2018): 2466.
- Anejionu, Obinna CD. "Satellite Mapping of Gas Flares in the Niger Delta."
- Sharma, Ambrish, Jun Wang, and Elizabeth M. Lennartson. "Intercomparison of MODIS and VIIRS fire products in Khanty-Mansiysk Russia: Implications for characterizing gas flaring from space." Atmosphere 8.6 (2017): 95.
- Ruecker, Gernot, et al. "Detection and characterization of small hot fires: Comparing FireBird, BIRD, S-NPP VIIRS and MODIS capacities over gas flares." EGUGA (2016): EPSC2016-15092.
- Sharma, Ambrish. "Evaluation of VIIRS Nightfire Product and Comparison with MODIS and VIIRS Active Fire Products in a Russian Gas Flaring Region." (2019).
- Anejionu, Obinna CD, G. Alan Blackburn, and J. Duncan Whyatt. "Detecting gas flares and estimating flaring volumes at individual flow stations using MODIS data." Remote Sensing of Environment 158 (2015): 81-94.
- Oom, Duarte, and José MC Pereira. "Exploratory spatial data analysis of global MODIS active fire data." International Journal of Applied Earth Observation and Geoinformation 21 (2013): 326-340.
- Kumar, Sanath Sathyachandran, Joshua J. Picotte, and Birgit Peterson. "Prototype downscaling algorithm for MODIS satellite 1 km daytime active fire detections." Fire 2.2 (2019): 29.
- Giglio, Louis, Wilfrid Schroeder, and Christopher O. Justice. "The collection 6 MODIS active fire detection algorithm and fire products." Remote Sensing of Environment 178 (2016): 31-41.
- Anejionu, O., Alan Blackburn, and Duncan Whyatt. "Remote mapping of gas fl ares in the Niger Delta with MODIS imagery." Earsel Special Research Forum dedicated to Remote Sensing for Developing Countries. Matera, Italy. Vol. 5. 2013.

SLSTR

- Fisher, Daniel, and Martin J. Wooster. "Multi-decade global gas flaring change inventoried using the ATSR-1, ATSR-2, AATSR and SLSTR data records." Remote Sensing of Environment 232 (2019): 111298.
- Caseiro, Alexandre, et al. "Gas flaring activity and black carbon emissions in 2017 derived from Sentinel-3A SLSTR." Earth Syst. Sci. Data Discuss 10 (2019).
- Caseiro, Alexandre, et al. "A methodology for gas flaring detection and characterisation using SLSTR." Remote Sens 10 (2018): 1118.
- Caseiro, Alexandre, et al. "Persistent hot spot detection and characterisation using SLSTR." Remote Sensing 10.7 (2018): 1118.
- Di Erasmo, Daniele, et al. "Utilisation of the GMES Sentinel satellites for off-shore platform oil spills and gas flaring monitoring." EGUGA (2013): EGU2013-9880.
- Caseiro, Alexandre, et al. "Gas flare characterisation with Sentinel-3." EGUGA (2017): 18314.
- Caseiro, Alexandre, et al. "Deriving a relationship between the radiative power and the SWIR radiance for Gas Flares." EGUGA (2016): EPSC2016-9176.

B Theoretical signal of a gas flare in spectral bands

BIROS				
GSD	GSD	350	m	
GSD^2	GSD^2	122500	m^2	
$\Delta\lambda$	Spectral range 3.4-4.2µm	8.00E-07	m	
		0.8	µm	

Flame				
τ	Atmospheric transmittance	0.7	mid-latitude summer	
LHV_{fuel}	Calorific value of methane	50	MJ/kg	
		50000000	J/kg	
χ	Combustion efficiency	0.9	1	
ρ	Proportion of energy radiated	0.07	1	
$\dot{m}$	Gas flow	2	t/h	
		0.556	kg/s	
s	Staggering correction factor	0.250	1	
$E_{\dot{m}}$	Radiated energy per gas flow	1.75E+06	W	$E_{\dot{m}} = H_s * \chi * \rho * \dot{m}$
$E_{\dot{m},GSD^2}$	Portion of energy in a given GSD^2	14.286	W/m^2	$E_{\dot{m},\,GSD} = \frac{E_{\dot{m}}}{GSD^2}$
$\psi(\lambda,\Delta\lambda,T)$	Proportion of radiation recorded in the spectral band for 1600 K	0.1069	1	$\psi = \frac{L_{\lambda_0 \ldots \lambda_n, T}}{L_{0.1 \ldots 20\mu m, T}}$
Φ	Spectral flux	1.91	$W/m^2/\mu m$	$\Phi = \frac{E_{\dot{m},GSD} * \psi}{\Delta\lambda}$
$L_{at\ sensor}$	Spectral radiance of a flame recorded in the band	0.106	$W/sr/m^2/\mu m$	$L_{flame} = \frac{\Phi}{4\pi sr} * \tau * \frac{1}{s}$

LANDSAT-8				
GSD	GSD	30	m	
GSD^2	GSD^2	900	m^2	
Δλ	Spectral range 1.57-1.65μm	8.00E-08	m	
		0.08	μm	

Flame				
τ	Atmospheric transmittance	0.97	mid-latitude summer	
LHV_{fuel}	Calorific value of methane	50	MJ/kg	
		50000000	J/kg	
χ	Combustion efficiency	0.9	1	
ρ	Proportion of energy radiated	0.07	1	
$\dot{m}$	Gas flow	2	t/h	
		0.556	kg/s	
s	Staggering correction factor	0.250	1	
$E_{\dot{m}}$	Radiated energy per gas flow	1.75E+06	W	$E_{\dot{m}} = H_s * \chi * \rho * \dot{m}$
$E_{\dot{m},GSD^2}$	Portion of energy in a given GSD^2	1944.444	W/m^2	$E_{\dot{m},\,GSD} = \frac{E_{\dot{m}}}{GSD^2}$
ψ(λ,Δλ,T)	Proportion of radiation recorded in the spectral band for 1600 K	0.048	1	$\psi = \frac{L_{\lambda_0 \ldots \lambda_n, T}}{L_{0.1 \ldots 20\mu m, T}}$
Φ	Spectral flux	1166.67	$W/m^2/\mu m$	$\Phi = \frac{E_{\dot{m},GSD} * \psi}{\Delta\lambda}$
$L_{at\ sensor}$	Spectral radiance of a flame recorded in the band	180.110	$W/sr/m^2/\mu m$	$L_{flame} = \frac{\Phi}{4\pi sr} * \tau * \frac{1}{s}$

LANDSAT-8				
GSD	GSD	30	m	
GSD^2	GSD^2	900	m^2	
Δλ	Spectral range 2.29-2.11µm	1.80E-07	m	
		0.18	µm	

Flame				
τ	Atmospheric transmittance	0.97	mid-latitude summer	
LHV_{fuel}	Calorific value of methane	50	MJ/kg	
		50000000	J/kg	
χ	Combustion efficiency	0.9	1	
ρ	Proportion of energy radiated	0.07	1	
$\dot{m}$	Gas flow	2	t/h	
		0.556	kg/s	
s	Staggering correction factor	0.250	1	
$E_{\dot{m}}$	Radiated energy per gas flow	1.75E+06	W	$E_{\dot{m}} = H_s * \chi * \rho * \dot{m}$
$E_{\dot{m},GSD^2}$	Portion of energy in a given GSD^2	1944.444	W/m^2	$E_{\dot{m},\,GSD} = \frac{E_{\dot{m}}}{GSD^2}$
ψ(λ,Δλ,T)	Proportion of radiation recorded in the spectral band for 1600 K	0.048	1	$\psi = \frac{L_{\lambda_0 \ldots \lambda_n, T}}{L_{0.1 \ldots 20\mu m, T}}$
Φ	Spectral flux	518.52	$W/m^2/\mu m$	$\Phi = \frac{E_{\dot{m},GSD} * \psi}{\Delta\lambda}$
$L_{at\ sensor}$	Spectral radiance of a flame recorded in the band	80.049	$W/sr/m^2/\mu m$	$L_{flame} = \frac{\Phi}{4\pi sr} * \tau * \frac{1}{s}$

SLSTR				
GSD	GSD	500	m	
GSD²	GSD²	250000	m²	
Δλ	Spectral range	6E-08	m	
	1.58-1.64µm	0.06	µm	

Flame				
τ	Atmospheric transmittance	0.98	mid-latitude summer	
LHV_{fuel}	Calorific value of methane	50	MJ/kg	
		50000000	J/kg	
χ	Combustion efficiency	0.9	1	
ρ	Proportion of energy radiated	0.07	1	
$\dot{m}$	Gas flow	2	t/h	
		0.556	kg/s	
s	Staggering correction factor	1.000	1	
$E_{\dot{m}}$	Radiated energy per gas flow	1.75E+06	W	$E_{\dot{m}} = H_s * \chi * \rho * \dot{m}$
$E_{\dot{m},GSD^2}$	Portion of energy in a given GSD²	7.000	W/m²	$E_{\dot{m},GSD} = \frac{E_{\dot{m}}}{GSD^2}$
ψ(λ,Δλ,T)	Proportion of radiation recorded in the spectral band for 1600 K	0.0211	1	$\psi = \frac{L_{\lambda_0 \ldots \lambda_n, T}}{L_{0.1 \ldots 20\mu m, T}}$
Φ	Spectral flux	2.46	W/m²/µm	$\Phi = \frac{E_{\dot{m},GSD} * \psi}{\Delta\lambda}$
$L_{at\ sensor}$	Spectral radiance of a flame recorded in the band	0.384	W/sr/m²/µm	$L_{flame} = \frac{\Phi}{4\pi sr} * \tau * \frac{1}{s}$

SLSTR				
GSD	GSD	500	m	
GSD^2	GSD^2	250000	m^2	
Δλ	Spectral range	5E-08	m	
	2.23-2.28µm	0.05	µm	

Flame				
τ	Atmospheric transmittance	0.94	mid-latitude summer	
LHV_{fuel}	Calorific value of methane	50	MJ/kg	
		50000000	J/kg	
χ	Combustion efficiency	0.9	1	
ρ	Proportion of energy radiated	0.07	1	
$\dot{m}$	Gas flow	2	t/h	
		0.556	kg/s	
s	Staggering correction factor	1.000	1	
$E_{\dot{m}}$	Radiated energy per gas flow	1.75E+06	W	$E_{\dot{m}} = H_s * \chi * \rho * \dot{m}$
$E_{\dot{m},GSD^2}$	Portion of energy in a given GSD^2	7.000	W/m^2	$E_{\dot{m},GSD} = \frac{E_{\dot{m}}}{GSD^2}$
ψ(λ,Δλ,T)	Proportion of radiation recorded in the spectral band for 1600 K	0.0164	1	$\psi = \frac{L_{\lambda_0 \ldots \lambda_n, T}}{L_{0.1 \ldots 20\mu m, T}}$
Φ	Spectral flux	2.30	$W/m^2/\mu m$	$\Phi = \frac{E_{\dot{m},GSD} * \psi}{\Delta\lambda}$
$L_{at\ sensor}$	Spectral radiance of a flame recorded in the band	0.343	$W/sr/m^2/\mu m$	$L_{flame} = \frac{\Phi}{4\pi sr} * \tau * \frac{1}{s}$

SLSTR				
GSD	GSD	1000	m	
GSD²	GSD²	1000000	m²	
Δλ	Spectral range	4.00E-07	m	
	3.54-3.94µm	0.4	µm	

Flame				
τ	Atmospheric transmittance	0.8	mid-latitude summer	
LHV_{fuel}	Calorific value of methane	50	MJ/kg	
		50000000	J/kg	
χ	Combustion efficiency	0.9	1	
ρ	Proportion of energy radiated	0.07	1	
ṁ	Gas flow	2	t/h	
		0.556	kg/s	
s	Staggering correction factor	1.000	1	
$E_{\dot{m}}$	Radiated energy per gas flow	1.75E+06	W	$E_{\dot{m}} = H_s * \chi * \rho * \dot{m}$
$E_{\dot{m},GSD^2}$	Portion of energy in a given GSD²	1.750	W/m²	$E_{\dot{m},GSD} = \frac{E_{\dot{m}}}{GSD^2}$
ψ(λ,Δλ,T)	Proportion of radiation recorded in the spectral band for 1600 K	0.055	1	$\psi = \frac{L_{\lambda_0 \ldots \lambda_n, T}}{L_{0.1 \ldots 20\mu m, T}}$
Φ	Spectral flux	0.24	W/m²/µm	$\Phi = \frac{E_{\dot{m},GSD} * \psi}{\Delta\lambda}$
$L_{at\ sensor}$	Spectral radiance of a flame recorded in the band	0.031	W/sr/m²/µm	$L_{flame} = \frac{\Phi}{4\pi sr} * \tau * \frac{1}{s}$

MODIS				
GSD	GSD	1000	m	
GSD^2	GSD^2	1000000	m^2	
Δλ	Spectral range	6.00E-08	m	
	3.929-3.989µm	0.06	µm	

Flame				
τ	Atmospheric transmittance	0.93	mid-latitude summer	
LHV_{fuel}	Calorific value of methane	50	MJ/kg	
		50000000	J/kg	
χ	Combustion efficiency	0.9	1	
ρ	Proportion of energy radiated	0.07	1	
$\dot{m}$	Gas flow	2	t/h	
		0.556	kg/s	
s	Staggering correction factor	1.000	1	
$E_{\dot{m}}$	Radiated energy per gas flow	1.75E+06	W	$E_{\dot{m}} = H_s * \chi * \rho * \dot{m}$
$E_{\dot{m},GSD^2}$	Portion of energy in a given GSD^2	1.750	W/m^2	$E_{\dot{m},GSD} = \frac{E_{\dot{m}}}{GSD^2}$
ψ(λ,Δλ,T)	Proportion of radiation recorded in the spectral band for 1600 K	0.0071	1	$\psi = \frac{L_{\lambda_0 \ldots \lambda_n, T}}{L_{0.1 \ldots 20\mu m, T}}$
Φ	Spectral flux	0.21	$W/m^2/\mu m$	$\Phi = \frac{E_{\dot{m},GSD} * \psi}{\Delta\lambda}$
$L_{at\ sensor}$	Spectral radiance of a flame recorded in the band	0.031	$W/sr/m^2/\mu m$	$L_{flame} = \frac{\Phi}{4\pi sr} * \tau * \frac{1}{s}$

VIIRS				
GSD	GSD	375	m	
GSD²	GSD²	140625	m²	
Δλ	Spectral range	3.80E-07	m	
	3.93-3.55µm	0.38	µm	

Flame				
τ	Atmospheric transmittance	0.78	mid-latitude summer	
LHV_{fuel}	Calorific value of methane	55.5	MJ/kg	
		55500000	J/kg	
χ	Combustion efficiency	0.9	1	
ρ	Proportion of energy radiated	0.07	1	
$\dot{m}$	Gas flow	2	t/h	
		0.556	kg/s	
s	Staggering correction factor	1.000	1	
$E_{\dot{m}}$	Radiated energy per gas flow	1.94E+06	W	$E_{\dot{m}} = H_s * \chi * \rho * \dot{m}$
$E_{\dot{m},GSD^2}$	Portion of energy in a given GSD²	13.813	W/m²	$E_{\dot{m},GSD} = \frac{E_{\dot{m}}}{GSD^2}$
ψ(λ,Δλ,T)	Proportion of radiation recorded in the spectral band for 1600 K	0.0523	1	$\psi = \frac{L_{\lambda_0 \ldots \lambda_n, T}}{L_{0.1 \ldots 20\mu m, T}}$
Φ	Spectral flux	1.90	W/m²/µm	$\Phi = \frac{E_{\dot{m},GSD} * \psi}{\Delta\lambda}$
$L_{at\ sensor}$	Spectral radiance of a flame recorded in the band	0.118	W/sr/m²/µm	$L_{flame} = \frac{\Phi}{4\pi sr} * \tau * \frac{1}{s}$

VIIRS				
GSD	GSD	375	m	
GSD²	GSD²	140625	m²	
Δλ	Spectral range	6.00E-08	m	
	1.58-1.64µm	0.06	µm	

Flame				
τ	Atmospheric transmittance	0.91	mid-latitude summer	
LHV_{fuel}	Calorific value of methane	55.5	MJ/kg	
		55500000	J/kg	
χ	Combustion efficiency	0.9	1	
ρ	Proportion of energy radiated	0.07	1	
ṁ	Gas flow	2	t/h	
		0.556	kg/s	
s	Staggering correction factor	1.000	1	
$E_{\dot{m}}$	Radiated energy per gas flow	1.94E+06	W	$E_{\dot{m}} = H_s * \chi * \rho * \dot{m}$
$E_{\dot{m},GSD^2}$	Portion of energy in a given GSD²	13.813	W/m²	$E_{\dot{m},GSD} = \frac{E_{\dot{m}}}{GSD^2}$
ψ(λ,Δλ,T)	Proportion of radiation recorded in the spectral band for 1600 K	0.0211	1	$\psi = \frac{L_{\lambda_0 \ldots \lambda_n, T}}{L_{0.1 \ldots 20\mu m, T}}$
Φ	Spectral flux	4.86	W/m²/µm	$\Phi = \frac{E_{\dot{m},GSD} * \psi}{\Delta\lambda}$
$L_{at\ sensor}$	Spectral radiance of a flame recorded in the band	0.352	W/sr/m²/µm	$L_{flame} = \frac{\Phi}{4\pi sr} * \tau * \frac{1}{s}$

C Calculated gas flow values from BIROS and VIIRS imagery for gas flares in Persian Gulf and North Dakota

Persian Gulf
BIROS MWIR
1200 K

Flare ID	22.07.2018	03.10.2018	06.10.2018	08.10.2018	13.12.2018	25.12.2018	28.12.2018	09.01.2019	11.01.2019	23.01.2019	03.03.2019	14.04.2019	15.04.2019	08.05.2019	10.05.2019
1	2807	nan	nan	nan	6423	3546	6550	5042	2339	3996	1766	3637	3761	3355	4285
2	6138	5827	3450	nan	10122	5120	6265	9416	5613	5318	4730	37272	2193	2857	5528
3	1137	1325	1837	2093	2208	1542	1529	1393	nan	3175	nan	nan	1278	1486	2962
4	15522	8758	4040	8282	9743	8166	5524	12366	5602	2515	4135	10534	6598	8109	12812
5	1801	nan	2151	3872	3976	2837	2006	1892	3054	2597	1199	20756	5067	2760	2796
6	4290	4486	27304	44382	7137	3728	7911	6182	3613	5096	3003	6222	2921	nan	52208
7	7462	8825	5356	10603	8096	7220	8242	9181	9229	4565	10235	5290	4672	7699	20199
8	14546	41172	9657	24769	17147	30879	26128	13315	37840	20242	16695	25383	28068	10447	7683
9	nan	nan	1827	nan	nan	nan	1112	nan	nan	nan	nan	nan	nan	2744	15733
10	nan	nan	1116	nan	1022	38992	1303	nan	1231	nan	nan	nan	1794	2116	nan
11	nan	nan	nan	nan	nan	nan	nan	nan	nan	nan	nan	nan	nan	nan	nan
12	nan	nan	nan	nan	nan	nan	nan	nan	nan	nan	nan	nan	nan	nan	nan
13	nan	nan	1028	nan	1107	nan	1097	1638	nan	nan	nan	1023	nan	1035	1647
14	3087	1763	2360	2461	4231	2379	4494	3585	nan	1802	1823	2016	3894	4509	3940
15	nan	nan	1268	nan	nan	nan	nan	1049	nan	nan	nan	nan	nan	nan	nan
16	1203	3353	2713	3890	3803	2421	2963	3016	nan	2832	2197	1814	2408	2960	2605
17	1596	1323	nan	nan	4750	1437	3580	2371	1102	1513	1770	2279	2734	2598	2023
18	nan	nan	nan	nan	1367	1017	nan	nan	nan	1046	nan	1116	1669	2237	2006
19	nan	nan	1145	nan	1048	nan	1877	nan	nan	1058	1228	1783	2691	5734	1852
20	nan	nan	nan	nan	2115	1792	nan	nan	nan	nan	1617	nan	nan	2189	nan
21	nan	nan	1114	nan	1014	nan	nan	nan	nan	nan	nan	nan	nan	nan	1071
22	nan	nan	nan	nan	nan	nan	nan	nan	nan	nan	1089	nan	nan	nan	nan
23	nan	nan	nan	nan	1293	nan	nan	nan	3386	nan	nan	nan	nan	1187	1449
24	nan	nan	nan	nan	nan	nan	nan	nan	1408	nan	nan	1146	1332	1488	1896
25	18087	nan	8132	nan	4630	4177	2935	4269	5203	1399	4266	7056	3826	8407	1771
26	nan	nan	nan	nan	nan	nan	nan	nan	nan	nan	nan	1033	nan	1213	nan
27	nan	nan	1607	nan	1567	1035	1258	nan	nan	nan	nan	1123	1270	1488	1348
28	nan	nan	nan	nan	nan	nan	nan	nan	nan	nan	nan	nan	nan	nan	18998
29	nan	nan	2138	nan	4732	3001	4411	2585	1390	2841	2239	2172	3993	3541	2422
30	nan	nan	nan	nan	1420	nan	1167	nan	4570	1236	nan	nan	nan	2777	1118
31	nan	nan	nan	nan	1170	nan	nan	nan	nan	nan	nan	nan	nan	nan	nan
32	1521	nan	1096	1243	2155	3743	1795	1114	2633	nan	1781	1329	2340	1612	1429
33	nan	nan	nan	nan	nan	nan	nan	nan	nan	nan	nan	nan	nan	nan	nan
34	nan	nan	1068	nan	1679	1455	1969	1830	nan	1466	nan	nan	nan	nan	nan

Persian Gulf
BIROS MWIR
1200 K

Flare ID	13.05.2019	19.05.2019	12.06.2019	22.06.2019	29.08.2019	07.09.2019	01.10.2019	11.10.2019	13.11.2019	14.11.2019	Median	Mean	Max	Standard deviation
1	5910	8040	3580	2371	8417	2442	3004	4577	10126	5560	3878	4615	10126	2196
2	4087	2094	2097	1981	5018	2274	2923	3006	3533	2693	4408	5815	37272	7042
3	3246	2614	1453	nan	4590	1658	nan	1564	4185	1952	1747	2161	4590	991
4	13717	2548	23588	6163	20434	29802	11454	4021	34728	12679	8758	11274	34728	8212
5	nan	2513	3116	1941	4382	7669	nan	2978	4551	1682	2816	3891	20756	4029
6	nan	1856	1783	nan	5258	2716	3327	nan	8585	2521	4486	9739	52208	13930
7	nan	85036	9825	15062	45369	49367	59828	12005	94218	27254	9527	21868	94218	25698
8	nan	10724	7171	6425	17391	8340	13908	nan	20797	7354	16695	18090	41172	9941
9	2111	nan	1495	nan	1659	nan	33635	nan	3391	1352	1969	6506	33635	10491
10	3291	1232	1506	1461	1175	1303	nan	nan	2506	nan	1382	4289	38992	10008
11	nan	nan	nan	nan	nan	nan	nan	nan	nan	nan	nan	nan	nan	nan
12	nan	nan	nan	nan	nan	nan	nan	nan	1225	nan	1225	1225	1225	nan
13	nan	nan	nan	nan	nan	nan	nan	nan	nan	nan	1097	1225	1647	287
14	3125	2583	2236	1553	3584	3006	1998	2775	6282	3968	2891	3061	6282	1149
15	nan	nan	nan	nan	nan	nan	nan	nan	nan	nan	1159	1159	1268	155
16	6423	4352	8005	1922	6828	nan	2392	nan	35047	6298	2962	4975	35047	6951
17	4198	2941	1258	1214	2739	1023	2055	1014	7669	4633	2055	2514	7669	1589
18	2144	1659	nan	nan	nan	nan	nan	nan	nan	nan	1659	1585	2237	475
19	2960	1524	1788	nan	1228	1136	1110	nan	1759	nan	1642	1870	5734	1176
20	2223	nan	nan	nan	nan	nan	nan	nan	nan	nan	2115	1987	2223	268
21	nan	nan	nan	nan	1406	nan	1513	nan	1665	nan	1260	1297	1665	267
22	1169	nan	nan	nan	1043	nan	nan	nan	1177	nan	1129	1120	1177	65
23	1277	nan	nan	nan	2472	nan	1338	nan	1466	nan	1394	1734	3386	783
24	1789	1823	1114	1251	3558	1008	2637	nan	2397	1209	1448	1718	3558	718
25	5664	4416	4396	8241	6901	7247	8096	3056	14221	10291	5203	6378	18087	3878
26	nan	nan	nan	nan	1237	nan	nan	nan	nan	nan	1213	1161	1237	111
27	1602	1658	1282	1177	1448	nan	1518	nan	1602	nan	1448	1399	1658	199
28	nan	42564	nan	nan	nan	nan	nan	nan	nan	nan	30781	30781	42564	16664
29	2343	2872	2046	2641	3363	1182	2133	2083	4337	3248	2613	2805	4732	949
30	nan	nan	1368	1104	1751	nan	1071	nan	2233	1692	1394	1792	4570	1016
31	nan	nan	nan	nan	nan	nan	nan	nan	nan	1126	1148	1148	1170	31
32	nan	nan	2144	1551	2601	2932	1290	nan	4007	1692	1737	2000	4007	830
33	nan	nan	nan	nan	nan	1249	nan	nan	nan	nan	1249	1249	1249	nan
34	nan	nan	1271	nan	1961	1329	nan	nan	2190	nan	1572	1622	2190	361

Persian Gulf
BIROS MWIR
1600 K

Flare ID	22.07.2018	03.10.2018	06.10.2018	08.10.2018	13.12.2018	25.12.2018	28.12.2018	09.01.2019	11.01.2019	23.01.2019	03.03.2019	14.04.2019	15.04.2019	08.05.2019
1	3803	nan	nan	nan	8702	4805	8874	6831	3169	5414	2393	4928	5095	4545
2	8317	7896	4675	nan	13715	6938	8488	12757	7606	7205	6408	50499	2971	3872
3	1541	1795	2489	2836	2991	2089	2071	1887	1347	4302	nan	1286	1732	2013
4	21031	11866	5474	11221	13201	11064	7485	16755	7590	3407	5603	14272	8939	10986
5	2440	nan	2914	5246	5388	3843	2718	2563	4138	3519	1625	28122	6865	3740
6	5813	6078	36994	60133	9670	5050	10719	8377	4896	6905	4069	8430	3958	nan
7	10110	11957	7257	14366	10970	9783	11167	12440	12504	6185	13867	7168	6331	10431
8	19708	55783	13084	33560	23233	41837	35401	18041	51269	27427	22620	34392	38029	14154
9	nan	nan	2476	nan	1056	nan	1506	nan	1132	nan	nan	1034	nan	3717
10	nan	nan	1512	nan	1384	52830	1765	1206	1668	1127	nan	nan	2431	2867
11	nan	nan	nan	nan	nan	nan	nan	nan	nan	nan	nan	nan	nan	nan
12	nan	nan	nan	nan	nan	nan	nan	nan	nan	nan	nan	nan	nan	1053
13	nan	1118	1393	1105	1500	nan	1486	2219	nan	nan	nan	1387	1019	1402
14	4183	2389	3197	3335	5733	3223	6088	4858	nan	2442	2470	2732	5276	6109
15	nan	1261	1718	1207	nan	nan	1197	1422	nan	nan	nan	nan	nan	nan
16	1629	4543	3676	5270	5152	3280	4015	4086	1304	3837	2977	2457	3263	4010
17	2162	1792	nan	1215	6435	1947	4851	3213	1493	2050	2398	3088	3704	3520
18	nan	1272	1249	nan	1852	1378	1352	1046	nan	1418	1345	1512	2262	3032
19	nan	nan	1552	nan	1420	nan	2543	nan	nan	1433	1664	2416	3646	7768
20	nan	nan	nan	nan	2866	2428	nan	nan	nan	nan	2191	1334	nan	2966
21	nan	nan	1510	nan	1374	nan	nan	nan	nan	nan	nan	nan	nan	nan
22	nan	nan	1218	nan	nan	nan	nan	nan	nan	1163	1476	nan	1089	1014
23	nan	nan	1096	nan	1752	1340	nan	1026	4588	1161	1017	1000	1073	1609
24	nan	nan	1176	nan	nan	nan	nan	nan	1908	nan	nan	1552	1804	2016
25	24506	nan	11018	nan	6274	5659	3977	5784	7050	1895	5780	9561	5183	11390
26	nan	nan	1108	nan	1338	1330	nan	nan	nan	nan	nan	1400	nan	1644
27	1037	nan	2177	nan	2124	1402	1704	1206	1127	1302	1090	1522	1720	2017
28	nan	nan	nan	nan	nan	nan	nan	nan	nan	nan	nan	nan	nan	nan
29	nan	nan	2897	nan	6411	4066	5977	3502	1883	3849	3034	2943	5410	4798
30	nan	nan	nan	nan	1923	nan	1581	1342	6192	1674	nan	nan	1045	3763
31	nan	nan	nan	nan	1585	nan	nan	nan	nan	nan	nan	nan	nan	nan
32	2061	1279	1485	1684	2920	5072	2432	1510	3567	1272	2413	1801	3170	2184
33	nan	nan	nan	nan	nan	nan	nan	nan	nan	nan	nan	nan	1032	nan
34	nan	nan	1447	nan	2275	1971	2668	2479	1190	1986	1320	1200	nan	nan

Persian Gulf
BIROS MWIR
1600 K

10.05.2019	13.05.2019	19.05.2019	12.06.2019	22.06.2019	29.08.2019	07.09.2019	01.10.2019	11.10.2019	13.11.2019	14.11.2019	Median	Mean	Max	Standard deviation
5806	8008	10894	4851	3212	11405	3309	4070	6201	13719	7533	5255	6253	13719	2975
7490	5537	2837	2841	2685	6798	3081	3960	4072	4787	3649	5973	7879	50499	9541
4013	4397	3541	1968	nan	6219	2246	nan	2119	5670	2645	2183	2782	6219	1363
17359	18586	3452	31959	8350	27686	40379	15519	5449	47053	17178	11866	15275	47053	11126
3789	nan	3405	4222	2630	5937	10391	nan	4034	6165	2280	3816	5271	28122	5459
70736	nan	2514	2415	1112	7125	3680	4508	nan	11632	3416	5946	12647	70736	18599
27368	nan	nan	13312	20407	61471	66887	81060	16266	nan	36926	12472	21283	81060	21174
10409	nan	14530	9716	8705	23563	11301	18844	nan	28177	9964	22620	24511	55783	13469
21316	2860	nan	2026	nan	2248	1325	45573	nan	4595	1832	2137	6621	45573	12362
1287	4460	1670	2040	1980	1592	1766	1156	1155	3395	nan	1670	4594	52830	11712
nan	nan	nan	nan	nan	nan	nan	nan	nan	nan	nan	nan	nan	nan	nan
nan	nan	nan	nan	nan	1227	nan	nan	nan	1660	nan	1227	1313	1660	313
2231	nan	nan	nan	nan	nan	nan	nan	nan	nan	nan	1398	1486	2231	424
5339	4234	3500	3030	2105	4856	4073	2707	3760	8512	5376	3916	4147	8512	1556
nan	nan	nan	nan	nan	nan	nan	nan	nan	nan	nan	1261	1361	1718	219
3530	8702	5897	10847	2604	9252	nan	3241	nan	47485	8533	4010	6504	47485	9271
2741	5688	3985	1704	1645	3711	1386	2785	1374	10391	6277	2763	3315	10391	2153
2718	2904	2248	nan	nan	nan	nan	nan	nan	1042	nan	1418	1775	3032	683
2510	4011	2065	2422	1251	1664	1539	1504	nan	2384	1279	1864	2393	7768	1552
nan	3012	1183	nan	nan	nan	nan	nan	nan	nan	nan	2428	2283	3012	761
1452	1151	nan	nan	nan	1905	nan	2049	nan	2255	nan	1510	1671	2255	403
nan	1584	nan	nan	nan	1413	nan	1163	nan	1595	nan	1218	1302	1595	219
1964	1730	1162	nan	1282	3350	nan	1813	nan	1986	1249	1311	1678	4588	923
2569	2424	2470	1509	1695	4821	1365	3573	nan	3247	1638	1908	2251	4821	984
2399	7674	5983	5957	11166	9350	9818	10970	4141	19268	13943	7050	8641	24506	5255
nan	nan	nan	1005	nan	1677	nan	nan	nan	nan	nan	1338	1357	1677	249
1827	2171	2246	1737	1595	1961	nan	2057	nan	2170	1079	1720	1680	2246	419
25741	1021	57670	nan	nan	nan	nan	nan	nan	nan	nan	25741	28144	57670	28401
3282	3174	3892	2772	3578	4557	1602	2890	2822	5876	4400	3540	3801	6411	1286
1514	nan	nan	1854	1496	2373	nan	1451	1165	3026	2292	1674	2179	6192	1326
nan	nan	nan	nan	nan	nan	nan	nan	nan	1276	1526	1526	1462	1585	164
1936	nan	1319	2905	2101	3524	3973	1748	nan	5429	2293	2184	2525	5429	1153
nan	nan	nan	nan	nan	nan	1693	1240	nan	1164	nan	1202	1282	1693	287
1029	nan	1059	1722	1116	2657	1801	nan	nan	2968	nan	1761	1806	2968	648

Persian Gulf
BIROS MWIR
1800 K

Flare ID	22.07.2018	03.10.2018	06.10.2018	08.10.2018	13.12.2018	25.12.2018	28.12.2018	09.01.2019	11.01.2019	23.01.2019	03.03.2019	14.04.2019	15.04.2019	08.05.2019
1	4527	nan	nan	nan	10358	5719	10563	8131	3772	6445	2848	5866	6065	5410
2	9900	9398	5565	nan	16325	8258	10103	15185	9053	8577	7628	60110	3537	4608
3	1834	2137	2963	3376	3561	2487	2465	2246	1603	5121	1141	1530	2062	2397
4	25034	14124	6515	13357	15713	13169	8909	19944	9034	4056	6669	16988	10641	13077
5	2904	nan	3469	6245	6413	4575	3235	3051	4925	4189	1934	33474	8171	4451
6	6919	7235	44034	71577	11511	6012	12759	9971	5827	8219	4843	10034	4711	nan
7	12034	14232	8638	17100	13057	11645	13293	14807	14884	7362	16506	8532	7535	12416
8	23459	66400	15574	39947	27655	49800	42138	21474	61026	32646	26925	40937	45267	16848
9	nan	nan	2947	1108	1257	nan	1793	1184	1348	nan	nan	1230	1043	4425
10	nan	1082	1799	1048	1648	62885	2101	1436	1985	1342	1158	1175	2894	3413
11	nan	nan	nan	nan	nan	nan	nan	nan	nan	nan	nan	nan	nan	nan
12	nan	nan	nan	nan	nan	nan	1140	nan	nan	nan	nan	nan	nan	1253
13	nan	1331	1658	1315	1785	nan	1769	2642	nan	nan	nan	1651	1212	1669
14	4979	2844	3805	3969	6824	3837	7247	5782	nan	2907	2940	3252	6280	7271
15	nan	1501	2045	1437	1181	nan	1425	1692	1142	nan	nan	nan	nan	nan
16	1940	5407	4375	6273	6133	3904	4779	4864	1553	4567	3544	2925	3884	4773
17	2573	2133	nan	1446	7660	2318	5774	3825	1778	2441	2854	3676	4409	4190
18	nan	1514	1487	nan	2204	1640	1610	1245	1004	1688	1601	1800	2692	3608
19	nan	1102	1847	1075	1690	1111	3027	nan	nan	1706	1981	2876	4340	9247
20	nan	nan	nan	nan	3411	2890	nan	nan	nan	nan	2608	1588	nan	3531
21	nan	nan	1797	nan	1636	nan	1113	nan	nan	nan	nan	nan	nan	1134
22	nan	nan	1450	nan	1090	1182	1080	nan	nan	1385	1757	1033	1297	1207
23	nan	nan	1305	nan	2086	1595	nan	1221	5461	1382	1210	1190	1277	1915
24	nan	nan	1400	nan	1080	nan	1055	nan	2272	nan	nan	1848	2148	2400
25	29170	nan	13114	nan	7468	6736	4734	6885	8391	2255	6880	11380	6170	13558
26	nan	nan	1318	nan	1593	1583	nan	nan	nan	nan	nan	1667	nan	1956
27	1234	nan	2591	nan	2528	1669	2028	1436	1342	1550	1298	1811	2048	2400
28	nan	nan	nan	nan	nan	nan	nan	nan	nan	nan	nan	nan	nan	1078
29	nan	nan	3449	nan	7631	4839	7114	4169	2242	4582	3611	3504	6439	5711
30	nan	nan	nan	nan	2289	nan	1882	1597	7371	1993	1082	nan	1243	4479
31	nan	nan	nan	nan	1887	nan	nan	nan	nan	nan	nan	nan	nan	nan
32	2453	1522	1768	2005	3476	6037	2895	1797	4246	1514	2873	2144	3773	2599
33	1115	nan	nan	nan	nan	nan	nan	nan	nan	nan	nan	nan	1229	nan
34	nan	nan	1722	nan	2708	2346	3176	2951	1417	2364	1572	1429	nan	1098

Persian Gulf
BIROS MWIR
1800 K

10.05.2019	13.05.2019	19.05.2019	12.06.2019	22.06.2019	29.08.2019	07.09.2019	01.10.2019	11.10.2019	13.11.2019	14.11.2019	Median	Mean	Max	Standard deviation
6911	9532	12967	5774	3823	13575	3939	4844	7381	16331	8967	6255	7443	16331	3541
8916	6591	3377	3382	3196	8092	3667	4714	4847	5698	4343	7110	9378	60110	11357
4777	5234	4215	2343	nan	7402	2673	nan	2523	6750	3148	2523	3217	7402	1648
20663	22123	4109	38042	9939	32955	48064	18473	6486	56009	20448	14124	18182	56009	13244
4510	nan	4053	5025	3131	7067	12369	nan	4802	7339	2713	4542	6275	33474	6498
84198	nan	2993	2875	1324	8480	4381	5366	nan	13846	4067	7077	15054	84198	22138
32577	nan	nan	15846	24291	73170	79617	96488	19362	nan	43954	14845	25334	96488	25204
12391	nan	17296	11565	10362	28047	13451	22430	nan	33540	11860	26925	29176	66400	16033
25373	3404	1180	2411	nan	2676	1577	54246	nan	5469	2181	1987	6381	54246	13188
1531	5308	1988	2429	2357	1895	2102	1376	1375	4041	1016	1847	4558	62885	12466
nan	nan	nan	nan	nan	nan	nan	nan	nan	nan	nan	nan	nan	nan	nan
1142	nan	1119	nan	nan	1461	nan	nan	nan	1976	nan	1197	1348	1976	333
2656	1099	nan	nan	nan	nan	nan	nan	nan	1099	1095	1651	1614	2656	527
6355	5040	4166	3607	2505	5780	4848	3222	4475	10132	6399	4662	4936	10132	1852
nan	nan	nan	nan	nan	nan	nan	nan	nan	nan	nan	1437	1489	2045	309
4202	10358	7019	12911	3100	11012	nan	3858	nan	56522	10157	4773	7742	56522	11035
3263	6770	4743	2029	1958	4417	1650	3315	1636	12369	7472	3289	3946	12369	2563
3235	3457	2676	nan	nan	nan	nan	nan	nan	1241	nan	1664	2044	3608	833
2987	4774	2458	2883	1489	1980	1832	1790	1158	2837	1522	1914	2532	9247	1798
nan	3586	1408	nan	nan	nan	nan	nan	nan	nan	nan	2890	2717	3586	906
1728	1370	1098	nan	nan	2267	nan	2439	1066	2684	1179	1503	1626	2684	572
1172	1885	1032	nan	nan	1682	nan	1384	nan	1899	1035	1252	1348	1899	306
2337	2059	1384	nan	1526	3988	nan	2158	1096	2364	1487	1526	1949	5461	1088
3058	2886	2940	1797	2018	5738	1625	4253	1060	3865	1950	2083	2411	5738	1230
2856	9134	7121	7090	13291	11130	11687	13057	4929	22935	16597	8391	10286	29170	6255
nan	nan	nan	1196	nan	1996	nan	nan	nan	nan	nan	1593	1616	1996	297
2175	2584	2674	2068	1898	2335	nan	2448	nan	2583	1284	2048	1999	2674	499
30639	1215	68646	nan	nan	nan	nan	nan	nan	nan	nan	15927	25395	68646	32011
3906	3779	4633	3300	4259	5424	1907	3440	3359	6994	5238	4214	4524	7631	1531
1803	nan	nan	2207	1781	2824	nan	1728	1387	3601	2728	1937	2500	7371	1571
nan	nan	nan	nan	nan	1128	nan	nan	nan	1519	1816	1668	1587	1887	346
2305	nan	1570	3458	2501	4195	4729	2080	nan	6462	2729	2599	3006	6462	1373
nan	nan	nan	nan	1090	nan	2015	1476	nan	1385	nan	1307	1385	2015	343
1225	nan	1261	2050	1328	3163	2143	1055	nan	3533	nan	1886	2030	3533	804

Persian Gulf
BIROS MWIR
2226 K

Flare ID	22.07.2018	03.10.2018	06.10.2018	08.10.2018	13.12.2018	25.12.2018	28.12.2018	09.01.2019	11.01.2019	23.01.2019	03.03.2019	14.04.2019	15.04.2019	08.05.2019
1	6573	nan	1381	nan	15041	8304	15338	11807	5478	9359	4136	8518	8807	7856
2	14375	13647	8080	nan	23705	11991	14671	22050	13146	12454	11077	87285	5135	6692
3	2663	3103	4302	4902	5170	3611	3580	3261	2328	7435	1656	2222	2994	3480
4	36351	20509	9461	19395	22816	19123	12937	28960	13119	5889	9684	24668	15451	18989
5	4217	nan	5037	9068	9312	6643	4698	4430	7152	6083	2808	48606	11865	6464
6	10047	10506	63941	nan	16715	8729	18527	14478	8462	11934	7032	14570	6841	nan
7	17475	20666	12543	24830	18960	16909	19302	21501	21612	10690	23968	12389	10942	18029
8	34065	96418	22615	58006	40157	72313	61188	31182	88615	47405	39097	59444	65731	24465
9	nan	nan	4280	1609	1825	1267	2603	1719	1957	nan	nan	1787	1514	6425
10	1181	1571	2613	1522	2392	91313	3051	2085	2882	1948	1681	1706	4202	4955
11	nan	nan	nan	nan	nan	nan	nan	nan	nan	nan	nan	nan	nan	nan
12	nan	nan	1220	nan	1135	nan	1656	nan	nan	nan	nan	nan	1409	1820
13	nan	1932	2408	1910	2592	nan	2568	3836	nan	1352	nan	2397	1761	2424
14	7230	4130	5526	5764	9909	5571	10523	8396	nan	4221	4270	4722	9120	10559
15	nan	2179	2970	2086	1714	1128	2069	2457	1659	nan	nan	nan	nan	nan
16	2816	7852	6353	9109	8905	5669	6939	7063	2254	6632	5146	4247	5639	6931
17	3736	3097	1253	2100	11123	3365	8385	5554	2581	3544	4144	5338	6403	6084
18	nan	2198	2159	nan	3201	2382	2338	1808	1458	2451	2324	2614	3909	5240
19	1081	1601	2682	1560	2454	1613	4395	nan	1061	2477	2876	4177	6302	13427
20	nan	nan	1012	nan	4953	4196	1106	nan	1012	nan	3787	2306	nan	5127
21	nan	nan	2610	nan	2375	nan	1616	1267	nan	nan	nan	1061	1176	1647
22	nan	nan	2105	nan	1582	1717	1568	1117	nan	2011	2551	1500	1883	1752
23	1155	nan	1895	nan	3029	2316	nan	1773	7930	2006	1757	1729	1854	2781
24	nan	nan	2033	nan	1569	nan	1532	nan	3298	nan	1180	2683	3118	3485
25	42357	nan	19043	nan	10844	9782	6874	9997	12185	3275	9990	16525	8959	19688
26	1149	nan	1914	nan	2313	2298	1337	nan	nan	1147	nan	2420	nan	2841
27	1792	nan	3763	nan	3671	2423	2945	2085	1948	2251	1884	2630	2973	3486
28	nan	nan	1045	nan	nan	nan	nan	nan	1392	nan	nan	1320	nan	1565
29	nan	nan	5008	nan	11081	7027	10331	6054	3255	6653	5244	5088	9350	8293
30	nan	nan	nan	nan	3324	nan	2732	2319	10703	2893	1571	1141	1805	6503
31	nan	nan	nan	nan	2740	nan	nan	nan	nan	nan	nan	nan	nan	nan
32	3563	2211	2567	2911	5047	8766	4204	2610	6166	2198	4172	3113	5479	3775
33	1620	nan	nan	nan	1413	nan	nan	nan	nan	nan	1041	1356	1784	nan
34	nan	nan	2501	nan	3932	3407	4611	4286	2057	3432	2282	2075	nan	1595

Persian Gulf
BIROS MWIR
2226 K

Flare ID	10.05.2019	13.05.2019	19.05.2019	12.06.2019	22.06.2019	29.08.2019	07.09.2019	01.10.2019	11.10.2019	13.11.2019	14.11.2019	Median	Mean	Max	Standard deviation
1	10035	13841	18829	8385	5552	19712	5719	7034	10718	23713	13021	8807	10398	23713	5394
2	12946	9571	4903	4911	4640	11751	5325	6845	7039	8273	6307	10324	13617	87285	16491
3	6937	7601	6121	3402	nan	10749	3882	nan	3663	9801	4572	3663	4671	10749	2393
4	30004	32124	5967	55240	14433	47853	69793	26824	9418	81329	29692	20509	26401	81329	19231
5	6548	nan	5886	7297	4546	10261	17960	nan	6973	10657	3940	6596	9111	48606	9436
6	nan	nan	4345	4175	1922	12314	6361	7792	nan	20105	5905	9388	12735	63941	13016
7	47304	nan	nan	23009	35272	nan	nan	nan	28115	nan	63824	20666	23544	63824	13088
8	17992	nan	25114	16794	15046	40727	19532	32570	nan	48703	17221	39097	42365	96418	23281
9	36843	4943	1713	3501	1335	3886	2290	78769	1154	7942	3167	2290	8120	78769	17888
10	2224	7708	2886	3526	3422	2751	3052	1998	1996	5868	1475	2613	6400	91313	17754
11	nan	nan	nan	nan	nan	nan	nan	nan	nan	nan	nan	nan	nan	nan	nan
12	1658	1435	1624	1412	1134	2121	nan	1065	nan	2869	1030	1424	1542	2869	494
13	3856	1596	1336	nan	1201	1312	nan	1451	1369	1596	1590	1761	2026	3856	789
14	9228	7318	6049	5237	3638	8393	7040	4678	6498	14712	9293	6769	7168	14712	2690
15	nan	nan	nan	nan	nan	nan	nan	nan	nan	nan	nan	2078	2033	2970	553
16	6102	15041	10192	18748	4501	15991	nan	5602	nan	82074	14748	6931	11242	82074	16024
17	4738	9831	6888	2946	2843	6414	2396	4813	2376	17961	10850	4738	5551	17961	3751
18	4698	5020	3886	nan	nan	nan	nan	nan	nan	1802	1302	2382	2870	5240	1238
19	4338	6933	3569	4187	2162	2875	2660	2599	1682	4120	2210	2671	3460	13427	2601
20	nan	5206	2045	1041	nan	nan	nan	nan	nan	nan	nan	2306	2890	5206	1785
21	2509	1989	1594	1215	1137	3292	nan	3542	1548	3898	1713	1647	2011	3898	888
22	1702	2737	1498	1345	nan	2443	1188	2010	nan	2757	1504	1717	1840	2757	493
23	3394	2989	2009	1208	2216	5790	1281	3133	1592	3432	2160	2084	2610	7930	1569
24	4441	4190	4269	2609	2930	8332	2360	6175	1539	5612	2831	2930	3378	8332	1816
25	4147	13264	10341	10296	19299	16161	16970	18960	7157	33303	24100	12185	14935	42357	9083
26	1008	nan	1241	1737	1268	2898	1347	1326	nan	1170	nan	1342	1713	2898	643
27	3158	3752	3883	3003	2757	3390	1437	3555	1395	3751	1864	2945	2774	3883	813
28	44491	1765	99680	nan	nan	1119	nan	nan	nan	nan	nan	1478	19047	99680	35906
29	5672	5487	6727	4792	6185	7876	2768	4995	4877	10156	7605	6119	6569	11081	2223
30	2618	nan	nan	3204	2586	4101	nan	2509	2014	5229	3961	2732	3483	10703	2290
31	1226	nan	nan	nan	nan	1637	nan	1037	nan	2206	2638	1922	1914	2740	722
32	3347	nan	2280	5021	3632	6091	6867	3021	nan	9383	3963	3775	4365	9383	1994
33	1253	nan	nan	nan	1583	nan	2926	2143	nan	2011	nan	1601	1713	2926	543
34	1779	nan	1830	2976	1929	4592	3112	1532	nan	5130	1388	2501	2866	5130	1189

Persian Gulf
VIIRS I4
1200 K

Flare ID	2018.10.06	2018.10.12	2018.10.12	2018.12.25	2019.03.05	2019.05.13	2019.05.19	2019.06.14	2019.09.08	2019.09.29	2019.11.11	Median	Mean	Max	Standard deviation
1	3676	2343	3109	6338	2740	2589	3805	2792	1442	2427	8076	2792	3576	8076	1945
2	5531	12740	6604	4964	3945	2250	nan	3253	1686	1928	2231	3599	4513	12740	3337
3	1059	1818	2005	1232	nan	nan	1430	1969	1146	2255	1282	1430	1577	2255	438
4	7155	13954	10353	12777	10702	6146	3464	6150	23032	14810	8233	10353	10616	23032	5444
5	2608	3364	3718	12277	1190	2193	3455	1737	nan	3678	1544	2986	3576	12277	3195
6	16462	19214	2872	18548	29448	14038	1127	1644	2555	3581	2293	3581	10162	29448	9744
7	7093	11017	8325	6595	4165	3125	2040	2948	20722	14203	13710	7093	8540	20722	5842
8	26922	25533	12178	21044	16044	5336	5537	4702	4054	17238	4898	12178	13044	26922	8789
9	nan	1253	nan	nan	nan	1091	nan	3667	1647	1040	1659	1450	1726	3667	988
10	nan	1067	nan	17784	1126	1476	nan	1081	1435	nan	1831	1435	3686	17784	6223
11	4869	1684	nan	4125	nan	nan	nan	nan	nan	nan	nan	4125	3559	4869	1666
12	5881	1542	1222	3772	nan	nan	nan	nan	nan	1336	nan	1542	2751	5881	2040
13	2839	1084	1192	5108	nan	nan	nan	nan	1377	1131	nan	1285	2122	5108	1607
14	nan	2272	1652	1542	1316	4166	nan	1523	2392	3456	2273	2272	2288	4166	961
15	2311	nan	nan	nan	nan	1326	nan	1424	nan	nan	nan	1424	1687	2311	542
16	2603	3190	2144	2606	1644	1405	3402	1123	3049	2642	13694	2606	3409	13694	3490
17	1477	nan	nan	2306	2854	1312	3647	1030	1180	1380	5995	1477	2354	5995	1625
18	6152	nan	1159	3168	nan	nan	1588	nan	1780	1300	nan	1684	2525	6152	1917
19	4749	nan	nan	3225	1323	1368	nan	1180	1619	nan	1378	1378	2120	4749	1355
20	5290	1310	nan	1595	1145	1142	nan	nan	1841	1023	1037	1228	1798	5290	1440
21	nan	nan	1216	nan	nan	nan	nan	1214	nan	nan	nan	1215	1215	1216	1
22	nan	nan	1075	4502	1117	1320	nan	1169	nan	nan	nan	1169	1837	4502	1493
23	nan	nan	nan	3196	nan	nan	nan	1551	nan	nan	3222	3196	2656	3222	957
24	nan	nan	nan	nan	nan	1145	nan	1418	nan	2051	1110	1282	1431	2051	436
25	5651	6357	8660	2211	6680	7329	4175	2982	5340	6937	7231	6357	5778	8660	1966
26	1079	1251	1190	nan	nan	nan	nan	nan	nan	nan	nan	1190	1173	1251	88
27	nan	nan	1213	nan	nan	1342	nan	1501	1084	1030	nan	1213	1234	1501	192
28	nan	1294	nan	nan	nan	1376	16596	1728	1083	nan	nan	1376	4415	16596	6813
29	2037	1204	nan	2271	2583	1730	2091	1864	1057	2409	2401	2064	1965	2583	511
30	4180	nan	2384	2896	1041	nan	nan	1269	1646	nan	1145	1646	2080	4180	1152
31	nan	1333	1638	2793	nan	nan	nan	nan	nan	nan	1601	1619	1841	2793	649
32	nan	1293	1337	2368	1266	1759	1068	1817	2865	1585	1376	1481	1673	2865	559
33	nan	nan	nan	nan	nan	nan	nan	nan	1315	nan	nan	1315	1315	1315	nan
34	nan	nan	nan	nan	4174	1081	nan	nan	nan	nan	7724	4174	4327	7724	3324

Persian Gulf
VIIRS I4
1600 K

Flare ID	2018.10.06	2018.10.12	2018.10.12	2018.12.25	2019.03.05	2019.05.13	2019.05.19	2019.06.14	2019.09.08	2019.09.29	2019.11.11	Median	Mean	Max	Standard deviation
1	4958	3160	4193	8549	3696	3492	5133	3766	1945	3273	10893	3766	4824	10893	2624
2	7461	17185	8908	6696	5321	3035	1112	4388	2275	2600	3009	4388	5635	17185	4526
3	1429	2452	2704	1661	nan	1313	1928	2656	1546	3041	1729	1829	2046	3041	614
4	9651	18822	13965	17235	14436	8291	4673	8296	31067	19977	11105	13965	14320	31067	7343
5	3518	4538	5015	16560	1605	2958	4660	2343	nan	4961	2082	4028	4824	16560	4309
6	22206	25917	3874	25019	39722	18936	1520	2218	3447	4831	3093	4831	13708	39722	13143
7	9568	14861	11230	8895	5618	4216	2752	3976	27952	19158	18492	9568	11520	27952	7879
8	36315	34440	16427	28386	21641	7198	7469	6343	5468	23252	6607	16427	17595	36315	11855
9	nan	1690	nan	nan	nan	1471	nan	4947	2222	1403	2238	1956	2328	4947	1332
10	nan	1440	nan	23989	1519	1991	1050	1458	1936	1270	2470	1519	4125	23989	7461
11	6568	2271	1258	5564	nan	1047	nan	1172	1039	1201	nan	1229	2515	6568	2243
12	7933	2079	1649	5088	nan	nan	nan	nan	nan	1802	nan	2079	3710	7933	2752
13	3829	1462	1608	6890	nan	nan	nan	nan	1858	1526	1175	1608	2621	6890	2079
14	nan	3065	2228	2079	1775	5620	nan	2054	3227	4661	3066	3065	3086	5620	1297
15	3117	1156	1148	nan	1070	1788	nan	1921	nan	nan	nan	1472	1700	3117	782
16	3511	4303	2893	3515	2217	1895	4589	1515	4112	3563	18471	3515	4599	18471	4707
17	1993	1080	nan	3111	3850	1769	4919	1390	1592	1861	8087	1927	2965	8087	2170
18	8299	1215	1564	4274	nan	1344	2141	1065	2401	1753	nan	1753	2673	8299	2322
19	6405	nan	1248	4350	1784	1845	nan	1592	2183	1112	1858	1845	2486	6405	1748
20	7135	1768	1054	2151	1545	1541	nan	nan	2483	1380	1398	1545	2273	7135	1873
21	nan	1100	1640	nan	nan	1072	nan	1637	nan	nan	nan	1369	1362	1640	319
22	nan	1075	1450	6073	1507	1781	nan	1577	nan	nan	1157	1507	2089	6073	1774
23	nan	nan	1078	4311	nan	nan	nan	2092	nan	1022	4346	2092	2570	4346	1661
24	nan	nan	nan	nan	1008	1545	1164	1913	nan	2767	1498	1521	1649	2767	632
25	7622	8575	11682	2983	9011	9886	5632	4022	7204	9358	9754	8575	7793	11682	2651
26	1455	1688	1605	1048	nan	nan	nan	nan	nan	nan	nan	1530	1449	1688	284
27	1130	1031	1636	1215	nan	1810	nan	2024	1463	1389	1101	1389	1422	2024	344
28	nan	1745	nan	1056	nan	1855	22386	2330	1461	1082	nan	1745	4560	22386	7874
29	2748	1624	1118	3063	3484	2334	2820	2515	1426	3250	3238	2748	2511	3484	801
30	5638	1286	3215	3906	1404	1090	1186	1711	2220	1225	1544	1544	2220	5638	1453
31	nan	1798	2209	3768	1116	nan	nan	1048	nan	1183	2159	1798	1897	3768	959
32	nan	1744	1803	3194	1708	2372	1440	2451	3864	2138	1856	1997	2257	3864	755
33	nan	nan	nan	nan	nan	nan	nan	nan	1773	nan	nan	1773	1773	1773	nan
34	nan	nan	nan	nan	5630	1458	nan	nan	1181	nan	10419	3544	4672	10419	4339

Persian Gulf
VIIRS I4
1800 K

Flare ID	2018.10.06	2018.10.12	2018.10.12	2018.12.25	2019.03.05	2019.05.13	2019.05.19	2019.06.14	2019.09.08	2019.09.29	2019.11.11	Median	Mean	Max	Standard deviation
1	5893	3755	4984	10160	4392	4151	6101	4476	2312	3890	12946	4476	5733	12946	3118
2	8867	20424	10587	7957	6324	3608	1322	5215	2704	3090	3577	5215	6698	20424	5379
3	1698	2915	3214	1975	nan	1560	2292	3156	1837	3614	2055	2174	2432	3614	730
4	11470	22370	16597	20483	17157	9853	5554	9859	36923	23743	13198	16597	17019	36923	8727
5	4181	5393	5960	19681	1907	3515	5538	2784	1046	5896	2474	4181	5307	19681	5060
6	26391	30802	4604	29734	47209	22505	1807	2636	4096	5741	3676	5741	16291	47209	15620
7	11371	17662	13347	10572	6677	5010	3271	4726	33220	22769	21978	11371	13691	33220	9365
8	43159	40931	19523	33736	25720	8555	8876	7539	6498	27634	7853	19523	20911	43159	14089
9	nan	2008	1001	nan	nan	1749	1016	5879	2640	1668	2660	1879	2328	5879	1566
10	nan	1711	1022	28510	1805	2366	1248	1733	2300	1510	2936	1769	4514	28510	8450
11	7806	2699	1496	6613	nan	1244	nan	1393	1235	1427	nan	1461	2989	7806	2666
12	9428	2471	1959	6047	nan	nan	nan	nan	nan	2141	1012	2306	3843	9428	3237
13	4551	1738	1911	8188	1143	1027	nan	nan	2208	1813	1396	1813	2664	8188	2319
14	nan	3642	2648	2471	2110	6679	nan	2441	3835	5540	3644	3642	3668	6679	1541
15	3704	1374	1364	nan	1271	2125	nan	2283	nan	nan	nan	1750	2020	3704	930
16	4172	5114	3438	4178	2635	2253	5454	1800	4888	4235	21953	4178	5465	21953	5595
17	2369	1283	nan	3697	4575	2103	5846	1652	1892	2212	9611	2290	3524	9611	2579
18	9863	1444	1858	5079	1157	1597	2545	1265	2853	2084	nan	1971	2975	9863	2679
19	7612	nan	1483	5170	2121	2193	nan	1892	2595	1321	2209	2193	2955	7612	2077
20	8480	2101	1253	2557	1836	1831	1176	nan	2951	1640	1662	1834	2549	8480	2154
21	nan	1308	1949	nan	1114	1274	nan	1946	nan	nan	1092	1291	1447	1949	397
22	nan	1278	1723	7218	1791	2117	nan	1875	nan	1040	1375	1757	2302	7218	2017
23	nan	nan	1281	5124	1035	1103	nan	2486	nan	1215	5165	1281	2487	5165	1881
24	nan	nan	1168	nan	1198	1836	1384	2273	1088	3288	1780	1582	1752	3288	743
25	9059	10191	13883	3545	10709	11749	6693	4781	8561	11121	11592	10191	9262	13883	3151
26	1729	2006	1907	1245	nan	nan	nan	nan	nan	1124	nan	1729	1602	2006	396
27	1343	1225	1944	1445	1173	2151	nan	2406	1738	1651	1309	1548	1638	2406	418
28	nan	2074	nan	1255	nan	2205	26606	2770	1736	1286	nan	2074	5419	26606	9358
29	3266	1930	1329	3640	4140	2774	3352	2989	1694	3863	3849	3266	2984	4140	952
30	6701	1528	3821	4643	1668	1295	1409	2034	2638	1456	1836	1836	2639	6701	1727
31	nan	2136	2626	4478	1326	nan	nan	1245	1103	1406	2566	1771	2111	4478	1131
32	nan	2073	2143	3796	2030	2819	1712	2913	4593	2541	2206	2374	2683	4593	897
33	nan	nan	nan	nan	nan	nan	nan	nan	2108	nan	1123	1615	1615	2108	696
34	nan	nan	nan	nan	6692	1733	nan	nan	1403	nan	12383	4212	5553	12383	5156

BIROS				
Flare ID	1200 K	1600 K	1800 K	2226 K
1	11152	15110	17986	26117
2	nan	1221	1454	2111
3	1225	1659	1975	2868
4	2199	2979	3546	5149
5	2861	3877	4615	6701
6	4693	6358	7568	10989
7	4328	5864	6980	10136
8	3228	4374	5206	7560
9	3624	4911	5845	8488
10	1540	2087	2484	3607
11	3723	5045	6005	8720
12	2083	2822	3359	4878
13	1992	2699	3212	4665
14	6354	8610	10248	14881
15	1953	2647	3150	4574
16	6080	8238	9806	14239
17	6800	9214	10967	15925
18	4554	6170	7344	10664
19	6946	9411	11202	16266
20	7260	9836	11708	17001
21	6627	8978	10687	15518
22	5451	7386	8792	12767
23	15355	20804	24764	35959
24	11391	15433	18370	26675
25	nan	1029	1225	1779
26	2821	3821	4549	6605
27	4269	5784	6885	9997
28	3340	4525	5386	7821
29	3349	4538	5401	7843
30	nan	nan	nan	nan
31	nan	nan	nan	1309
32	nan	1230	1464	2125
33	nan	nan	nan	1052
34	nan	1119	1332	1934
35	12668	17164	20431	29667
36	6448	8736	10399	15100
37	3652	4949	5891	8554
38	5176	7013	8348	12122
39	4001	5421	6452	9369
40	13700	18562	22095	32083
41	4960	6720	7999	11616
42	1341	1817	2163	3141
43	2704	3664	4362	6333
44	4278	5796	6899	10018
45	8050	10907	12983	18852
46	9533	12916	15374	22325
47	4411	5977	7114	10330
48	2582	3498	4163	6046
49	3613	4895	5826	8460
50	3362	4555	5422	7873
51	3581	4851	5775	8385
52	4817	6526	7768	11280
53	4035	5466	6507	9448
54	nan	nan	1064	1545
55	nan	1121	1334	1937

VIIRS				
Flare ID	1200 K	1600 K	1800 K	2226 K
1	1370	1848	2197	3186
2	nan	1048	1246	1807
3	6314	8516	10122	14678
4	5744	7748	9208	13353
5	8834	11916	14162	20537
6	4060	5476	6508	9437
7	8698	11732	13943	20220
8	8849	11936	14185	20571
9	21353	28803	34232	49641
10	5412	7300	8676	12581
11	5177	6983	8299	12035
12	1685	2273	2701	3917
13	2136	2881	3424	4966
14	5175	6980	8295	12030
15	5279	7121	8463	12273
16	25733	34711	41252	59823
17	3362	4535	5390	7816
18	3207	4325	5140	7454
19	4191	5653	6719	9743
20	2280	3075	3655	5300
21	26908	36296	43136	62554
22	14845	20024	23798	34512
23	2430	3278	3896	5650
24	8701	11736	13948	20227
25	2768	3733	4437	6434
26	1877	2532	3009	4363
27	3143	4239	5038	7307
28	3225	4351	5171	7498
29	1318	1778	2113	3064
30	nan	nan	nan	1193
31	3464	4672	5552	8052
32	3451	4654	5532	8022
33	4027	5431	6455	9361
34	nan	nan	1027	1489
35	28851	38917	46251	67072
36	3757	5067	6022	8733
37	11497	15508	18431	26728
38	22122	29840	35464	51429
39	1103	1488	1768	2564
40	18374	24784	29455	42715
41	13929	18789	22330	32382
42	3575	4823	5732	8312
43	14844	20023	23797	34509
44	34070	45957	54618	79205
45	21840	29460	35012	50773
46	4208	5676	6746	9783
47	10944	14762	17544	25441
48	2983	4024	4782	6935
49	11574	15612	18555	26907
50	2057	2775	3298	4783
51	4200	5665	6733	9764
52	4099	5530	6572	9530
53	2156	2908	3456	5011
54	2060	2779	3303	4790
55	2506	3381	4018	5827

BIROS				
Flare ID	1200 K	1600 K	1800 K	2226 K
56	1034	1402	1668	2423
57	1032	1398	1664	2416
58	1344	1821	2168	3147
59	2322	3146	3745	5438
60	1905	2582	3073	4462
61	1610	2182	2597	3771
62	1347	1825	2172	3154
63	1632	2211	2631	3821
64	1348	1826	2174	3156
65	3370	4566	5435	7892
66	2152	2916	3471	5040
67	nan	1065	1267	1840
68	nan	nan	nan	nan
69	2650	3590	4273	6205
70	nan	nan	nan	1362
71	nan	1164	1385	2012
72	4119	5580	6642	9645
73	1970	2669	3177	4613
74	nan	nan	nan	1249
75	7542	10218	12163	17662
76	1288	1745	2077	3016
77	1789	2423	2884	4188
78	nan	nan	nan	nan
79	nan	nan	nan	1004
80	nan	1329	1581	2296
81	nan	nan	nan	1281
82	8212	11126	13244	19231
83	7172	9718	11567	16796
84	2690	3644	4338	6299
85	4978	6745	8028	11658
86	2604	3529	4200	6099
87	2228	3018	3593	5217
88	nan	nan	nan	nan
89	nan	nan	nan	nan
90	nan	nan	nan	nan
91	6926	9384	11170	16220
92	3894	5276	6280	9119
93	nan	1164	1385	2011
94	nan	1254	1493	2168
95	nan	nan	nan	nan
96	nan	nan	nan	1094
97	nan	nan	nan	1253
98	6554	8880	10570	15349
99	3888	5267	6270	9104
100	nan	nan	nan	nan

VIIRS				
Flare ID	1200 K	1600 K	1800 K	2226 K
56	1481	1997	2374	3442
57	3098	4179	4967	7202
58	2109	2845	3381	4903
59	18674	25189	29937	43413
60	9863	13304	15811	22929
61	5026	6779	8057	11684
62	3372	4549	5406	7840
63	3292	4440	5277	7653
64	31423	42386	50374	73051
65	31292	42209	50164	72746
66	6665	8991	10685	15496
67	3668	4948	5880	8527
68	1083	1461	1737	2519
69	14674	19793	23524	34113
70	1090	1470	1747	2534
71	4863	6559	7796	11305
72	7120	9605	11415	16553
73	7303	9851	11708	16978
74	7468	10073	11972	17361
75	12636	17044	20256	29375
76	8762	11819	14047	20370
77	3386	4568	5428	7872
78	nan	nan	nan	nan
79	nan	nan	nan	1117
80	6938	9358	11122	16128
81	4917	6633	7883	11432
82	21458	28944	34400	49885
83	23170	31254	37144	53865
84	14215	19175	22789	33047
85	12226	16492	19600	28423
86	1293	1745	2073	3007
87	nan	nan	nan	1392
88	nan	nan	nan	1433
89	1248	1684	2001	2902
90	nan	1134	1348	1955
91	12087	16304	19377	28099
92	1859	2507	2980	4322
93	nan	nan	1123	1628
94	2031	2740	3256	4722
95	1447	1952	2320	3364
96	1122	1513	1798	2608
97	1351	1823	2166	3142
98	28875	38949	46290	67128
99	6603	8906	10585	15350
100	nan	1329	1580	2291

Kurzfassung

Bei der Förderung von Erdöl wird auch Erdgas gefördert, das oft abgefackelt wird. Das Abfackeln von Erdgas ist sehr schädlich für die Umwelt und die Bewohner einer Umgebung in der Gas abgefackelt wird. Demzufolge ist die Reduktion dieses Prozesses eine wichtige Aufgabe, die durch Monitoring von Gasfackeln unterstützt werden kann. Dies gelingt am besten durch Fernerkundung mit Satellitendaten.

Die vorliegende Dissertation widmet sich der Parametrisierung von Gasfackeln anhand von Infrarot-Satellitenaufnahmen. Eine Gruppe von Sensoren wurde verglichen, woraus optimale Eigenschaften eines Sensors zur Gasfackelanalyse abgeleitet wurden. Danach wurde ein Modell zur Berechnung des Gasflusses aus Infrarot-Satellitenaufnahmen entwickelt. Das vorgeschlagene Modell basiert auf der Physik der Verbrennung und wird von Teilmodellen zur Berechnung der Verbrennungsparameter unterstütz. Dadurch werden Prozesse mitberücksichtigt, die bisher in der Gasfackelforschung wenig adressiert wurden. Eine Experimentenreihe erlaubte eine Charakterisierung der Flamme in Bezug auf sich verändernde Bedingungen, z.B. Gasfluss. Zusätzlich wurde das Modell durch die Experimente validiert. Die abgeleitete Genauigkeit der Gasflusswerte ist verhältnismäßig hoch, insbesondere wenn man die Komplexität und Variabilität einer Gasflamme berücksichtigt.

Durch Analysieren des Sensordesigns des BIROS Sensors aus der FireBIRD-Mission des Deutschen Zentrums für Luft- und Raumfahrt konnten die Sensorparameter charakterisiert und deren Einfluss auf ein abgeleitetes Bildprodukt quantifiziert werden. Die Fähigkeit des Modells mit unterschiedlichen Sensordaten zu funktionieren, wurde geprüft durch einen Vergleich der geschätzten Gasflusswerte aus Daten von zwei Satellitensensoren. Die verglichenen Gasflusswerte sind sehr ähnlich, was die Fähigkeit des Models mit unterschiedlichen Daten gut zu funktionieren, bestätigt. Das vorgeschlagene Model hat Potenzial, das globale Monitoring von Gasfackeln zu verbessern.

Summary

Routine gas flaring is harmful to the environment and people living in the vicinity of gas flares. Therefore, the reduction of this process is an important task, which can be supported by monitoring of gas flares, which can be done with remote sensing techniques.

The presented work is devoted to the monitoring of gas flaring. The first aspect of the analysis was to compare a group of sensors with respect to the features crucial for gas flaring analysis. A set of requirements for an optimal sensor for this purpose was proposed. Next, a model for calculating gas flow from infrared satellite imagery was proposed, which relies on several other models, allowing to derive the values of the combustion parameters. By modelling these parameters in a gas flare, processes are accounted for that were scarcely addressed in the research conducted on gas flaring until now. To describe the characteristics of the flame coming from combustion in a flare, an experimental series was designed and conducted.

The experimental series allowed to characterise the flame with respect to changing conditions, e.g. gas flow. Thus, the characteristics derived from the experiments could be included in the model for gas flow calculation. Additionally, the experiments served as a mean to validate the model. The accuracy of the derived gas flow values is relatively high, especially considering the variability of a gas flare flame. One design goal of the model for gas flow calculation was to ensure feasibility to work with data from different sensors producing equally accurate results. By analysing the design of the BIROS sensor of the DLR, the sensor parameters could be described, and their influence on the resulting imagery could be quantified. The feasibility was verified by comparing the gas flow values calculated using data from two different satellite sensors. The results obtained are very similar. The model proposed reveals potential to improve the global monitoring of gas flaring.